Spatiotemporal organisation of protein nanoclusters in adhesion complexes

PhD Thesis

Sarah Keary

February 2022

ICFO-Institut de Ciències Fotòniques

UPC-Universitat Politècnica de Catalunya

Supervised by:

Prof. Dr. María García-Parajo (Supervisor)

Dr. Felix Campelo (Co-Supervisor)

Sciences provide an understanding of a universal experience, Arts are a universal understanding of a personal experience... they are both a part of us and a manifestation of the same thing... the arts and sciences are avatars of human creativity

-Mae Jemison

Abstract

Adhesion complexes are dense protein platforms that initially form at the cell membrane as unstable nascent adhesions to then transition through different maturation steps to form more stable structures such as focal adhesions (FAs) and fibrillar adhesions (fAs). These adhesions have been studied at length for many years and have been shown to play critical roles in cell migration, differentiation, mechanosensing and many other fundamental cellular processes. Although extensive studies have been carried out over tens of years, many aspects regarding the spatiotemporal organisation of adhesion complexes still remain ill-defined. This is, in part, owing to the immense number of interacting partners involved, but also due to the lack of suitable techniques to address the smallest scales of spatial organisation. In a pioneering contribution from the Waterman´s group in 2010, it was shown that proteins of the adhesion complex are organised at the nanoscale as stratified layers in the axial direction. Importantly, such layers and their particular axial location are directly connected with their specific function: in the process of adhesion, mechanosensing, signalling, linkage to the actin cytoskeleton and force generation for mechanotransduction and mechanoresponse. A conclusion from these studies is that organisation is directly linked to function. Surprisingly, the existence and/or potential importance of an equivalent nanoscale organisation at the lateral plane of the membrane has received, until now, much less attention. Indeed, most studies today still consider adhesion complexes as large patches of laterally homogenously distributed proteins.

The main goal of this thesis has been to contribute to the understanding of the nanoscale lateral organisation of key proteins in adhesion complexes. For this, we exploited single molecule localisation-based super-resolution microscopy STORM to visualise with nanometre spatial resolution the lateral organisation of five key components of the adhesion complex: the two integrins, $\alpha_5\beta_1$ and $\alpha_v\beta_3$, and three of their adaptor proteins: paxillin, talin, and vinculin.

We first established that these proteins form nanoclusters of around 50 nm size that are preserved across the key proteins we investigated. Interestingly, these nanoclusters have similar size and number of localisations regardless of their localisation on the membrane, i.e., in the different adhesion structures studied, namely, FA and fAs as well as outside, and were maintained for different cell seeding times, from 90 minutes to 24 hours. These results suggest that nanoclustering

constitutes a general mechanism of adhesion protein organisation, constituting nano-hubs of functional activity. When studying how protein organisation in nanoclusters changes as a function of adhesion time, we revealed a two- and a four-fold increase in the density of $\alpha_5\beta_1$ and $\alpha_v\beta_3$ clusters, respectively, for cells that spread for 24 h as compared to those that spread for 90 min. Surprisingly, no significant increase in cluster density as a function of seeding time was observed for the adaptor proteins. Furthermore, an in-depth analysis of our integrin data suggests that the increase in the density of integrin nanoclusters is due to selective targeting of new integrin nanoclusters to the basal membrane. The disparity between the nanocluster density of integrins and their adaptors indicate that only a fraction of integrins are fully engaged with their partners, consistent with the dynamic activation-deactivation states of integrins.

Following on from this, we then focused on mapping the distribution of these nanoclusters, first by measuring the shortest intercluster distance (nearest neighbour distance; NND) between clusters of the same protein, and second by considering the shortest distance between clusters of different proteins. We found a clear physical segregation of nanoclusters of the same protein around $\sim$55 nm, which is established early on after cell seeding (we observed it already at 90 min after seeding) for $\alpha_5\beta_1$ and their adaptors and maintained after 24 hours. Interestingly, $\alpha_v\beta_3$ nanoclusters exhibited a more random distribution at earlier seeding times and progressively reached similar lateral segregation at 24 hours. Concomitant with this lateral segregation, we observed an enrichment of all proteins at distances between 100-200 nm. Our observations are fully consistent with the existence of a critical distance spacing between integrins needed to support adhesion and for the stabilisation of focal adhesions. Furthermore, we found that the relative distribution of nanoclusters of different proteins is predominantly random, with the exception of $\alpha_5\beta_1$ and paxillin, which organise with a separation of 50 nm. Such an unexpected random distribution between integrins and their adaptors might reflect the dynamic and short-live active state of integrins, so that together with our imaging conditions, we are not currently able to capture full engagement of integrins within the full population of proteins inside adhesion complexes.

Finally, we evaluated and described the mesoscale organisation of nanoclusters inside adhesions. Specifically, we computed the shortest distance between a nanocluster and the edge of the adhesion and studied how the distance to the edge depends on the NND between clusters of different proteins. Remarkably, we found a preference for $\alpha_5\beta_1$ nanoclusters to be at the edge of the adhesions and in close proximity to their adaptors in a peripheral belt region of the adhesions.

Altogether, the results of this thesis demonstrate a clear lateral and hierarchical organisation of integrins and their adaptors inside FAs. Based on our results (together with extensive literature in the field), we propose that one population of $\alpha_5\beta_1$ nanoclusters and their adaptors preferentially localise close to the edge of adhesion complexes regulating the process of adhesion and probably actively engaged to the actomyosin machinery. A second population of $\alpha_5\beta_1$ and most of the $\alpha_v\beta_3$ nanoclusters organise more randomly at the centre of the adhesions, with a dynamic and brief engagement to their adaptors, probably committed to the process of mechanotransduction. As a whole, similarly to the axial organisation of adhesion proteins, we postulate that the lateral nano- and meso-scale organisation of adhesion proteins are strictly related to and important for the functions of adhesion, mechanosensing and mechanotransduction.

Resumen

Los complejos de adhesión son plataformas densas en contenido de proteínas que se forman inicialmente en la membrana celular como adhesiones nacientes inestables para luego pasar a través de diferentes pasos de maduración y formar estructuras más estables, como las adhesiones focales (FA) y las adhesiones fibrilares (fAs). Estas adhesiones se han estudiado extensamente durante muchos años demostrándose que desempeñan funciones críticas en la migración celular, la diferenciación celular, la percepción y respuesta a fuerzas mecánicas, y muchos otros procesos celulares fundamentales. A pesar de todos estos estudios, muchos aspectos relacionados con la organización espacio-temporal de los complejos de adhesión siguen estando vagamente definidos. Esto se debe, en parte, al inmenso número de proteínas que interactúan entre sí, pero también a la falta de técnicas adecuadas para abordar las escalas más pequeñas de su organización espacial. En una contribución pionera del grupo de Waterman en 2010, se demostró que las proteínas de los complejos de adhesión se organizan en la nanoescala formando capas estratificadas en la dirección axial. Es importante destacar que tales capas y su particular ubicación axial están directamente relacionadas con su función específica: en el proceso de adhesión, mecanosensitividad, señalización, unión al citoesqueleto de actina y generación de fuerza para la mecanotransducción y la mecanorrespuesta. Una conclusión primordial de estos estudios es que la organización está directamente relacionada con la función. Sorprendentemente, la existencia y/o la importancia potencial de una organización equivalente en la nanoescala en el plano lateral de la membrana ha recibido mucha menos atención. De hecho, todavía hoy en día, la mayoría de estudios consideran los complejos de adhesión como grandes parches de proteínas distribuidas lateralmente de manera homogénea.

El objetivo de esta tesis ha sido contribuir a la comprensión de la organización lateral en la nanoescala de proteínas clave de los complejos de adhesión. Para ello, usamos la técnica de microscopía de super-resolución STORM para visualizar, con resolución espacial nanométrica, la organización lateral de cinco proteínas del complejo de adhesión: dos integrinas, $\alpha_5\beta_1$ y $\alpha_v\beta_3$, y las proteínas adaptadoras, paxilina, talina y vinculina.

En primer lugar, establecimos que estas cinco proteínas forman nanoagregados de $\sim$50 nm de tamaño. Curiosamente, tanto su tamaño como el número de

localizaciones son similares, independientemente de su localización en la membrana, es decir, tanto en FAs y fAs, así como fuera de las adhesiones, manteniéndose constantes durante diferentes tiempos de siembra celular. Estos resultados sugieren que la nanoagregación constituye un mecanismo general de organización de proteínas de adhesión, constituyendo nanocentros de actividad funcional. Además, revelamos un aumento en la densidad de los agregados de $\alpha_5\beta_1$ y $\alpha_v\beta_3$ en células extendidas por 24 h en comparación con 90 min, mientras que la densidad de agregados de las proteínas adaptadoras se mantuvo constante. Esta disparidad en densidades indica que solo una fracción de las integrinas interacciona con sus adaptadores, consistente con la existencia de estados dinámicos de activación-desactivación de las integrinas.

También nos focalizamos en mapear la distribución de estos nanoagregados, midiendo la distancia más corta entre agregados de la misma proteína, y luego, considerando la distancia más corta entre agregados de diferentes proteínas. Encontramos una clara segregación física de agregados de la misma proteína de alrededor de ~55 nm, y que ésta se establece temprano después de la siembra celular para $\alpha_5\beta_1$ y sus adaptadores, y se mantiene hasta 24 h. Curiosamente, los agregados de $\alpha_v\beta_3$ exhibieron una distribución más aleatoria en tiempos tempranos de siembra, alcanzando progresivamente una segregación lateral similar a 24 h. Junto con esta segregación lateral, observamos también un enriquecimiento de todas las proteínas a distancias entre 100–200 nm. Nuestras observaciones son consistentes con la existencia de un espaciado crítico entre las integrinas, necesario para sustentar la adhesión y estabilizar las FAs. Además, encontramos que la distribución espacial relativa para los nanoagregados de diferentes proteínas es aleatoria, lo cual podría reflejar el estado activo dinámico y de corta duración de las integrinas, de modo que con nuestras condiciones experimentales en este momento no podemos discernir la participación de aquellas integrinas activas dentro de la población total.

Finalmente, evaluamos la organización en la mesoescala de los nanoagregados en las FAs, específicamente, en los bordes y el centro. Sorprendentemente, encontramos una preferencia de los nanoagregados de $\alpha_5\beta_1$ para situarse en el borde de las FAs y cerca de sus adaptadores en una región periférica a los bordes.

En conjunto, nuestros resultados demuestran una clara organización lateral y jerárquica de las integrinas y sus adaptadores dentro de las FAs. Proponemos que una población de nanoagregados de $\alpha_5\beta_1$ y sus adaptadores se localizan preferentemente cerca del borde de los complejos de adhesión para regular el proceso de adhesión y probablemente interaccionando activamente con la maquinaria de actomiosina. Una segunda población de $\alpha_5\beta_1$ y la mayoría de los nanoagregados de $\alpha_v\beta_3$ se organizan de forma aleatoria en el centro de las FAs con una interacción dinámica y breve con sus adaptadores, posiblemente involucrados en el proceso de mecanotransducción. En conjunto, y en analogía a su organización axial, postulamos que la organización lateral en la nanoescala y mesoescala dentro de las FAs es importante para las funciones de adhesión, mecanosensibilidad y mecanotransducción.

Table of Contents

Chapter 1

Biological background and state-of-the-art techniques

The aim of this chapter is to provide the reader with the necessary general background information that will aid in the understanding of the methodologies used throughout this thesis as well as the biological background to rationalise our findings and experimental plans for the future. We first provide a description of adhesion complexes and the main proteins studied in the thesis. We then provide a section that introduces the field of mechanobiology and the involvement of adhesion proteins for mechanosensing and mechanotransduction. The chapter continues with two more technical sections, one of them describing the various techniques used in our field for cell imaging and a second final one that provides an overview on different approaches to probe the effect of mechanical stimuli on cells.

1.1 Introduction

In order to tackle many diseases affecting our lives today, it is vital that we understand what is occurring at the cellular level. A common example is cancer. While this is a very general term for a disease that can manifest itself in very different variations, it is a useful example, as most people, even those outside of the scientific field, are familiar with it. Although there are many variations of the disease there are also certain commonalities, for example, cells proliferate at a higher rate and often cell migration increases leading to what is known as metastasis (Friedl and Wolf, 2003; Feitelson et al., 2015). At the cellular level, we now know that cancerous cells proliferate and migrate more. However, in order to address this behaviour, we must understand the molecules that play a role in these cellular processes. A family of molecules that feature strongly in these processes is known as integrins (Desgrosellier and Cheresh, 2010). These proteins are transmembrane receptors found on the surface of many cell types and are the central component of adhesion complexes. It is around these proteins and the complexes that they form that this thesis is centred.

Various imaging techniques have been exploited over more than 30 years in order to visualise how the different molecular components in living cells and subcellular structures interact and even the timescales involved. Since the earliest electron microscopy images of the dense adhesion areas in the 1970s (Abercrombie et al., 1971) through to the modern day use of fluorescence imaging to study the behaviour of adhesions in migrating cells (Hu et al., 2014) or the behaviour of individual proteins inside adhesions (Orré et al., 2021), we have gained a wealth of information. Now, with the technical developments that led to the merging of cell manipulation devices with super-resolution fluorescence imaging techniques, we can image specific proteins of interest in adhesions with improved resolution under different conditions (Massou et al., 2020). This chapter will first cover an introduction to adhesion complexes, why they are fascinating and the challenges we face while trying to decipher the details of their inner workings, with a look at the key components that we believe are vital background for this thesis. We will then provide an overview of different imaging techniques used to study them. Finally, we introduce a number of different techniques used to probe cellular response to changes in the local environment and the application of mechanical stimuli.

1.2 Adhesion complexes: an overview

Adhesion complexes can be generally classified into two major groups: cell-cell adhesions and cell-matrix/extracellular matrix (ECM) adhesions. Cell-cell adhesions, as the name suggests, are formed between adjacent cells, and they use cadherin proteins, such as E-cadherin, as adhesion receptors. Cell-cell junctions not only allow cells to communicate during periods of collective cell migration (Cai et al., 2014), but also control epithelial integrity, embryonic development, and, in general, are key for tissue formation and multicellularity (Van Roy and Berx, 2008). In contrast, cell-matrix adhesions form between cells and their extracellular environment. Specifically, cell-matrix adhesions are established by the interaction between integrin adhesion receptors on the cell membrane and their ligands on the ECM. The ECM is the macromolecule-rich network that is assembled by polysaccharides and proteins secreted by the cell, which fill the interstitial space between cells in the tissue, covered in more detail below. Cell-matrix interactions allow cells to attach, migrate, degrade or sense the local environment, depending on the cell type and ECM molecular composition (Chen et al., 1998; Oharazawa et al., 1999). For example, cells of the immune system form structures termed podosomes, which allow the cells to adhere to their substrates while degrading the local environment enabling migration across barriers (Calle et al., 2006; Rottiers et al., 2009; Cougoule et al., 2010); while adherent cells, such as fibroblasts, attach to their substrate through so-called adhesion complexes, which are required for essential cellular processes like migration (Kim and Wirtz, 2013). In this thesis, we will focus on the latter integrin-based, cell-matrix adhesion complexes formed in fibroblasts.

Cell-matrix adhesion platforms, which originate at the cell membrane when integrins form contacts with their extracellular ligands are known as nascent adhesions (Henning Stumpf et al., 2020). These nascent adhesions are seen in abundance at the leading edge of the cell, in the lamellipodia, Figure 1.1.

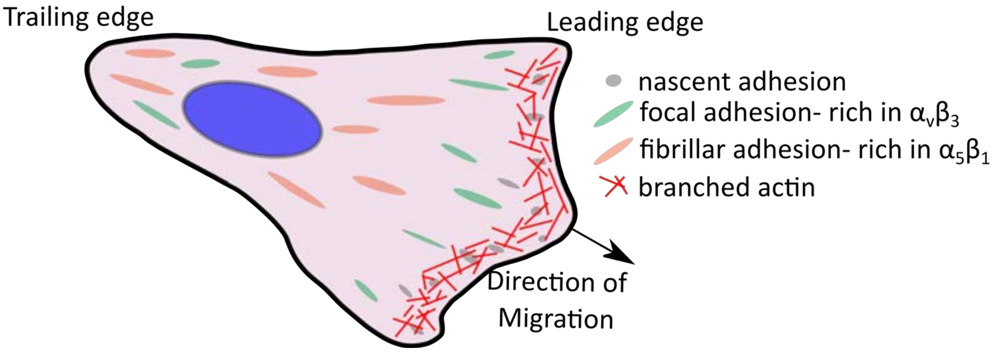

Figure 1.1 *Migrating cell and its integrin-mediated adhesions*

The cartoon shows how a cell polarises for cell migration with the leading edge with is lamellipodium and the trailing edge. The lamellipodium has a high rate of nascent adhesion formation amongst the branched actin. The mature adhesions are shown in the body of the cell. Fibrillar adhesions being rich in $\alpha_5\beta_1$ integrins and the focal adhesions are shown to be rich in $\alpha_v\beta_3$. Adapted from *Seetharaman and Etienne-Manneville, 2018*.

Nascent adhesions are dynamic structures that assemble and disassemble rapidly, with only a small percentage maturing into larger adhesion complexes, known as focal adhesions (Thievessen et al., 2013). Although we do not yet have a complete picture of how they form and progress through the maturation steps, there is evidence indicating that the biochemical composition of adhesion complexes varies during their maturation, with adaptor proteins such as paxillin, talin, and vinculin being important components (Zaidel-Bar et al., 2003; Thievessen et al., 2013; Saxena et al., 2017). Interestingly, a recent study showed that the timing of adaptor protein arrival to the adhesions is important for the maturation to FAs, and that nascent adhesions that bind a pre-formed complex of talin and vinculin are more likely to mature into FAs (Han et al., 2021). Another important factor for nascent adhesion maturation into FA is the application of integrin-transmitted forces between the ligand at the ECM and the actin cytoskeleton, which contribute to adhesion stabilisation and final maturation to an FA (Choi et al., 2008; Oakes et al., 2012). Although not always considered to be a part of the adhesion maturation process, it has been shown that another type of adhesion known as fibrillar adhesions (fAs) originate from mature FAs. The translocation of proteins – in particular the integrin $\alpha_5\beta_1$ and the adaptor protein tensin – from FAs leads to the formation of these thin linear structures, fAs, in the central region of the basal cell membrane (Smilenov et al., 1999; Zamir et al., 2000).

The different cellular processes regulated by adhesion complexes are highly influenced by the biochemical and mechanical environment. Importantly, the extent of many of these biochemical interactions has been shown to be regulated by the mechanical properties of the cell environment, such as the rigidity and viscosity of the substrate to which cells adhere (Guerra et al., 2010; Elosegui-Artola et al., 2016; Bennett et al., 2018). In this thesis, we focus specifically on two types of adhesion complexes: focal adhesions (FAs), and fibrillar adhesions (fAs), which mediate cell attachment to the ECM, and on how key adhesion proteins –that are involved in adhesion to and sensing of the glass substrate – are spatially organised within these dense cell-ECM adhesions. FAs are often considered the final stage of maturation of adhesion complexes. This process is initiated with the formation of force-independent nascent adhesions, which upon force application grow and mature to large FAs (with sizes > 3 μm^2) (Gardel et al., 2010). The dynamic assembly and disassembly of adhesion complexes play a role in cell migration and they have been shown to be influenced by the stiffness of the local environment (Wormer et al., 2014). In this way, FAs act as mechanosensitive platforms. FA size and stability are influenced by the substrate they form on, because a number of FA components undergo conformational changes upon force application, which in turn trigger or disrupt downstream signalling pathways thereby influencing the final physiological outcomes, in a process known as mechanotransduction (Hoffman et al., 2011; DuFort et al., 2011; Li et al., 2016; Sun et al., 2016a). In comparison to FAs, fAs have not been so extensively studied. Despite this, we know that fAs are preferentially found in the central regions of the cell membrane where proteins such as $\alpha_5\beta_1$ and tensin colocalise. Tensin is seen to relocate from FA areas and this relocation is influenced by actin interactions (Zamir et al., 2000). These adhesions have also been shown to restructure the underlying fibronectin (FN) into fibrillar structures (Zamir et al., 2000; Katz et al., 2000; Pankov et al., 2000). More recently, a study from the Ivaska lab showed that fAs are mechanosensitive (Barber-Pérez et al., 2020). They used stiffness gradient gels and showed that for cells plated on soft substrates the active $\alpha_5\beta_1$-positive fAs are significantly shorter in comparison to the same type of adhesion on stiff substrates (Barber-Pérez et al., 2020). They also showed that this mechanosensitive elongation of fAs is tensin-dependent by running the same experiments in cells with tensin expression silenced using siRNA. As fAs are responsible for the organisation of FN and therefore aspects of their own microenvironment, further studies into the mechanisms controlling their mechanosensitive nature will provide important insights into the cell's ability to respond to mechanical cues as a whole.

1.2.3 Integrins

Integrins are obligate heterodimeric receptors that consist of an α and a β subunit, each of which is a single-pass type I transmembrane protein with an N-terminal extracellular domain, an α-helical transmembrane domain, and a short C-terminal cytoplasmic tail (Tamkun et al., 1986). In mammalian cells, there are 18 different α subunits and 8 β subunits, which generate the 24 known integrin heterodimers (Kechagia et al., 2019). The roles that these different integrin heterodimers play depend on the dimer subunits as well as on the ECM ligands to which they engage. Moreover, integrins can adopt different conformations: bent, extended closed, and extended open, which correspond to their activation state (see Figure 1.2) (Su et al., 2016).

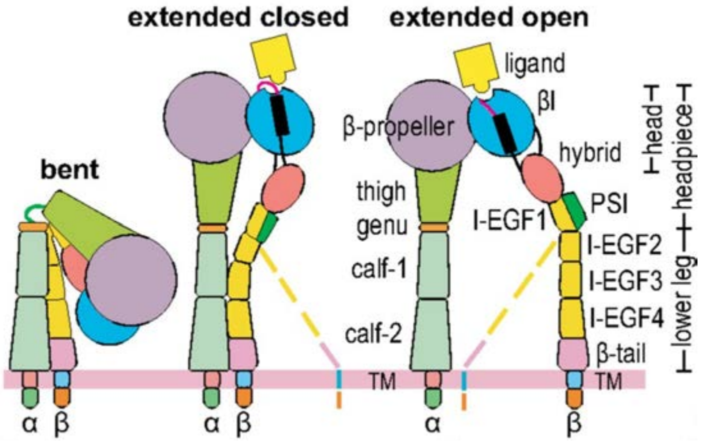

Figure 1.2 *Different conformational states of an integrin heterodimer*

The left of the image shows the α and β subunits in a bent conformation where the ligand binding site is not accessible. The integrin in the centre is in an extended closed conformation, with the α and β subunits extended but still closed on the lower leg (the extracellular domains that are the most proximal to the transmembrane (TM) domain), preventing ligand binding to the β subunit head. On the right, the integrin is in the extended open conformation, where the α and β subunits are extended and the lower β-leg is separated from α subunit, altering the conformation of the head group to open and thereby allowing ligand binding. Dashed lines show the possible variations for the flexible β-leg, and the names of the different extracellular domains and regions are shown. Image adapted from *Su et al., 2016.*

The activation of integrins is a stochastic process and the length of time they remain active depends on a number of factors, such as the ECM ligand they bind to at the extracellular domain, or the adaptors that bind to the cytosolic domain, which are controlled via outside-in and inside-out signalling, respectively (Takagi et al., 2003; Wegener et al., 2007). Inside-out signalling is how integrins are activated from cytosolic cues where adaptors interact with the short cytosolic tail and induce a conformational change that allows ligand binding (Hu and Luo, 2013). For example the cytosolic protein Rap 1 binds talin via its partner Rap 1-GTP-interacting adaptor molecule (RIAM), which aids in the delivery of talin to the cytoplasmic tail of the β subunit (Han et al., 2006). Talin then binds to the β subunit activating the integrin (Calderwood et al., 1999). On the other hand, outside-in signalling occurs when integrins bind to their ligand stabilising the conformational state of the integrin, which in turn leads to integrin clustering further enhancing the valency and avidity for the EMC ligand (Hu and Luo, 2013). The multitude of heterodimeric pairs, the different possible interactions with adaptors and ligands, as well as the complex feedback and crosstalk between them makes the study of integrins and the roles they play in adhesion complexes a very challenging task. To illustrate this point, let us consider the two integrins at the centre of this thesis: $\alpha_5\beta_1$ and $\alpha_v\beta_3$, which are both found in FAs. These two integrins bind to the tripeptide of Arginine (R), Glycine

(G), and Aspartate (D), commonly referred to as the RGD sequences, which is found in certain ECM proteins (Pytela et al., 1985; Ruoslahti, 1996). However, this sequence is not unique but it is shared amongst a number of ECM proteins, such as FN and vitronectin (VN). It has been shown that $\alpha_5\beta_1$ has a higher affinity for FN whereas $\alpha_v\beta_3$ can bind both ECM ligands, with a preference for VN (Bharadwaj et al., 2017; Bachmann et al., 2020). Another level of complexity arises from the different intracellular proteins that directly or indirectly interact with the integrin cytosolic tails. For example, the pair $\alpha_5\beta_1$/talin is more commonly found in FAs whereas $\alpha_5\beta_1$/tensin are found to be engaged in fAs (Katz et al., 2000). Despite these challenges, an ongoing area of research is centred around understanding the specific roles of $\alpha_5\beta_1$ and $\alpha_v\beta_3$ integrins in adhesion complexes, and how these roles are determined and controlled (Roca-Cusachs et al., 2009; Schiller et al., 2013; Bharadwaj et al., 2017; Diaz et al., 2019).

The signalling cascades triggered by ligand and adaptor interactions and integrin activation regulate the phosphorylation levels of certain proteins, like myosin light chain (MLC), as well as the activity of different actin polymerisation factors. These downstream events in turn influence the forces transmitted across the adhesion complex, due to actomyosin contractility and by actin polymerisation and retrograde flow, which feed back to the state of the ligand-integrin-adaptors interactions. This reaction and translation of forces by the cell is a major research topic and more details will be covered in the mechanobiology section 1.3 below.

A final important characteristic of integrins is their ability to form nanoclusters at the plasma membrane, as has been reported for different integrins in different cell types (van Zanten et al., 2009; Changede and Sheetz, 2017; Spiess et al., 2018). Interestingly, individual integrin nanoclusters were shown to solely contain either active or inactive integrins, but not a mix of integrins in different states (van Zanten et al., 2009; Spiess et al., 2018). Despite this, we do not yet fully understand the precise need for integrin nanoclustering, whether it is a universal characteristic for all integrins, the number of molecules involved, or what determines and controls the nanocluster sizes. This is why we continue to study these proteins, and the complexes they form, with the aim of providing a greater insight and understanding to some of the cells most fundamental processes and how they are controlled.

1.2.4 Extracellular matrix

The ECM is the non-cellular network that consists of macromolecules produced and secreted by the cell, which contributes to a tissue's structural stability and mechanical properties (Frantz et al., 2010). Cells interact with the ECM via different receptors localized on the plasma membrane and this interaction, as mentioned previously, is finely tuned by the composition and organisation of the matrix. Collagens, FN, VN, and laminins are well-known examples of fibrous proteins forming the ECM (Yue, 2014). Collagens are the most abundant proteins in the human body and, as such, play a fundamental role in ECM structure and function. In addition, FN is also a vital component of the ECM that forms dimers to physically link collagen fibrils in the ECM to cell membrane receptors, such as integrins. Particularly, FN binds α_v-class and $\alpha_5\beta_1$ integrins via its RGD motif and $\alpha_5\beta_1$ also interacts with the synergy site found in the ninth type-III domain of FN, which has been shown to be necessary for this integrin to form a stronger tensioned state bond (Friedland et al., 2009). When cells bind to FN, they restructure the ECM protein into fibrils mainly through $\alpha_5\beta_1$ bonds (Mao and Schwarzbauer, 2005), which enable the cell to migrate within the ECM. Because of the important role of FN in cell adhesion and migration, we decided to carry out our experiments by seeding cells on FN-coated glass, allowing $\alpha_5\beta_1$ and $\alpha_v\beta_3$ to bind it forming adhesion complexes, FAs and fAs.

1.2.5 Cytosolic components of the adhesion complexes

Compiling a full review of all the cytosolic proteins involved in adhesion complexes would result in a tome at least as long as the thesis itself, which we think illustrates the complexity and richness of these cellular structures. In the quest to map out all the proteins involved in integrin adhesion complexes, the Humphries lab integrated several proteomes and came up with a “meta adhesome” containing 2,412 proteins (Horton et al., 2015). This meta adhesome was curated and analysed to establish a consensus adhesome formed by 60 proteins (Horton et al., 2015). Even this reduced number exceeds the scope of this thesis so we will therefore only cover the details of the key adhesion proteins that we have experimentally addressed in this thesis: paxillin, talin, and vinculin.

Paxillin was identified over three decades ago (Turner et al., 1990) and is now commonly used as a marker protein for FA visualisation by fluorescence microscopy. Paxillin localisation to adhesion sites is controlled by its four C-terminal LIM domains, which directly bind vinculin, focal adhesion kinase (FAK), and kindlin (Brown et al., 1996; Theodosiou et al., 2016; Zhu et al., 2019). Paxillin is considered to be a signalling protein and more recently it has been shown that there is an association with the β-tail of integrin also via its LIM domain (Soto-Ribeiro et al., 2019; Ripamonti et al., 2021).

Talin is one of the key proteins that can directly bind to both integrins and to actin, and so it is an important link in connecting the ECM to the cell's cytoskeleton. Although they are commonly referred to as simply talin, vertebrates express two talin isoforms, talin1 and talin2, which, despite sharing a high sequence similarity, play non-redundant roles in e.g., fine-tuning signalling in adhesions (Gough and Goult, 2018). Talin structure comprises an N-terminal head domain and, connected via a linker neck domain, a C-terminal rod domain (Figure 1.3). The talin head region includes a FERM domain consisting of four subdomains (F0, F1, F2, and F3). Although the FERM domain accounts for only ∼400 of the ∼2500 amino acids comprising the full talin, it is vital for talin-integrin binding. In particular, the F3 subdomain directly binds to the β subunit's cytosolic tail. However, this is not sufficient to activate the integrin, requiring the other head domains to maintain the integrin in a high-affinity conformation through interactions with components of the cell membrane such as the F2 domains with PtdIns(4,5)P_2 (Saltel et al., 2009; Iwamoto and Calderwood, 2015). The talin rod consists of 13 domains (R1–13), two of which contain actin binding sites (ABS), while the rod also contains at least 11 vinculin binding sites (VBS) (Gingras et al., 2005). When talin is bound to actin via its C-terminal ABS there is force transmission across the rod revealing many VBS that are normally buried and only get exposed upon application of mechanical forces that stretch the molecule open (Gough and Goult, 2018). Interestingly, talin's R3 domain is the weakest domain and the first to unfold under force (Yao et al., 2016), and it has the capability to bind both the effector protein RIAM and vinculin. RIAM can bind talin in its relaxed conformation, which contributes to inside-out integrin activation (Lee et al., 2009). It has been shown that a force of ∼5 pN is required to reversibly unfold talin R3 domain (Yao et al., 2016). Furthermore, actomyosin has been seen to act as a catch bond with a peak lifetime at 6 pN (Guo and Guilford, 2006) and rupture forces were measured to be between 8–15 pN (Nakajima et al., 1997; Nishizaka et al., 1995). All of these measurements show that myosin is capable of withstanding the forces need to unfold talin. Application of such force leads to the exposure of talin's cryptic VBS, which leads to vinculin binding and concomitant RIAM unbinding, and the eventual stabilisation of the complex for the growth of mature FAs. Therefore, talin is a perfect example of a mechanosensitive switch molecule whose role depends on its environment and the force exerted across it.

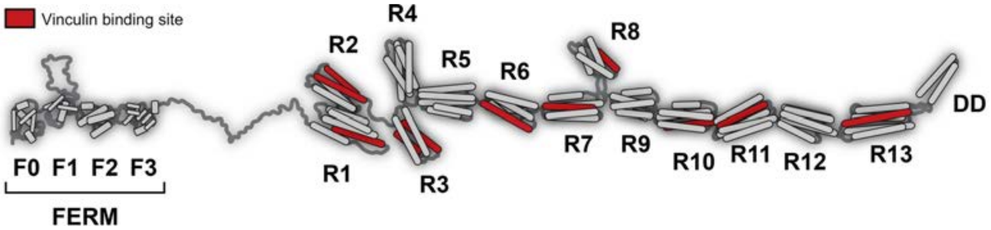

Figure 1.3 *Talin structure*
The structure of talin is shown, depicting the N-terminal FERM domain (F0–F3) linked to the rod domain via an unstructured linker. The talin rod contains 13 domains (R1–R13) and a dimerisation domain (DD), with the VBS shown in red (Gough and Goult, 2018).

Vinculin was discovered in 1979 (Geiger, 1979) and originally named simply as 130 k protein, because of its 130 kDa molecular weight. It was only later that vinculin was given its current name, when it was seen to localise at cell adhesions and was proposed to be involved in tethering actin to the membrane (Geiger et al., 1980). In the following decades, as the field uncovered more about the inner workings of cell-ECM adhesions, it became clear that vinculin is involved in important interactions that control adhesion dynamics. We now know that vinculin is found in two conformational states (Figure 1.4): an auto-inhibitory conformation, where the head and tail are bound blocking the binding sites for many ligands; and an open conformation, often referred to as the “active” form, which localises to adhesions and binds talin and actin (Johnson and Craig, 1994; Bakolitsa et al., 2004). The binding of two ligands is required to engage vinculin and open the conformation from the auto-inhibitory head-tail bond to the active state, Figure 1.4 (Chen et al., 2006; Peng et al., 2011). This engagement of vinculin with adhesion molecules influences the adhesion turnover as well as rate of formation for nascent adhesions and the percentage of adhesions that go on to form mature FAs (Saunders et al., 2006; Thievessen et al., 2013).

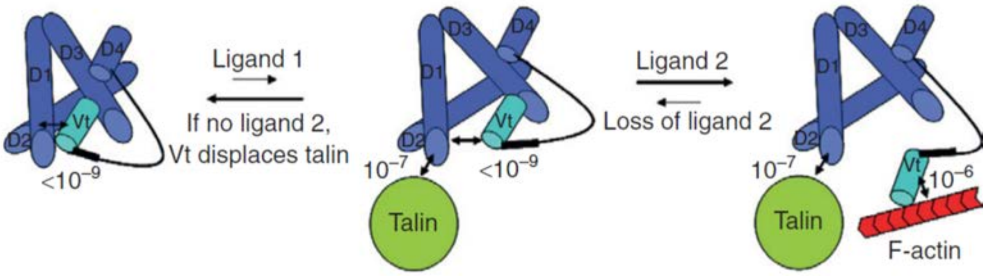

Figure 1.4 *Schematic of the disruption of vinculin auto-inhibition by talin and actin*
Left panel shows the structure of vinculin in its auto-inhibitory conformation with vinculin tail, Vt, bound to the head domain with a strong head-tail interaction of K_d less than 10^{-9} indicated. Middle panel shows that talin can bind the vinculin head but the binding affinity ($\sim 10^{-7}$ M) is not great enough to overcome the binding between head and tail. Finally, the right panel depicts the need for two ligands (vinculin and F-actin) to bind and unfold vinculin (Peng et al., 2011).

1.3 Mechanobiology and the involvement of adhesion proteins

Mechanobiology is the study of how cells and tissues respond and adapt to mechanical stimuli such as forces. This includes the study of how cells *(i)* apply mechanical forces to their surroundings, *(ii)* sense external mechanical forces, *(iii)* relay or transduce mechanical signals, and *(iv)* eventually respond to these mechanical stimuli. A key finding in mechanobiology, which serves to illustrate the importance of this field, was the discovery that pluripotent stem cells differentiate into different cell lines depending on the rigidity of the substrate they are grown on (Engler et al., 2006; Kshitiz et al., 2012). Hence, stem cells on stiff substrates differentiate into osteoblasts whereas cells on soft substrates become neurons (Engler et al., 2006; Kshitiz et al., 2012). Mechanobiology is often subdivided into two major but intertwined areas: mechanosensing and mechanotransduction. Mechanosensing is the set of mechanisms by which a cell or group of cells detect (*sense*) the forces applied, for example when the application of external force results in the squeezing open of ion channels or in conformational changes of proteins that changes cell behaviour. Mechanotransduction describes the mechanisms by which cells convert (*transduce*) mechanical forces into biochemical responses. Although it is not the purpose of this thesis to review in detail the field of mechanobiology, it would be remiss of us to discuss adhesion complexes without providing an overview of some key details in particular to understand the direction and long-term goals of our research. Along those lines, it is important to note that integrins are capable of forming different types of bonds with their ligands, such as catch bonds and slip bonds. A catch bond is a non-covalent bond whose dissociation lifetime increases with tensile force applied. Whereas, a slip bond is one where the opposite is true, meaning that the dissociation lifetime decreases with an increase in tensile force applied across it. At the molecular level the bond formed between $\alpha_5\beta_1$ and FN acts as a catch bond for pulling forces less than 30 pN and above this force it is a slip bond (Kong et al., 2009).

The molecular clutch model is another important concept in mechanobiology, where it represents the serial link between the actin cytoskeleton and the ECM, and is based on the analogy of the clutch of an automobile engine, where the clutch engages or disengages so the car can move. In this case the cell requires engagement of the adaptor proteins in order to transmit the signal and initiate cellular response. The molecular clutch model was first proposed as a way to understand what drives and controls the speed of actin retrograde flow (Mitchison and Kirschner, 1988). Even in this early publication, the authors described how the engagement of talin with the integrin and actin can act as a molecular clutch controlling the rate of actin retrograde movement. More recently, the molecular clutch model was proposed as a mechanism to explain how the cell interprets its local environment (Chan and Odde, 2008). In there, the authors proposed an expanded version of the clutch model to explain how cells change their behaviour when adhered to substrates of different stiffness. This model considers that myosin exerts forces on actin that result in constant retrograde flow of actin. Next, because molecular clutches bind (unbind) actin at a certain k_{on} (k_{off}) rate, when the system is engaged and force is transmitted to the ECM, this binding acts against the retrograde flow. Due to the force exerted by myosin on actin, the clutch is stretched until the force transmitted is large enough, so the bonds are destabilised and the interactions break apart. How abruptly this rupture occurs depends on the stiffness of the clutch and the substrate. If the substrate stiffness is relatively high, the force builds up rapidly across the clutch and the bond breaks. This regime is termed “frictional slippage”. However, if the substrate is soft and malleable, the force exerted across the clutch builds more slowly allowing sharing of the load among neighbouring clutch bonds. This leads to a higher overall tension build-up until it becomes too high and results in a cascade of ruptured clutch bonds. This scenario is termed “load-and-fail”. The initial molecular clutch model has been recently adapted by the group of Roca-Cusachs to account for the importance of talin unfolding (Elosegui-Artola et al., 2016). The model shows that when only considering the on-off talin binding rates, one achieves a biphasic relationship between traction force and substrate stiffness. However, when the force-dependent unfolding rate of talin, which results in vinculin binding and molecular clutch stabilisation, is included into the model, the outcome is that of a monotonically increasing relationship between substrate stiffness and cell traction forces. The predictions of this mathematical model were experimentally tested by seeding cells on substrates of increasing rigidity and embedding beads to allow for traction force microscopy measurements. In control cells, where talin can unfold and vinculin bind to it, their results matched with the model predictions. Furthermore, when the same experiment was carried out using either talin1 knock-out cells depleted of talin2 by shRNA or cells expressing talin mutants that did not bind integrins or could bind but not activate integrins, the results indicated the existence of a biphasic relationship, as theoretically predicted by the model in the absence of talin unfolding. They also showed that in wild-type cells, as the substrate stiffness increases, there is translocation of the transcriptional regulator YAP from the cytosol to the nucleus, indicating that substrate stiffnesses regulates the way cells control gene transcription and, consequently, protein synthesis, i.e., mechanotransduction.

1.4 State-of-the-art techniques for imaging adhesion complexes

The use of microscopy to study minute specimens stretches back to the time of Galileo Galilei, 1609. At that time, the magnification was very modest (in the order of 10x), and there were no other detectors than the human eyes, so the observations relied on the observer to transcribe what was seen. Nowadays, and thanks to our current understanding of optics and how light works, we have been able to build microscopes that allow us to observe the inner structures and behaviour of individual cells. In parallel to the advancement of light microscopy, the development of electron microscopy (EM) as far back as the early 1930 allowed the exploration of different cellular structures (Kruger et al., 2000). These advances were incredibly important for the development of modern cell biology from the 1950s onwards. However, as scientists, we always want more, more detail providing greater understanding. It is this quest for expanding our knowledge of the natural world that has driven scientific discoveries over the past decades.

Although EM provided exquisite detail of the structure of certain organelles, the development of antibody labelling and the expression of fluorescent proteins opened up many doors in the field of cell biology. The use of genetically-encoded fluorescent proteins revolutionised the field allowing the distribution and dynamic behaviour of specific proteins to be studied in living cells. Furthermore, the development of organic fluorescent dyes with various different absorption and emission spectra as well as high stability and quantum yield allowed for multicolour fluorescent imaging of nanostructures in fixed cells. The following sections will cover the basics of fluorescence as well as an overview of some of the techniques where it is implemented.

1.4.2 Fundamentals of fluorescence

Fluorescence is the physical phenomenon by which a molecule emits photons after being irradiated with light (Valeur, 2001). Upon irradiation of a fluorescent molecule in the ground state (usually a singlet state, S_0), the molecule absorbs a photon of a given frequency, v_{ex}, causing the excitation of the molecule’s electrons to a higher energy state (commonly the first excited single state, S_1). These excited electrons eventually relax to the ground state and in doing so there is a certain probability that this energy relaxation is accompanied with the emission of a photon, which is the process known as fluorescence. The emitted fluorescence photon has a lower energy (smaller frequency, ν_{em}) than the initially absorbed photon, a phenomenon known as Stokes shift. Ideally, a fluorescent molecule should have a relatively large Stokes shift, such that the excitation light can be filtered out from the emitted light (Sanderson et al., 2014).

The use of fluorescence microscopy in biology benefitted from advances in biochemical tools, such as the discovery of antibodies, which allow for the specific targeting of proteins of interest. Hence, the coupling of antibodies with fluorescent molecules allows for the labelling and visualisation of such proteins in their native cellular context. This makes it possible to investigate if proteins are associated to particular cellular structures. Further developments, such as multicolour fluorescence microscopy, made it possible to study the spatial relationship between different proteins, whereas the development of confocal microscopy allowed for a reduction of background coming from surrounding cellular structures. However, there is a very important aspect to consider when discussing microscopy and that is the resolution achievable. Biological samples often have a large number of proteins packed into a very same area and the aim is often to say if these proteins colocalise or not and this can only be determined within the limitation of the system being used.

1.4.3 Resolution and the diffraction limit

The level of detail of a fluorescence microscopy image is determined by the resolution of the microscope, which is ultimately limited by the combination of the wavelength of the excitation light and the optics implemented in the setup. This is so because the spatial resolution is fundamentally limited by the fact that light is diffracted when it passes through an aperture. In practice, this means that a point-like light source (such as each of the individual fluorescent molecules in the specimen), after being transmitted and diffracted throughout the optical components of the microscope, is detected as a broadly distributed function in the detection plane: the point spread function (PSF), which for a simple single lens system corresponds to an Airy function. This limitation was first described by Ernst Abbe in 1873 (Abbe, 1873), and therefore known as the Abbe diffraction limit, and states that for light with wavelength λ traveling through a system (optical lens) of refractive index *n* converging to a point with a half-angle θ, the minimum distance between two objects that can be resolved, *d*, is

$$d = \frac{\lambda}{2n\, sin\theta} = \frac{\lambda}{2\, NA}, \tag{1.1}$$

where $NA = n\ sin\theta$ is the numerical aperture of the optical system, which is usually in the range of ∼1–1.5, and therefore $d \approx \lambda/2$. Thus, for instance, with an NA=0.5 and λ=633 nm, the optical resolution is approximately ∼633 nm, while for an NA=1.5 and λ=488 nm, the maximum achievable optical resolution would be ∼164 nm.

1.4.4 Diffraction-limited microscopy techniques

Despite these fundamental limitations on the spatial resolution, diffraction-limited microscopy has been a very valuable tool to investigate the distribution and dynamics of cellular structures and proteins. There exist different types of microscopy depending on, for example, the illumination strategy, where certain illumination schemes are more suited to particular samples or imaging needs. Hence, choosing the optimal microscopy technique and illumination scheme depends on the cell region to be imaged (plasma membrane, cytoplasm, or nucleus), the resolution required, and/or the timescales in case dynamic information is needed. Here, we essentially restrict to two microscopy modalities that have been extensively used to investigate adhesion complexes on fixed and living cells.

1. Total internal reflection fluorescence (TIRF) microscopy

TIRF is a microscopy technique that allows imaging a very thin region of a cell just above the surface of a glass slide. TIRF takes advantage of the difference in refractive index between the glass and the cell. Depending on the angle at which the excitation laser beam arrives to the interface between the glass and the cell, light can be either refracted and propagate forward at a different angle, or reflected back into the objective. When the incidence angle is such that the beam is fully reflected, although there is no transmitted light, there appears an evanescent electromagnetic field – of the same wavelength as the incident light – that decays exponentially as it penetrates into the cell. Usually, the exponential decay of this evanescent field makes that it only penetrates the first ∼100 nm region above the glass slide. This means that imaging fluorophores on the basal cell membrane or very close to the membrane is extremely efficient (Figure 1.5, A) because there is a very strong reduction of out-of-plane and background signal emanating from the cytosol or other regions well above the cell membrane. This highly enhanced signal-to-background ratio contrasts with the situation one would observe when illuminating the sample straight through the objective in an epifluorescence configuration ("Epi", see Figure 1.5 B), where fluorescence emitted from a large volume above the glass slide is equally detected. TIRF imaging is very well suited to study membrane structures such as FAs, and, as it is a wide-field optical technique, it is also well suited to study the dynamics of membrane structures or individual proteins (see Section on Single particle tracking (SPT) below). In some circumstances, such as if one requires high-speed imaging of intracellular processes that take place well above the glass slide, the shallow penetration depth of the evanescent wave used in TIRF microscopy is a disadvantage. To overcome this, a modified illumination scheme can be applied, by shining the incident light at an angle smaller than the critical angle reached for TIRF. This results in a highly inclined and laminated optical sheet (HILO, see Figure 1.5 A), which propagates into the cell and reduces out-of-sheet light compared to epifluorescence illumination. HILO illumination has been used for fast imaging of intracellular structures (Tokunaga et al., 2008).

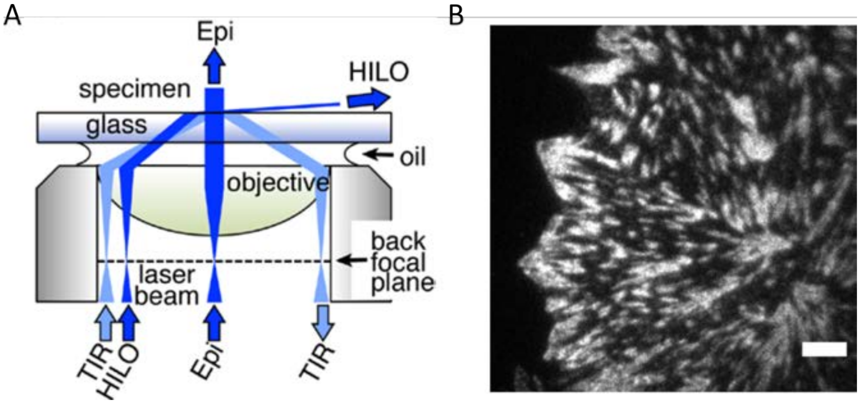

Figure 1.5 *TIRF microscopy*
(A) Different illumination paths implemented for TIRF, Epifluorescence, and HILO illumination adapted from *Manzo and Garcia-Parajo, 2015*. (B) TIRF microscopy image of FAs (paxillin and $\alpha_5\beta_1$) taken in HFF-1 cells after 90 min spreading on FN-coated glass. Scale bar 5 µm.

2. Confocal laser-scanning microscopy

As one of the most widely used imaging techniques in cell biology, confocal microscopy has led to a vast amount of scientific discoveries and beautiful multicolour images of cellular structures. On the one hand, this technique uses point-by-point illumination by focusing the excitation laser on a single point of the specimen, and the laser then scans – usually in a line-scanning mode – over the desired field of view, thereby providing a point-by-point read-out. On the other hand, with the aim of reducing the fluorescence signal originating from fluorophores outside of the focal plane, confocal microscopy uses a pinhole placed before the detector that filters out most of the out-of-focus light. This configuration results in a focal plane image of the sample (in modern confocal setups, the thickness of the focal plane is usually of the order of the wavelength of excitation laser) with high signal-to-noise ratio. The sample can also be moved through the focus of the laser in steps, resulting in z-stacks of the sample that provide insights into the three-dimensional structure of cellular components. Thanks to the improvements in optical engineering, it is nowadays possible to have a supercontinuum white light source, from which the excitation wavelengths can be tuned with high accuracy, so it is possible to devise the optimal combination of excitation lines, fluorophores, and detection filters for multicolour confocal imaging (Figure 1.6).

Many of the initial studies on FAs used diffraction-limited fluorescence microscopy techniques, such as confocal microscopy. Figure 1.6 shows an example of such images, where we can notice how similar the distribution of paxillin and vinculin are. At this level of lateral resolution (~250–300 nm), we can appreciate that the signals for these two FA proteins appear to almost perfectly colocalise. Therefore, being able to image adhesion complexes with a higher spatial resolution might provide finer details that would help in our understanding of these complexes.

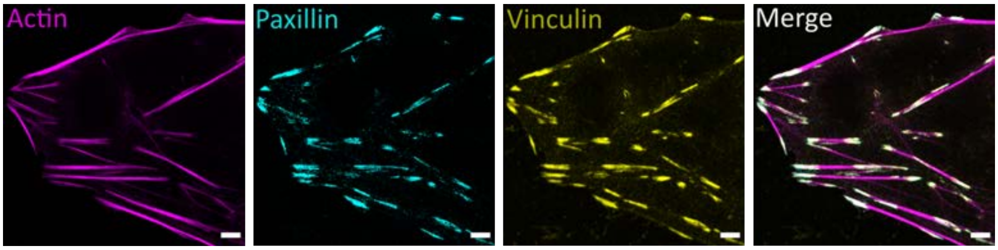

Figure 1.6 *Three-colour confocal microscopy image of FAs*
Single-plane, three-colour confocal microscopy image of mouse embryonic fibroblasts (MEFs) seeded on FN for 24 h, where the actin cytoskeleton (magenta), paxillin (cyan), and vinculin (yellow) have been labelled and imaged using a Leica SP8 setup with 100x oil objective (NA 1.4). Labelling of paxillin and vinculin was done using primary and secondary antibodies, for details see Table 2.2 and Table 2.3 of the Methods Chapter; and actin was labelled using Phalloidin-Alexa 488. Scale bar 5µm.

1.4.5 Super-resolution microscopy

The concept of super-resolution imaging is a general umbrella that covers a broad range of fluorescence microscopy techniques, where the common underlying feature is that they overcome the diffraction limit of light, providing higher spatial resolution than conventional diffraction-limited fluorescence microscopy.

1. Structured illumination microscopy (SIM)

This technique uses gratings to manipulate the excitation wave into a standing wave by illuminating the sample with patterned light (e.g., a striped pattern with a known high periodicity). Due to the interferences with the fluorescence from the small structures, this illumination scheme shifts high-frequency information (below the diffraction limit of light) into low-frequency information that can be detected after passing through the objective (the Moiré pattern effect). This frequency pattern contains sub-diffraction limit information from the small features of the cell, and if the pattern is then rotated and imaged with the sample a number of times there is an increase in the level of detail acquired from the sample. This technique then requires image processing to retrieve an image from the Fourier plane, which shows greater structural detail, see Figure 1.7 for an overview of SIM imaging (Gustafsson, 2000).

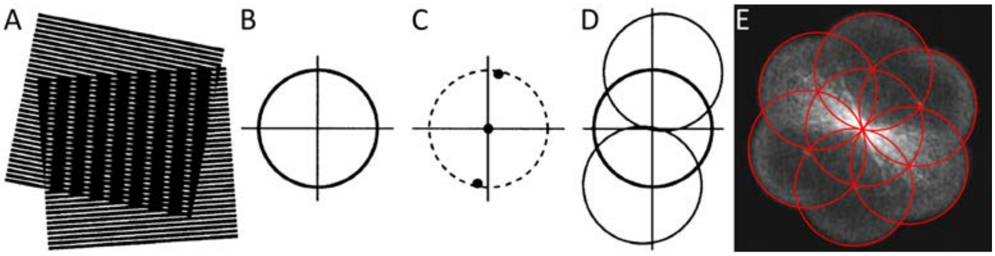

Figure 1.7 Concept behind structured illumination microscopy
(a) Two gratings, one rotated at an angle with respect to the other. The Moiré pattern is seen in the overlapping region. (b) Imaging region in reciprocal space for a diffraction-limited microscope. (c) The three Fourier components of the sinusoidal illumination pattern. (d) The original observation region plus two offset regions arising from the Moiré pattern. (e) The outlines of the image regions when the grating is rotated to different angles with respect to the sample overlaid with the resulting Fourier image. Adapted from *Gustafsson, 2000*

A comparison between TIRF and SIM images of different FA proteins can be seen in Figure 1.8. Although the resolution of conventional SIM is limited at ~100 nm, this technique provides a greater insight into the distribution of proteins within structures (Figure 1.8, F–J). Moreover, it is relatively easy to implement using any standard immunofluorescent dyes, and most importantly, it is fully compatible with live cell imaging allowing dynamic studies with increased spatial resolution.

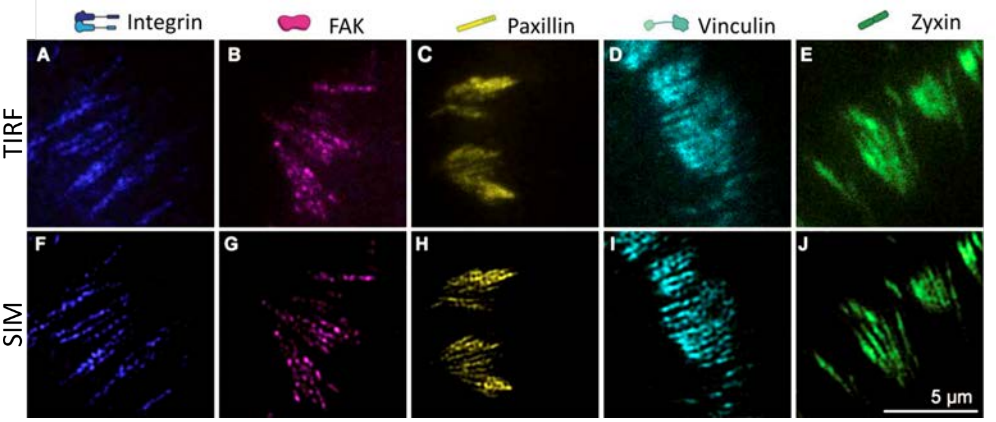

***Figure 1.8** Comparing TIRF and SIM images of five different adhesion complex components*
Single-colour images of different FA proteins: integrin β$_1$ (A,F; blue), focal adhesion kinase (FAK) (B,G; magenta), paxillin (C, H; yellow), vinculin (D, I; cyan), and zyxin (E, J; green) imaged using TIRF (A–E) and SIM (F–J). Adapted from *Hu et al., 2015*.

2. Stimulated emission depletion (STED) microscopy

STED microscopy has become a popular, widely-used super-resolution technique since its development in the lab of Stefan Hell in 1994 (Hell and Wichmann, 1994). STED is made possible by combining the principle of stimulated emission with the reshaping of beam profiles. As mentioned in the introduction of this chapter, fluorescence emission occurs when the molecule is excited with laser of energy $h\nu_{ex}$ to the S_1 state where it then has a probability to decay spontaneously with the emission of a photon of lower energy $h\nu_f$. However, if before the molecule has time to relax to the ground state (time scale ~ns), it is illuminated with a laser of longer wavelength, there is a probability that the molecule relaxes to the ground state S_0 with the emission of two photons with energy identical to the incident depletion photon, $h\nu_{STED}$, (Figure 1.9 A) (Leutenegger et al., 2010). In order to benefit from the process of stimulated emission to increase spatial resolution, STED microscopy uses two laser beams to illuminate the sample, the standard excitation beam and the STED or depletion laser beam. To generate the characteristic doughnut shaped beam, the STED laser passes through a phase plate resulting in an intensity profile with a minimum in the centre. The minimum of the depletion beam is overlapped with the maximum of excitation beam profile (see Figure 1.9 B, excitation and STED boxes). In this way, the STED and excitation beams are co-aligned such that the area from which the fluorescence is detected is determined by the width of the central minimum of the STED beam. The excitation beam is focused onto the sample and excites the molecules into their excited state, whereas the co-aligned doughnut-shaped STED beam induces stimulated emission of these molecules from the excited to the ground state. This overlap of the two lasers ensures the photons detected are originating from the minimum of the doughnut and the molecules outside of this region undergo stimulated emission of photons, which are spectrally filtered out. These two lasers are then scanned over the entire sample with a pixel size smaller than that defined by the Nyquist criterion for imaging techniques like confocal. This 'oversampling' ensures that the intensity profiles of densely packed molecules can be distinguished as discrete photon sources. The efficiency of depletion of fluorescence is shown in Figure 1.9 C as a function of STED laser power. As a consequence, the effective resolution improvement of STED microscopy with respect to conventional diffraction-limited microscopy is determined by the STED laser power as,

$$d = \frac{\lambda}{2NA\sqrt{1+{}^{I}/_{I_{sat}}}}, \qquad (1.2)$$

where I is the STED laser power, and I_{sat} is the saturation intensity.

The requirement of high STED laser powers (~tens or hundreds of mW, Figure 1.9 C) for super-resolution STED microscopy is seen by many as a serious drawback, in particular when applying STED for live cell imaging. However, in fixed samples, one can certainly achieve an increase in resolution as compared to confocal. This increased resolution reveals finer details of protein distributions in cells as seen in our example targeting the two FA proteins, paxillin and vinculin, Figure 1.10. It is also worth mentioning that new developments such as gated STED are able to reduce photobleaching by reducing the effective power of the STED laser beam (Vicidomini et al., 2011). Moreover, there is extensive and continuous work from different groups towards the development of brighter dyes with reduced photobleaching for STED applications, including commercially available dyes from the Abberior company.

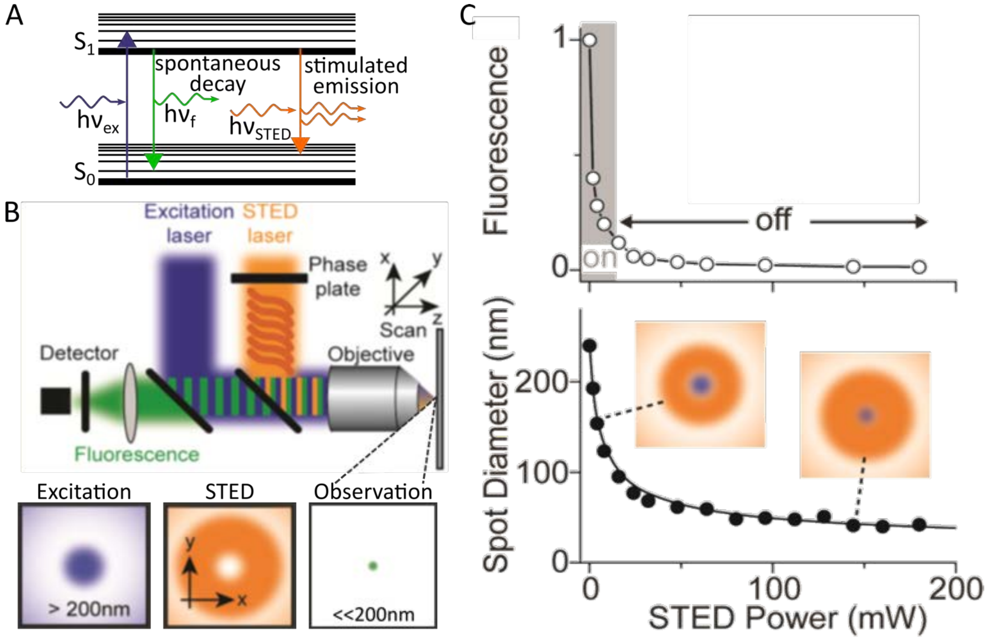

Figure 1.9 *Overview of STED microscopy*

(A) The typical Jablonski diagram for STED microscopy, based on (Leutenegger et al., 2010). (B) Scheme for the beams that are focused onto the sample, where the overlap of the excitation and STED beams results in detection of fluorescence from a spot with a diameter much smaller than 200 nm. (C) Dependence of the detected fluorescence on the STED laser power. Top graph shows that the drop off of detected fluorescence as a function of the STED laser power is very steep, and that above a certain laser power threshold ("off" denoted area) the fluorescence detected from the area overlapping the STED beam is negligible. Bottom graph shows how the diameter of the central spot of the doughnut beam, and so the spatial resolution of the technique increases with increasing STED laser power. Adapted from *Clausen et al., 2013*.

The proper choice of fluorophores is a hallmark to obtain high quality multicolour STED microscopy images, which can provide important information to investigate the relative (co-)localisation of different proteins at the nanoscale. Another important advantage of using STED microscopy is that it is possible to quantify changes in protein nanoclustering. For instance, STED microscopy was coupled to image deconvolution to study the nanoclustering of active and inactive integrins in FAs, as well as the relative localisation of some key proteins with respect to active/inactive integrins (Spiess et al., 2018).

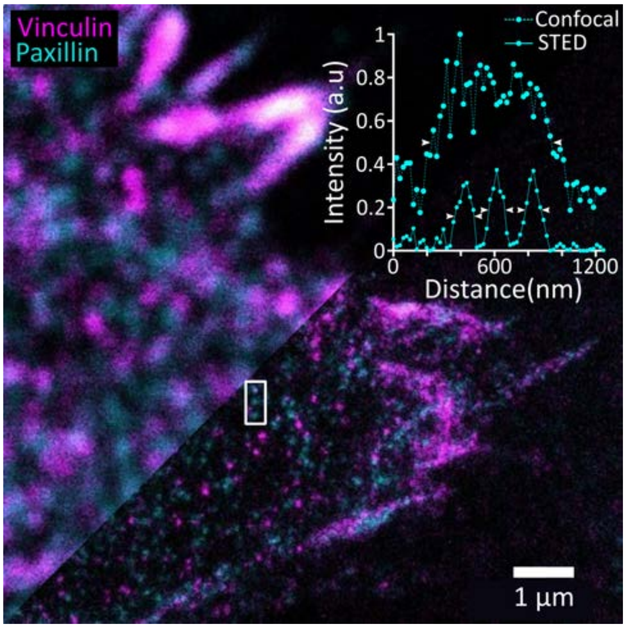

Figure 1.10 *Confocal versus STED microscopy in MEFs on FN-coated glass*
Upper left of the image shows vinculin (magenta) and paxillin (cyan) imaged with confocal settings and the lower right of the image shows the same cell imaged using dual colour STED microscopy. The image was taken using a Leica SP8 commercial setup, where proteins were labelled with primary and secondary antibodies, see details in the methods chapter Table 2.2 and Table 2.3. The inset illustrates the gain in resolution of the protein spots shown in the white box. In confocal, the protein spots were seen to have a FWHM of ~500 nm, whereas in STED it was possible to identify three distinct clusters of ~100 nm, 80 nm, and 60 nm FWHM, respectively (from left to right on the graph and top to bottom on the image).

Furthermore, in a publication of our lab from 2021, we used STED microscopy to investigate the changes on the nanoclustering of the cell surface protein ICAM-1 upon exposure of the cell to shear flow (Piechocka et al., 2021). We showed that, by comparing the spot intensities of ICAM-1 nanoclusters localised on the cell surface, to those spots found on the glass (corresponding to single antibodies absorbed on glass), we were able to quantify the characteristic sizes and intensities of those nanoclusters. Our results indicated that ICAM-1 clustering increases as a response to the application of shear flow (8 dyn/cm^2) for 4 h, and that such enhanced nanoclustering depends on the actin cytoskeleton as we observed a reduction of the cluster descriptors back to the basal levels in the absence of shear flow when we treated the cells with cytochalasin D (Figure 1.11), which disrupts actin polymerisation and leads to actin cytoskeleton disassembly (Piechocka et al., 2021).

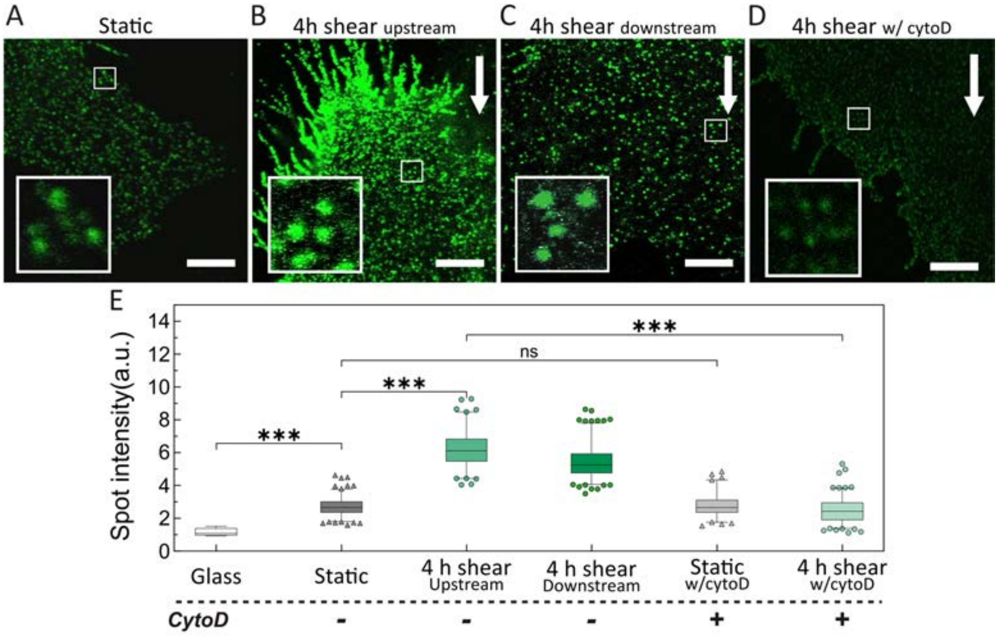

Figure 1.11 *ICAM-1 clustering after exposure to shear flow*
Endothelial cells (ECs) on FN-coated glass coverslips were immunofluorescently labelled for the membrane protein ICAM-1 (green). (A) Representative image of the ICAM-1 on an EC not exposed to shear flow. (B–D) Representative images of the ICAM-1 on an ECs exposed to shear flow, showing a region of interest (ROI) upstream of flow (B), downstream of flow (C), and a cell that was exposed to 4 h of flow and then treated with cytochalasin D (cytoD) (D). Scale bars are 4 µm. (E) Quantification of the fluorescent spots where 'glass' is considered to be the intensity coming from individual fluorophores. Figure adapted from *Piechocka et al., 2021*.

3. Near-field scanning optical microscopy (NSOM)

NSOM exploits the near-field interaction of light with matter to effectively increase the optical resolution. This is commonly achieved by using a subwavelength aperture probe as excitation source, instead of the standard focused light through an objective lens. The probe is scanned over the sample surface to locally excite the fluorophores, and the emitted fluorescence is collected in the far-field using standard optics. The resolution of the technique depends on the size of the aperture and the distance between the sample and the scanning probe, see Figure 1.12, (Garcia-Parajo et al., 2005). In the past, our group used this technique to image the integrin $\alpha_L\beta_2$ on the surface of monocytes prior to ligand binding (van Zanten et al., 2009). They showed that $\alpha_L\beta_2$ forms nanoclusters of ~85 nm in size when imaged with NSOM, and not of ~270 nm as measured using confocal microscopy, see Figure 1.12 B, C (van Zanten et al., 2009). Although NSOM provides high spatial resolution, it requires highly complex setups and it is a low-throughput technique, so it has been rarely used in the field of super-resolution microscopy of biological samples.

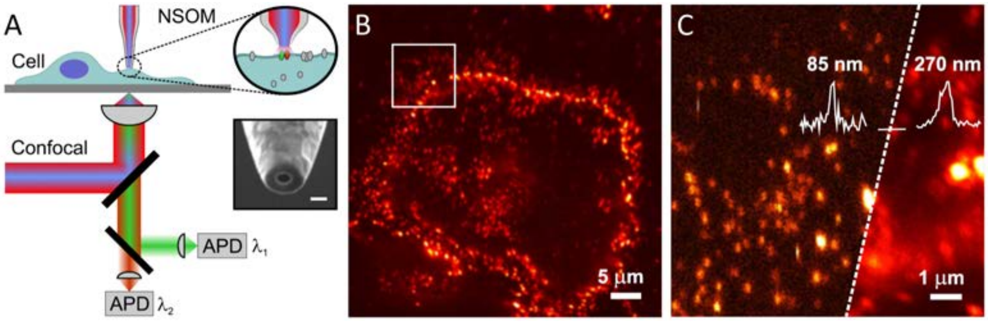

Figure 1.12 *NSOM for imaging* $\alpha_L\beta_2$ *integrins on monocytes*

(A) Scheme of the setup used for imaging cells with NSOM. The zoom-in and inset show the NSOM probe with a sub-diffraction aperture (scale bar = 100 nm) used to excite the sample. (B) Signal from $\alpha_L\beta_2$ on a monocyte imaged using NSOM. (C) Zoom area of the white box shown in panel (B), showing individual $\alpha_L\beta_2$ nanoclusters and the comparison between NSOM (left half) and confocal microscopy (right part). Figure adapted from *van Zanten et al., 2009*.

4. Single molecule localisation microscopy (SMLM)

SMLM is a family of imaging techniques, which provide super-resolution images using either TIRF or a HILO illumination scheme. The general commonality shared between all SMLM techniques is that they rely on the localisation of the centre-of-mass positions of individual molecules, and they do that by sequentially imaging different subpopulations of sparsely-distributed fluorescent molecules on the region to be imaged. The localisation of each individual molecule is obtained by fitting its intensity profile (the point-spread function, PSF) with a Gaussian profile and detecting its centre position. This procedure is repeated over thousands of cycles (corresponding to the sequential images – frames – of different fluorescent molecule subpopulations), and then the identified localisations of all the molecules in each frame are collapsed to create a single reconstructed super-resolved image. A key requisite for SMLM techniques is to be able to fluorescently detect single molecules, which requires their sparse distribution. There are different ways to achieve that, which is what distinguishes the different SMLM methods from each other. The birth of this field came from two seminal publications in 2006, one showing sub-diffraction-limit imaging using fluorescently-labelled antibodies in a technique named stochastic optical reconstruction microscopy (STORM) (Rust et al., 2006), and the other one achieving super-resolution by imaging photoactivatable fluorescent proteins in a technique known as photoactivated localisation microscopy (PALM) (Betzig et al., 2006). As already hinted above, the critical difference between these two techniques is that while STORM relies on immunolabelling with specific dyes, PALM uses genetically-encoded fluorescent proteins. They both depend on the capacity of the fluorophores to undergo a series of photophysical cycles from dark (off) to fluorescent (on) states, which guarantees the requirement that only a subpopulation of the molecules is detected in each imaging frame.

In PALM, autofluorescent proteins can either be photoactivatable or photoconvertible which are both irreversible processes. This means one wavelength is initially used to activate (switch from off to on) or convert (switch from one wavelength to another) these probes and once activated (or converted) a second laser is used to read out the desired signal (Lukyanov et al., 2005; Lelek et al., 2021). Eos is the photoconvertible fluorescent protein that arguably is the most commonly used PALM probe. Eos, in its "natural", non-photoconverted state, has a green excitation wavelength, $\lambda_{G\text{-}OFF}$ = 488 nm, but when exposed to UV light, $\lambda_{G\text{-}R}$ = 405 nm, it undergoes chemical changes and is red shifted such that its new excited wavelength is $\lambda_{R\text{-}OFF}$ = 561 nm (Lelek et al., 2021). Therefore, periodically illuminating a sample expressing Eos with UV light induces photoconversion of a subpopulation of the fluorescent proteins, which can be imaged at the single molecule level by using a continuous excitation laser at 561 nm. Taking advantage of the expanding palette of photoconvertible fluorophores, in 2007 the Betzig's lab established dual-colour PALM and used it to image cells expressing Eos and Dronpa (Shroff et al., 2007). That study revealed for the first time the capabilities of PALM to study the nanoscale segregation of proteins in dense cellular environments as is the case for paxillin and vinculin in FAs (Figure 1.13 A). PALM has been developed over the years to include modifications and improvements, such as those that led to interferometric-PALM (iPALM) (Shtengel et al., 2009). This technique combines an interferometer with PALM to provide 3D structural information at the nanometre scale. For our work, the most influential example of the use of iPALM came in 2010, when the Waterman lab presented their work revealing the axial nanoscale architecture of FAs. The results from that seminal work showed that proteins of the adhesion complex inhabit different layers positioned at different heights above the cell membrane (Figure 1.13 B, C) (Kanchanawong et al., 2010).

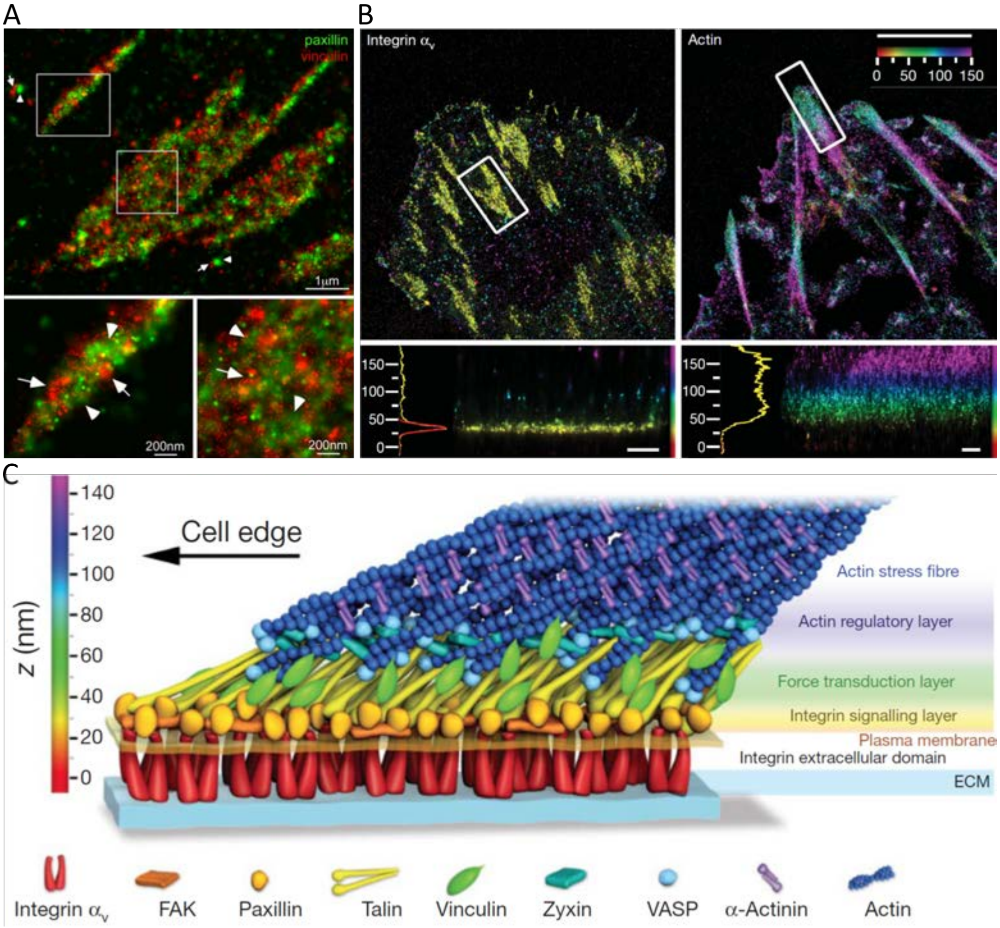

Figure 1.13 *PALM imaging of cell-ECM adhesions*

(A) The first example of dual-colour PALM imaging revealed the lateral segregation of paxillin (green) and vinculin (red) within FAs at the nanoscale. Adapted from *Shroff et al., 2007*. (B) Examples of iPALM images of integrin α_v and actin where the colourmap represents the proteins axial distance from the glass coverslip. In the left panel, α_v is seen as a largely uniform yellow colour indicating its location in a single layer close to the sample slide <50 nm from the surface. In the right panel, actin is found at different heights above the substrate. Scale bars are 500 nm. (C) The iconic model of the 3D distribution of the key FA proteins and the functional layer they occupy. (B) and (C) are adapted from *Kanchanawong et al., 2010*.

In the case of STORM, different photophysical processes can be exploited to achieve the activation of a subpopulation of fluorophores, which define the exact type of STORM. In general, STORM relies on the use of photoswitchable dyes that undergo reversible light-induced on-off transitions (blinking). Originally, STORM was carried out using a dye pair (Cy3 and Cy5) in a buffer containing a thiol and an oxygen scavenger to enhance reliable photoswitching when irradiated with green or red lasers, respectively (Rust et al., 2006). In that report, the dye pair was exposed to a high-power red laser to force the molecules into a dark state (off state), after which a green laser was used to switch a fraction of the molecules back to the ground state (on state) so they can be excited by the red laser again and their emission detected as a diffraction-limited PSF. This on-off photoswitching can be repeated multiple times resulting in cycles of stochastic activation and detection of a subset of fluorophores. Since photoswitching is reversible, a single fluorophore can be activated several times and in temporally distinct acquisition frames until its photon budget is exhausted (Rust et al., 2006). Direct STORM (dSTORM) is a technique very similar to STORM, which is carried out using just one fluorophore per channel so it does not depend on the crosstalk between an activator-reporter pair (it is activator-free) like in original STORM. More in-depth discussion of this topic can be found in Chapter 2 section 2.4, where we focus on the methods we used in the thesis. dSTORM is possible thanks to the finding that Cy5, independently of Cy3, cycles between on and off states when exposed simultaneously to green and red laser light (Heilemann et al., 2008). Interestingly, organic dyes such as some Alexa Fluor and ATTO dyes, were also shown to undergo photoswitching in the presence of thiols as reducing agents (Van De Linde et al., 2011). In the last decade or so, other SMLM techniques, such as PAINT and DNA-PAINT have been proposed and successfully used in different biological contexts (Lelek et al., 2021).

Both STORM and dSTORM have been exploited by many research groups spanning through a wide range of biological applications. Of particular interest in the context of this thesis, these techniques have provided great insight into how proteins distribute in force-exerting FAs, Figure 1.14 A (Hoorn et al., 2014), revealing the nanoscale organisation of $\alpha_5\beta_1$ integrin in separate active and inactive clusters inside FAs, Figure 1.14 B (Spiess et al., 2018), as well as the rearrangement of actin and formation of actin patches as a response to the application of mechanical stimuli in the form of shear flow, Figure 1.14 C (Piechocka et al., 2021).

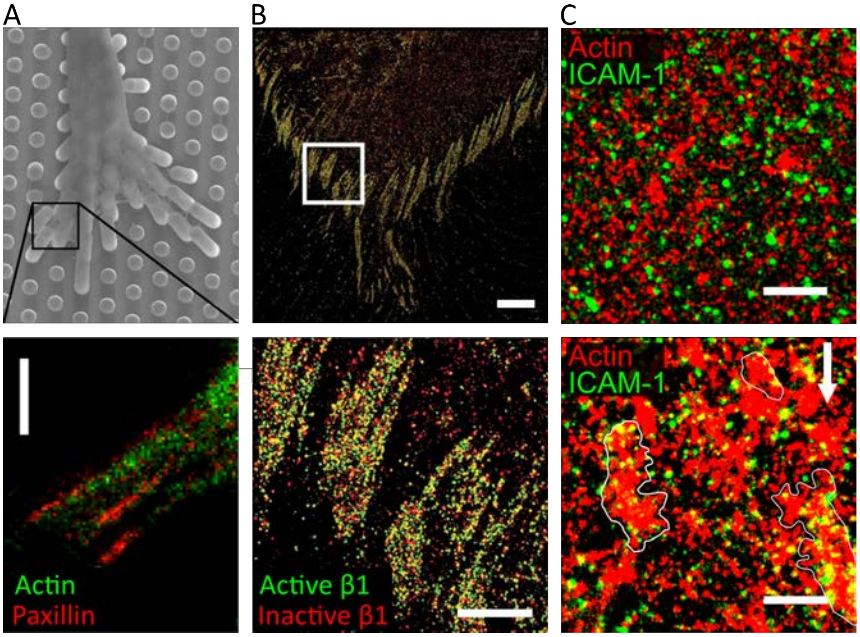

Figure 1.14 *Examples of dSTORM and STORM for the study of FAs and actin response to mechanical stimuli*

(A) Top panel shows an EM image of a cell protrusion on micropillars, whereas the bottom panel shows a two-colour dSTORM image of the area marked by the black box in the top panel, where actin (green) and paxillin (red) were labelled. Scale bar is 1 µm. Figure adapted from *Hoorn et al., 2014*. (B) Reconstructed STORM image (and zoom in the bottom panel) of active (green) and inactive (red) integrin β_1 nanoclusters. Scale bars are 5 µm and 1 µm in the top and bottom panels, respectively. Figure adapted from *Spiess et al., 2018*. (C) Two-colour STORM imaging to study cell response to the application of forces. The images show ICAM-1 (green) distribution together with actin (red) on unstimulated ECs (top panel) and on cells exposed to 4 h shear flow (bottom panel). Arrow marks direction of the shear flow, and the scale bars are 1 µm. Figure adapted from *Piechocka et al., 2021*.

1.4.6 Single molecule dynamic approaches

So far, we have reviewed different imaging techniques with particular emphasis on static imaging, where the development of super-resolution approaches has contributed to a greater understanding of fundamental cell biology. However, imaging of static, fixed cells provides a limited view because in living cells proteins are mobile and transiently interacting with one another. To circumvent these limitations, complementary techniques that can reveal the dynamic behaviour of proteins in the cell are required. Fluorescence recovery after photobleaching (FRAP) is a diffraction-limited optical technique that has been used over decades to study the diffusion of specific proteins in living cells (Stutchbury et al., 2017; Legerstee et al., 2019). Although the technique has excellent temporal resolution, it lacks the spatial resolution and sensitivity required to investigate the dynamics of individual molecules at the nanometre scale. Fluorescence correlation spectroscopy (FCS) is another technique highly suitable for studying fast protein dynamics *in vitro* and in living cells with single molecule detection sensitivity. FCS, commonly implemented in a confocal configuration, is based on the time-dependent recording and detection of bursts of fluorescence signal as a dye moves through the microscope detection volume. Statistical analysis (time correlation) of the recorded fluorescence intensity traces provides information on the number and diffusion time of molecules in the detection volume (Maiti et al., 1997; He and Marguet, 2011; Regmi et al., 2017; Winkler et al., 2017). Due to its high temporal resolution, FCS has been commonly applied to measure fast diffusion processes in living cells and much less applied to study adhesion complexes which have been thought to evolve slowly in time. Below we concentrate on another technique (single particle tracking), which is being increasingly used to study individual molecules within adhesion complexes.

1. *Single particle tracking (SPT)*

One of the most common techniques for studying the dynamics of individual molecules in living cells is single particle tracking (SPT). Similar to SMLM techniques, each frame of an SPT experiment captures a sub population of proteins in order to study their dynamics. However, in traditional SPT unlike SMLM techniques, this is achieved by sub-labelling the protein of interest. The imaging is commonly carried out using TIRF or HILO illumination, so the signal-to-background ratio is large enough for accurate single molecule detection, and hence the technique is highly favoured for basal membrane studies. In the past, our group has used this technique to investigate the dynamic behaviour of integrins on the cell membrane, for example $\alpha_4\beta_1$ expressed on T cells (Sosa-Costa et al., 2016). In another study from our group, the authors took advantage of conformation-sensitive antibodies that specifically target active $\alpha_L\beta_2$ integrins to study how their dynamics changed in comparison to the general population. The concept of the experiments is to record individual molecules on the surface of the cell (Figure 1.15 B), and find their localisation individually frame by frame (Figure 1.15 C). The analysis of these trajectories (Figure 1.15 D) in terms of their diffusion behaviour or their rate of occurrence allowed the authors to reveal that integrins in the extended conformation are mostly stationary on the cell membrane (Bakker et al., 2012).

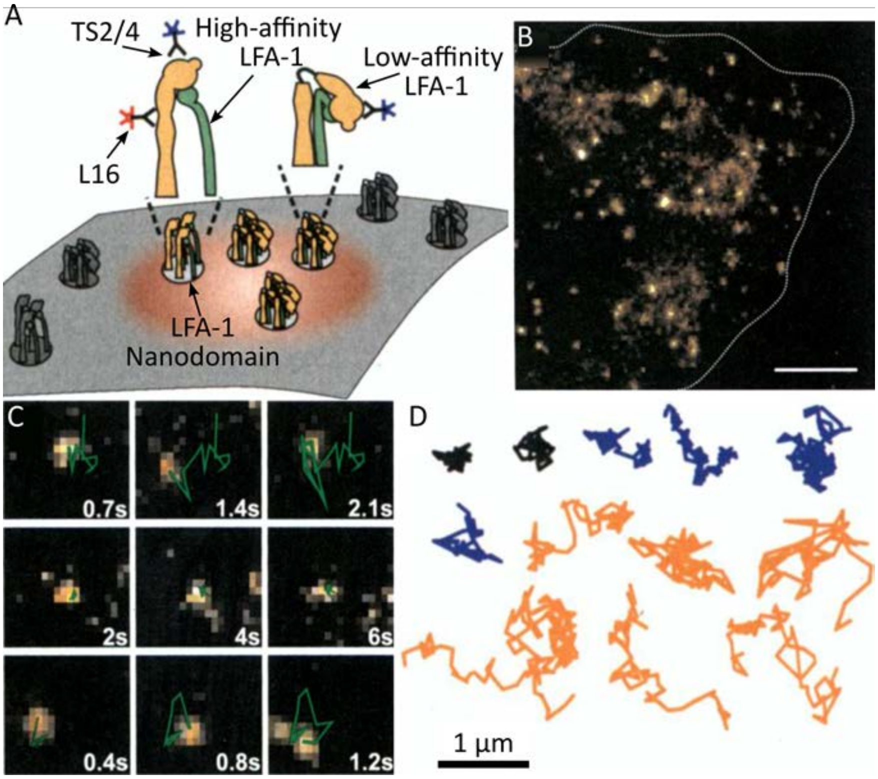

***Figure 1.15** SPT of $\alpha_L\beta_2$ integrins on the cell membrane of monocytes*
(A) Schematic representation of the different $\alpha_L\beta_2$ (also known as LFA-1) conformations being labelled by the antibodies and tracked on the cell surface. (B) Representative image of the labelling density at the cell membrane, using the antibody TS2/4 to label $\alpha_L\beta_2$ irrespective of its conformational state. Scale bar, 5 µm. (C) Images of three individual molecules are shown in each row (top, middle, and bottom) at different times, to illustrate the different kinds of diffusion behaviour observed. (D) Example of reconstructed trajectories obtained for different particles where orange indicated a fast-moving particle, blue is slow, and black is immobile. Adapted from *Bakker et al., 2012*.

Also in 2012, another study revealed that β_3 and β_1 integrins have different dynamics depending on the region of the cell membrane they are exploring (Rossier et al., 2012). In this work, the authors used SPT-PALM which, as the name suggests, relies on the use of photoactivatable fluorescent proteins such as those used in PALM, to effectively reach sub-labelling conditions for SPT (Manley et al., 2010). Using this approach, Rossier et al. showed for the first time that β_3 (Figure 1.16 A top) and β_1 (Figure 1.16 A bottom) integrins exhibit remarkably similar diffusion behaviour, but very different dynamics inside or outside FAs (Figure 1.16 B). In addition, the authors explored different integrin mutants to assess the role of ligand binding (β1-D130Y mutant) and actin binding proteins, such as talin (β1-Y783A mutant) on the mobility of the integrins (Figure 1.16 B). Interestingly, this work showed that inhibition of the binding to actin, and thus, inhibiting full integrin activation, increased the mobility of the integrin. These results are fully consistent with those from our group, where activation of $\alpha_L\beta_2$ integrins also resulted in reduced mobility (Bakker et al 2012). Together, these two publications established integrin mobility as a proxy for their activation state, i.e., active integrins engage with the actin cytoskeleton and thus remain immobile on the cell surface.

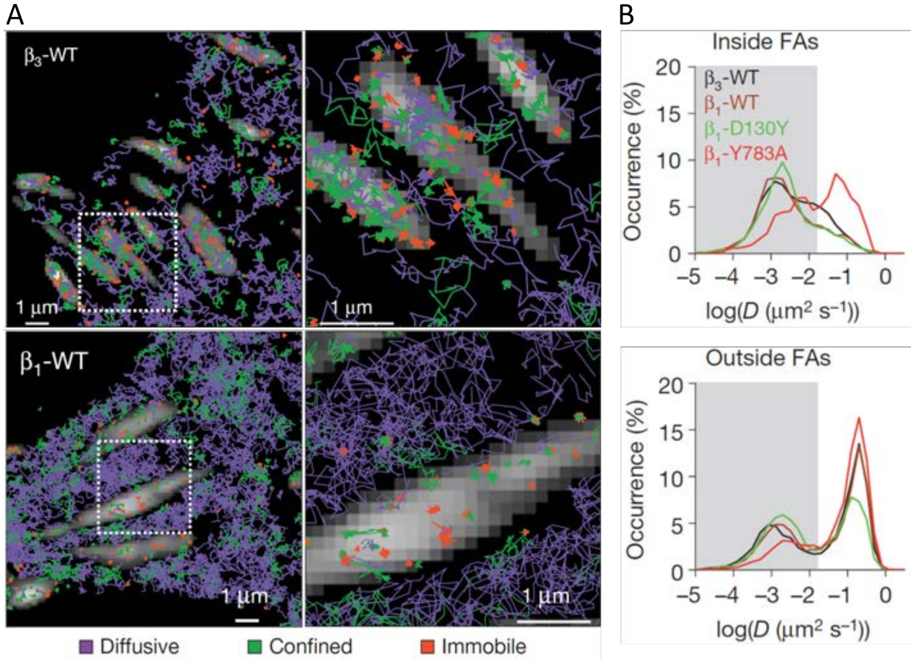

Figure 1.16 *Dynamics of β_3 and β_1 integrins inside and outside FAs*

(A) SPT tracks superimposed on a paxillin-based mask (grey scale) of β_3 (top row) and β_1 (bottom row), where the tracks are colour-coded according to the type of dynamics, as shown in the legend. The right column shows the zoom-in images for FAs regions. Scale bars are 1 µm. (B) shows the log of the diffusion coefficients inside (top) and outside (bottom) in FAs. For wild type (WT) β3 and β1 (black and brown, respectively) and two β1 mutants, D130Y, which prevents RGD binding (green) and Y783A, which inhibits talin-dependent activation (red). The grey shaded regions on both histograms correspond to immobile integrins. Adapted from *Rossier et al., 2012*.

A main limitation of SPT based on the use of organic dyes or autofluorescent proteins is that the length of the trajectories is generally limited to few seconds, which is in turn dictated by fluorophore photobleaching. Research from the Kusumi lab has focused on overcoming this challenge and extending the length of the trajectories. They achieve this by controlling the molecular oxygen available to limit photobleaching and still insure cell survival. In addition, they also used a reduction and oxidisation system, termed ROXS, to reduce the residence time of the molecules in the triplet states, and thus reduce photoblinking, which is problematic for trajectory reconnection, and photobleaching (Tsunoyama et al., 2018). Following this approach, the Kusumi lab showed that the integrins β_1 and β_3 change their dynamic behaviour depending on whether they are inside or outside an adhesion (see Figure 1.17). Specifically, they confirmed that inside the adhesions, integrins are less mobile. Most importantly, the authors found that integrins inside FAs are more likely to experience a long-lasting temporary arrest of lateral diffusion (TALL) as compared to outside FAs (Tsunoyama et al., 2018). Considering that immobilisation is a proxy for integrin activation, these results confirmed that integrins can change their conformational state from inactive (mobile) to active (arrested or immobile) in a highly dynamic manner, even inside FAs.

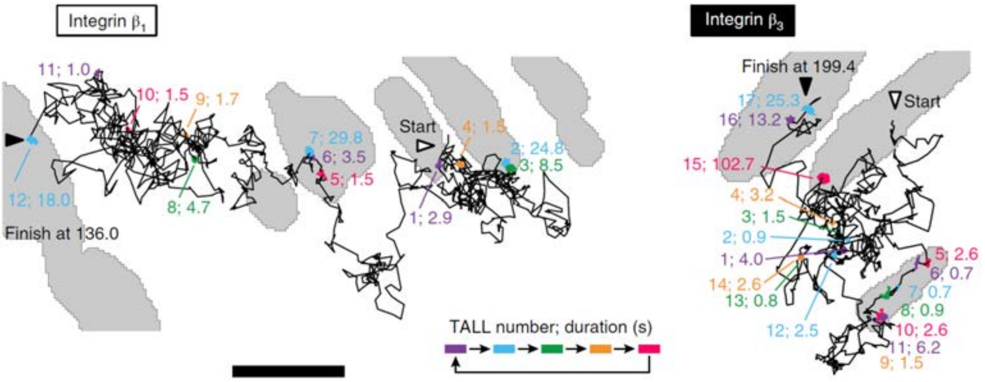

Figure 1.17 *Super-long SPT trajectories for β_1 and β_3 integrins*
Super-long trajectories (136 s) for β_1 (left panel) and β_3 (199 s) (right panel) integrins across a number of FAs (grey regions) where the TALL events are colour-coded according to their duration (where purple is shortest and pink the longest). Scale bar is 2 µm. Figure taken from *Tsunoyama et al., 2018*.

In this section, we have covered a wide array of techniques used to image proteins in fixed or living cells, each one with its advantages and disadvantages and better suited to specific tasks. In the final section of the introduction chapter, we look at different experimental approaches to mechanically manipulate and stimulate cells, with the aim of studying their response.

1.5 Techniques to probe the effect of mechanical stimuli on cells

Cells react to changes in their environment, meaning that they can sense those changes and respond accordingly by adapting their biological response. Examples of this are the variation in cell spreading depending on the ligand distribution on the substrate, or how cells change their migration mode as a response to gradients in the rigidity of the substrate (durotaxis) or in the chemical composition of the environment (chemotaxis or haptotaxis). However, although assaying for global changes in cellular function is obviously important, if we are truly going to understand the mechanisms by which a cell reacts to mechanical stimuli, then we need methods that allow a controlled environment combined with techniques to probe the changes at the molecular level. In particular, in the study of mechanosensitive structures such as adhesion complexes, a number of techniques have been used to externally exert forces on the cell as well as to engineer different types of substrates to investigate how the cells themselves exert forces on their environment. This section gives an overview of these techniques used to decipher the inner mechanisms of mechanosensing and mechanotransduction.

1.5.2 Shear flow application

In order to gain a detailed understanding of how complex biological systems work, we need to find the right balance between choosing the minimum set of experimental variables (and being able to experimentally control them) and keeping a physiologically-relevant system. In here, we will explain our work in the field of immunobiology, where we aim at understanding how T cells (a type of lymphocytes) adhere to and roll on the endothelial cells (ECs) that line the blood vessels. Although one would ideally study this at high resolution in an *in vivo* system, this is not at present a realistic situation because the more complex the system is, the more difficult it is to control and to image. Therefore, our group used a parallel plate flow chamber (PPFC) to study how T cells interact with ECs and how ECs react to the application of shear flow, mimicking the flow conditions in the blood vessels. Specifically, we used a system consisting of a PPFC and a peristaltic pump (Figure 1.18) to apply a controlled shear flow over a monolayer of ECs for 4 hours.

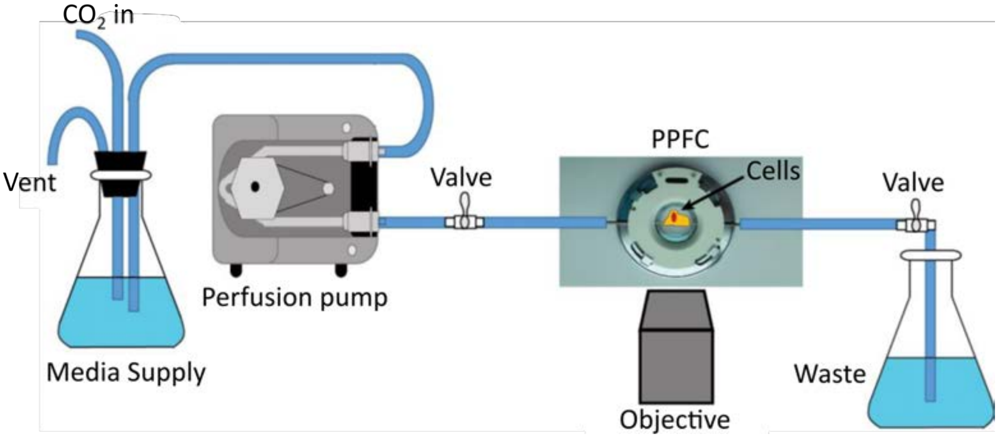

Figure 1.18 *Setup for the application of shear flow to ECs*
This system was made up of a perfusion pump supplying media at 8 dyn/cm^2 to the PPFC and over the cells within. The PPCF is in a temperature-controlled environment over an inverted Olympus x71 microscope. Adapted from *Sosa Costa, 2017*.

The experiments then focused on studying the two sides of the system: *(i)* the EC reaction to the application of shear force; and *(ii)* the behaviour of T cells that were introduced into the PPFC after the ECs were exposed to shear flow, particularly whether and how T cells altered their migratory behaviour as a response to EC exposure to shear flow. Our results showed that upon the application of shear flow, the ECs rearranged and aligned to the direction of the flow (Figure 1.19 A). We fixed and labelled those cells for the membrane receptor ICAM-1, which is the ligand for LFA-1, an integrin on the surface of T cells. Our results indicated that ICAM-1 is upregulated on the membrane when ECs are exposed to TNF-α (Tumour Necrosis Factor alpha), a cytokine that is produced during acute inflammation when an immune response is required (Figure 1.19 B). We also saw that with the application of shear flow there was a further upregulation of ICAM-1 in the first 2 h, and after this time the ICAM-1 signal plateaus (Figure 1.19 C). The confocal fluorescence microscopy images revealed that as well as there being a global increase of ICAM-1 in cells after flow compared to static cells, the spatial distribution of the ICAM-1 was also altered as a response to the flow. In static cells, ICAM-1 was seen to be uniformly distributed on the membrane, whereas in cells exposed to flow we observed the redistribution of the receptor upstream of flow (Figure 1.19 A). As a follow-up to the observation that cells align along the direction of flow, we imaged the actin cytoskeleton by confocal microscopy, and saw a rearrangement of the actin architecture with the main fibres found to form downstream of flow. STORM imaging revealed that, upstream of the flow, the actin at the basal membrane forms patches rather than fibres. After observing these changes in the actin cytoskeleton, we sought to determine the effect of shear flow on the myosin distribution. Interestingly, our results showed that, while in static cells actin and myosin form a characteristic sarcomeric pattern along the stress fibres, upon exposure to 4 h of shear flow myosin appears to be disengaged from actin fibres and to reside in the cytosol (Figure 1.19 D).

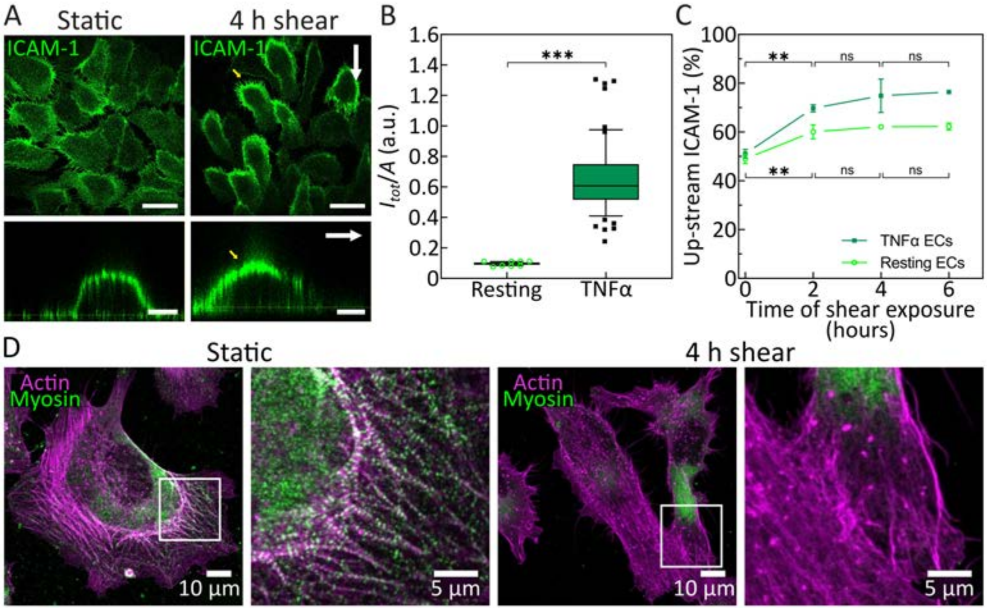

Figure 1.19 *EC response to application of shear flow*

(A) Fluorescence microscopy image of ICAM-1 (green signal) in static (left panels), and 4 h shear flow (right panels) conditions. White arrows indicate the direction of the flow. Yellow arrows point at the upstream accumulation of ICAM-1 upon shear-force application. Scale bars, 50 µm in top images and 15 µm in bottom images. (B) Plot of the intensity of the ICAM-1 fluorescence over the cell normalised to the area of the cell for cells incubated with TNFα and in resting cells with no TNFα. (C) Percentage of upstream ICAM-1 fluorescence signal taken from individual ECs under resting (open light green symbols) and TNFα (closed dark green symbols) conditions as a function of shear flow application. The signal was estimated from 50% of the desired cell area and divided by the total intensity calculated over the entire cell. (D) Confocal images of actin (magenta) and myosin-II (green) in static ECs (left panels) and in ECs after exposure to 4 h shear flow (right panels). Panels (A–C) are adapted from *Piechocka et al., 2021*, and panel (D) is unpublished data.

This set of experiments provided us some understanding of how ECs respond to the exposure to shear flow. However, as mentioned earlier, there are two sides to this story and so we also wanted to understand how these changes in the protein distribution on the EC membrane influence T cell interaction and migration. In that respect, we showed that T cells resting on ECs that were subjected to 4 h shear flow were more promigratory and adopted an amoeba-like shape, as compared to a higher percentage of T cells showing a round shape when resting on static ECs. We hypothesised that this was a result of the increased ICAM-1 clustering observed by STED microscopy (Figure 1.11). In order to test this hypothesis, we carried out experiments where we coated glass cover slips with either monomeric or nanoclustered ICAM-1, on which we seeded T cells (in the absence of shear flow) and studied their migratory phenotype. Our results indeed validated our hypothesis, showing that T cells seeded on nanoclustered ICAM-1-coated slides had a more amoeba-like, promigratory phenotype and migrated faster (Piechocka et al., 2021).

As a whole, these experiments demonstrated that shear-forces have a profound effect in the nanoscale organisation of ICAM-1 on ECs, promoting their nanoclustering prior to T cell engagement. Such shear-flow-induced nanoclustering increases T cell migration, a process that might be relevant in the context in the immune adhesion cascade.

1.5.3 Nanostructures to probe mechanical forces exerted by cells

An important aspect of mechanobiology is to understand how cells apply forces to their surroundings. Hence, from the technical side, the development of methods to measure such cell-exerted forces has been of utmost importance in the field. One of these tools is the use of nanopillars and beads embedded into elastic substrates, which have been used to study how cells interact with and mechanically deform their local environment. The force applied by the cell can be measured by the deflection of the nanopillars in one case (Figure 1.20 B), or by the displacement of the beads upon cell contact (Figure 1.21, left panel). Having a quantitative readout of the magnitude of these forces is an important first step, but it is also important to know the molecular machinery involved in force application. In the work by Hoorn et al., cells were plated for 16–24 h on micropillar arrays with dimensions 2 µm diameter, 2 µm spacing, and with a height of 6.9 µm. The pillars were characterised and then the deflection of the pillars was measured when cells were adhered to them. The deflection of the pillar was then correlated to the force exerted by the cell on its surroundings. Using dSTORM, the authors observed that actin and paxillin were enriched at the cell protrusions (Figure 1.20 A, right) and furthermore using confocal imaging of the pillars together with actin and paxillin, they saw that the deflection of the pillars was highest in these protrusive regions of the cell (Figure 1.20 B) (Hoorn et al., 2014).

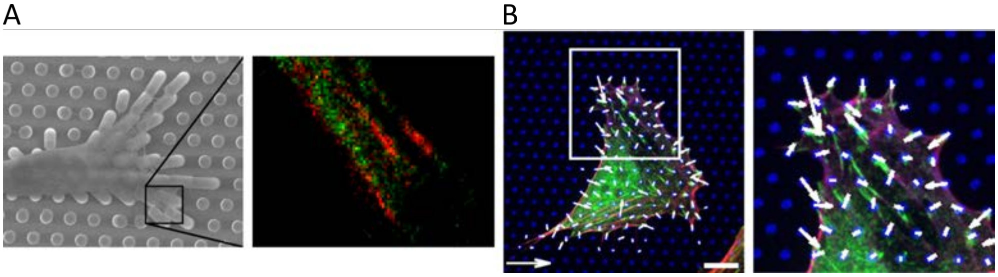

Figure 1.20 *Study of the forces exerted by cells using nanopillar structures*
(A) left is an EM image of a section of a cell on the nanopillar array and right shows the dSTORM reconstruction with paxillin (red) and actin (green) labelled. (B) Confocal images of an entire cell (left) and a zoomed-in region (right), seeded on nanopillars coated with FN (shown in blue), where paxillin (green) and actin (red) were labelled and their signal is overlaid with the force vectors calculated from the nanopillar displacement. Scale bar is 10 µm and force scale bar (arrow) is 20 nN. Adapted from *Hoorn et al., 2014*.

As mentioned above, in traction force microscopy, small beads are embedded in a polymer so the traction force exerted by the cell on the substrate can be extracted from the measured bead displacement. An additional advantage of this technique is that, by varying the embedding polymer composition, it is possible to control the rigidity of the substrate the cells attach to. Hence, it is not only possible to measure the forces applied by the cell to the substrate, but also to investigate how such forces change with the substrate stiffness (Figure 1.21). Remarkably, increasing the substrate stiffness also caused the nuclear translocation of the transcriptional regulator YAP (Figure 1.21, middle column). The increased localisation of YAP in the nucleus as a response to mechanical forces applied on and by the cell lies at the end of the mechanosignalling cascade that leads to the cell responding by the production of new proteins. As such, YAP nuclear translocation has become a popular readout of mechanotransduction.

As previously indicated, it would be remiss of a researcher to study forces applied by the cell to substrates of different rigidities and not study how this influences the formation of FAs. Elosegui-Artola et al. showed that in cells seeded on soft substrates, there is a reduction in the FA area, which parallels the reduced forces exerted by the cell on the substrate and low levels of YAP in the nucleus. By contrast, cells seeded on stiff substrates show a high traction force, and YAP translocation to the nucleus occurs on those cells with mature FAs (see Figure 1.21, right) (Elosegui-Artola et al., 2016). The same authors also revealed in a subsequent publication that the application of external forces by pressing on the nucleus leads to nuclear entry of YAP (Elosegui-Artola et al., 2017). These publications highlight that exciting experiments can be carried out to understand how cells control their responses to mechanical stimuli.

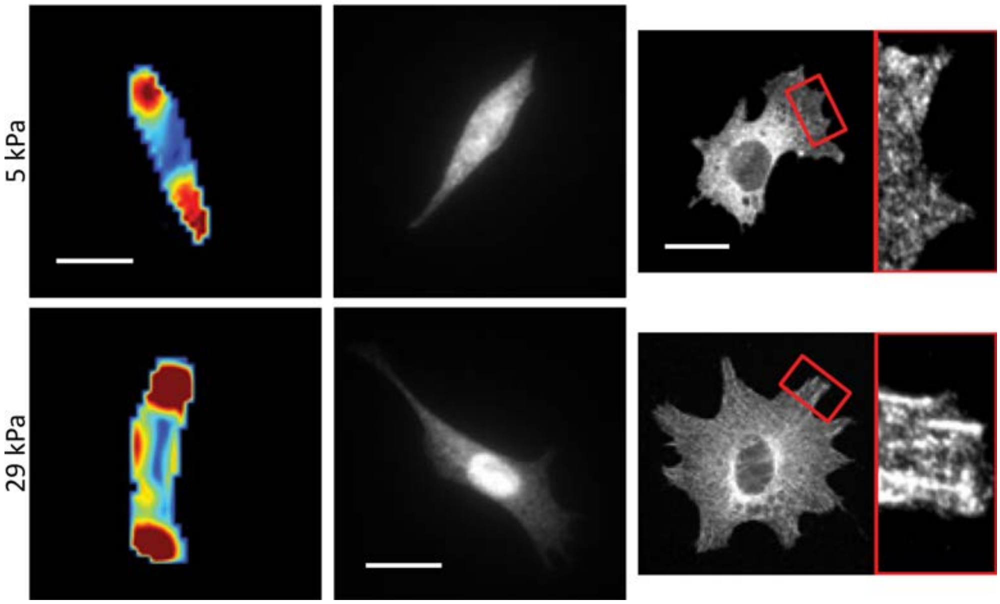

Figure 1.21 The response of fibroblasts to different substrate rigidities
Left panels: traction force microscopy images with the colour map indicating the regions of the cell that deform the substrates and displace the beads the most, where red indicates high forces and blue low force. Middle panels: Fluorescence microscopy image of YAP labelled in cells seeded on soft surfaces (top) or stiff surfaces (bottom), showing an enhanced nuclear YAP signal on the stiff surface-seeded cells. Right panels: fluorescence microscopy image of a cell as it spreads on the two surfaces of different rigidities. Cells were labelled for vinculin with the red inset showing a zoom-in of membrane regions with and without FAs. All scale bars are 20 µm. Adapted from *Elosegui-Artola et al., 2016*.

As we progress with our research in mechanobiology, we aim to improve the accuracy and sensitivity of our experimental setups as well as being able to use biological systems that are as (patho-)physiologically relevant as possible. With that in mind, we do not only need to consider the effects of the rigidity of a substrate where the ligand is attached and immobile, but we must also consider the case where the ligand is not fixed in the substrate but can move once force is applied to it. In an effort to investigate this latter situation, work coming from a collaboration between the Roca-Cusachs and Salmeron-Sanchez labs showed how the cell respond to changes in substrate viscosity (Bennett et al., 2018). Specifically, in those experiments, the authors seeded the cells in RGD ligand-containing supported lipid bilayers (SLBs) of different viscosity or fluidity. By altering the lipid bilayer composition, they could mimic conditions of high diffusive ligand mobility (1,2-dioleoyl-sn-glycero-3-phosphocholine (DOPC) bilayers) or reduced ligand mobility (1,2-dipalmitoyl-sn-glycero-3-phosphocholine (DPPC) bilayers) (Figure 1.22).

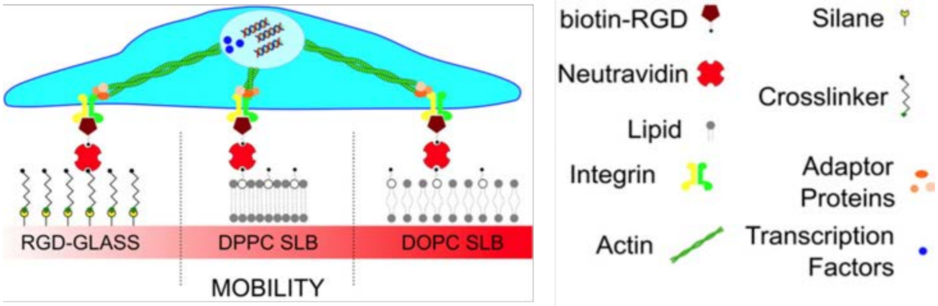

Figure 1.22 *Schematic representation of the experimental assay to study the cell response to changes in viscosity*
This graphic shows the system used to measure the cellular response to substrate viscosity as well as the layers of functionalisation to present the RGD for the cell to bind. The cell in blue is plated on a surface of either glass (rigid), DPPC (gel), or DOPC (fluid-like). The substrates are functionalised using a low percentage of biotinylated lipid which can bind neutravidin, which in turn binds to the biotin-RGD motifs presenting the ligand so that the cell adheres primarily via the desired integrins, $\alpha_5\beta_1$ and $\alpha_v\beta_3$. Adapted from *Bennett et al., 2018.*

Their results showed that, after the cells were allowed to attach and spread on the different substrates for 3 h, their phenotypes were strongly influenced by the substrate viscosity. On DPPC bilayers, which have reduced ligand mobility but are still a viscous environment, cells spread (Figure 1.23, middle) but not to the same extent as those cells seeded on glass (Figure 1.23, left). Notably, cells seeded on DOPC bilayers were unable to properly spread (Figure 1.23, right). In summary, this study showed that FA formation is severely influenced by the viscosity and the ligand density of the substrate onto which the cells are seeded.

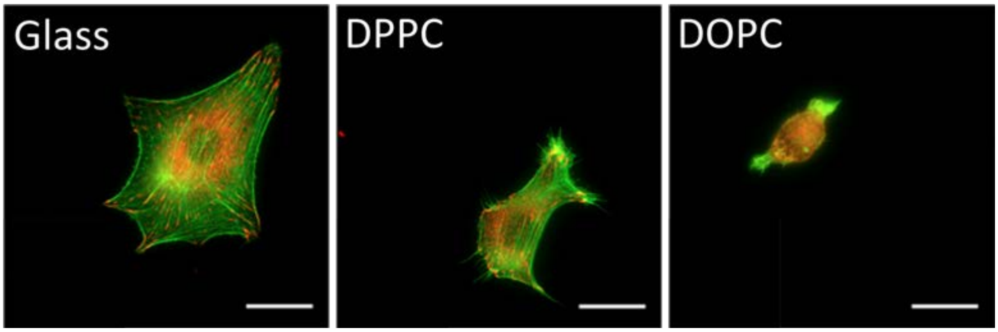

Figure 1.23 *How a cell responds to substrate viscosity*
Fluorescence microscopy imaging of actin (green) and vinculin (red) in cells plated on surfaces with different mechanical properties: rigid substrate (RGD-coated glass, left); high viscosity, low fluidity substrate (RGD-containing DPPC bilayer, middle); and low viscosity, high fluidity substrate (RGD-containing DOPC bilayer, right. Scale bars are 25 µm. Adapted from *Bennett et al., 2018*.

Indeed, the combination of mechanical probing of cells with super-resolution imaging techniques, would provide us with an even greater understanding of how protein organisation is influenced by changes in the environment or the application of external forces. As is often the case with experiments that combine many techniques, it has proven to be extremely challenging to image the effects of mechanical forces on cells at high spatial and/or temporal resolution. It was as recent as recent as 2020 that we saw the results of combining cell stretching devices with super-resolution imaging (Massou et al., 2020). Giannone's lab developed a stretching device which overcame the challenge of imaging through PDMS by using an ultra-thin PDMS layer mounted on a glass coverslip with glycerol between the PDMS and the glass to allow for unhindered stretching. They saw that integrin displacement before, during and after stretching has the same response as a bead embedded in the PDMS, meaning it is elastic in nature. However, their technique showed that talin has an inelastic response to the stretching which corresponds to the unfolding of talin (Massou et al., 2020). Although this technique is very promising for future research in the field and proves that cell stretching combined with super-resolution imaging is feasible, it remains extremely challenging.

Chapter 2

Detailed overview of the techniques implemented in this thesis

Super-resolution fluorescence microscopy requires contributions from techniques incorporating a number of scientific disciplines, especially when exploiting it to obtain quantitative information. In this chapter, we provide the details of the methods implemented and common to all the subsequent results chapters. These methods range from cell culture and sample preparation for microscopy to the manipulation of the stochastic blinking of organic dyes required for single molecule localisation-based super-resolution imaging. In the last section of this chapter, we describe the implementation and development of algorithms to extract quantitative details out of the super-resolution microscopy data.

2.1 Introduction

When striving to obtain insightful, objective, and reliable quantitative information from a biological system using fluorescence microscopy, the combination of many fields of expertise is usually required. The experimental work presented in this thesis combines biological sample preparation, super-resolution fluorescence microscopy, and the development and use of data and image analysis algorithms. As such, we implemented commonly-used techniques and combined them with analytical tools that we have developed and/or tailored to our own needs. In the following sections, we provide a detailed description of the materials and methods that are commonly used throughout our results chapters, while we leave other more specific methods to be explained in their own chapter.

2.2 Preparation of biological samples

Cell seeding and fixation

HFF-1 cells (human foreskin fibroblasts, obtained from ATCC) were cultured in DMEM + 10% FBS (cell culture medium) until passage 15 (see Table 2.1 for details of the cell culture reagents). FN coating was achieved by preparing fresh 10 µg/ml FN in sterile PBS and incubating the glass bottom dishes with the solution for 40 min at room temperature (RT). After incubation, the dishes were rinsed using sterile PBS and each was filled with cell culture medium. The cells were trypsinised for 3 min at 37°C and plated in the FN-coated 8-chambered glass bottom dishes and allowed to settle and attach by incubating them in a humidified incubator at 37°C with 5% CO_2. After 90 min, 3 h, or 24 h, the cells were fixed with 4% PFA in PBS for 15 min at RT, after which they were washed three times in PBS. Samples were then subjected to an immunofluorescence labelling protocol (see subsection below), using primary and secondary antibodies with the appropriate fluorophores for confocal or STORM experiments (see Table 2.2–Table 2.4).

Immunofluorescence labelling

The proteins that we set to immunolabel in our experiments fall into two very general classes. The first class is that of the integrins ($\alpha_5\beta_1$ and $\alpha_v\beta_3$), which are cell surface-localised, transmembrane proteins and hence are accessible for labelling on the extracellular side. The second class is that of the adaptor proteins (paxillin, talin, and vinculin), which are cytosolic proteins and therefore – for antibody-based labelling – require the cell membrane to be perforated to allow the antibodies to cross it and access their target epitopes. The procedure of "perforating the cell membrane" is known as permeabilization or extraction, which can be carried out by incubating the cells with a weak detergent.

Specifically, the permeabilization and blocking steps were performed simultaneously by incubating fixed cells in a blocking buffer, consisting of 3% BSA, 0.2% Triton X-100 in PBS, for 40 min at RT. The blocking buffer was removed and the cells were incubated with the primary antibodies diluted in blocking buffer for 1 hour at RT. We used commercially available primary antibodies targeting the two main integrins of the adhesion complex ($\alpha_5\beta_1$, $\alpha_v\beta_3$) and the key adaptor proteins (paxillin, talin, and vinculin) (Table 2.2). All the antibodies are pan-specific antibodies, meaning that they do not target a particular state of activation or conformation of the protein, but label the entire population regardless of the activation state. We optimised the labelling protocol to achieve full labelling of all the proteins. This was achieved by carrying out titrated labelling, finding the concentration of primary antibody above which we do not achieve an increase in signal from the secondary antibody as measured in confocal mode. In super-resolution microscopy standard practice, as an extra precaution, it is common to use the secondary antibodies in excess to ensure also that all the primary antibodies are labelled.

Next, after primary antibody incubation, the cells were washed three times with washing buffer (0.2% BSA, 0.05% Triton X-100 in PBS) and incubated with the secondary antibodies diluted in blocking buffer for 40 min at RT in a dark environment (see Table 2.3 and Table 2.4). For the majority of STORM images obtained for this thesis, we used commercially-available secondary antibodies (goat anti-mouse and goat anti-rabbit) that were conjugated to dye pairs Alexa Fluor 405-Alexa Fluor 647 or Cy3-Alexa Fluor 647. The conjugation was done in house, to obtain a final product at a concentration of ~0.1 mg/ml, with ~6:1 composition for activator:reporter dyes per antibody, following a protocol described in previous work from our group (Borgman et al., 2020). We used these labelled secondary antibodies at a dilution of 1:20 (final working concentration of 5 µg/ml). After labelling, cells were washed three times in washing buffer and stored in PBS until imaging. Any confocal or STED images obtained for this thesis were immunolabelled using the aforementioned primary antibodies (Table 2.2) and commercially-available dye-conjugated secondary antibodies obtained from Abberior (Table 2.3).

Table 2.1 Reagents for cell culture and sample preparation

Reagent	Abbreviation	Company	Cat #
Fetal Bovine Serum	FBS	Biowest	S181B
Dulbecco's Modified Eagle Medium	DMEM	Capricorn–Scientific	DMEM-HXRXA
Trypsin		Biowest	L0910-100

Bovine Serum Albumin	BSA	Capricorn–Scientific	BSA-1S
Phosphate-Buffered Saline	PBS	Capricorn-Scientific	PBS 1A
Fibronectin	FN	Sigma Aldrich	11080938001
Paraformaldehyde	PFA	Sigma Aldrich	F1635-500
Triton X-100		Fisher Scientific	BP151

Table 2.2 Primary antibodies used in the experiments

Target Protein	Host	Stock conc* (mg/ml)	Working dilution	Company	Cat #	Comments
$\alpha_5\beta_1$	Mouse	0.5	1:100	BD Bio-sciences	555510	CD49e Targets α_5
$\alpha_v\beta_3$	Mouse	0.1	1:20	abcam	Ab7166	
Paxillin	Rabbit	0.14	1:100	abcam	Ab32084	Anti-Paxillin [Y113]
Talin	Rabbit	0.9–1	1:100	abcam	Ab71333	Talin-1
Vinculin	Rabbit	1.0–1.3	1:100	Sigma Aldrich	v4139	
Vinculin	Mouse	2.0–4.0	1:100	Sigma Aldrich	v4505	

Table 2.3 Secondary antibodies and their fluorophores used for confocal and STED images

Target Species	Conjugated dye	Host	Stock conc* (mg/ml)	Working dilution	Company	Cat #
Mouse	Abberior STAR 635P	Donkey	1	1:200	Abberior	ST635P-1001-500UG
Rabbit	Abberior STAR 580	Donkey	1	1:200	Abberior	ST580-1001-500UG

Table 2.4 Secondary antibodies and their fluorophores used in STORM experiments

Target species	In-house conjugated dye pair		Host	Stock conc* (mg/ml)	Working dilution	Company	Cat #
	activator	reporter					
	(dyes per antibody)						
Mouse	Alexa Fluor 405	Alexa Fluor 647	Donkey	0.1	1:20	Jackson Immuno Research	715-005-150
	(6:1)						
Rabbit	Cy3	Alexa Fluor 647	Donkey	0.1	1:20	Jackson Immuno Research	711-005-152
	(6:1)						

*conc=concentration

2.3 Confocal and STED imaging

Although the large majority of the results presented in this thesis were obtained using SMLM, we also performed confocal and STED imaging of some FA components (see Chapter 1). Therefore, for completeness, we include here the description of the set-ups and imaging strategy used. All confocal and STED images were acquired on commercial Leica TCS SP5 or TCS SP8 STED 3x microscopes. The excitation light source on the Leica TCS SP5 system consists of three lasers at 488 nm, 543 nm, and 633 nm and the images were acquired sequentially with line accumulation of four and an average over four frames, with a pixel size of 60.6 nm. The frequency of the accumulation was 400 lines per second. The signal was recorded using photomultiplier tube (PMT) detectors. For the TCS SP8 STED 3x setup, excitation was achieved using a pulsed supercontinuum white light laser source, which we tuned for our STED images to 499 nm, 587 nm, and 633 nm (excitation wavelengths). The depletion laser used for STED imaging is a ps-pulsed laser at 775 nm, which we used to deplete both Abberior STAR 580 and Abberior STAR 635p fluorescence signal. The confocal images were taken with a 63x or 100x oil immersion objective with a numerical aperture of 1.4, and the STED images were taken using a Leica 100x HC PL APO CS2 oil immersion objective with a numerical aperture of 1.4. The two channels were imaged sequentially. Images were taken with six-line accumulation in a 19.98 x 19.98 μm field of view (1024 x 1024 pixels) with a pixel size of 20 nm, with unidirectional scanning at 600 lines per second. The detection of the two channels was done with two separate hybrid (HyD SMD) detectors in standard mode and acquisition windows set to 595–650 nm (for the paxillin channel) and using time gating (gating from 2.53–6.3 ns) and to 643–753 nm (for the vinculin channel) and using time gating (gating from 2.53–6.3 ns).

2.4 STORM imaging

In order to explore the lateral nanoscale distribution of adhesion complexes, we used STORM, a SMLM technique (Rust et al., 2006; Huang et al., 2010; Vaughan and Zhuang, 2011), which we introduced in Chapter 1. This technique is carried out at label saturation (full labelling conditions), and exploits the photophysical phenomenon of on-off switching (blinking) of certain organic dyes to detect individual, sparsely-distributed molecules with high signal-to-background ratio, which is obtained thanks to the use of TIRF illumination. Detection of individual, sparsely-distributed molecules is mandatory in STORM, because image acquisition is diffraction-limited and therefore a large number of diffraction-limited images are taken sequentially in time in order to obtain a super-resolved image. This allows that each individual molecule that emits fluorescence can be detected as a diffraction limited PSF, which, after fitting it with a 2D Gaussian profile, provides the x-y coordinates of that single emitter as the fitted PSF centroid position (Rust et al., 2006; Oddone et al., 2014). The precision of this centroid position determination depends on the number of photons detected by the camera (the localization precision scales with the square root of the number of detected photons, see subsection below for more details).

Fluorescent probes for SMLM

In this thesis, we use the organic dye Alexa Fluor 647 (Alexa647) as our reporter fluorescent dye, and Alexa Fluor 405 (Alexa405) or Cy3 as the activator molecules. Alexa647 is derived from the cyanine dye Cy5, which, like other cyanine dyes, cycles between a singlet ground state (S_0) and the first excited state (S_1), emitting photons during direct S_1 to S_0 radiative decay (fluorescence) (Figure 2.1 A). However, once in the S_1 excited state, the excited molecule has a certain probability to undergo intersystem crossing (ISC) and internal conversion (IC) to enter a lower-energy state with a longer lifetime, known as a triplet state (T_1). The T_1 state has a longer lifetime than the S_1 state because the T_1 state consists of an electron pair with parallel spins (total molecule spin = ±1). Hence, for the molecule to decay to the ground state, and according to Pauli exclusion principle, it needs to first reverse one of the spins (so the molecule is back at a spin = 0 configuration) so the two electrons can be in the same orbital. In addition to the triplet state, the molecules can visit a series of other "dark states", which can be reached by, e.g., reversible *cis*/*trans* photoisomerisation transitions in the fluorescent molecule (Figure 2.1 B). This phenomenon is common to most cyanine dyes. The energy landscape as a function of the twist angle in the molecule, i.e., when photoisomerisation occurs in cyanine dyes, is shown in Figure 2.1 B, where the mismatch in energy levels arises due to changes in the fluorophore's chemical structure. This photoisomerization reaction from the *trans* (emitting state) to a *cis* (non-emitting state) isomer occurs when unstable π bonds between electrons in the S_1 state allow the twisting around a carbon bond. The transition from *trans* S_1 to *cis* S_0 occurs at a rate k_{iso} while back-isomerisation from *cis* S_1 to *trans* S_0 occurs at rate k_{biso} (Tornmalm, 2019). To achieve optimal conditions of fluorophore blinking for STORM imaging, the rate of transitions to a dark state ("off" state), k_{off}, needs to be high, and the rate of escape from the dark state back to the ground state ("on" state), k_{on}, needs to be low. Under these conditions, only a small subpopulation of the molecules will be capable of emitting fluorescence photons in each imaging acquisition frame.

In addition to *cis*/*trans* photoisomerisation, there are two other important mechanisms that help in efficient fluorophore blinking for STORM. One is by the influence of a second dye. This effect was identified using a Cy3–Cy5 dye pair, for which it was observed that the addition of Cy3 in close proximity (~1–2 nm) to Cy5 allowed for a more controlled blinking behaviour of the reporter dye (Cy5) after activator dye (Cy3) excitation (Figure 2.1 C) (Bates et al., 2005). Specifically, a high-power red laser was used to take Cy5 to a dark state and it was found that illuminating the sample with a lower-power green laser, which leads to Cy3 excitation, induced Cy5 to switch to an on-state and therefore to fluoresce (see Figure 2.1 C). The benefits of using an activator-reporter dye pair holds true for a number of reporters, including Alexa647, and activators, including Cy3 and Alexa Fluor 405, which are the activator-reporter dye pairs we used in our experiments. A second way to control the blinking behaviour of the STORM dyes is by using special imaging buffers. It has been shown that the residence time in the dark states of these dyes can be prolonged by using specific buffers that *(i)* act as reducing agents, by providing electrons to the excited dyes thereby increasing the probability of the transition to a dark state; and *(ii)* include an oxygen scavenging component to maintain the molecule in the excited dark state and therefore increase the lifetime in that state and reduce oxygen-dependent photobleaching.

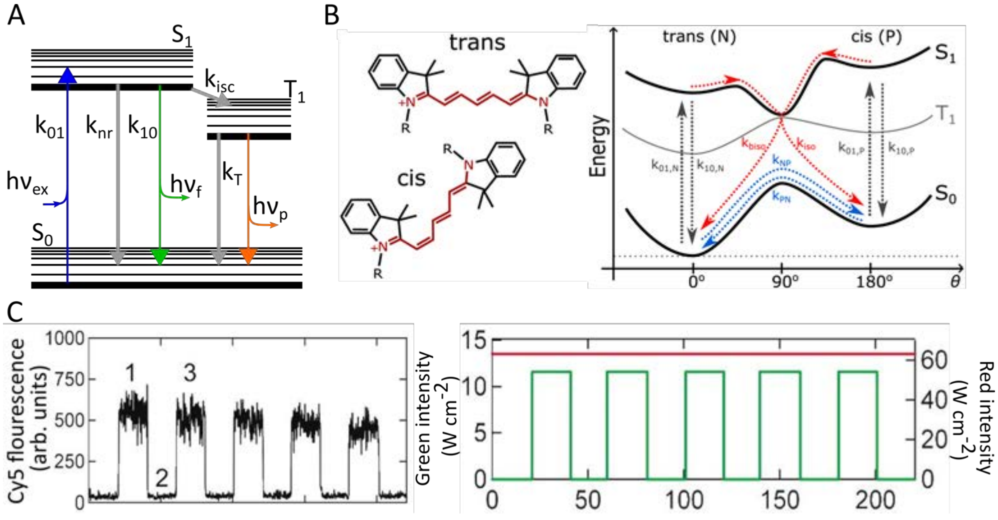

Figure 2.1 *Transitions between emissive (on) and non-emissive (off) states of organic dyes needed for STORM imaging*

(A) Jablonski diagram for fluorescence and intersystem crossing (ISC) leading to molecules in a triplet state (T_1). Energy (hv_{ex}) is absorbed by the molecule and electrons are transferred to the first singlet excited state, S_1, from where the molecule can relax to the ground state, S_0, either radiatively with the emission of a photon of lower energy than the absorbed one (hv_f) at a rate of k_{10} – this is termed fluorescence –, or through a nonradiative process, which usually occurs with a lower probability (with rate k_{nr}). Alternatively, the molecule in the S_1 state can undergo ISC and eventually enter the triplet state, T_1. The return to S_0 from T_1 occurs at a total rate of k_T, and the release of energy of this transition is in the form of phosphorescence (because there is a change in the spin multiplicity from a triplet to a singlet state), which we do not detect experimentally, adapted from *Tornmalm, 2019*. (B) Chemical structure of the dye Cy5 in two isoforms, where *trans* is fluorescent and *cis* is not. The energy levels for the *trans* and *cis* configurations are depicted on the right (*Tornmalm, 2019*). (C) Fluorescence response of the dye pair Cy3–Cy5, where the left graph shows the fluorescence signal detected. The right graph shows the laser illumination scheme, where the green laser (green line) excites the activator Cy3 molecule, and the red laser (continuous red line) excites the reporter dye Cy5 from which the fluorescence is detected. Activation of Cy3 controls the emission behaviour of Cy5 by inducing its on-off blinking. Adapted from *Bates et al., 2005*.

In our experiments, we relied on the use of activator-reporter dyes and, in addition, included the use of appropriate buffers to further control on-off-blinking. Specifically, STORM was performed in an imaging buffer containing 100 mM of the reducing agent cysteamine mercaptoethylamine (MEA) (77 mg of MEA in 1 ml of 360 mM HCl, stock solution 1 M), and the enzymatic oxygen scavenger Glox solution (0.5 mg/ml glucose oxidase, 40 µg/ml catalase), and 6.25% glucose in PBS.

All our two-colour STORM images were acquired on a commercial Nikon Eclipse Ti system (N-STORM) with a 100x oil objective with NA 1.49 using TIRF illumination. The detector was an ANDOR technology EMCCD iXon 897 camera, with a 256x256 pixel ROI and a pixel size of 160 nm. The excitation of the dyes was achieved using an Agilent technologies laser box with laser lines 405 nm (∼22 mW), 561 nm (∼35 mW), and 647 nm (∼153 mW). The Nikon-developed NIS software was used for acquiring the data. In a pre-acquisition step the sample was irradiated with the 647 nm laser at 70% (∼107 mW) to force the majority of molecules into a long-lived dark state. We then begin the STORM acquisition maintaining the 647 nm laser at a constant power and using low power activator (405 nm or 561 nm) excitation, which we increase incrementally, from 0.5% to 100%, as the acquisition progresses. With each laser power increase we achieve an increase in detected reporter molecules followed by a subsequent decline, as the molecules bleach (Figure 2.2 B). The acquisition is stopped when there are no longer sufficient reported molecules being detected, which in our case was after ∼70,000 frames.

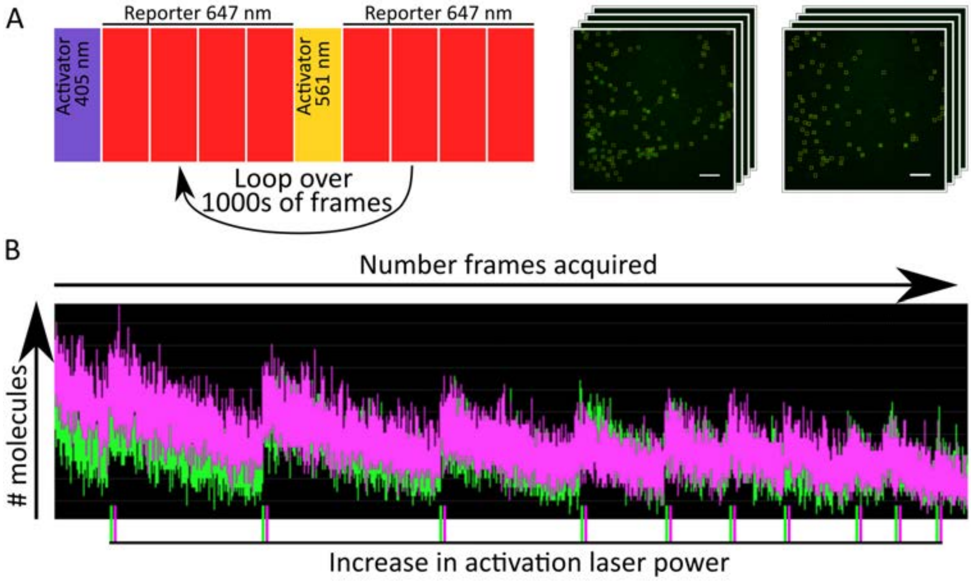

Figure 2.2 *Number of molecules detected as a function of frames acquired*
(A) The laser sequence in our dual-colour STORM image acquisition. One frame of 405 nm laser illumination (purple), followed by four frames of 647 nm laser illumination (red), followed by one frame of 561 nm laser illumination (yellow) and four frames of 647 nm laser illumination (red). The right image in (A) shows a representative set of images of the molecules detected in the first frame of a 647 nm illumination cycle. Scale bar = 5 µm. (B) After each increase of activator laser (marked by the green and magenta lines) there is a clear increase in the number of detected reporter molecules, which progressively reduce in time because of photobleaching. Figure adapted from *Borgman et al., 2020*.

For our two-colour STORM image acquisition, we used activator-reporter-conjugated secondary antibodies. Specifically, we used Alexa405 paired with Alexa647 for targeting integrins, and Cy3 paired with Alexa647 for targeting the adaptor proteins. To obtain two-colour STORM images, we acquired images sequentially by repeating cycles of a frame-based illumination scheme (each frame has a duration of 20 ms), as follows. First, one frame with the 405 nm laser on, which excites the Alexa405 activator dye, which – due to an energy transfer mechanism different to Förster resonance energy transfer (FRET) (Bates et al., 2005) – induces a population of the reporter dye Alexa647 in a dark off state to return to the ground state. Second, four frames are recorded with the 647 nm laser on, which excites the subpopulation of molecules in the on state (Figure 2.2 A). We use a four-frame readout to allow for the full population of the reporter dye that was activated by Alexa405 dyes to be excited and detected and therefore reduce crosstalk between the channels. Next, a similar activation/reporter excitation sequence is done for the Cy3–Alexa647 dye pair, consisting of one frame with the 561 nm laser on, and four extra frames with the 647 nm laser on. This imaging cycle that switches between activator and reporter excitation is carried out iteratively over thousands of times, which results in thousands of images where individual molecules can be identified and localised (Figure 2.2, A, right). Details of all the reagents for the imaging buffer are laid out in Table 2.5.

Table 2.5 Reagents and dyes for STORM imaging

Reagent	Abbreviation	Company	Cat #
Glucose Oxidase from Aspergillus niger		Sigma-Aldrich	G2133
Hydrochloric-Acid	HCl	Sigma-Aldrich	258148
Cysteamine mercaptoethylamine	Cysteamine MEA	Sigma-Aldrich	30070
α-D-glucose		Sigma-Aldrich	158968
Catalase from bovine liver		Sigma-Aldrich	C100
Cy3		Sigma-Aldrich	GEPA23001
Alexa Fluor 647 carboxylic acid succinimidyl (NHS) ester	Alexa647	Invitrogen	A20006
Alexa Fluor 405 carboxylic acid succinimidyl (NHS) ester	Alexa405	Invitrogen	A30000

Molecule detection and localisation precision

The output of our STORM image acquisition consists of many TIRF microscopy images showing the fluorescence signal resulting from stochastically-activated, sparsely-distributed individual molecules. The signal from each of these molecules appears as a diffraction-limited point spread function (PSF), so the centre position of each PSF is localised with high precision, and represents the position of each individual molecule. Being able to localise the molecules with very high precision is fundamental to obtain a super-resolved STORM image. This precision is limited by the number of detected photons in each blinking event. In each imaging frame, the individual molecules (Figure 2.3 A) are identified using intensity thresholding and, one by one (Figure 2.3 B), each intensity profile (Figure 2.3 C) is fitted with a Gaussian to identify the central position (Figure 2.3 C, red circle). The final output of this molecule localisation algorithm provides a list of x,y coordinates for each individual molecule that has been identified, together with the frame number in which they were found. The precision of the localisation is given by:

$$\sigma_{x,y} \propto \frac{s}{\sqrt{N}} \qquad (2.1)$$

Where $\sigma_{x,y}$ is the precision, s is the standard deviation of the fitted PSF, and N is the number of detected photons from the molecule. Each molecule can experience numerous blinking events and how the x,y coordinates vary from frame to frame determines the accuracy and resolution of the system. In our system, the precision of the single molecule localisations is ~7 nm, while the localisation accuracy or resolution is ~15 nm. The latter was determined by running a clustering algorithm on multiple localisations events arising from individual molecules deposited on glass, and calculating the standard deviation of the localisation positions.

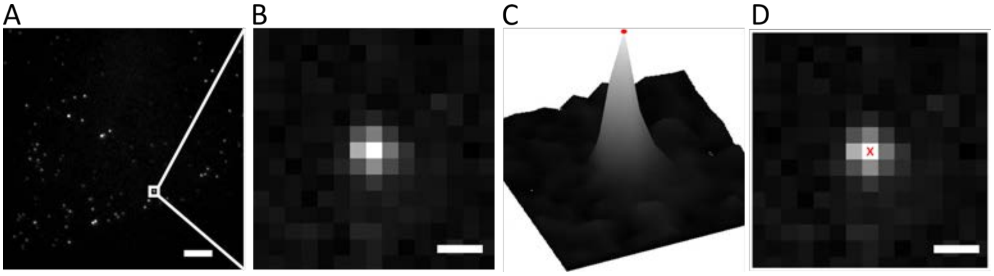

Figure 2.3 *Detection and localisation of single molecules*
(A) A single camera frame obtained in a typical STORM image acquisition. (B) PSF of a single fluorescent molecule as detected in the camera frame. (C) Intensity profile of (B), which is then fitted with a Gaussian to find the location of the central peak, marked with the red dot. (D) Representation of the localisation of the centre of this molecule (red cross) overlaid with the camera frame shown in (B). Scale bars are 5 µm in (A) and 500 nm in (B, D). Generated from our data based on *Oddone et al., 2014*.

2.5 Image reconstruction

Dual-colour STORM image reconstruction was done using Insight3, provided by Bo Huang (UCSF, initially developed in Xiaowei Zhuang's Lab). The molecule localisation analysis was run over the entire data sets but recording only those localisations detected in the second frame of the five-frame cycle (see Figure 2.2 A), that is the first of the four reporter frames. We only considered single spots with an intensity above a threshold (set to 600 grayscale levels on a 14-bit image), which was then fitted with a two-dimensional Gaussian function, where the x-y coordinates of the Gaussian centroid determine the localisation position. Each localisation was allocated to channel one or to channel two depending on what frame it originally belonged to. The data were then corrected for sample drift and colour crosstalk. Insight3 software allows for drift correction using the correlated function of the image, see (Huang et al., 2008). In this multicolour imaging scheme, the main source of crosstalk is the nonspecific activation of the Alexa 647 by the 647 nm laser (Dani et al., 2010), which is activator-independent and can occur in any frame. In order to minimise this crosstalk, the number of frames between activators can be increased. We implemented statistical crosstalk correction where the Insight3 software analyses the full image in 50x50 nm regions of interest (ROIs) and determines if each ROI is predominantly one colour of the other. Based on the acquisition design (in our case, one activator frame followed by four reporter frames) the software determines the probability of detecting a nonspecific reporter molecule (Dani et al., 2010). The final image is corrected for crosstalk and is then built by the superposition of all the remaining localisations, which can be rendered by a cross marking their centres or a Gaussian profile convoluted with the point position.

2.6 Image Analysis

Together with the emergence of super-resolution imaging techniques came the need for stronger, more robust analytical tools. In order to quantitatively exploit the vast amount of detailed information contained in super-resolution images, one requires different types of specialised, custom-made algorithms and dedicated software. Ideally, these tools should be able to handle large data sets (big data) and require little or no inputs from the user in order to allow for analysis with minimal user bias. In particular, the data analysis pipeline used in this thesis is centred primarily around an algorithm developed in 1996 by Xiaowei Xu's lab, named density-based spatial clustering of applications with noise (DBSCAN) (Ester et al., 1996). Once the clusters were detected, we ran various custom-made MATLAB algorithms. In addition, we used Fiji and its plugins for less complex processes.

2.6.2 Image analysis using Fiji

A Fiji plugin, developed by the Lakadamyali lab during their time at ICFO, was implemented as an initial step to split the localisation data from the STORM images into separate data sets corresponding to the localisations contained in certain ROIs. Figure 2.4 shows the steps involved in the categorisation of the data. First, the data from the two channels of the reconstructed STORM image are imported and the localisations are rendered together in a 1024x1024 pixels image (Figure 2.4 A). Next, we apply an intensity threshold, until visually the adhesion areas are detected, a Gaussian blur of the image (by 2 pixels), and a second threshold filter until a smooth binary mask is obtained. The final mask retaining only the adhesion areas (Figure 2.4 B) is obtained by manually selecting the regions corresponding to the adhesion complexes (identified by visual inspection based on their size and appearance). The Fiji plugin then creates new files that contain only the localisations that fall within the selected ROIs: all adhesions, only FAs, only fAs, glass, and outside adhesions (i.e., cell membrane that contains the remaining areas of the image that do not correspond to all adhesions or glass). Finally, any of the ROI-associated files can be rendered with Insight3, for example "all adhesions", as shown in Figure 2.4 C and Figure 3.4. These final two-colour files for different cell regions can then be individually and independently analysed with the DBSCAN algorithm.

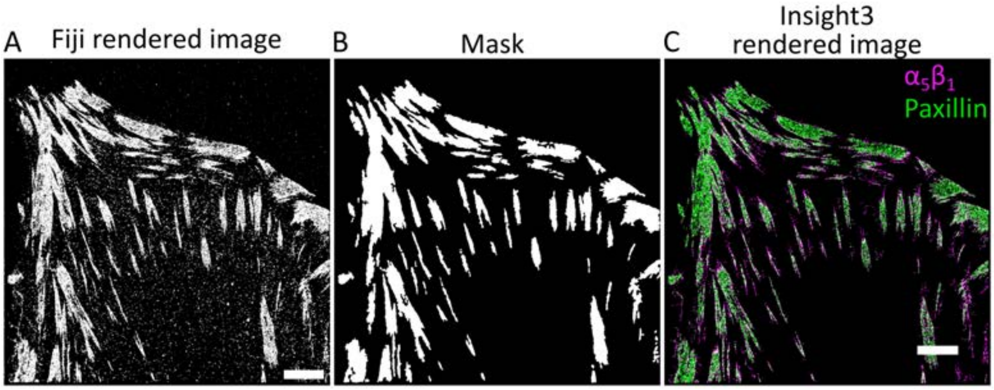

Figure 2.4 *Separation of all the adhesions for analysis*
(A) Localisations of both channels collapsed into one single rendered image. (B) Mask of the manually-selected adhesions. (C) Rendered image of all the localisations of $\alpha_5\beta_1$ (magenta) and paxillin (green) found to be in all adhesions (falling in the mask region shown in white in panel B). Scale bars = 5 µm.

2.6.3 DBSCAN algorithm

The DBSCAN algorithm (Ester et al., 1996) is a density-based data clustering algorithm designed to be executed on arbitrary data sets with minimal input from the user. Previous to DBSCAN development, there were basically two types of data clustering algorithms: partitioning and hierarchical algorithms, examples of which are CLARANS (Clustering Large Applications based on RANdomized Search) (Ng and Han, 1994) and Ejcluster (García et al., 1995), respectively. However, these two types of clustering algorithms have drawbacks, especially when handling large data sets (Ester et al., 1996). DBSCAN is a lower-complexity algorithm and therefore overcomes this limitation. DBSCAN works by identifying arbitrary-shaped clusters of data points with just two user-defined input values: epsilon (eps), which is a radial distance that serves to define a local neighbourhood from a randomly selected initial data point; and N_{min}, which is the minimum number of points required to be within the initial point's neighbourhood so it is considered part of the cluster seed (Figure 2.5). If the initial data point is not found to meet the cluster seed conditions, it is initially characterised to be noise (although it can still be part of another cluster, see below). Otherwise, if the initial data point is a cluster seed, then each point in the eps-neighbourhood of the seed is similarly analysed to test if their eps-neighbourhood contains at least N_{min} points (green points and circles in Figure 2.5). If this condition is satisfied, these new points are considered to be core points of the cluster, and the process is iterated for them. If not, the points identified to be in the eps-neighbourhood of the core point but not satisfying the core criteria themselves are considered to be boundary points (orange points in Figure 2.5) and also assigned to the cluster. This process is then iterated for all the data points that have not been identified as part of a cluster. Finally, the points that are not connected to a growing cluster and do not satisfy the cluster seeding conditions for another cluster are considered to be a non-clustered point or noise (blue points in Figure 2.5).

For the analysis of the STORM data presented in this thesis, we took eps=20 nm and N_{min}=3 localisations. This means that areas with at least three localisations in a circle of radius 20 nm serve as minimum seeds for cluster identification. The value of eps=20 nm was chosen based on the localisation precision (resolution) of our STORM images, which is common practice in the field (Pageon et al., 2016; Spiess et al., 2018). Our choice of N_{min}=3 localisations was also based on common practise in the field, see, e.g., (Pageon et al., 2016; Spiess et al., 2018), which also used DBSCAN for SMLM analysis.

Importantly, in our cluster analysis we need to take into consideration the fact that, during STORM image acquisition, a single fluorophore can undergo multiple blinking events and therefore a single molecule can appear as multiple localisations. It is therefore important to underscore that a cluster of localisations does not necessarily infer cluster of proteins. To measure the number of localisations per individual fluorophore, we ran the DBSCAN algorithm on the regions of our STORM images that were outside of the cell, where we considered the localisations detected to be from individual molecules on glass. In order to ensure we detected small clusters, in this case attributed to single molecules, we reduced N_{min}=2 and maintained eps=20 nm. We found the mean and median number of localisations per spot on glass for both dye pairs to be less than 10 (see Chapter 3). Therefore, of the clusters of localisations we identified on the cell area by using DBSCAN (with N_{min}=3 and eps=20 nm), we only considered those with a number of localisations ≥ 10 to be real protein clusters, as the rest were assumed to correspond to single molecules. Hence, only those clusters with number of localisations ≥ 10 were used for all follow-up analyses carried out in this thesis. In addition to identifying the localisations belonging to each cluster, the DBSCAN algorithm also provides the centre of mass position (CoM) and the surface area of each identified cluster, allowing us to perform further quantitative analyses. The surface area of a cluster was found by taking the boundary localisations of each clusters and calculating the area of the polygon enclosed by them.

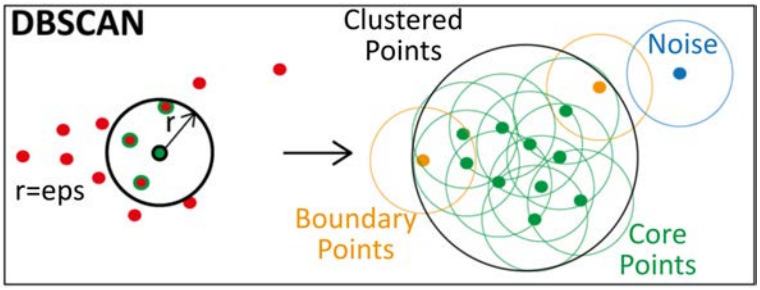

Figure 2.5 *Working principle of DBSCAN algorithm*
In the left, a set of data points is shown, where a point (green point with black outline) is chosen at random, and its eps-neighbourhood is explored (black circumference) and tested if it contains at least N_{min} data points (N_{min}=4 in this example). In this case, the newly-identified points in this neighbourhood (red points with green outline) satisfy this condition and are therefore defined as core points of the cluster (see panel in the right). The right panel shows the final result of DBSCAN in this set of data points, indicating the different classifications of points in a cluster determined by their local density of neighbouring points, adapted from *Pageon et al., 2016*.

2.6.4 Nearest neighbour distance (NND) computation

In order to establish how the protein nanoclusters are distributed relative to each other, we used the MATLAB function *knnsearch* to compute the NND between the CoM of nanoclusters of the same protein, $NND_{A\text{-}A}$ (see Chapter 4). The distribution of $NND_{A\text{-}A}$ values provides quantitative information on how the nanoclusters of each protein are distributed within the adhesions. We also used this function to determine the preferential distance between clusters of different proteins, in this case being $NND_{A\text{-}B}$ (Chapter 5), and the preferential distance between clusters and the edge of adhesions (Chapter 6).

2.6.5 Computational generation of random nanocluster distributions

To assess whether the NND distributions obtained from the experimental data correspond to a preferential type of organisation or to a random distribution, we performed simulations by generating *in silico* NND histograms of randomly distributed nanoclusters inside the adhesion structures, both FAs and fAs. In order to proceed, we essentially needed two ingredients: *First*, to extract from the experimental data the exact number of nanoclusters per adhesion; and *second,* to distribute the same number of nanoclusters in a random fashion within the adhesions, while excluding their spatial overlapping. We therefore followed the different steps outlined below.

Step 1: Identification of nanoclusters inside a given adhesion. We first paired the mask of the adhesions in a cell to the corresponding experimental data. Each particular adhesion, An, contains a certain number of nanoclusters. The algorithm, coded in MATLAB, went sequentially through each mask, identified which adhesions contained clusters, counted the number of nanoclusters belonging to each adhesion, extracted their CoM position, and measured their physical size. Figure 2.6 shows, as example, the binary adhesion mask of a given cell and the CoM positions of the individual nanoclusters (red points) identified in fAs.

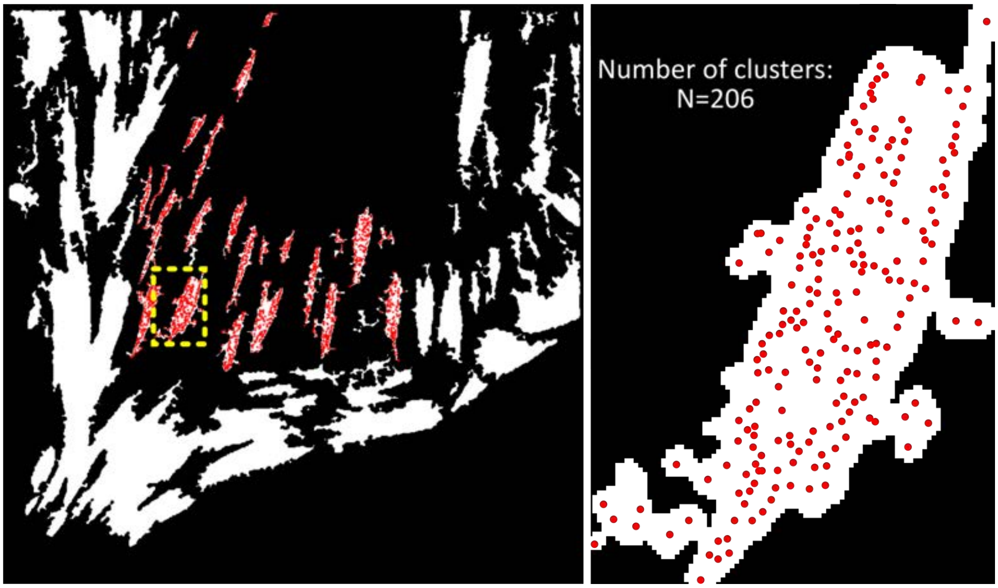

Figure 2.6 *Mask and CoM of clusters in fAs on an HFF-1 cell 24 h after seeding*
The left panel shows the binary mask of all the adhesions (white regions) of the cell and the clusters found in fAs plotted using their CoM (red dots). The right panel is a zoom-in of the region marked by the broken yellow box on the left, that shows one fA and the clusters therein contained. In this particular example, there are 206 experimentally identified nanoclusters.

Step 2: Sorting the nanoclusters as function of their physical size. Although our initial approach was to computationally generate the same number of nanoclusters and distribute them randomly over the adhesion masks regardless of their physical size, we found that this approach was not suitable. The reason for it is that in many cases the large nanoclusters did not fit in the remaining space available by the adhesions after randomly positioning the large majority of smaller nanoclusters. We thus opted for classifying the nanoclusters according to their physical size and then start our procedure by randomly positioning first the largest nanoclusters and later all the remaining smaller ones. In addition, as our experimental data renders well segregated nanoclusters, we imposed in our algorithm the condition that nanoclusters should not overlap with each other.

To classify the nanoclusters as a function of size, we plotted the experimental cluster radii as a cumulative distribution function, determined a threshold cluster radius, R_{th}, which corresponds to the lower bound of the 80th percentile. We sorted the radii according to their size and segregated the clusters into two groups: the 20% largest and the 80% smallest (see Figure 2.7 panel 1). Therefore, the number of large clusters, N_{big}, for any adhesion was equal to the number of clusters N with a radius greater than the threshold, $r>R_{th}$.

Step 3: Random distribution of the largest clusters and size assignment. First, we generated $100xN_{big}$ random points distributed over the minimum non-tilted boundary box containing the adhesion (see panel 2 in Figure 2.7). We then identified and kept only those points inside the adhesion (see panel 3 in Figure 2.7). If the number of points that fell inside the adhesion, N_{in}, was larger than N_{big} we then randomly removed points to ensure that $N_{in}=N_{big}$. If $N_{in}<N_{big}$ we then repeated the procedure to generate new sets of N_{in} until $N_{in}=N_{big}$, (see panel 4 in Figure 2.7). With $N_{in}=N_{big}$ achieved, we then randomly assigned a radius to each point in N_{in} from the set of large radii determined by $r>R_{th}$

Step 4: Identification and rejection of overlapping nanoclusters. To identify nanoclusters that spatially overlapped, we calculated the centre-to-centre distance from each cluster to its k-th nearest neighbours, kND, where if the number of clusters in an adhesion was greater than 10, $N_{in}>10$, then k=10, and if $N_{in}\leq 10$ then $k=N_{in}$. We then calculated the intercluster distance (i.e., edge-to-edge distance between nanoclusters), IC, which we defined as:

$$IC = kND - R_{ref} - R_k \,, \tag{2.2}$$

where R_{ref} and R_k correspond to the radius of the reference and the k-neighbour nanoclusters, respectively. If clusters overlap, i.e., $IC\leq 0$, for any of the k-neighbours, then both the reference cluster and the neighbour were rejected.

We followed this approach for all large clusters, resulting in two possible outputs: clusters that survived the overlapping criteria (green dots panel 5 in Figure 2.7), and those rejected due to overlapping with a neighbour (red dots in panel 5 in Figure 2.7). Thus:

$$IC > 0 \rightarrow XY_S, \text{with radius}, R_S. \tag{2.3}$$

$$IC \leq 0 \rightarrow XY_{rej}, \text{with radius}, R_{rej}. \tag{2.4}$$

The number of clusters that survived the overlapping criteria, N_S, were then fixed in place with their randomly assigned XY_s coordinates and radius R_s. All the other clusters that failed the overlapping criteria were rejected, N_{rej}.

Step 5: Generation of newly proposed random clusters, N_{prop}. We then took the rejected clusters from the previous step, N_{rej}, and repeated the steps portrayed in panels 6–8 of Figure 2.7, resulting in new random points $N_{prop} = N_{rej}$ (see red dots in panel 6 of Figure 2.7). These points were once again assigned a radius from the set of radii initially rejected, R_{rej}.

Step 6: Assessment of cluster overlap between those newly proposed nanoclusters and Ns. The total number of randomly generated clusters was:

$$N_{tot} = N_S + N_{prop}. \tag{2.5}$$

We calculated the kND as before, but this time we calculated them from each point in N_{prop} to each point in N_{tot}. We once again calculated the IC (Eq 2.2), however, for this step if $IC \leq 0$ we only rejected the reference cluster from the newly proposed set. If $IC > 0$ we added the reference cluster from the newly proposed set to the N_S pool. This step once again gave two outputs: an updated set of clusters that survived along with the radii they were assigned, and a number of clusters that were rejected.

We repeated the last two steps, generating newly proposed points equal in number to the previously rejected ones and assessing if they overlap with the pre-existing clusters, until we achieved $N_{rej}=0$, and therefore $N_S=N_{big}$. In this way we generated a set of randomly distributed large clusters that do not physically overlap with one another, and with a size that was randomly extracted from the experimentally measured nanoclusters that had radii larger than the threshold, i.e., $r>R_{th}$.

Step 7: Generation and placement of small clusters, N_{small}. With all large clusters in place, we again repeated the last two steps above (steps 5,6) using this time N_{small}, the remaining 80% of clusters whose $r<R_{th}$, as the input. We generated newly proposed clusters, with $N_{prop}=N_{small}$ (see the step-by-step procedure in Figure 2.8), and evaluated if the new clusters overlap, either with themselves or with the large clusters that had been placed previously. We did this sequential loop of generation and assessment until the number of small clusters that were rejected due to overlap was less than or equal to 10, $N_{rej} \leq 10$.

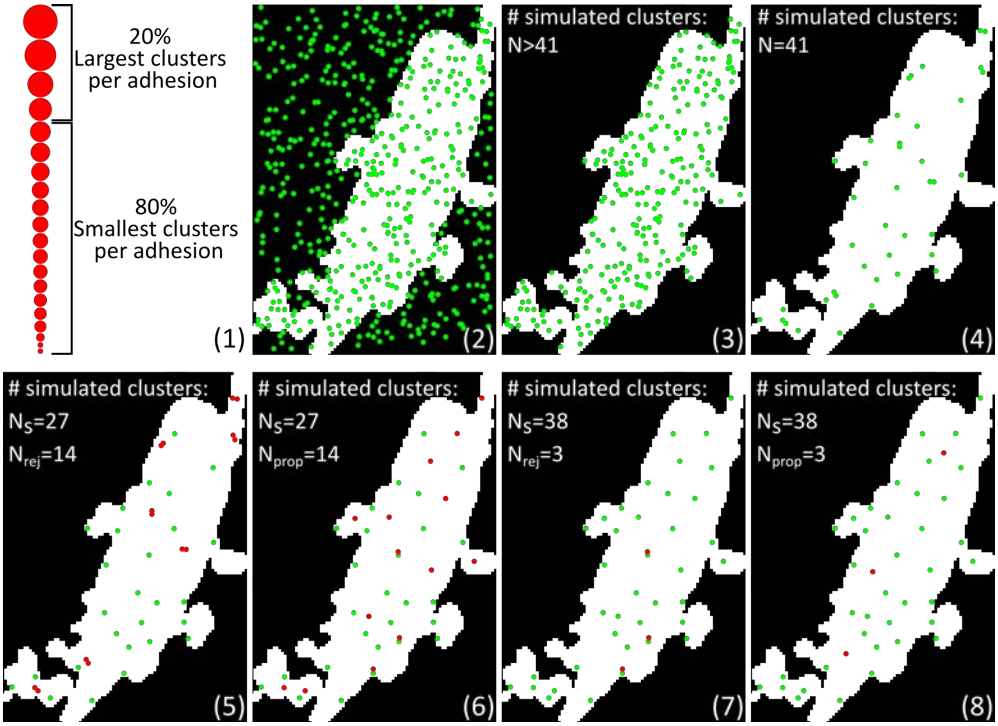

Figure 2.7 *Step-by-step description of the generation of random non-overlapping circles for the 20% largest clusters in a given adhesion*

Top row (from left to right): 1, sort experimental clusters by size and find the 20% largest clusters. 2, generate 100xN_{big} random points (green dots) that fall within the minimum non-tilted boundary box of the adhesion. 3, identify the points that fall inside the adhesion area. 4, assess whether N_{in}=N_{big}. Bottom row (from left to right): 5, Identify the clusters that overlap (red points), define N_s as the points that survive, i.e., do not overlap with any other point, and N_{rej} as the points that are rejected because they overlap. 6, propose new points, N_{prop}=N_{rej}, shown as red points, where the green points are those that survived the first evaluation. 7, evaluate these N_{prop} to see if they overlap with any other cluster and reject those that do (red points). 8, continue to propose new points until no overlap is found (red points) N_{rej}=0.

Step 8: Placement of the last 10 random clusters in the adhesion. Once N_{rej} ≤10, we placed the clusters individually, one-by-one. To this end, we generated 1000 points inside the adhesion of interest and assigned them all the same radius, r, from the list of R_{rej}. We then assessed each of these 1000 clusters and found those that had an IC>0, implying they did not overlap with another cluster. We then randomly selected one of these nanoclusters and added it to the survived list with its radius, r, and XY coordinates. We repeated this cycle until N_{rej}=0.

We followed all these steps on all adhesions, and 10 times per cell to reach a close-to-theoretical random distribution of non-overlapping nanoclusters.

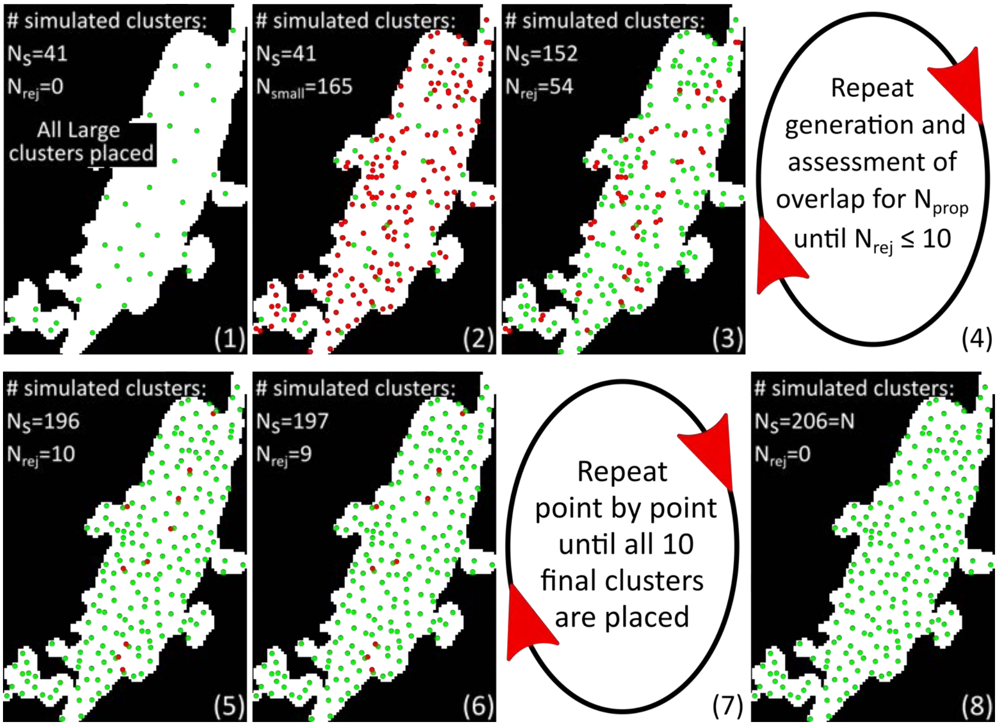

Figure 2.8 *Step-by-step procedure for the generation of random non-overlapping circles, corresponding to the 80% smallest clusters in an adhesion*

Top row (from left to right): 1, all large clusters (green dots) are in place. 2, generate random points inside the adhesion (red dots) where the number of points is equal to the number of experimentally determined small clusters whose $r<R_{th}$ and assign them a radius $r<R_{th}$. 3, calculate IC, and retain (green dots) or reject (red dots) overlapping nanoclusters. The generation and assessment for overlap on newly proposed nanoclusters is then repeated until $N_{rej} \leq 10$. Bottom row (from left to right): 5, all non-overlapping clusters have been positioned randomly (green dots) with the red dots representing the 10 remaining clusters that have IC ≤ 0. Panels 6–7 show the one-by-one placement of the 10 last remaining nanoclusters. Panel 8 shows the final *in silico* reconstructed adhesion with all the nanoclusters randomly distributed and with no overlap between them.

2.6.6 Data representation with GraphPad Prism

We used GraphPad Prism, version 9.1.2, as a means to represent certain data where we had individual values of a given parameter for each cell, and wanted to assess the distribution over the cells. In general, we used the box-and-whisker plots where the box shows the interquartile range (IQR), the bar marks the median and the whiskers extend to the 10th and 90th percentile. Alternatively, we also used scatter plots where each point is a value for a cell, and where the included bars mark the mean or median and whiskers over the distribution of cells. Whether we use mean or median and the details of the whiskers are specified in each chapter.

2.6.7 Statistical analysis

In order to ascertain if the variation seen between data sets is statistically significant, we run the appropriate statistical tests for each individual case. In general, we use the one-way ANOVA tests in the case of multiple data sets to be compared or the paired Student's t-Test when comparing experimental with simulated data on a protein-by-protein basis. We used a confidence interval of 95% and the p-values categorised as: ns = not significative, $p>0.05$; *, $p<0.05$; **, $p<0.01$; ***, $p<0.001$. Which tests were carried out will be stated in the methods section of each chapter

2.7 Summary of data acquired

The combinations and number of images per seeding time points and labelled proteins are detailed in the following tables. Table 2.6 shows a complete summary of the number of images and different experiments for each protein at each time point. These data were used in the analysis carried out for Chapter 3, Chapter 4 and part of Chapter 6 where the analysis being performed was dependent on the individual protein and it was not necessary to consider the partner it was originally imaged with.

Table 2.6 Summary of all STORM images and experiments for each protein at each time point

Time	Protein	# Experiments	# Images	FAs	fAs	out
90 min	$\alpha_5\beta_1$	11	28	28	28	28
	$\alpha_v\beta_3$	12	29	30	18	30
	paxillin	11	24	24	20	24
	talin	7	16	16	13	16
	vinculin	5	18	18	13	18
3 h	$\alpha_5\beta_1$	9	17	17	17	17
	$\alpha_v\beta_3$	10	24	24	16	24
	paxillin	7	16	16	14	16
	talin	6	13	13	8	13
	vinculin	6	12	12	11	12
24 h	$\alpha_5\beta_1$	7	18	18	18	18
	$\alpha_v\beta_3$	8	21	21	8	21
	paxillin	5	16	16	12	16
	talin	4	12	12	8	12
	vinculin	6	11	11	6	11

The following two tables (Tables 2.7 and 2.8) show a summary of the data acquired for each protein pair at each time point. These data were used for the analysis of Chapter 5 where we studied the distances between clusters of different proteins and the second half of chapter 6 when assessing the correlation between the proximity of different protein nanoclusters and their distance-to-the-edge of the adhesions.

Table 2.7 Summary of images for $\alpha_5\beta_1$ experiments

Time	Protein pairs		#Samples	#Images	#FA data sets	#fA data sets
	Ch1	Ch2				
90 min	$\alpha_5\beta_1$	paxillin	5	8	8	8
	$\alpha_5\beta_1$	talin	4	10	10	10
	$\alpha_5\beta_1$	vinculin	2	10	10	10
3 h	$\alpha_5\beta_1$	paxillin	3	6	6	6
	$\alpha_5\beta_1$	talin	3	5	5	5
	$\alpha_5\beta_1$	vinculin	3	6	6	6
24 h	$\alpha_5\beta_1$	paxillin	2	8	8	8
	$\alpha_5\beta_1$	talin	2	5	5	5
	$\alpha_5\beta_1$	vinculin	2	5	5	5

Table 2.8 Summary of images for $\alpha_v\beta_3$ experiments

Time	Protein pairs		#Samples	#Images	#FA data sets	#fA data sets
	Ch 1	Ch 2				
90 min	$\alpha_v\beta_3$	paxillin	6	16	16	12
	$\alpha_v\beta_3$	talin	3	6	6	3
	$\alpha_v\beta_3$	vinculin	3	8	8	3
3 h	$\alpha_v\beta_3$	paxillin	4	10	10	8
	$\alpha_v\beta_3$	talin	3	8	8	3
	$\alpha_v\beta_3$	vinculin	3	6	6	5
24 h	$\alpha_v\beta_3$	paxillin	3	8	8	4
	$\alpha_v\beta_3$	talin	2	7	7	3
	$\alpha_v\beta_3$	vinculin	3	6	6	1

Chapter 3

Focal adhesion proteins form spatially-segregated nanohubs at the cell membrane

Adhesion complexes are protein-rich regions of the cell membrane, composed of hundreds of different proteins. When imaged using diffraction-limited fluorescence microscopy, adhesion complexes appear as highly-packed homogeneous structures, wherein the adhesion proteins colocalise with one another. In this chapter, we investigated the organisation of adhesion complexes at the nanoscale by using the super-resolution microscopy technique STORM. We demonstrate, through the implementation of various software algorithms to analyse the images, that a subset of adhesion proteins (the integrins $\alpha_5\beta_1$ *and* $\alpha_v\beta_3$*, and the adaptor proteins paxillin, talin, and vinculin) form spatially-segregated nanoclusters at the cell membrane. Moreover, the characteristics of these nanoclusters remain unchanged as a function of the cell spreading time and are not influenced by the region of the basal membrane they are populating, such as FAs, fAs, or the membrane regions outside adhesions. We also present our analysis on the number of nanoclusters per unit area for the different adhesion proteins, and revealed that the density of nanoclusters per unit area increases with time for the two integrins involved at the centre of the study. In contrast, the density of adaptor protein clusters remains unchanged regardless of the time allowed for cell attachment and spreading, and for all the adhesion structures investigated. We aimed to reveal the source of this increase in integrins cluster density. Our results indicate that the increase of the number of integrin nanoclusters in adhesions with time is likely to arise from the arrival of new proteins at the basal membrane.*

3.1 Introduction

Adhesion complexes are high-density protein platforms that form at the cell membrane coupling proteins of the extracellular matrix (ECM) with the cell's cytoskeleton. This partition is bridged by a class of transmembrane proteins, known as integrins, and assisted by a number of different adaptor proteins. Integrins are heterodimeric proteins found in the cell membrane responsible for cell adhesion and migration, and also for mechanosensing (Hood and Cheresh, 2002; Schwartz and DeSimone, 2008; Strohmeyer et al., 2017). Integrins can transiently bind their ligand and dynamically switch between different structural conformations that correlate to their activation state and function (Su et al., 2016; Takagi et al., 2003). The integrin-generated link between the internal and external cell environments allows adhesion complexes to act as bidirectional signalling platforms of the cell (Hu and Luo, 2013; Montanez et al., 2008). The accurate binding of integrins to their ligands and signalling to their adaptor proteins is vital for accurate cellular function, in processes such as migration (Egles et al., 2010; Wood et al., 2011; Colburn and Jones, 2017), differentiation (Watt et al., 1993; Neiman et al., 2019), and proliferation (Walker and Assoian, 2005).

Exactly how these different signals, which are transmitted and transduced by the cell, depend on the types of adhesions and how the proteins are organised at the nanoscale are still not well understood. The lack of experimental data is not only due to the inherent complexity of adhesion complexes, but also in part because, until recently, it was not possible to overcome the diffraction limit of light and observe how adhesion proteins were laterally distributed at the nanoscale. Thanks to the emergence and development of super-resolution imaging techniques over the last number of years, it has become feasible to investigate how the proteins of the adhesion complexes are organised and distributed at the nanoscale in both axial and lateral directions. In a seminal work, Kanchanawong et al. established, using a technique known as interferometric PALM (see Chapter 1 for details), that adhesion proteins segregate in the axial direction to form functional three-dimensional layers in FAs (Kanchanawong et al., 2010). Besides being segregated in the axial direction, other groups have reported that the main adhesion proteins also organise laterally by forming small patches or nanoclusters within the dense adhesion complexes (Shroff et al., 2007; Hoorn et al., 2014; Hu et al., 2015). However, despite these groundbreaking observations, very few in-depth characterisations of these nanostructures have been carried out. In a recent study using both STED microscopy and STORM, Spiess et al. showed that inside adhesions, the $\alpha_5\beta_1$ integrin forms segregated nanoclusters in both the active and inactive states (Spiess et al., 2018).

Moreover, dual-colour STED imaging and colocalization analysis for talin, kindlin and vinculin indicated that other adhesion proteins may also nanocluster within adhesion complexes. Here, “adhesion complex” is a general term that covers a range of different attachment areas at the cell membrane. Two distinct types of adhesion complexes are FAs and fAs. More details of the different adhesion complexes and their dynamic evolution can be found in Chapter 1 of the thesis.

In this study, we explored the attachment areas on the basal surface of the cell membrane. In particular, we separately investigated three major regions of the basal membrane: FAs, located preferentially at the peripheral areas of the membrane; fAs, mostly present on the central parts of the membrane; and the remaining membrane area outside of these two former structures, where adhesion proteins are present at a much lower density. Moreover, we performed experiments at different cell seeding times, from 90 min to 24 h. By using dual-colour super-resolution STORM microscopy, our aim has been to provide greater insight on the nanoscale organisation of the proteins in these three different regions of the cell membrane. We considered that by ascertaining how these proteins segregate at the nanoscale, we would be able to contribute to the greater picture of how cells interact with their environment in order to carry out their functional roles.

3.2 Methods

3.2.2 Sample preparation and immunolabelling

Samples were prepared by seeding HFF-1 cells on FN coated 8-well plates. The cells were allowed to spread for different times (90 min, 3 h, and 24 h), were fixed and then immunolabelled using primary and secondary antibodies, as described in detail in Chapter 2.

3.2.3 Image acquisition

All the STORM images analysed in this chapter were taken on a Nikon Eclipse Ti system using a 100x oil objective with NA of 1.49, a 256x256 pixel ROI and a pixel size of 160 nm using TIRF illumination. The system has lasers with wavelengths of 405 nm, 560 nm and 647 nm. Confocal images were taken on a Leica TCS SP8 STED 3X with a Leica 100x oil immersion objective of N.A. 1.4. For a full description of the image acquisition, see Chapter 2 section 2.4.

3.2.4 Image reconstruction

Dual-colour STORM image reconstruction was done using Insight3, provided by Bo Huang (UCSF, initially developed in Xiaowei Zhuang’s Lab). The analysis was run over the entire data sets but recording only those localisations detected in the second frame of the five-frame cycle, that is the first of the four reporter frames, the localisations can be represented by a cross marking their centres or rendered with a Gaussian profile convoluted with the point. For more detailed description, see Chapter 2 section 2.5.

3.2.5 Image analysis

MATLAB algorithms

The majority of the analysis carried out in this chapter were completed using scripts written and developed using MATLAB 2019b. In particular, we incorporated already-existing algorithms such as DBSCAN (Ester et al., 1996) into our scripts. Details of how the DBSCAN algorithm works can be found in Chapter 2 section 2.6. In brief, DBSCAN is a density-based algorithm that we implemented as our initial analytical step to establish if the proteins of interest formed clusters and to extract the details for the clusters found, such as centre of mass position (CoM), number of localisations, and area of clusters.

Data representation with GraphPad Prism

The median value per cell is calculated from the cluster analysis per cell. These values are represented using the box-and-whisker plots in GraphPad Prism, version 9.1.2, where the line shows the median over all cells, the box extends to the quartiles and the whiskers show the range over 90% of the distribution of the cells for each protein. All box-and-whisker plots in this chapter will follow these limits. Scatter plots are also used to display the distribution over individual cells where the horizontal line marks the mean of the distribution and the whiskers show the standard deviation. Finally, we also use stacked bar graphs in order to compare the two integrins to talin and vinculin. The bars show the mean of each protein and the whisker shows the standard deviation.

Statistical analysis with GraphPad Prism

The statistical analysis used in this chapter to assess the statistical significance of the variation of the median values per cell was carried out using GraphPad Prism (version 9.1.2). Specifically, when testing the statistical significance of the differences between the distribution mean values of each protein, we ran one-way ANOVA tests. The confidence interval was 95%. We only include on the graph those pairs that show statistical significance, i.e., p-value < 0.05.

3.3 Results

3.3.2 Dual-colour super-resolution STORM reveals nanoscale segregation of adhesion complex components

In order to visualise the lateral distribution and organisation of adhesion complex proteins with enhanced spatial resolution, we seeded HFF cells on FN for 24 h, fixed them and labelled different adhesion proteins for dual-colour STORM inspection. Representative confocal and STORM images taken at the basal membrane of two different HFF cells labelled for $\alpha_5\beta_1$ and paxillin are shown in Figure 3.1. While the spatial resolution of confocal imaging is set by diffraction (around ~340–450 nm in this particular example), the STORM image shows greater details and increased spatial resolution, with a localisation precision of ~7 nm and an accuracy of 15 nm, as stated in Chapter 2.

Visual inspection of these images shows that while paxillin and $\alpha_5\beta_1$ appear to be homogenously distributed inside FAs in the confocal micrographs (Figure 3.1 A), the STORM image reveals that these proteins are laterally segregated from each other and organised into discrete spots inside the adhesion structures (Figure 3.1 B). These first observations indicate that the old but still commonly-spoken idea of proteins being homogeneously distributed and colocalising with each other within the adhesion complex is outdated and requires a re-evaluation.

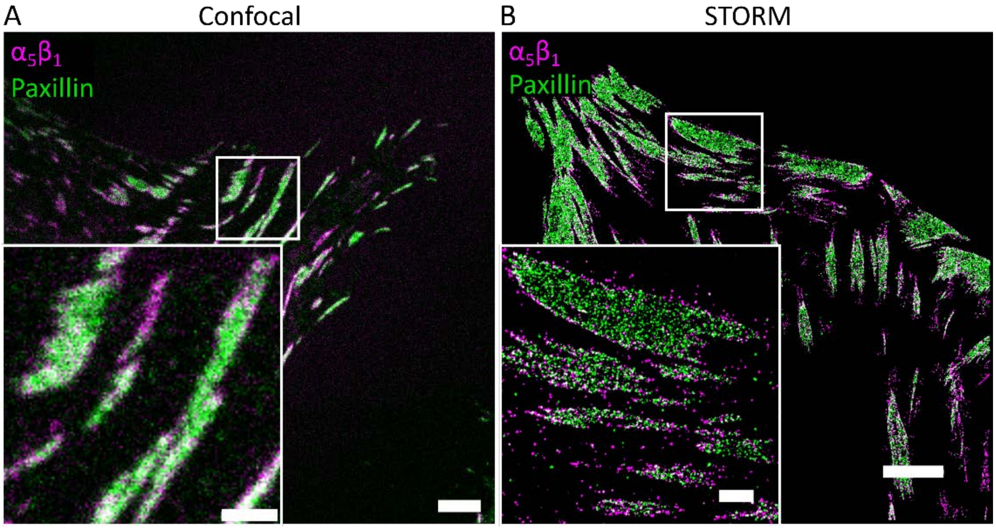

***Figure 3.1** Confocal and STORM images of fibroblasts seeded for 24 h*

The confocal image in (A) is of an HFF-1 cell seeded on FN for 24 h, labelled for $\alpha_5\beta_1$ and paxillin and imaged using a Leica TCS SP8 STED 3X system. (B) is a representative image for a cell seeded for 24 h on FN, labelled for $\alpha_5\beta_1$ and paxillin, and imaged by STORM. Scale bars of main images are 5 µm and of insets are 1 µm.

To further enquire whether the lateral segregation observed for paxillin and $\alpha_5\beta_1$ also holds for other proteins associated to adhesion complexes, we performed extensive STORM imaging of $\alpha_5\beta_1$, $\alpha_v\beta_3$, paxillin, talin, and vinculin on multiple cells. Figure 3.2 shows representative STORM images for all five adhesion complex components we consider here. The large field of view in all panels of Figure 3.2 shows that due to high density of the localisations in these regions the distribution seems to appear homogeneously distributed on the adhesion complexes, similar to the images obtained by confocal microscopy (Figure 3.1 A). However, when inspected with greater detail (see zoom-ins in Figure 3.2), the reconstructed images show a non-homogeneous distribution for all the adhesion proteins, laterally segregating from each other within the adhesion complexes.

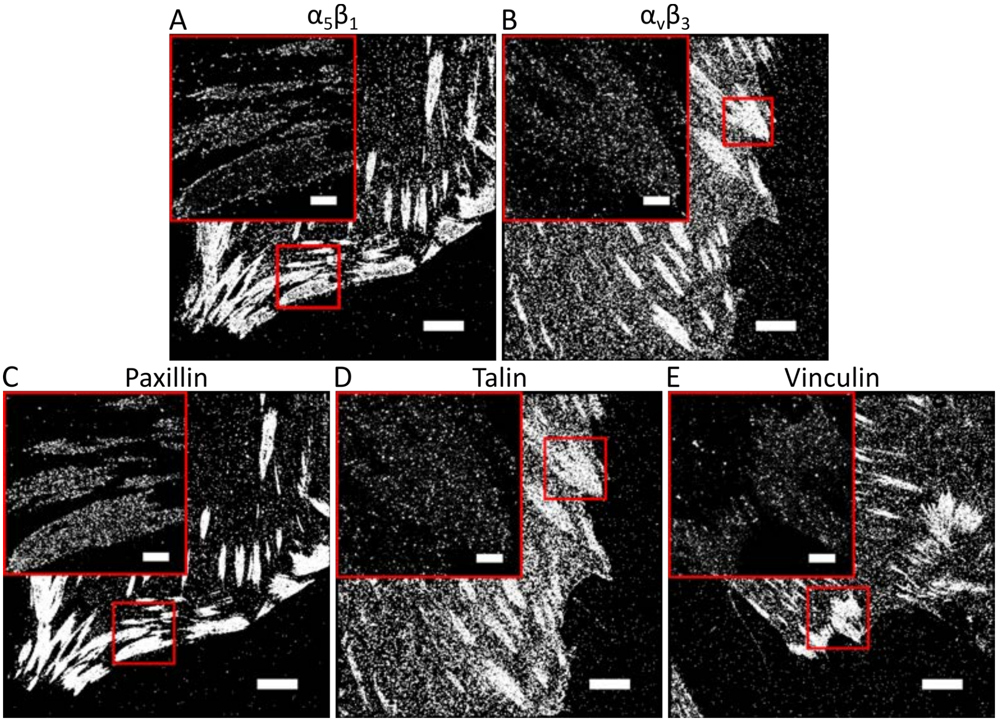

Figure 3.2 *Reconstructed STORM images for five components of the adhesions complex labelled in HFF-1 cells seeded for 24 h on FN*

Panels (A–E) show the proteins studied in this thesis. (A) and (B) are reconstructed images of $\alpha_5\beta_1$ and $\alpha_v\beta_3$. Panels (C–E) show paxillin, talin, and vinculin reconstructions, respectively. The insets show a zoom in on an adhesion area for each cell. Scale bar = 5 µm, inset scale bar = 1 µm.

In addition, the images also show differences in the density of proteins inside adhesions as inferred from the difference in terms of the number of localisations, with for instance a higher number of localisations from paxillin as compared to talin or vinculin (Figure 3.2 C, D). These differences do not arise from variations in the labelling of the adaptor proteins, since we controlled that in all cases, we work at fully saturating labelling conditions. It can also be noted that although the adaptor protein spots (paxillin, talin, and vinculin) appear to be distributed evenly over the area of the adhesions, the distributions of the two integrins ($\alpha_5\beta_1$ and $\alpha_v\beta_3$) appear quite distinct to one another. While $\alpha_v\beta_3$ appears to follow a homogenous distribution similar to that of the adaptors, $\alpha_5\beta_1$ exhibits a tendency to be more enriched at the boundaries of the adhesions. To quantitatively substantiate these observations, here and in the following chapters we will use various computational tools to analyse the STORM images and obtain an in-depth description of the lateral distribution of key adhesion proteins.

3.3.3 Key adhesion proteins organise as nanoclusters inside adhesions

In this section, we quantitatively analyse the lateral distribution on the basal cell membrane of key adhesion proteins, as observed in our STORM images (Figure 3.2). We used the DBSCAN algorithm to determine if the proteins of the adhesion complex form nanoclusters and, if so, characterise these nanoclusters by using different metrics, such as their size, number of localisations per cluster, and molecular density inside nanoclusters. As an initial step, the STORM data were split into three distinct data sets, corresponding to the localisations found to be inside adhesion complexes, on the rest of the basal cell membrane, and outside of the cell (on glass). This allowed us to specifically analyse the localisations associated to adhesions and characterise the protein clusters. In order to do that, we first needed to establish what we mean by a nanocluster. As discussed in the methods chapter (section 2.6), we require a way to distinguish individual conjugated antibodies from nanoclusters of proteins. To establish this lower limit, we analysed individual spots on glass (next to the cells) and extracted the distribution for the number of localisations per spot detected, using DBSCAN with N_{min}=2 and *eps*=20 nm (Figure 3.3 A). The median number of localisations per spot on glass was 5 for Alexa405-Alexa647-conjugated antibodies, and 3 for Cy3-Alexa647-conjugated antibodies. It is worth noting that Figure 3.3 A does not solely reflect the distribution of localisations per single antibody, but is rather convolved with dimers, or multimers arising from cell debris deposited on the glass. This explains why the distribution has a larger spread (as defined by the whiskers) than those obtained in other studies where spots on glass were characterised in the absence of cells (Spiess et al., 2018). Yet, we believe that our approach is more rigorous since the determination of the number of localisations/individual antibody is performed on the same sample containing the cells and thus under identical experimental conditions.

These values serve us to refine the clustering analysis on cells, in order to mainly select those nanoclusters formed by multiple proteins, and not apparent nanoclusters of localisations emanating from multiple blinking events of a single fluorophore. To that end, the DBSCAN parameters were fixed at N_{min}=3 and *eps*=20 for the initial nanocluster detection on cells, as described in detail in Chapter 2, section 2.6.3. Once these nanoclusters were detected, a further threshold was set to exclude all spots with less than 10 localisations. Our choice of parameters was based on other publications in the field (Pageon et al., 2016; Spiess et al., 2018) and the reasoning that if the median of localisations per single antibody is 3–5 molecules then the majority of spots with 10 of more localisations are likely to correspond to true nanoclusters. Moreover, we used the Fiji plugin as explained in the methods chapter, to exclusively select localisations contained in the adhesion structures (Figure 3.3 B).

Our analysis revealed that the proteins considered in these experiments form nanoclusters in the adhesion complexes (Figure 3.3 C–E). Interestingly, the number of localisations per nanocluster, nanocluster area, and the density of localisations per unit area appear to be conserved without any significant difference found, when comparing the data of each protein to the others. We used the parametric one-way ANOVA test with 95% confidence, and found all p-values were > 0.05, indicating the variations seen between data sets are not significant. The detected clusters are small both with respect to size and number of localisations. Taking the clusters of $\alpha_5\beta_1$ as a representative example, our data indicate that they have a median surface area of 1768 nm^2, which, if we assume the clusters to have a circular shape, corresponds to a median cluster diameter of 47 nm. This observation is in agreement with similar studies carried out on active and inactive integrin $\alpha_5\beta_1$, where the authors used STORM imaging and found that active and inactive integrin nanoclusters have a median diameter of 40 nm and 35 nm, respectively (Spiess et al., 2018). We find the median number of localisations in a nanocluster of $\alpha_5\beta_1$ to be around 25, resulting in a median localisation density of 0.015 locs/nm^2.

Although we extracted the number of localisations per individual antibody on glass and used this value to discriminate for nanoclustering, it is still not quantitative enough to accurately determine the number of proteins contained in each nanocluster. In addition, we also quantified the percentage of localisations inside adhesion complexes that belong to nanoclusters for each of the proteins investigated, and obtained for $\alpha_5\beta_1$, 84.6%; for $\alpha_v\beta_3$, 77.6%; for paxillin, 80.2%; for talin, 73.2%, and for vinculin, 78.1%.

Overall, our results quantitatively show that integrin receptors and their main adaptor proteins form nanoclusters inside adhesion complexes of remarkable similar size, number of molecules, and molecular density. Moreover, these nanoclusters appeared laterally-segregated within adhesions.

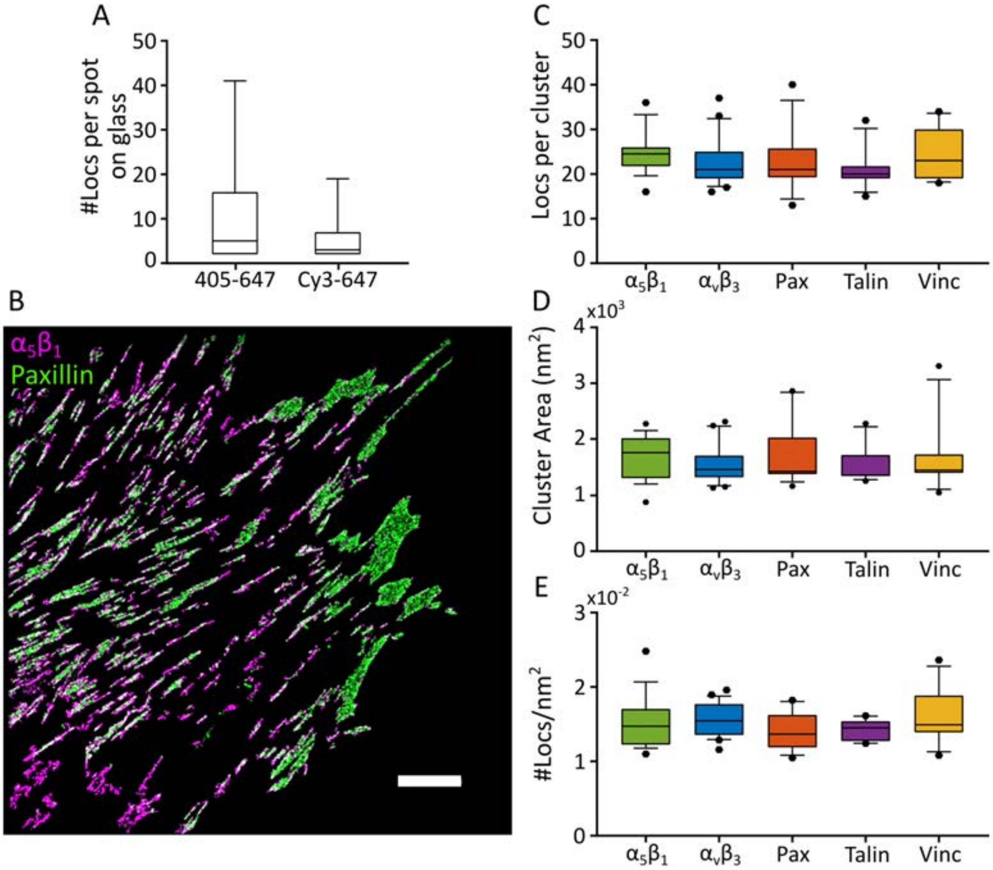

Figure 3.3 *Nanocluster analysis of different proteins inside adhesions*

Panel (A) shows the distribution for the number of localisations (locs) per secondary antibody for either of the antibodies, goat anti-mouse Alexa 405–Alexa 647 and goat anti rabbit Cy3–Alexa 647 on glass. (B) A representative STORM image of an HFF-1 cell fixed after 24 h on FN and labelled for paxillin (shown in green) and $\alpha_5\beta_1$ (shown in magenta), where only the localisations present in the adhesions are considered for analysis. Scale bar = 5 µm. (C–E) Box-and-whisker plots showing the number of localisations per nanocluster (C), the nanocluster area (D), and the density of localisations per nanocluster area (E) for the proteins in this study. Each data point corresponds to the median value over all nanoclusters for each cell (for N values, i.e., number of independent experiments, see number of images for the 24 h condition in Table 2.6). Only the pairs with statistical differences are marked. not significant (ns), $p>0.05$; *, $p<0.05$; **, $p<0.01$; ***, $p<0.001$; one-way ANOVA.

3.3.4 Protein nanoclustering does not change depending on the region of the cell membrane studied

We next examined whether there are any differences between the nanoclusters formed in different types of adhesion complexes, in particular FAs and fAs. To study

FAs and fAs, we acquired images that incorporate both the edge of the cell, where FAs are primarily found, as well as a central area, which is highly enriched in fAs, having a narrow, elongated shape. Representative images outlining these regions are shown in Figure 3.4. The data were split into FA and fA data, as explained in the methods section.

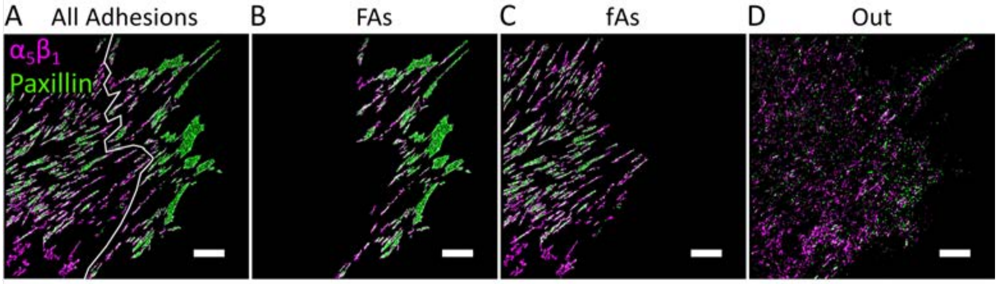

Figure 3.4 *Definition of different regions of cell membrane containing focal and fibrillar adhesions*

(A) Representative STORM image of $\alpha_5\beta_1$ (magenta) and paxillin (green) of an HFF-1 cell spread on FN for 24 h. Only localisations in adhesions are shown, with the localisations on glass already removed. The white line is the manually drawn boundary to define the separation of FAs from fAs. (B–C) Images resulting from that separation. (D) Localisations on the cell membrane not associated to adhesions, i.e., outside adhesions. Scale bars = 5 µm

We then ran the DBSCAN algorithm on all files containing the localisations found specifically on FAs, fAs, or outside adhesions. We maintained the same DBSCAN parameters for all these analyses. We first measured the cluster descriptors for the two integrins, $\alpha_5\beta_1$ and $\alpha_v\beta_3$, in the different regions of the cell membrane (Figure 3.5 A, B). Interestingly, these results revealed that there are no significant differences in the clusters found in FAs compared to those found in fAs for either integrin (Figure 3.5 C–E).

Surprisingly, we observed a significant difference in the median localisation density of the clusters for $\alpha_5\beta_1$ depending on whether they are found inside or outside adhesions: they are denser outside adhesions than inside (Figure 3.5 E). This difference essentially arises from a smaller $\alpha_5\beta_1$ nanocluster area inside adhesions (either FAs or fAs) as compared to outside (Figure 3.5 D). These results are at first glance counterintuitive, as one may expect that inside adhesions, which are areas of high integrin density, the nanoclusters themselves would be more packed and therefore have a higher density of localisations. However, our results indicate that, at least for $\alpha_5\beta_1$ nanoclusters, this is not the case. Although a better understanding of the mechanism behind this reduction in density would require a more in-depth study, we speculate that the observed lower density of localisations in adhesion regions could arise from the engagement of the integrins with their adaptor partners and, consequently, the integrin nanoclusters would be expanded due to molecular crowding.

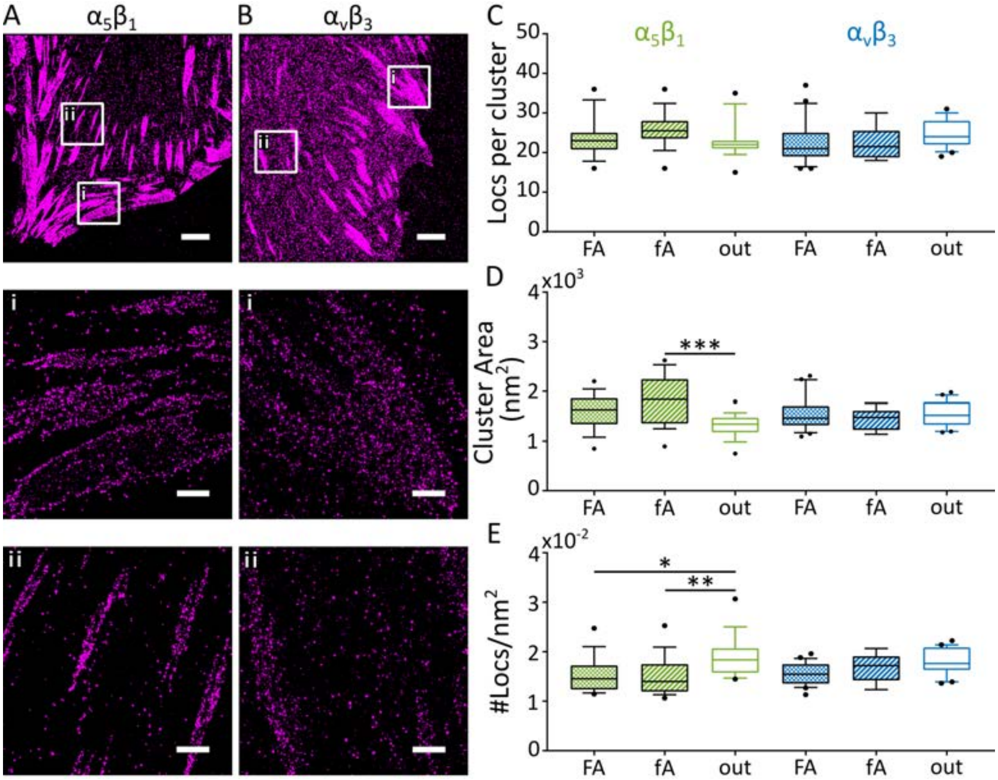

__Figure 3.5__ Analysis of STORM data for integrins $\alpha_5\beta_1$ and $\alpha_v\beta_3$ after 24 h of spreading on FN, and split by membrane regions

(A,B) Top panels show the full area of the cell membrane imaged by STORM and rendered using Insight3, where each localisation is depicted with a cross. (A) shows $\alpha_5\beta_1$, and (B) shows $\alpha_v\beta_3$. The subpanels (i) and (ii) show zoom-in ROIs on high density areas, defined as FAs and fAs, respectively. The scale bars are 5 µm (A,B; top panels) and 1 µm (subpanels i, ii). (C–E) Nanocluster characteristics for $\alpha_5\beta_1$ (green) or $\alpha_v\beta_3$ (blue) nanoclusters on FAs, fAs, or outside adhesions (out). For a summary of the number of cells analysed per integrin and per region, see Table 2.6. Only the pairs with statistical differences are marked. *, $p<0.05$; **, $p<0.01$; ***, $p<0.001$; one-way ANOVA.

Similarly, we next analysed the data of the adaptor proteins paxillin, talin, and vinculin (Figure 3.6). Remarkably, we found no significant differences in the nanocluster properties for any of these adaptors, except for vinculin outside adhesions, which exhibited a larger number of localisations as compared to fA regions, although with no changes in terms of nanocluster molecular density. We also noticed that as compared to integrins, which show a narrow distribution in the nanocluster parameters (Figure 3.5), we systematically recovered a larger spread on the number of localisations and nanocluster area for all three adaptors. These differences might be related to the degree of integrin engagement and activation of these adaptor proteins (see also discussion).

Taken together, these data (Figure 3.5 and Figure 3.6) show that nanoclusters formed by all the adhesion proteins we studied have a well-defined number of localisations and median size, and regardless of whether they are inside (FAs or fAs) or outside adhesion complexes, with the sole exception of $\alpha_5\beta_1$, whose localisation density is lower inside adhesions as compared to outside. Overall, our data thus indicate that nanoclustering is a common feature of adhesion proteins and their lateral segregation suggests that they might constitute nanomodules with different function.

3.3.5 The nanocluster characteristics of adhesion proteins are preserved regardless of cell seeding time

So far, we have reported all the experiments on cells seeded for 24 hours on FN. When cells are seeded on a flat substrate, they attach to the surface and spread over a period of time until they reach a stationary attachment area (Nisenholtz et al., 2014). The initial attachment occurs within minutes whereas the spreading that follows is a slower process, taking hours for the cell to reach a steady state (Thurston et al., 1988). Because adhesion complexes play important roles in both these processes (initial attachment and subsequent spreading), we next aimed at investigating how the adhesion proteins are organised and segregated as a function of cell seeding time.

To investigate how nanocluster sizes and other characteristics might vary depending on the attachment and spread state of the cell, we seeded cells on FN for different times (90 minutes, 3 hours, or 24 hours), and imaged them using STORM. As before, we started by analysing the integrin clusters, retaining the separation into FAs, fAs, and outside adhesions, with the extra layer of complexity arising from the seeding time (90 min, 3 h, or 24 h).

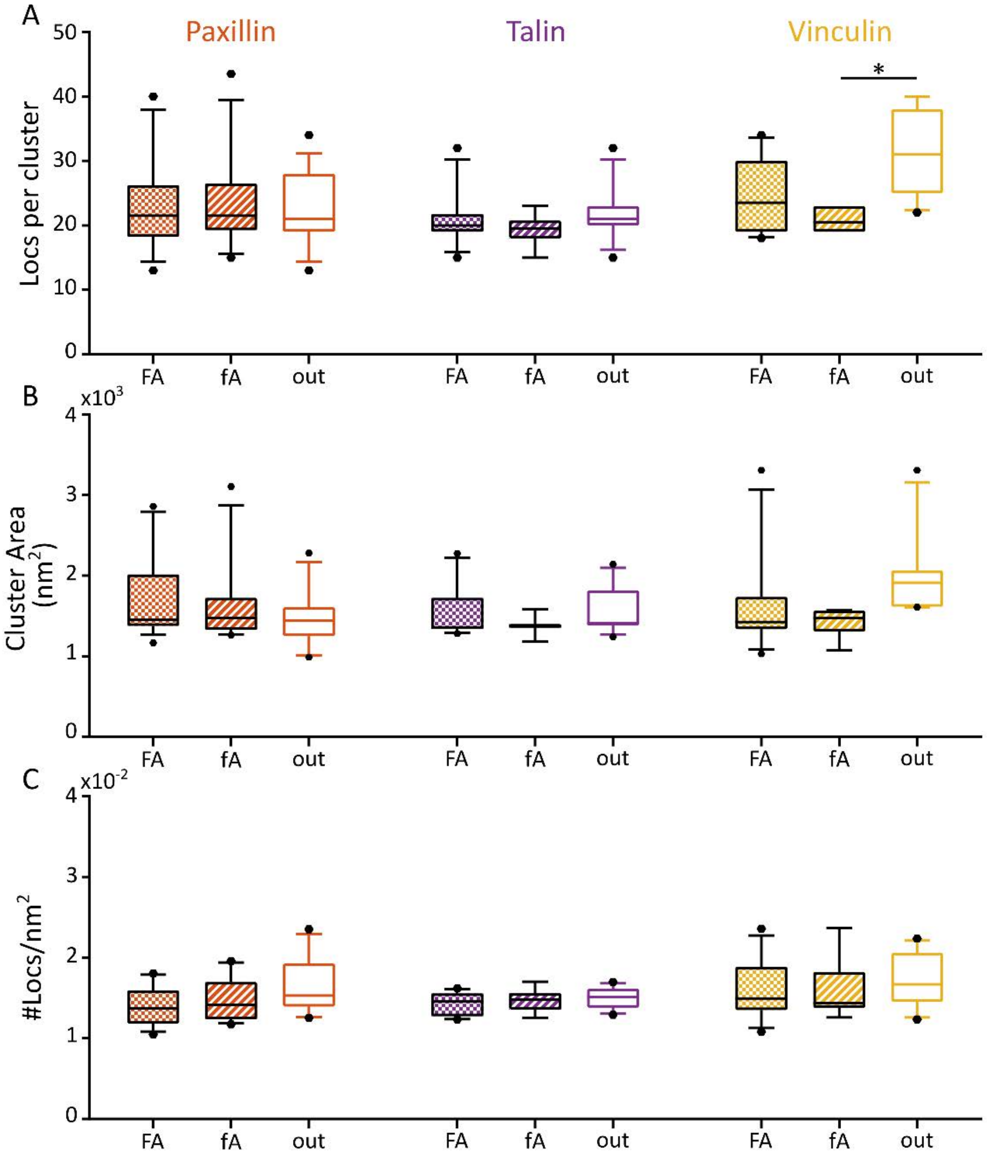

Figure 3.6 *Analysis of STORM data for the adaptor proteins paxillin, talin, and vinculin, after 24 h of spreading on FN and split by membrane regions*

(A–C) Cluster characteristics for paxillin (orange), talin (purple), and vinculin (yellow) nanoclusters on FAs, fAs, or outside adhesions (out). For a summary of the number of cells analysed per adaptor and per region, see Table 2.6. Only the pairs with statistical differences are marked. *, $p<0.05$; **, $p<0.01$; ***, $p<0.001$; one-way ANOVA.

Strikingly, the cluster analysis again revealed sizes and localisation densities at early (90 min) and intermediate (3 h) time points similar to those found for the late time point (24 h) (Figure 3.7). In order to test if any of the observed differences are statistically significant, we ran an unpaired one-way ANOVA test. This revealed that there was no significant difference for $\alpha_v\beta_3$ clusters over time (Figure 3.7 B,D,F). The

$\alpha_5\beta_1$ clusters present on cells seeded for 90 min show *(i)* a higher number of localisations per cluster in fAs compared to FAs (Figure 3.7 A); and *(ii)* a larger area for fA clusters (Figure 3.7 C), as compared to those clusters found on cells seeded for 3 h or 24 h. Interestingly, these two measures balance each other, resulting in the localisation densities for clusters in FAs and fAs to be statistically equivalent for all three studied seeding times (Figure 3.7 E).

As previously mentioned, on cells seeded for 24 h, we found that the localisation density in clusters outside adhesions was significantly higher than that in FA- and fA-located clusters (Figure 3.5). However, this difference does not hold for the shorter cell spreading time of 90 min, where the localisation densities for all clusters are statistically equivalent regardless of their location within the basal cell membrane (Figure 3.7).

We next performed an analogous analysis on the STORM data of the adaptor proteins (paxillin, talin, and vinculin). Similar to what we saw for the integrins, we found that the cluster characteristics for the adaptor proteins are remarkably stable over time in terms of the quantities we analysed over time in the different regions of the cell membrane (Figure 3.8). One observation to note is that the spread of the median area of the vinculin clusters per cell is strikingly broader as compared to paxillin or talin. These results might indicate that vinculin nanoclusters vary depending on the specific role they perform. Vinculin has a well-established role in stabilising talin-actin bonds at FAs (Humphries et al., 2007; Atherton et al., 2015) and it has also been shown to be involved in clustering of GPI-anchored proteins (Kalappurakkal et al., 2019). Because our labelling strategy targets all vinculin proteins, it is possible that a fraction of the detected vinculin clusters is not engaged with their usual partner proteins talin and actin. Further work will be required to investigate this.

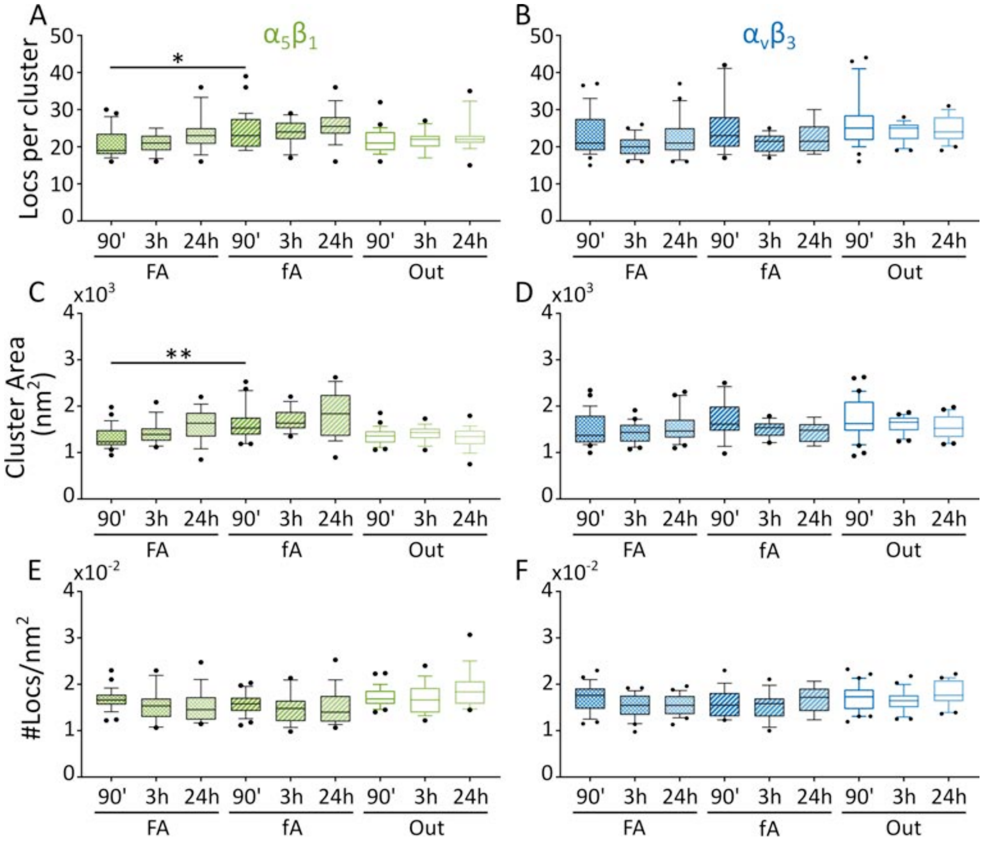

***Figure 3.7** Characterisation of integrin clusters for different cell spreading times and regions on the cell membrane*

(A–F) Cluster properties inside FAs, fAs, and outside adhesions (Out) for the integrins $\alpha_5\beta_1$ (in green, panels A,C,E), and $\alpha_v\beta_3$ (in blue, panels B, D, F). (A,B) show the number of localisations (Locs) per cluster; (C,D) show the cluster area; and (E,F) show the localisation density per unit area. For a summary of the number of cells analysed per integrin in each region and at each time point, see Table 2.6. Only the pairs with statistical differences are marked. *, $p<0.05$; **, $p<0.01$; ***, $p<0.001$; one-way ANOVA.

Our STORM data, analysed using the DBSCAN algorithm, show that the proteins of the adhesion complex are segregated into small clusters (of ~50 nm in diameter) at the nanoscale. We showed that, in general terms, these clusters exhibit the same characteristics regardless of the type of adhesion they form or the time duration of their spreading on FN. This leads us to propose that the adhesion proteins we studied form universal nanohubs that allow them to efficiently interact in a functional manner to form the adhesion platforms. We know that these proteins play different roles in the adhesion complexes, whether that be signalling or anchoring to the cytoskeleton. Remarkably, these very different roles and interactions are not mirrored in their clustering behaviour.

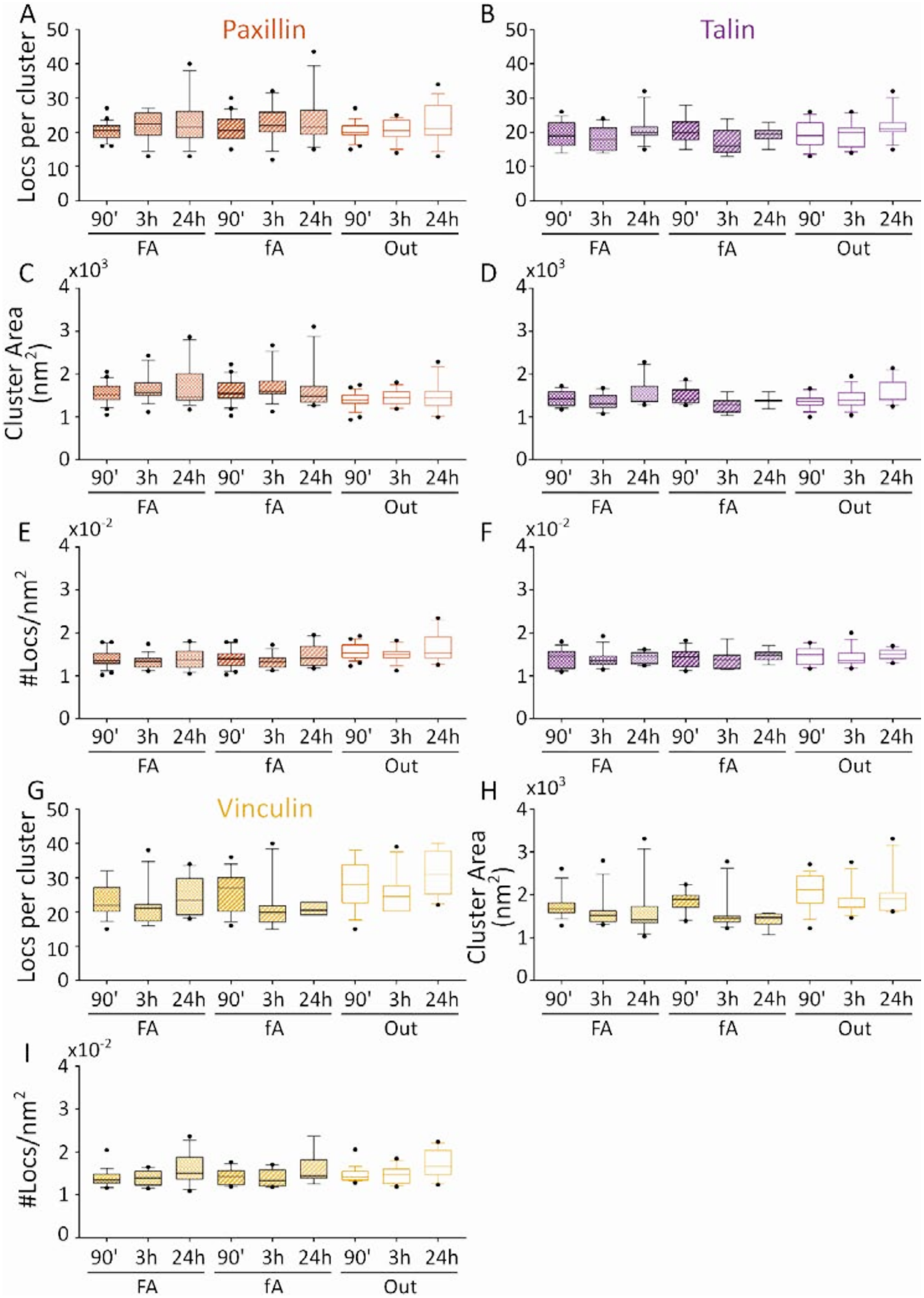

Figure 3.8 *Characterisation of adaptor proteins clusters inside FAs, fAs, and outside (Out) adhesions, for different cell spreading times and regions on the cell membrane*

Cluster properties for paxillin (in orange, panels (A,C,E)), talin (in purple, panels (B, D, F)), and vinculin (in yellow, panels (G, H, I)). (A,B,G) show the number of localisations (Locs) per cluster; (C,D,H) show the cluster area; and (E,F,I) show the localisation density per unit area. For a summary of the number of cells analysed per adaptor in each region and at each time point, see Table 2.6. Only the pairs with statistical differences are marked. *, $p<0.05$; **, $p<0.01$; ***, $p<0.001$; one-way ANOVA.

3.3.6 The number of integrin clusters per unit area, but not of adaptor proteins, increases with cell spreading time

Our data thus far indicate that adhesion protein nanoclusters hold some universal features, such as their sizes and localisation densities (Figure 3.7 and Figure 3.8). Hence, we hypothesised that other characteristics of these nanoclusters, particularly their overall organisation within the basal membrane, could determine the way different proteins regulate adhesion size and dynamics to ultimately mediate their physiological roles in processes such as cell attachment and migration.

In order to identify these determinants, we first quantified the evolution of the number of nanoclusters per unit area as a function of the spreading time for the different adhesion proteins in the different cell regions. To that end, we took advantage of the fact that the output of the DBSCAN analysis includes the x-y coordinates of the centre of mass (CoM) of each cluster. With this information we coded a script to plot the CoM of each cluster onto the binary mask of the adhesions (see Chapter 2, Figure 2.6). We next assigned the nanoclusters to the individual adhesion type they belong to, from which we were able to count the number of nanoclusters in each adhesion. These adhesion areas are topologically-disconnected regions detected by MATLAB from the binary mask (see Chapter 2, Figure 2.6). This, together with the area of each adhesion that was obtained from the adhesion mask, allowed us to calculate the number of clusters per unit area inside the different adhesion regions. We further categorised the individual regions as FAs, fAs, or outside adhesions.

Our results show that for the integrins $\alpha_5\beta_1$ and $\alpha_v\beta_3$, the number of clusters per unit area increases with the spreading time, both in FAs and in fAs (Figure 3.9 A,B). Specifically, for $\alpha_5\beta_1$ the density increased from ~8.4 and 12 clusters/μm^2, for FAs and fAs, respectively, at 90 min to ~23 clusters/μm^2 for both FAs and fAs at 24 h. Moreover, the increase in $\alpha_v\beta_3$ cluster density went from ~3.5 clusters/μm^2 (90 min) to ~15.5 clusters/μm^2 (24 h), for both FAs and fAs (Figure 3.9 A,B). As expected, the number of nanoclusters of both integrins per unit area outside adhesions was much lower (median values ~1–3 clusters/μm^2) and remained unchanged over time (Figure 3.9 A,B). These findings suggest that the cell requires higher densities of integrin nanoclusters at the adhesion sites as cell spreading time increases. Interestingly, although the nanocluster characteristics of both integrin receptors appeared to be constant in time and similar for both integrins (Figure 3.7), their lateral distribution and temporal evolution inside adhesions was markedly different. Indeed, regardless of spreading time and type of adhesion structure, we observed an enrichment of $\alpha_5\beta_1$ nanoclusters over $\alpha_v\beta_3$ nanoclusters (Figure 3.9 A,B). Moreover, this enrichment was more pronounced at earlier spreading times (90 min) with a 2.4-fold $\alpha_5\beta_1$ enrichment on FAs and 3.4-fold enrichment in fAs as compared to $\alpha_v\beta_3$. At 24 hours, a 1.5-fold enrichment of $\alpha_5\beta_1$ over $\alpha_v\beta_3$ was retrieved, in both FAs and fAs. These results are quite different to the ones reported by Rossier et al., where the authors reported an enrichment of $\alpha_v\beta_3$ over $\alpha_5\beta_1$ in FAs at 3 h of cell spreading time (Rossier et al., 2012). These differences might be due to different expression levels between our experiments, where we labelled endogenously-expressed $\alpha_5\beta_1$ and $\alpha_v\beta_3$ in human fibroblasts, and Rossier et al's experiments, where the integrins were exogenously-overexpressed in mouse fibroblasts used (Rossier et al., 2012). On the other hand, the strong enrichment of $\alpha_5\beta_1$ as compared to $\alpha_v\beta_3$ at fAs, in particular at earlier spreading times (3.4-fold enrichment), is fully consistent with earlier literature (Zamir et al., 2000; Katz et al., 2000). In addition, our data also revealed the presence of $\alpha_v\beta_3$ integrins in these adhesion regions. Finally, it is interesting to note that even when the total $\alpha_5\beta_1$ population in adhesions is larger than that of $\alpha_v\beta_3$, their relative increase as a function of cell spreading time was much more pronounced for $\alpha_v\beta_3$, i.e., with a 4.4-fold increase at 24 h as compared to 90 min, while for $\alpha_5\beta_1$ more modest 2.7- and 1.9-fold increases were found for FAs and fAs, respectively. These results suggest that as cell spreading time proceeds, the requirement for $\alpha_v\beta_3$ integrins at the sites of adhesion becomes increasingly more relevant.

Next, we analysed the adaptor protein nanocluster densities following the same workflow. Surprisingly, our results show that the density of adaptor protein nanoclusters in adhesions remained unchanged over time for the different basal membrane regions analysed (Figure 3.9 C–E). Paxillin nanoclusters are highly enriched at the adhesions with ~20–22 clusters/μm^2 in FAs and ~12–15 clusters/μm^2 in fAs. Interestingly, the density of talin nanoclusters (median values ~5–12 clusters/μm^2) and of vinculin nanoclusters (~6–12 clusters/μm^2) was much lower than that of paxillin and remarkably similar to each other for these two adaptors in the two types of adhesion complexes (FAs and fAs) (Figure 3.9 D,E).

Figure 3.10 A,B shows the comparative results for both integrins, talin, and vinculin as function of cell spreading time. Whereas the number of integrin nanoclusters ($\alpha_5\beta_1$ and $\alpha_v\beta_3$) per unit area at FAs are comparable to the density of talin and vinculin at 90 min cell spreading time (Figure 3.10 A), at longer times, there are many more integrins than adaptors, with a more than three-fold excess of integrins at FAs as compared to talin and vinculin. These results indicate that at longer spreading times, a significant number of integrin nanoclusters in FAs might not be engaged with their adaptor partners. A similar behaviour was also observed in fAs and outside adhesions, irrespective of the cell spreading time (Figure 3.10 B,C).

These data (Figure 3.9, Figure 3.10) opened up a new question: what is the source for the increase in the number of integrin clusters per unit area in the adhesion complexes as a function of cell spreading time? To address this question, we considered six possible scenarios by which the number of clusters per unit area could increase, which we addressed one by one.

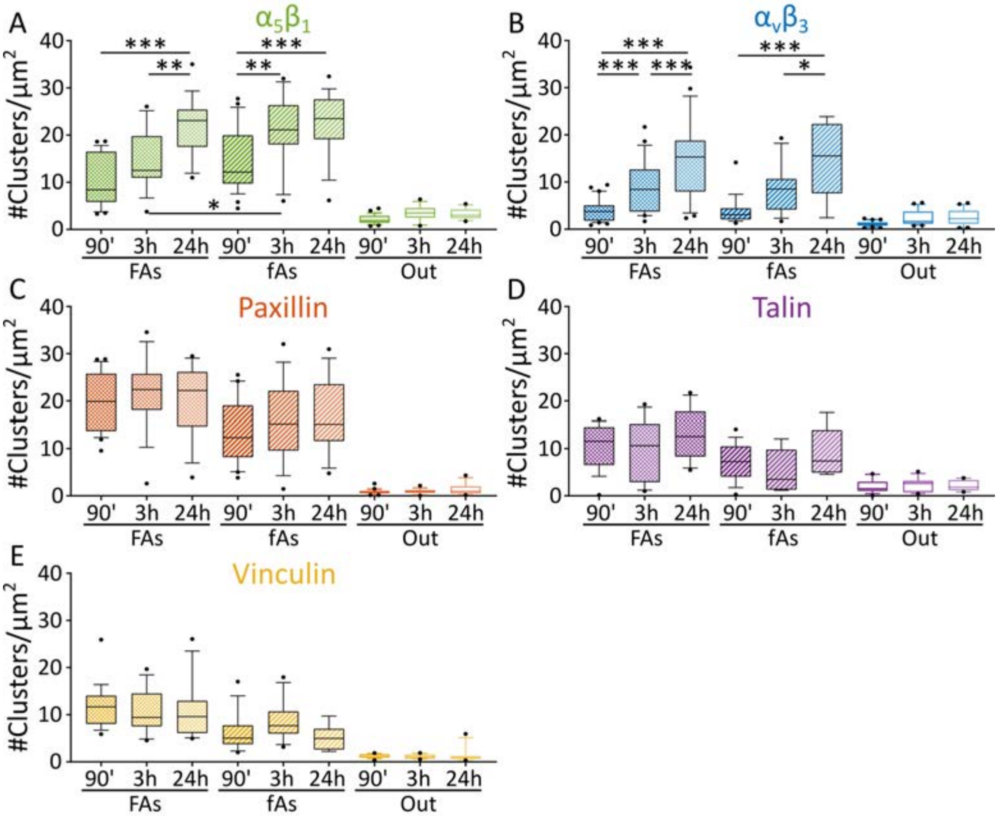

***Figure 3.9** Number of protein clusters per unit area in different basal membrane regions as function of spreading times*

Density of clusters per unit area for the proteins, $\alpha_5\beta_1$ (green; (A)), $\alpha_v\beta_3$ (blue; (B)), paxillin (orange; (C)), talin (purple; (D)), and vinculin (yellow; (E)) for different cell spreading times and classified according to their location on the basal membrane, i.e., inside FAs, fAs, and outside (Out) adhesions. For a summary of the number of cells analysed per integrin in each region and at each time point, see Table 2.6. Only the pairs with statistical differences are marked. *, $p<0.05$; **, $p<0.01$; ***, $p<0.001$; one-way ANOVA.

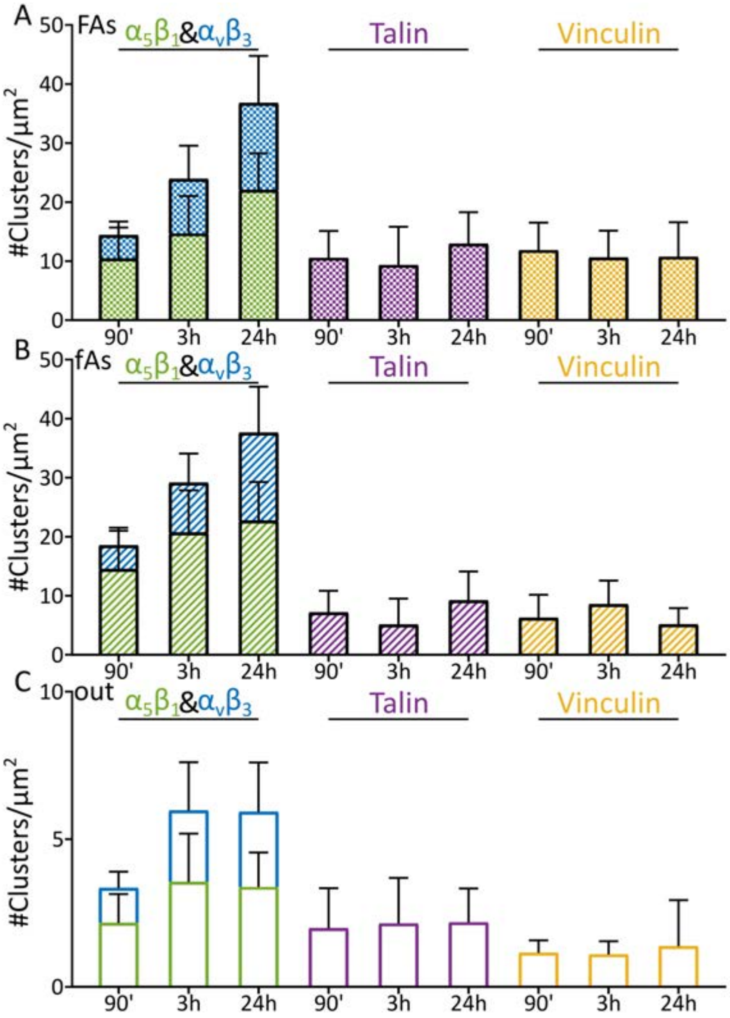

Figure 3.10 Comparison of number of clusters per unit area for integrins, talin, and vinculin
Density of nanoclusters per unit area for the two integrins $\alpha_5\beta_1$ (green) and $\alpha_v\beta_3$ (blue) shown in a stacked plot, and compared to the mean density of nanoclusters per unit area for talin (purple) and vinculin (yellow), for FAs (A), fAs (B), and outside adhesions (C). Notice that the vertical axis range is different in (C) than in (A) and (B)

1) Adhesions would decrease in area with time, resulting in an apparent increase of the density of nanoclusters.

The first hypothesis we tested is whether the total number of integrin clusters on the basal membrane remains constant while it is the adhesion area that decreases with time, resulting in an effective increase of the density of nanoclusters per unit area. To address this first point, we took the adhesion masks and measured the area of the adhesions for different spreading times. Figure 3.11 A,B shows a representative example of how two masks are generated from a STORM image: the first mask corresponds to the adhesion complexes (panel A), and the second one to the entire basal membrane (panel B). We use the first mask to measure the distribution of surface areas of the individual adhesions (Figure 3.11 C). With the information obtained from the second mask, we then computed the fraction of the cell membrane area covered by adhesions (Figure 3.11 D). These results reveal that there are no significant changes of the adhesion area depending on the spreading time. Although it shows that at 3 h there is a relatively small but statistically significant dip in the area of adhesions as compared to 90 min, the area fraction of the basal membrane occupied by adhesions remains constant with time. This, together with the finding that the increase in the integrin cluster density is progressive with time, led us to rule out this first scenario.

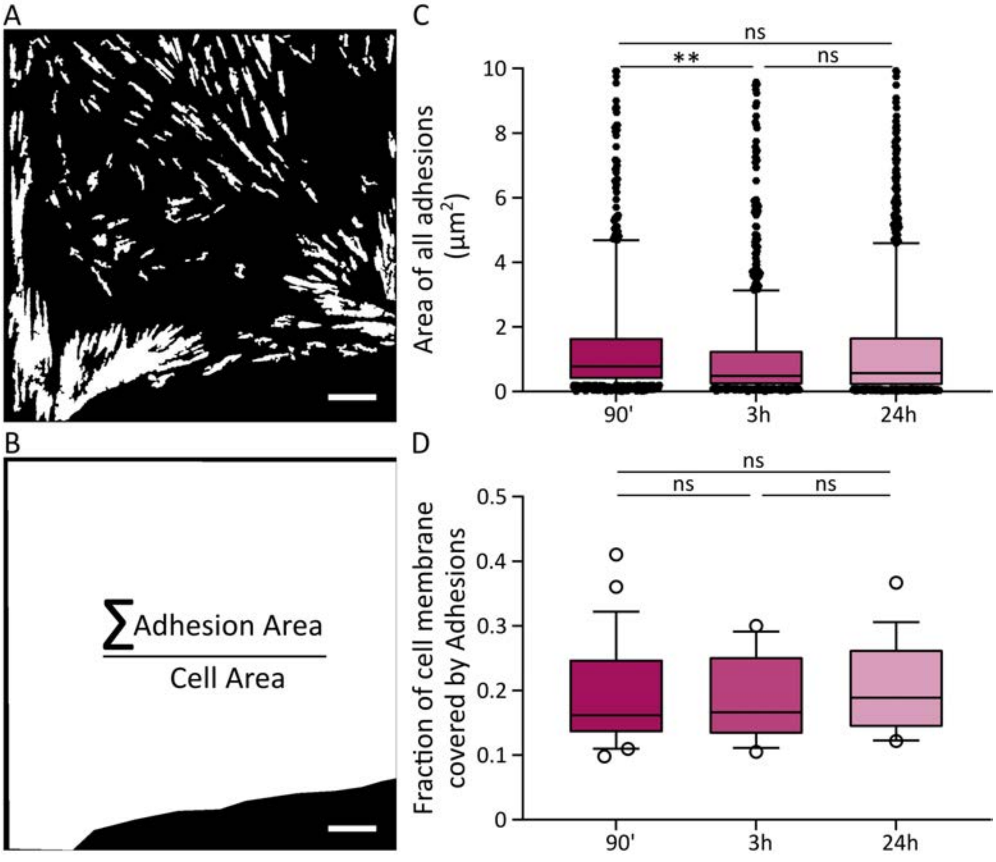

Figure 3.11 *Area of all adhesions with time*

(A) and (B) show the masks of all adhesions and the mask of the full membrane area imaged, respectively. Scale bar = 5 µm. (C) Distribution of total adhesion area. (D) Fraction of the cell membrane covered by the adhesions, i.e., sum of all the adhesion areas of a cell divided by the total cell area, for all cells studied. The data points in (C) correspond to all the adhesion areas for all the cells, and each point in panel (D) corresponds to a fraction of a cell area for each cell analysed. For this analysis we took all masks pertaining to all experiments targeting paxillin, imaged together with $\alpha_5\beta_1$ or $\alpha_v\beta_3$. ns, $p>0.05$; *, $p<0.05$; **, $p<0.01$; ***, $p<0.001$; one-way ANOVA.

2) Integrin nanoclusters formed outside adhesions could be recruited to the adhesion sites.

A second possible explanation for the observed increased density of integrin nanoclusters with time at adhesion sites is that a fraction of integrin clusters that localise outside adhesions are recruited towards the adhesion sites. If so, one would expect an increase in the cluster density in those regions with the concomitant decrease in the density outside adhesions. In fact, this information is already contained in our results shown in Figure 3.9, which, for the sake of visual clarity, we plot again showing the density of integrin clusters only outside adhesions (Figure 3.12). These results clearly indicate that there is no reduction of the density of clusters outside of the adhesions with time. In fact, the trend is that there seems to even be an increase in the density of integrin clusters at 3 h and 24 h as compared to 90 min. Therefore, we conclude that the increase in integrin cluster density in adhesions with time is not due to an active recruitment of clusters into the adhesions from the surrounding regions of the basal membrane.

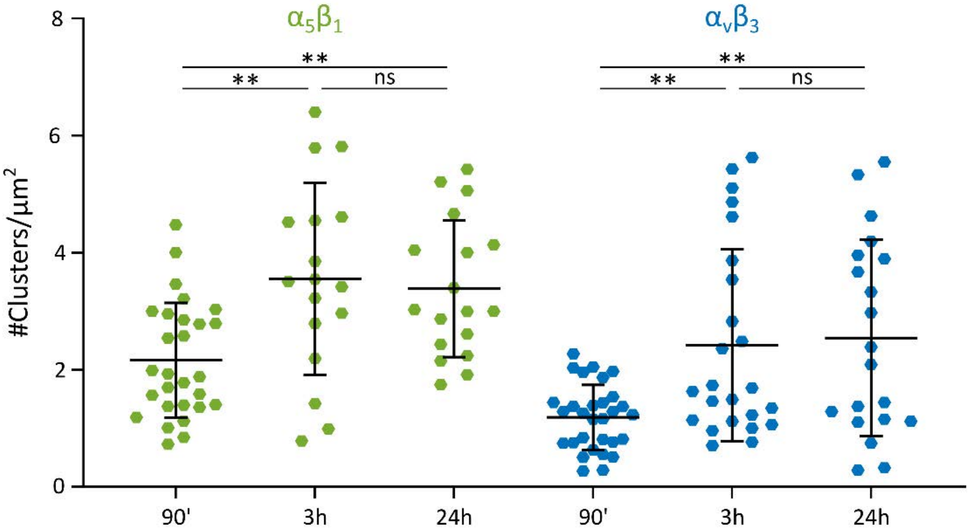

Figure 3.12 *Density of integrin nanoclusters outside of the adhesions as function of cell spreading times*

Same data as shown in Figure 3.9 A,B (only outside adhesions), but with the vertical scale expanded, with $\alpha_5\beta_1$ (green) and $\alpha_v\beta_3$ (blue) data. Each data point represents a cell, the horizontal line marks the mean of the distribution with the whiskers extending over the standard deviation. ns, $p>0.05$; *, $p<0.05$; **, $p<0.01$; ***, $p<0.001$; one-way ANOVA.

3) The number of integrin nanoclusters at the adhesion sites could increase at the expense of the non-clustered integrins.

A third possibility we explored is whether the amount of "free" integrin localisations, i.e., those that do not belong to nanoclusters, decreases with time in adhesions leading to an enhanced nanoclustering capacity as function of spreading time. We thus calculated the percentage of localisations associated to nanoclusters in adhesions over time. If this number increases with time, it will indicate that free, non-clustered localisations present on adhesions at early seeding time points (90 min) go on to form new nanoclusters within adhesions as the cells settles with time. Our results (Figure 3.13) show that there is a modest and significant increase in the percentage of localisations associated to clusters for $\alpha_v\beta_3$ when comparing 90 min to 24 h. This increase although deemed significant is slight (increase of ~13% from 90 min to 24 h, median values) so it cannot explain the 4.4-fold increase in $\alpha_v\beta_3$ nanocluster density that we earlier determined when going from 90 min to 24 h spreading time (Figure 3.9 A, B and Figure 3.10). The enhanced $\alpha_5\beta_1$ nanoclustering from free localisations is even more modest, with an increase of ~7% from 90 min to 24 h, median values (Figure 3.13). These results thus rule out the possibility that free integrins join together to form new nanoclusters that can account for the increased integrin nanoclustering density as function of spreading time.

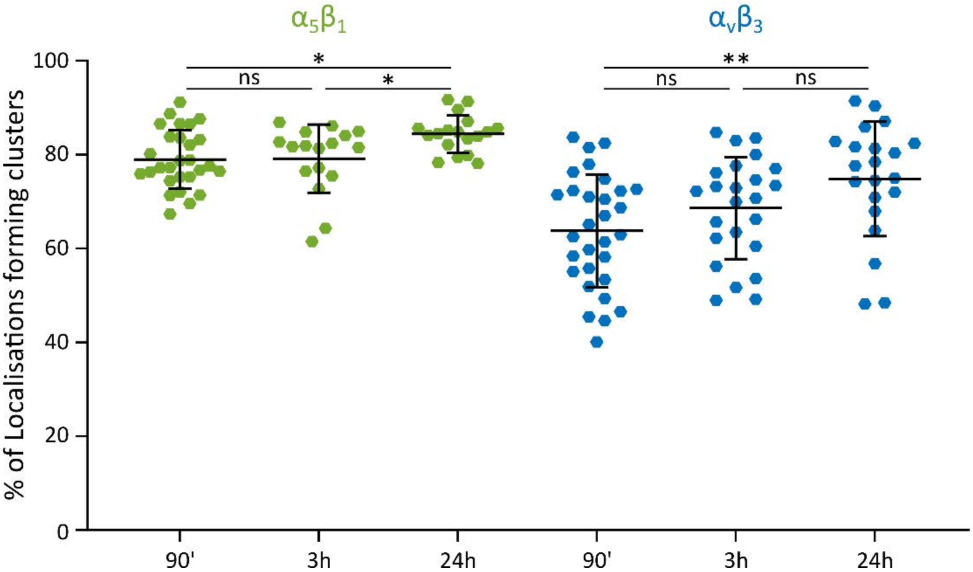

Figure 3.13 *Percentage of integrin ($\alpha_5\beta_1$, in green; $\alpha_v\beta_3$, in blue) localisations in adhesion complexes forming nanoclusters*

Percentage of localisations belonging to nanoclusters inside adhesions. The plot has been obtained by taking the number of localisations considered to be part of a cluster by DBSCAN, and dividing it by the total number of localisations found to be in all the adhesions. Each data point represents a cell, the horizontal line marks the mean of the distribution with the whiskers extending over the standard deviation. ns, $p>0.05$; *, $p<0.05$; **, $p<0.01$; ***, $p<0.001$; one-way ANOVA.

4) Integrin nanoclusters could split as function of spreading time leading to an effective increase of nanoclusters per unit area.

Although the fraction of clustered localisations on adhesions seems to be constant with time (Figure 3.13), it is possible that as spreading time proceeds, nanoclusters would shrink in the number of localisations they contain and therefore more nanoclusters per unit area would be formed. Again, we already have the results to invalidate this hypothesis, since we found no change in the number of localisations per nanocluster for either integrin (Figure 3.7 A, B).

5) Monomers (non-clustered localisations) could be recruited to the adhesion complexes from the membrane region outside adhesions.

A fifth possibility we considered is that free integrin localisations, which do not form nanoclusters outside the adhesion areas, are progressively recruited towards the adhesion complexes, with a fraction of them contributing to the formation of new nanoclusters. To test this possibility, we quantified at the number of non-clustered localisations per unit area outside adhesions to see if this value decreases with time. Our results (Figure 3.14) show that this is not that case. On the contrary, the density of non-clustered localisations outside adhesion complexes follows an incremental trend with time for both integrins (Figure 3.14). These data allow us to rule out the possibility that the recruitment of non-clustered proteins from outside adhesions to adhesion complexes leads to the observed increase in integrin cluster density with time.

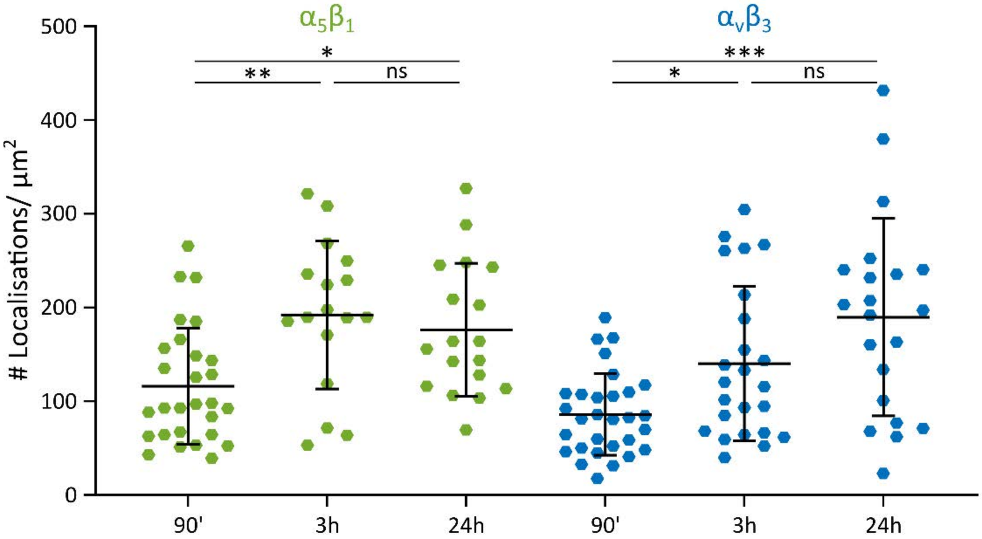

Figure 3.14 *Density of non-clustered localisations outside of adhesions for different cell spreading times*

Number of non-clustered localisations per unit area outside of adhesions with time, for $\alpha_5\beta_1$, in green, and $\alpha_v\beta_3$, in blue. In this case, the area considered is the area of the basal membrane in the cell mask minus the sum of all the adhesion areas of the cell. Each data point represents a cell. Each data point represents a cell, the horizontal line marks the mean of the distribution with the whiskers extending over the standard deviation. ns, $p>0.05$; *, $p<0.05$; **, $p<0.01$; ***, $p<0.001$; one-way ANOVA.

6) *New integrins arrive at the basal membrane over time*

Finally, we show that the number of localisations for $\alpha_5\beta_1$ and $\alpha_v\beta_3$ increase with time (Figure 3.15) and we therefore conclude that the increase in density of integrin clusters comes from and overall increase in integrin expression at the basal membrane with time. However, the source of these new proteins is not clear: they could diffuse into the basal membrane from the apical membrane, be newly synthesised proteins trafficked from the Golgi apparatus, or recycled integrins arriving from the endo-lysosomal system.

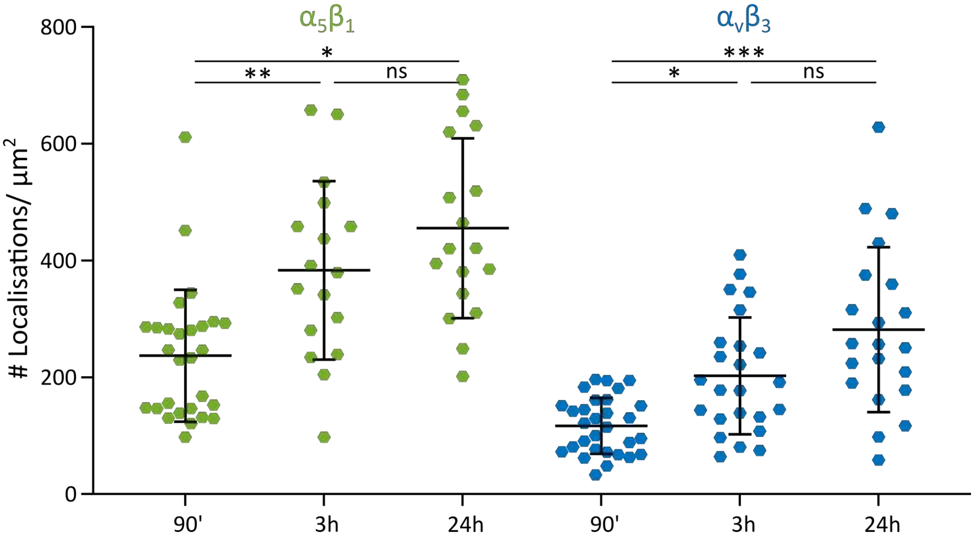

Figure 3.15 *Density of localisations in the entire basal cell membrane for different cell spreading times*

Number of all localisations per unit area for the full basal cell membrane with time, for $\alpha_5\beta_1$, in green, and $\alpha_v\beta_3$, in blue. In this case, the area considered is the area of the basal membrane in the cell mask. Each data point represents a cell, the horizontal line marks the mean of the distribution with the whiskers extending over the standard deviation. ns, $p>0.05$; *, $p<0.05$; **, $p<0.01$; ***, $p<0.001$; one-way ANOVA.

3.4 Discussion

This chapter aspired to understand the nanoscale organisation of adhesion complex proteins, particularly focusing on characterising their partitioning into small nanoclusters. We investigated the characteristic properties of these nanoclusters, such as their sizes and number of localisations per cluster, and whether/how they vary as a function of their location on the basal membrane or as a function of the spreading time. The aim was to understand these clusters to know if they had different characteristics depending on the protein or if they were dynamic structures that grew over time. By using STORM imaging on fixed human fibroblasts (HFF-1 cells) along with quantitative analysis tools, we first showed that the adhesion proteins that we have tested (the two integrins $\alpha_5\beta_1$ and $\alpha_v\beta_3$, and the adaptor proteins paxillin, talin, and vinculin) form small nanoclusters. Interestingly, our data revealed that these clusters have, in general, a very similar area and localisation density regardless of the type of adhesions they are found in, and that this even holds true for those found on the regions of the basal membrane outside the adhesions. We also performed experiments at different times after seeding the cells on a FN-coated glass substrate (90 min, 3 h, or 24 h). Our data showed that adhesion protein nanoclusters remained unaltered independently on the time the cells had to attach and spread on the substrate. Based on the outcome of our in-depth quantitative analyses on adhesion protein clustering, we would like to propose that these clusters constitute universal nanohubs of adhesion proteins. Then, these nanohubs further organise as higher-level super-structures of high cluster density, which correspond to adhesion complex structures, such as FAs and fAs. Nonetheless, we would like to stress once more that this mesoscale organisation of adhesion proteins into adhesion complexes (> 1 µm) is not accompanied by any change in the nanoscale organisation of the adhesion proteins in small nanoclusters (of ~50 nm in size).

This finding, namely that there is continuity across all the clusters we studied, struck us as a very interesting and intriguing one, because adhesion proteins play very different roles in cells. One would expect that these varied roles could be indicated in varying cluster sizes, but instead they appear to have a universal size, consistent across ROIs and cell spreading time.

We then carried out further analysis on these nanoclusters, aiming at understanding the overall evolution of the nanocluster organisation. In particular, we looked at the number of nanoclusters per unit area for the different adhesion proteins, and how this quantity evolved depending on the protein, the membrane region where they are found, and the length of time the cell is allowed to attach and spread. The outcome of these analyses showed that for the integrins $\alpha_5\beta_1$ and $\alpha_v\beta_3$ there is an increase in the cluster density with time, and that this increase specifically occurs inside adhesion complexes. These data also revealed that the density of $\alpha_5\beta_1$ clusters is consistently higher than that of $\alpha_v\beta_3$ clusters inside of the adhesions, regardless of the type of adhesion (FAs or fAs) or of the cell spreading time. Strikingly, the density of clusters per unit area for $\alpha_v\beta_3$ is significantly lower than for $\alpha_5\beta_1$ in the experiments looking at early time point after seeding (90 min), which could be an indicator that $\alpha_5\beta_1$ arrives to the adhesions first to establish the initial cell attachment points. This hypothesis is also consistent with the larger bond strength reported for FN–$\alpha_5\beta_1$ as compared to FN–$\alpha_v\beta_3$ (Kong et al., 2009; Elosegui-Artola et al., 2016; Bharadwaj et al., 2017). Thus, the enrichment of $\alpha_5\beta_1$ integrin at FAs together with its higher bond strength would serve to maintain stable adhesions, which are particularly important during early spreading times. Intriguingly, despite the overall amount of $\alpha_5\beta_1$ clusters is always larger than that of $\alpha_v\beta_3$, we found that the fold increase along cell spreading time is much larger for $\alpha_v\beta_3$ than for $\alpha_5\beta_1$ (4.4-fold $\alpha_v\beta_3$ nanocluster density increase from 90 min to 24 h, and 2.7- and 1.9-fold increase for FAs and fAs, respectively, for $\alpha_5\beta_1$ clusters). Our results suggest that as spreading time proceeds, the role of $\alpha_v\beta_3$ becomes more prominent or necessary for the cells. Using in-vitro experiments, Roca-Cusachs et al. determined that the bond strength of $\alpha_v\beta_3$ to FN is lower than that of $\alpha_5\beta_1$, leading to its faster binding and unbinding rates and suggested a possible function of $\alpha_v\beta_3$ in mechanosensing (Roca-Cusachs et al., 2009). In addition, using a stretching device coupled to single molecule studies, Massou et al. recently showed that $\alpha_v\beta_3$ is involved in mechanosensing (Massou et al., 2020). Together with our results, we would like to suggest that as cell spreading proceeds, it is possible that events of mechanosensing and mechanotransduction mediated by $\alpha_v\beta_3$, become more important as compared to earlier seeding times when the cells are primarily involved in adhesion establishment, and thus require a larger pool of $\alpha_5\beta_1$.

There is still a lot of controversy in the field over the specific roles that different integrins play. In particular, the two integrins we have focused on in this thesis ($\alpha_5\beta_1$ and $\alpha_v\beta_3$) are present in adhesions and they have the ability to bind the RGD domains of the same ECM protein (FN) with $\alpha_v\beta_3$ additionally binding another protein, VN (Van der Flier and Sonnenberg, 2001). Despite these similarities, some studies have shown that $\alpha_5\beta_1$ is more responsible for adhesion strengthening, whereas $\alpha_v\beta_3$ functions in mechanotransduction (Li et al., 2003; Sun et al., 2005; Jiang et al., 2006; Roca-Cusachs et al., 2009). However, there are many recent studies that show that integrin job splitting is not so black and white, with integrin cross talk playing a major role (Bharadwaj et al., 2017; Diaz et al., 2019; Robert et al., 2021; Seetharaman and Etienne-Manneville, 2018). In summary, although a clear picture for the roles the distinct integrins play has not been reached, there is some consensus in the field on the fact that, although different integrin heterodimers may specifically have some primary roles, they have been seen to work together to efficiently perform cell processes (Schiller et al., 2013; Diaz et al., 2019). This reported adaptability and versatility of integrin roles adds an extra layer of complexity and hence makes our quest to distinguish the specific primary roles of each integrin more challenging (Huveneers and Danen, 2009; Zaidel-Bar, 2013; Seetharaman and Etienne-Manneville, 2018).

As $\alpha_5\beta_1$ is the integrin primarily associated to the fibrillar adhesions (Pankov et al., 2000), it was our expectation that a distinct difference in the integrin clusters would be observed here, either in terms of the cluster characteristics or the number of clusters per unit area depending on their location. However, our results did not reveal such a straightforward outcome. By contrast, our data clearly indicated that $\alpha_v\beta_3$ clusters are in general present, albeit at lower density for this cell type, as compared to $\alpha_5\beta_1$ clusters, in both FAs and fAs.

When studying the density of clusters for the adaptor proteins, we noted that talin and vinculin had similar densities (Figure 3.9), independent of the adhesion type or spreading time. This might not be so surprising as both of them are partners in forming and reinforcing the connection between integrins and the actin cytoskeleton. However, when compared to the densities of integrin clusters, our observation raises some questions. After a relatively short time allowed for cell spreading (90 min), $\alpha_v\beta_3$ clusters are at very low density both in FAs (median of $\sim$3.8 clusters/μm^2) and in fAs (median of $\sim$3.1 clusters/μm^2). Considering the two integrins together, the mean number of integrin clusters per unit area is $\sim$13 clusters/μm^2 in FAs at 90 min, whereas the mean density of talin and vinculin clusters is $\sim$11 clusters/μm^2 for both. Because talin and vinculin are cytosolic proteins that get recruited upon integrin activation (Rossier et al., 2012), it seems plausible that at 90 min the majority of the integrin nanoclusters are engaged with talin and vinculin. As cell spreading time proceeds, the total density of integrin clusters increases to $\sim$34 clusters/μm^2 in FA but, remarkably, a similar increase is not seen for talin and vinculin, with only 12 and 10.7 clusters/μm^2, respectively. Thus, the fraction of integrin nanoclusters that can be interacting with talin and vinculin has reduced from $\sim$1:1 at 90 min to one third by 24 h (Figure 3.10). Although unexpected at first glance, it has been reported that there are nanoclusters of both active and inactive integrins in FAs (Spiess et al., 2018). At early time points, when the cells are actively spreading, it is therefore reasonable to suggest that the cells require a large majority of the integrins localised on the basal membrane to be active and engaged with talin and vinculin. After 24 h of attachment and spreading, the cell has reached a plateau where the FAs are undergoing assembly and disassembly in a balanced manner to enable the cell to remain attached while migrating in its local environment (Webb et al., 2002). FAs are dynamic structures (reviewed in chapter 1), but our experiments provide only static snapshots of their organisation. As one cluster of integrins disengages with their adaptors, there would need to be another integrin cluster close by to bind this adaptor in order to keep the steady state of the attached cell. However, this hypothesis remains untested, to the best of our knowledge, so further investigations would be required to determine if it is correct or not.

Finally, we focused on identifying the most relevant source of the increased density of integrin clusters in the adhesions over spreading time. After addressing a number of different possibilities that could have explained the observed increase in the number of integrin clusters per unit area over time, we conclude that the origin of these new integrins at the basal membrane is likely intracellular pools (either recycled integrins stored in endosomes, or newly synthesised proteins arriving from the Golgi apparatus) or by transcytosis or diffusion from the apical cell membrane. Along these lines, a recent report has revealed targeted delivery of integrin-containing transport carriers to FAs (Huet-Calderwood et al., 2017), indicating that integrin exocytosis directly targeted to FAs and could constitute the main mechanism that leads to a larger number of integrin nanoclusters as function of cell spreading time.

As is the case in many exciting scientific projects, these experiments answered many questions about the adhesion proteins. In particular, establishing that all these adhesion proteins segregate into nanoclusters with a universal size independent of membrane region or time after seeding. We also discovered that the number of clusters per unit area increases with time for integrins but not for their adaptors. This leaves use with many more exciting questions to answer: how are these clusters organised with respect to clusters of the same protein? How are they organised with respect to other proteins? Is there a preferred organisation or positioning within the adhesions? We have at our disposal dual-colour super-resolution microscopy data so we have the opportunity to investigate how these proteins are distributed with respect to each other. The following chapters of this thesis aim to investigate and discuss these topics in greater detail, aiming at contributing to a better understanding of the organisation of the proteins in adhesion complexes.

Chapter 4

Nanoscale lateral control of integrin nanoclusters and their adaptors inside adhesions

In the previous chapter, we showed that integrins and the main adaptor proteins involved in adhesion complexes laterally organise as small nanoclusters, which are present both on focal and fibrillar adhesions, and even outside adhesions. Using super-resolution microscopy and newly-developed algorithms, here we aimed at elucidating whether there is a preferred lateral distribution of these protein nanoclusters inside adhesion complexes. Remarkably, we found that $\alpha_5\beta_1$ *integrin nanoclusters and the main adaptor proteins have an inherent nanoscale distribution that keeps them segregated at a lateral spacing of 50–60 nm independent of the spreading times investigated. Such a lateral nanoscale spacing is maintained in both focal and fibrillar adhesions. Concomitant with their lateral segregation at 50–60 nm, we observed a lateral enrichment at distances of ~100 nm. Interestingly,* $\alpha_v\beta_3$ *integrin clusters developed a similar nanoscale organisation at later spreading times, which parallels with their increased cluster density and focal adhesion stabilisation in time. Our results are in line with earlier observations suggesting the existence of an integrin-ligand spacing threshold below 70 nm that regulates the dynamics of cell spreading, adhesion and migration. Based on our results, we postulate that this spatial sensing of integrin ligands is, in fact, dictated by the inherent nanoscale spacing of integrin nanoclusters inside adhesion complexes. The nanoscale clustering and lateral spacing of integrins thus play an essential role in controlling the dynamics and fate of the adhesive response.*

4.1 Introduction

Adhesion complexes are dense protein platforms that initially form at the cell membrane as unstable nascent adhesions that then transition through different maturation steps to eventually form more stable structures such as FAs or fAs. These adhesions have been studied at length for many years and have been shown to play critical roles in cell migration, differentiation, mechanosensing, and many other fundamental cellular processes (Egles et al., 2010; Colburn and Jones, 2017; Watt et al., 1993; Schwartz and DeSimone, 2008; Neiman et al., 2019). Although extensive studies have been carried out, many aspects regarding their spatiotemporal organisation still remain ill-defined, in part due to the immense number of interacting partners involved, and in part due to the lack of suitable techniques to address the smallest scales of spatial organisation.

Integrins are membrane-spanning proteins at the centre of adhesion structures, where they link the external environment of the cell with the internal actin cytoskeleton via a myriad of adaptor proteins. The adhesion complex proteome (the adhesome) includes components such as the RGD-binding cell surface integrin receptors $\alpha_5\beta_1$ and $\alpha_v\beta_3$, extracellular matrix proteins such as FN and VN, and adaptor proteins, such as paxillin, talin, and vinculin. However, it has been shown that the integrin adhesome includes in excess of 200 different proteins (Winograd-Katz et al., 2014), with $\sim$60 of them identified as commonly found in proteomes of integrin-based adhesions complexes (Horton et al., 2016). The enrichment of this large amount of proteins is an indicator of how complicated it has proven to be to decrypt the inner workings of the cell's adhesion complex. In particular, new focus and studies on proteins such as tensin, zyxin, or kindlin, have contributed to our current understanding of the adhesion complex, mechanobiology and the mechanisms at work to carry out its roles in the cell (Harburger et al., 2009; Stutchbury et al., 2017; Böttcher et al., 2017; Legerstee et al., 2019; Barber-Pérez et al., 2020; Legerstee and Houtsmuller, 2021; Orré et al., 2021).

Many technical advances have assisted in the gain of invaluable insights on the biology of cell adhesions. In particular, the development of multicolour fluorescence microscopy techniques provided a tool to visualise the cellular localisation of multiple proteins simultaneously, thus informing us about functional interactions between adhesion components. Unfortunately, these diffraction-limited microscopy techniques still left us lacking the finer details in the sub-diffraction, nanoscale regime. Fortunately though, with the emergence of super-resolution techniques (Huang et al., 2009a; Lelek et al., 2021) we are now equipped with suitable techniques to investigate the nanoscale organisation of these dense cellular structures. Yet, progress is slow as many of these techniques are time-consuming and multicolour imaging with nanoscale resolution is still not a trivial task. In this study we performed dual-colour super-resolution STORM imaging on fixed human fibroblasts (HFF-1 cells), where the samples were always labelled for an integrin (either $\alpha_5\beta_1$ or $\alpha_v\beta_3$) together with one of the three adaptor proteins of interest (paxillin, talin, or vinculin). This strategy allowed us to gain insight on the nanoscale organisation of individual proteins (see Table 2.6), covered in this chapter and also provided an opportunity to study the relative distribution and possible interactions of the two integrins with respect to each of the three adaptors (see Table 2.7 and Table 2.8), which we cover in the following chapter.

In chapter 3, we demonstrated that each of the proteins we have studied forms physically segregated nanoclusters at the cell membrane, as opposed to the classical view that FAs are homogeneous patches of fully-colocalising adhesion complex proteins (Humphries et al., 2007). In a study from the Spatz group (Cavalcanti-Adam et al., 2006), it was demonstrated that the nanoscale distribution of integrin ligands influences cell spreading and FA dynamics. In their studies, they used nano-patterning of RGD-coated nanospheres where, due to the small size of the sphere, 8 nm, only one integrin can be engaged at a time. They found that there is an optimum distance of 58 nm for the separation between individual integrin ligands in order for the cells to spread and form FAs. Above this distance, in particular, at a ligand separation of 108 nm, cells can attach but their ability to spread and form FAs is diminished. By studying FA turnover and examining the dynamics of cell protrusions like the lamellipodium, they showed that adhesions formed on 108 nm patterns have increased FAs instability. Based on these and earlier data, the authors suggested that ligand spacing plays a crucial role in cell spreading and FA formation, with a threshold ~73 nm (Arnold et al., 2004). However, the mechanism setting the distance of this molecular ruler is, until now, poorly understood. More recently, the group of Roca-Cusachs recapitulated these earlier results and assessed the role of substrate rigidity on ligand spacing (Oria et al., 2017). When incorporating patterned nanospheres on surfaces of different rigidities, they found that the optimal separation of integrin molecules depends on the organisation of the ligand distribution and on the loading-forces applied, which in turn depend on the substrate rigidity. From these studies we learned that the organisation and distribution of the ligand, and therefore indirectly of the integrins, influences the cell's ability to attach and form FAs and that this strongly depends on the substrate rigidity. However, these studies did not provide direct evidence of how integrins are distributed on the cell membrane or the mechanisms by which these critical spacing distances are established.

The work described in this chapter presents our results on the lateral organisation of the clustered proteins that we have characterised in Chapter 3. Exploiting already-established analytical functions and combining them with custom-made algorithms, we studied the distribution of individual protein nanoclusters within adhesions. In particular, we present the results obtained by computing the nearest neighbour distances (NND) between the centroids of clusters of the same protein (e.g., $\alpha_5\beta_1$ to $\alpha_5\beta_1$), as identified from our super-resolution STORM images. We studied how this distance distribution depended on the cell membrane regions (FAs vs fAs vs outside adhesions), and how it changed over cell spreading time (90 min, 3 h, or 24 h). As we already presented in Section 3.3.6, the number of integrin clusters per unit area increases with time, which, as we show here, parallels a reduction of the NND between integrin clusters with time. We further compared our experimental data to simulated random data sets to ascertain if the distributions and changes with time are different to what we would expect from randomly distributed protein clusters. Remarkably, we discovered that integrin nanoclusters and their adaptor proteins inside adhesion complexes are laterally spaced at the nanoscale. Our work thus reveals for the first time a highly hierarchical lateral ordering of proteins inside adhesions, from nanoclustering to their lateral spacing at the nanoscale.

4.2 Materials and methods

4.2.2 Sample preparation and imaging

Samples were prepared by seeding HFF-1 cells on FN coated 8-well plates. The cells were allowed to spread for different times (90 min, 3 h or 24 h), after which they were fixed and then immunolabelled using primary and secondary antibodies as described in detail in Chapter 2.

4.2.3 Image acquisition

All the STORM images analysed in this chapter were taken on a Nikon Eclipse Ti system using a 100x oil objective with NA of 1.49, a 256x256 pixel ROI and a pixel size of 160 nm using TIRF illumination. The system has lasers with wavelengths of 405 nm, 560 nm and 647 nm. For a full description of the image acquisition see Section 2.4 Chapter 2.

4.2.4 Image reconstruction

Dual-colour STORM image reconstruction was done using Insight3, provided by Bo Huang (UCSF, initially developed in Xiaowei Zhuang's Lab). The analysis was run over the entire data sets but recording only those localisations detected in the second frame of the five-frame cycle, that is the first of the four reporter frames, the localisations can be represented by a cross marking their centres or rendered with a Gaussian profile convoluted with the point. For more detailed description, see Chapter 2 section 2.5.

4.2.5 Image analysis

All the analysis carried out in this chapter was completed using scripts written and developed in house using MATLAB 2019b. We also made use of binary masks defined by manually selecting the adhesions from the dual-colour data sets. These data sets are imported using a Fiji plugin, developed by the group of Melike Lakadamyali during their time at ICFO. The data are analysed using the DBSCAN algorithm (eps=20 nm and N_{min}=3) to detect clusters of proteins. This algorithm then provides the centre of mass (CoM) of each cluster (along with other properties as described in Chapters 2 and 3).

Nearest neighbour distance (NND) computation

In order to establish how the protein nanoclusters are distributed relative to each other, we used the MATLAB function *knnsearch* to compute the NND between nanoclusters of the same protein, $NND_{A\text{-}A}$. The distribution of $NND_{A\text{-}A}$ values provides quantitative information on how the nanoclusters of each protein are distributed within the adhesions.

Computational generation of random nanocluster distributions

To assess whether the NND distributions obtained from the experimental data correspond to a preferential type of organisation or to random, we further performed simulations by generating *in silico* NND histograms of randomly distributed nanoclusters inside the adhesion structures, both FAs and fAs. In order to proceed, we essentially needed two ingredients: *First,* to extract from the experimental data the exact number of nanoclusters per adhesion; *Second,* to distribute the same number of nanoclusters in a random fashion within the adhesions, while excluding their spatial overlapping. For detailed description on how the *in silico* histograms were generated see Chapter 2 section 2.6.5.

Statistical analysis with GraphPad Prism:

We performed paired t-tests between experimental and simulated data for each of the proteins in FAs and fAs, with a confidence level of 95%; ns, $p>0.05$;*, $p<0.05$; **, $p<0.01$; ***, $p<0.001$.

4.3 Results

4.3.2 Super-resolution microscopy reveals laterally segregated nanoclusters of adhesion complex proteins

As shown and discussed in detail in Chapter 3, our super-resolution microscopy data indicated that proteins found in adhesions form segregated nanoclusters that are distributed throughout adhesions. Here, we quantitatively analyse the mesoscopic organisation of those clusters on the different regions of the basal membrane (FA, fA, and outside adhesions). Representative examples of reconstructed STORM images of integrins and the main adaptor adhesion proteins are shown in shown Figure 4.1 and Figure 4.2, respectively.

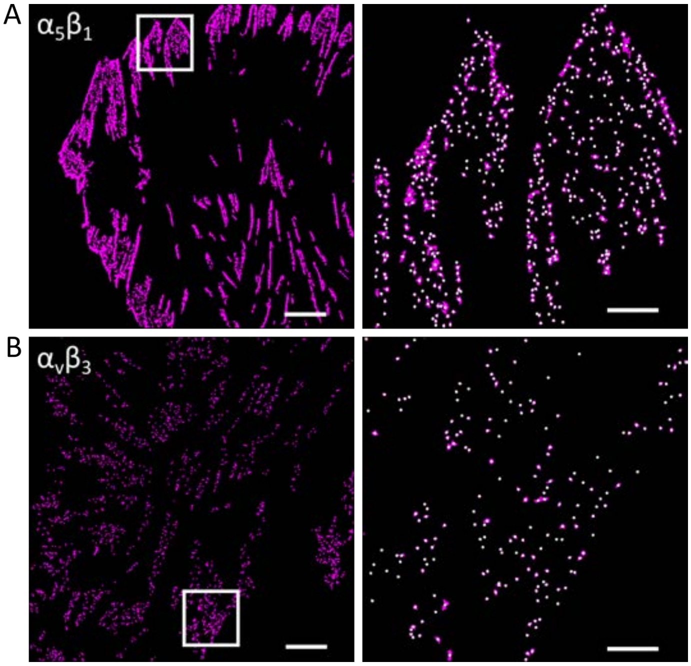

Figure 4.1 *Lateral distribution of integrin nanoclusters in adhesion complexes*
(A, B) Representative STORM images showing the individual localisations (magenta) belonging to clusters, as identified by the DBSCAN algorithm (with a threshold of a minimum of 10 localisations per cluster), for the integrins $\alpha_5\beta_1$ (A) and $\alpha_v\beta_3$ (B). The right panels show representative zooms in areas of adhesions corresponding to the regions denoted by white boxes in the left images. The white dots indicate the CoM of each cluster. Scale bar 5 µm, left panels, and 1 µm, right panels.

The reconstructed STORM images show that all the adhesion proteins studied form physically segregated nanoclusters within the high-density adhesion areas at the basal cell membrane. The integrin $\alpha_5\beta_1$ is the only protein that appears, at least upon initial visual inspection, to be distributed in a semi-organised manner within the adhesions, showing high density regions around the edge of the adhesion (Figure 4.1 A). In order to follow up on these observations and conclude quantitively for each of the proteins whether these clusters have a given mesoscale organisation that may not be apparent by visual inspection, we designed an analytical workflow based on the computation of the nearest neighbour distances (NND) between nanoclusters of the same protein.

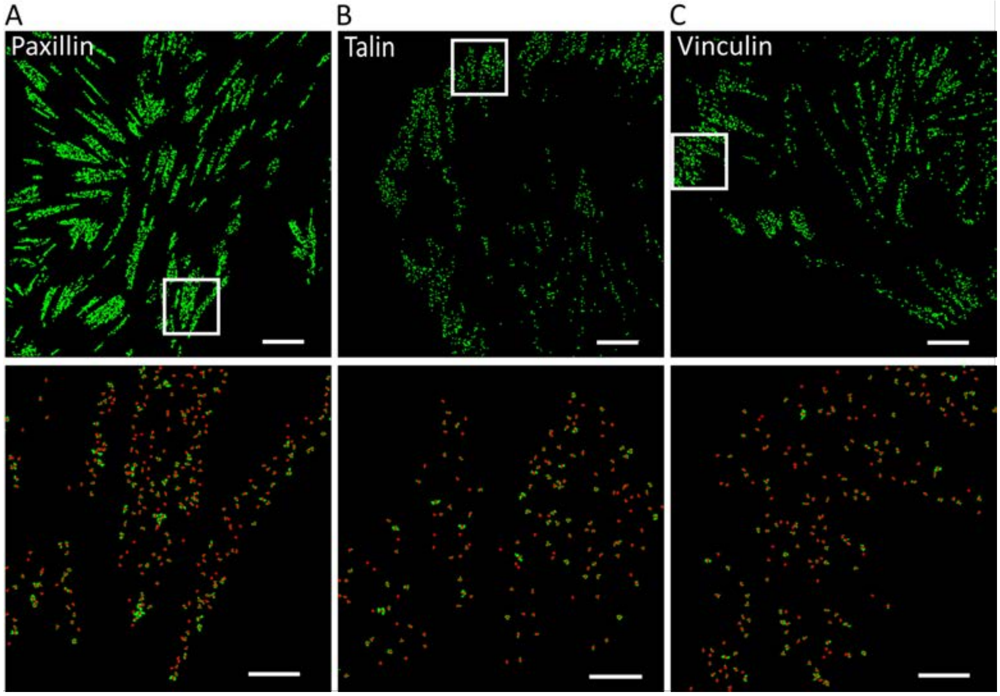

Figure 4.2 Lateral distribution of adaptor protein nanoclusters in adhesion complexes
Representative STORM images showing the individual localisations (green) belonging to clusters, as identified by the DBSCAN algorithm (with a threshold of a minimum of 10 localisations per cluster), for the adaptor proteins, paxillin (A), talin (B), and vinculin (C). The images on the bottom show the zoomed in areas of adhesions (white boxes top panels), where the red dots indicate the CoM of each cluster. Scale bars are 5 µm (left panels) and 1 µm (right panels).

4.3.3 Quantification of $NND_{A\text{-}A}$ of adhesion protein nanoclusters

In order to quantify the lateral organisation of adhesion protein nanoclusters, we computed the distribution of NND between clusters of the same protein. This quantity provides a general measure of the distribution of the clusters. Importantly, the experimental NND distributions can be compared to *in silico* generated NND distributions corresponding to different patterns of nanocluster organisation. In particular, to establish if the protein nanoclusters are randomly distributed on different membrane regions, we computationally generated random sets of data for each protein (the details of how the random simulation was generated can be found in Chapter 2).

Similar to Chapter 3, we split the analysis in two parts by considering the NND between nanoclusters of the same protein being localised either in FAs or fAs. In this section, we analyse the nanoclusters on cells that had been seeded 24 h before fixation. In general, we observed that the experimental data of $\alpha_5\beta_1$, $\alpha_v\beta_3$ and paxillin have very similar NND distribution shapes (Figure 4.3 and Figure 4.4 A,B) with narrow distributions and peaks at ~100 nm. In contrast, the distributions of NND for talin and vinculin (Figure 4.4 C–F) are broader with longer tails. We also noted that the distributions for $\alpha_5\beta_1$ in FAs and fAs are very similar whereas for the others, in particular, talin and vinculin, the fA distributions have a larger spread, and are also noisier for $\alpha_v\beta_3$, talin and vinculin in fAs. Altogether, these observations provided a valuable overview of the data, but this analysis remained insufficient. As we described in Chapter 3 these proteins have differences in the number of clusters per μm^2, with $\alpha_5\beta_1$ and paxillin having the highest density of nanoclusters of ~20 clusters per μm^2 (Figure 3.9), which could account for the narrow distribution retrieved by the NND analysis, i.e., the higher the density of the nanoclusters, the larger their packing and therefore the distance between nanoclusters is reduced.

As a means to disentangle the impact of cluster density from NND distributions, we generated randomly distributed nanoclusters on an adhesions-by-adhesion basis (details in Chapter 2), and calculated the NND for these *in silico* generated nanoclusters (see black lines in Figure 4.3 and Figure 4.4). We then compared experimental and *in silico* distributions and observed that, in all instances, the experimental distributions for the short NND values were slightly shifted to the right as compared to the simulated random data. This trend was not maintained for the longer tails of the distributions where the experimental and random simulations were always very similar.

The "shift-to-the-right" of the experimental data with respect to the simulated random data implies that the preferred distance between two close-by nanoclusters of the same protein is larger than if the nanoclusters were distributed randomly within the adhesions. In other words, there appears to be some factor that spatially segregates the adhesion protein clusters from one another.

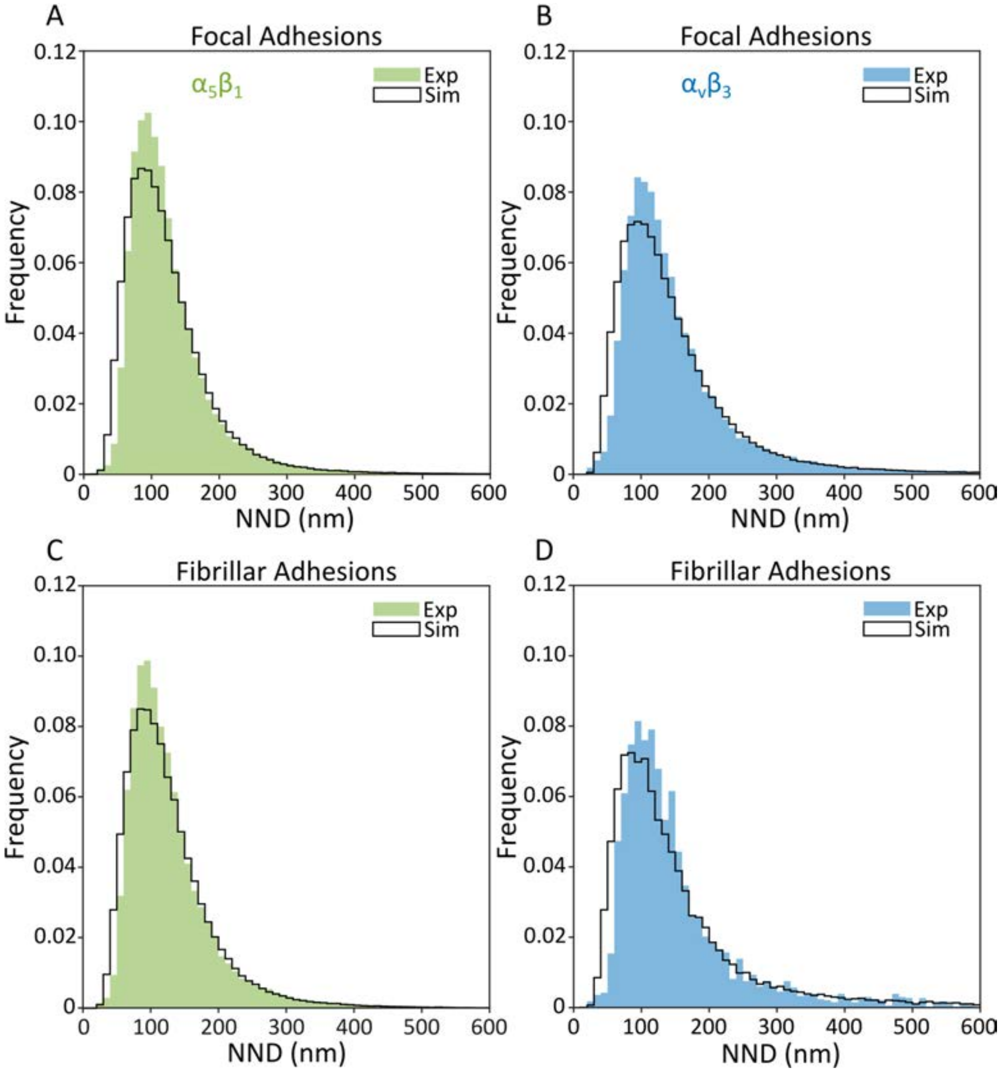

Figure 4.3 *Histograms of NND between integrin nanoclusters*
NND distributions obtained from DBSCAN-analysed STORM images of HFF-1 cells at 24 h seeding. Each histogram consists of the NNDs between clusters of the same protein over all cells. Experimental (Exp) data for the two integrins are shown in each panel as the filled colour histograms, (A,C) for $\alpha_5\beta_1$ (green), and (B,D) for $\alpha_v\beta_3$ (blue), whereas the simulated random distributions (Sim) are shown with the empty black histograms. The data were split depending on whether the nanoclusters were detected in FAs (A,B), or fAs (C,D). Number of cells for the $\alpha_5\beta_1$ and $\alpha_v\beta_3$ plots can be found in Table 2.6. Simulated data in each plot correspond to ten independent random distributions of the experimentally identified nanoclusters. The bin width is 10 nm.

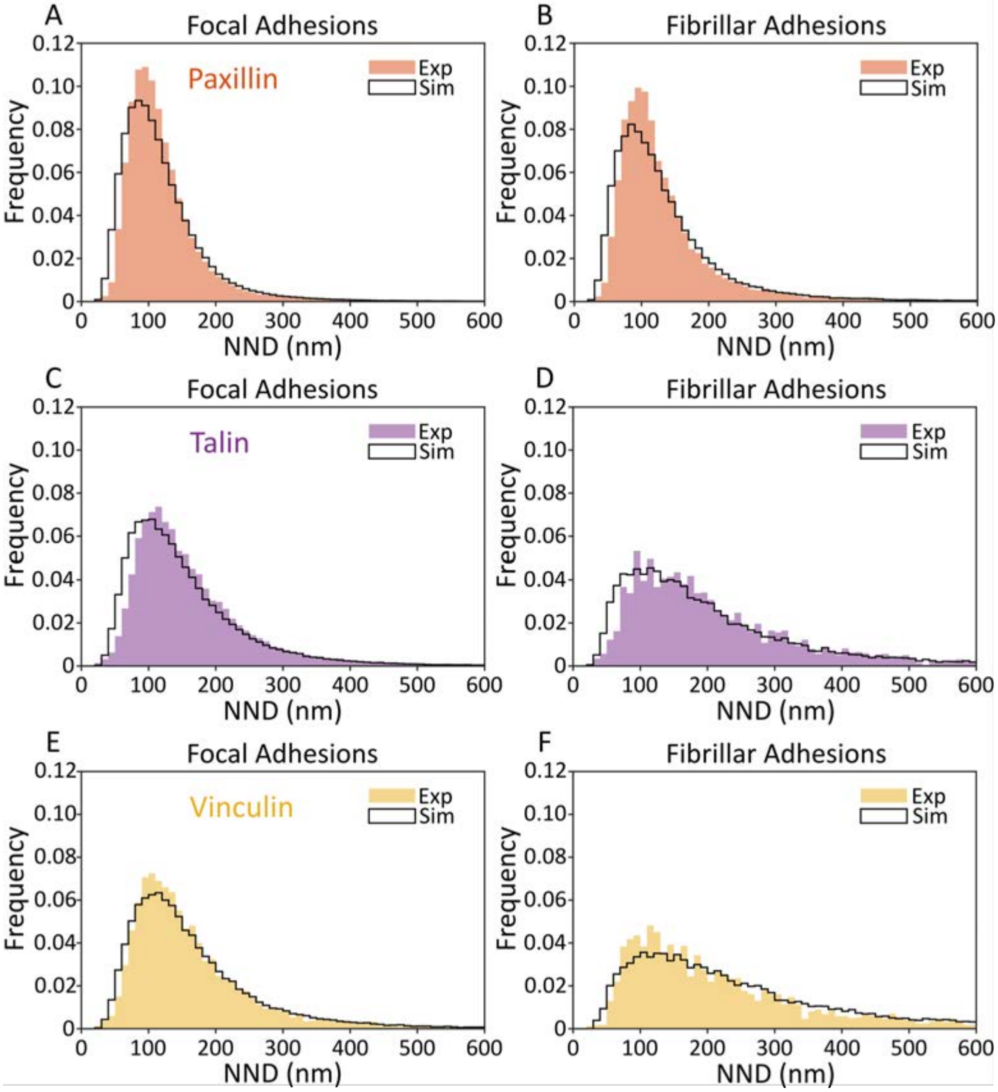

Figure 4.4 Histograms of NND for three different adaptor protein nanoclusters
NND distributions obtained from DBSCAN-analysed STORM images of HFF-1 cells at 24 h seeding. Each histogram consists of the NNDs between clusters of the same protein over all cells. Experimental data for the three adaptor proteins is shown as the filled histogram, paxillin (orange), talin (purple) and vinculin (yellow), whereas the simulated random distributions (Sim) are shown with the empty black histograms. The data were split depending on whether the nanoclusters were detected in FAs (left panels), or fAs (right panels). Number of cells per plot for the different adaptor proteins, paxillin, talin and vinculin clusters in FAs and fAs, can be found in Table 2.6. The simulations contain data pooled from ten independent random redistributions of the experimentally identified nanoclusters. The bin width is 10 nm.

In order to test the statistical significance of the observed differences between the experimental and the simulated data, there are a number of different values that can be extracted and compared: the peak of the distributions, their full width at half maximum (FWHM), their mean, or their median. We chose the median as it is a value independent of the histogram bin size and moreover, it is a more representative value for skewed distributions such as ours. We calculated the median NND value for each cell, and represented the results as box-and-whisker plots for each of the proteins (Figure 4.5 and Figure 4.6). Paired t-tests were used to determine whether the subtle differences we observed are statistically significant. The results from these analyses indicated that the median NNDs values of experimental and *in silico* random distributions are not significantly different for $\alpha_5\beta_1$ or paxillin in either FAs or fAs (Figure 4.5 A and Figure 4.6 A). By contrast, we saw that for $\alpha_v\beta_3$ the difference is significant for the distance between clusters in FA but not in fAs (Figure 4.5 B). These data indicate that the $\alpha_v\beta_3$ clusters in FAs are significantly further apart from each other than if they were randomly distributed, whereas the clusters in fAs have a median NND similar to that of a random distribution of clusters. Talin is the only protein studied that shows a significantly larger median NND per cell for both FAs and fAs (Figure 4.6 B). Interestingly, the median NND of vinculin also exhibits a significant difference from random but with the opposite trend, meaning that the NND between vinculin clusters is smaller than that of the random distribution (Figure 4.6 C).

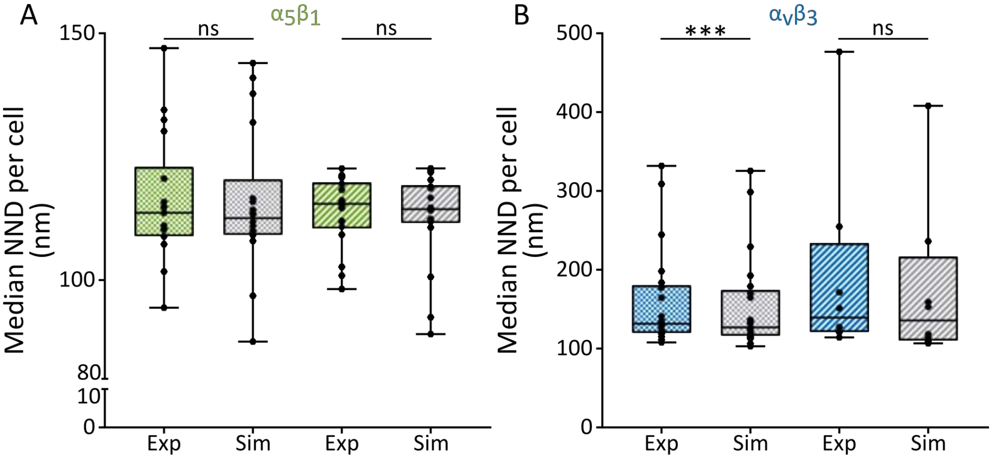

Figure 4.5 *Box-and-whisker plots of the distribution of median NND values per cell comparing experimental (Exp) and randomly distributed (Sim) data, for both integrin clusters in FAs and fAs at 24 h after cell seeding*

Box-and-whisker plots show the median NND per cell of nanoclusters of the same protein, $\alpha_5\beta_1$ (A) and $\alpha_v\beta_3$ (B). The details of the box-and-whisker plots are described in the methods section along with the details of the statistical tests carried out. *, $p<0.05$; **, $p<0.01$; ***, $p<0.001$. Paired Student's *t* test. Number of cells for the $\alpha_5\beta_1$ and $\alpha_v\beta_3$ plots can be found in Table 2.6.

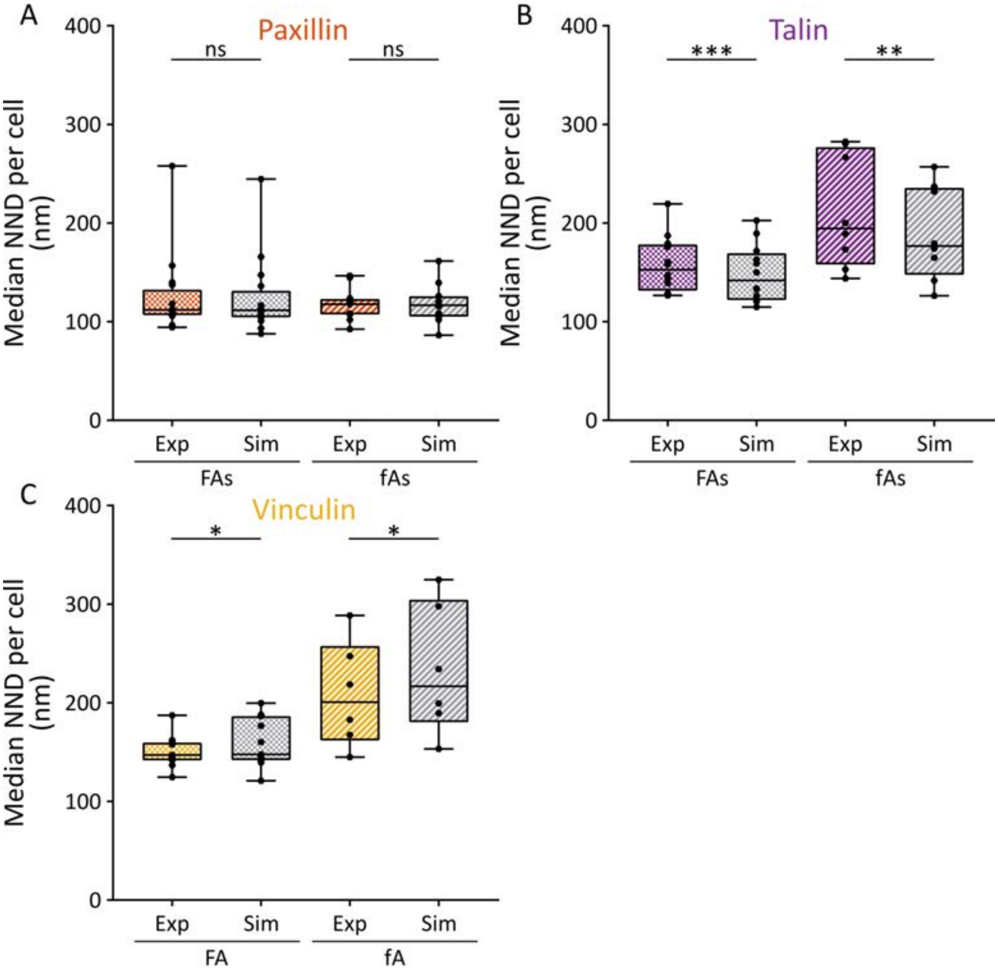

Figure 4.6 *Box-and-whisker plots of the distribution of median NND values per cell comparing experimental (Exp) and randomly re-distributed (Sim) data, for adaptor protein nanoclusters in FAs and fAs at 24 h after cell seeding*

Box-and-whisker plots show the median NND per cell of nanoclusters of the same protein, paxillin (A), talin (B) and Vinculin (C). The details of the box-and-whisker plots are described in the methods section along with the details of the statistical tests carried out. *, $p<0.05$; **, $p<0.01$; ***, $p<0.001$. Paired Student's *t* test. Number of cells per plot for the different adaptor proteins can be found in Table 2.6.

Together, these data provide a general overview of the lateral distribution of these five components in both FAs and fAs when the cells are fully spread on the substrate (at 24 h after seeding). While full distributions are all encompassing and often contain too much information obscuring finer details of the data, they act as a useful first step in the analysis pipeline to indicate what information might be extracted and what further evaluation is required.

4.3.4 Clusters of the same proteins are segregated from each other at a characteristic preferred distance

In the previous section, we characterised the main tendency of the NND distributions by their median value, which we used to run comparison tests to evaluate if the protein clusters are randomly distributed. Although this assessment provided us with valuable quantitative information on the spatial organisation of the nanoclusters, the analysis was limited, as evaluating a full distribution by a single value does not provide a complete picture. To circumvent this limitation, we undertook a more robust evaluation by directly comparing the full experimental and random distributions. In order to achieve this, we defined the *delta-value* distribution as the difference between the experimental and the simulated random data distributions,

$$\Delta NND_H = H_{exp}(NND) - H_{sim}(NND)\,, \qquad (4.1)$$

where H_{exp}(NND) and H_{sim}(NND) correspond to the histogram values for the experimental and simulated data, respectively. The x-axis NND values correspond to the centres of each histogram bin (bin width=10 nm). The ΔNND_H distribution removes the influence of the density of nanoclusters in an adhesion because the simulated data sets are generated by randomly redistributing the experimentally obtained nanoclusters at an adhesion-by-adhesion basis. This way of representing the data provides us with new insights on subtle but relevant differences between the experimental and simulated data sets (Figure 4.7 and Figure 4.8). The negative troughs and positive peaks of the ΔNND_H distribution represent depletion and enrichment, respectively, of nanocluster population with these centre-to-centre distances between them. Strikingly, the trough of each ΔNND_H-plot lies at NND values ranging between 45 nm and 65 nm, for all of our proteins of interest, regardless of whether they are on FAs or fAs (Figure 4.7 and Figure 4.8). Furthermore, the peaks of the ΔNND_H-plots lie at NND values ranging from 95 nm (for $\alpha_5\beta_1$) to 115 nm (for $\alpha_v\beta_3$ and talin), meaning that these nanoclusters are preferentially segregated at distance of ∼95 and ∼115 nm, respectively, as compared to what would be expected if the clusters were randomly distributed within adhesions. Exceptionally, we observed that the peak value for talin nanoclusters in fAs corresponds to an NND of 175 nm (Figure 4.11 D). However, as this plot shows very large fluctuations an accurate determination of the peak position was very challenging, we did not take this into further consideration.

Next, when comparing the ΔNND_H-plots for the nanoclusters in FAs to those in fAs, we essentially saw no marked differences between them, indicating that the exclusion and enrichment regions are generally preserved in both types of adhesion structures. Interestingly, for all the proteins studied, the width of the trough regions was narrower with a well-defined minimum value, while the enrichment regions were somewhat broader and extending over longer NND values. In the cases of $\alpha_5\beta_1$ and paxillin (both FAs and fAs) the enrichment was clearly more pronounced at distances of 95 nm and 105 nm, respectively and around 115 nm for $\alpha_v\beta_3$. Overall, these results indicate the occurrence of a clear lateral spacing between nanoclusters, i.e., a physical exclusion at ~55 nm intercluster distances, with those excluded nanoclusters then progressively enriching the space up to distances around 200 nm.

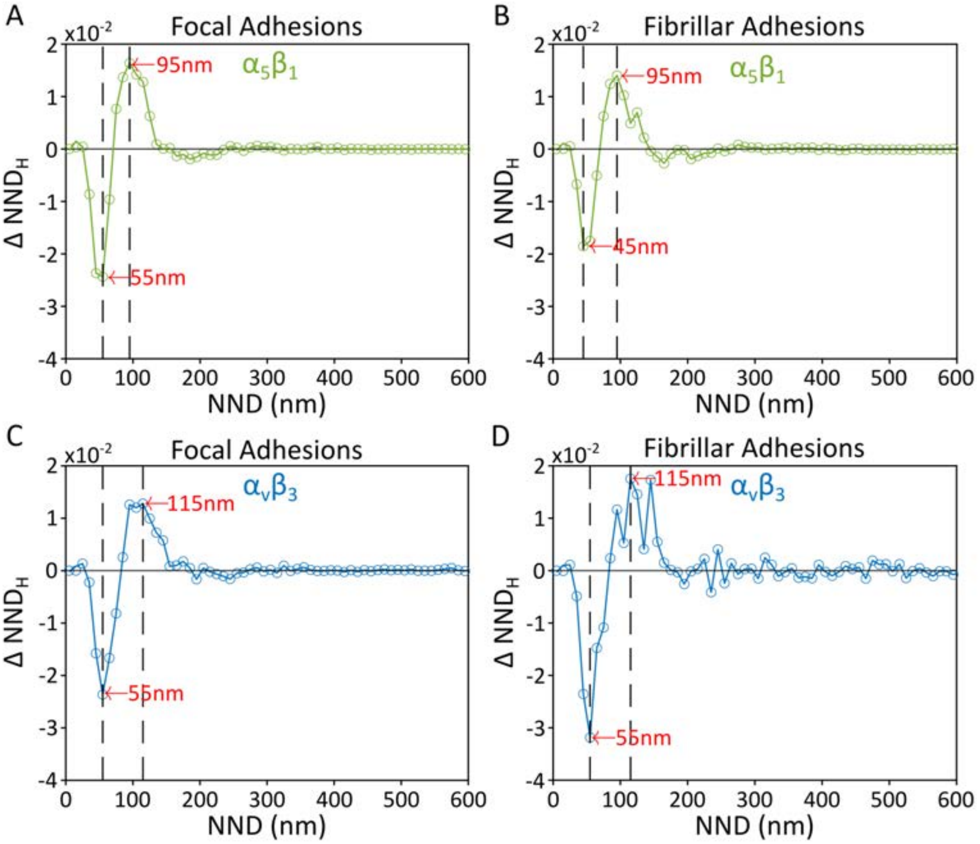

Figure 4.7 *ΔNND_H-plots for integrins in FAs and fAs after 24 h cell spreading*
(A–D) show the Δ-values (ΔNND_H, see Eq. 4.1) in FAs (A,C) and fAs (B,D) for the two integrins $\alpha_5\beta_1$ (A,B) and $\alpha_v\beta_3$ (C,D). Red arrows and numerical values indicate the NND corresponding to the maximum and minimum values of the ΔNND_H-histograms.

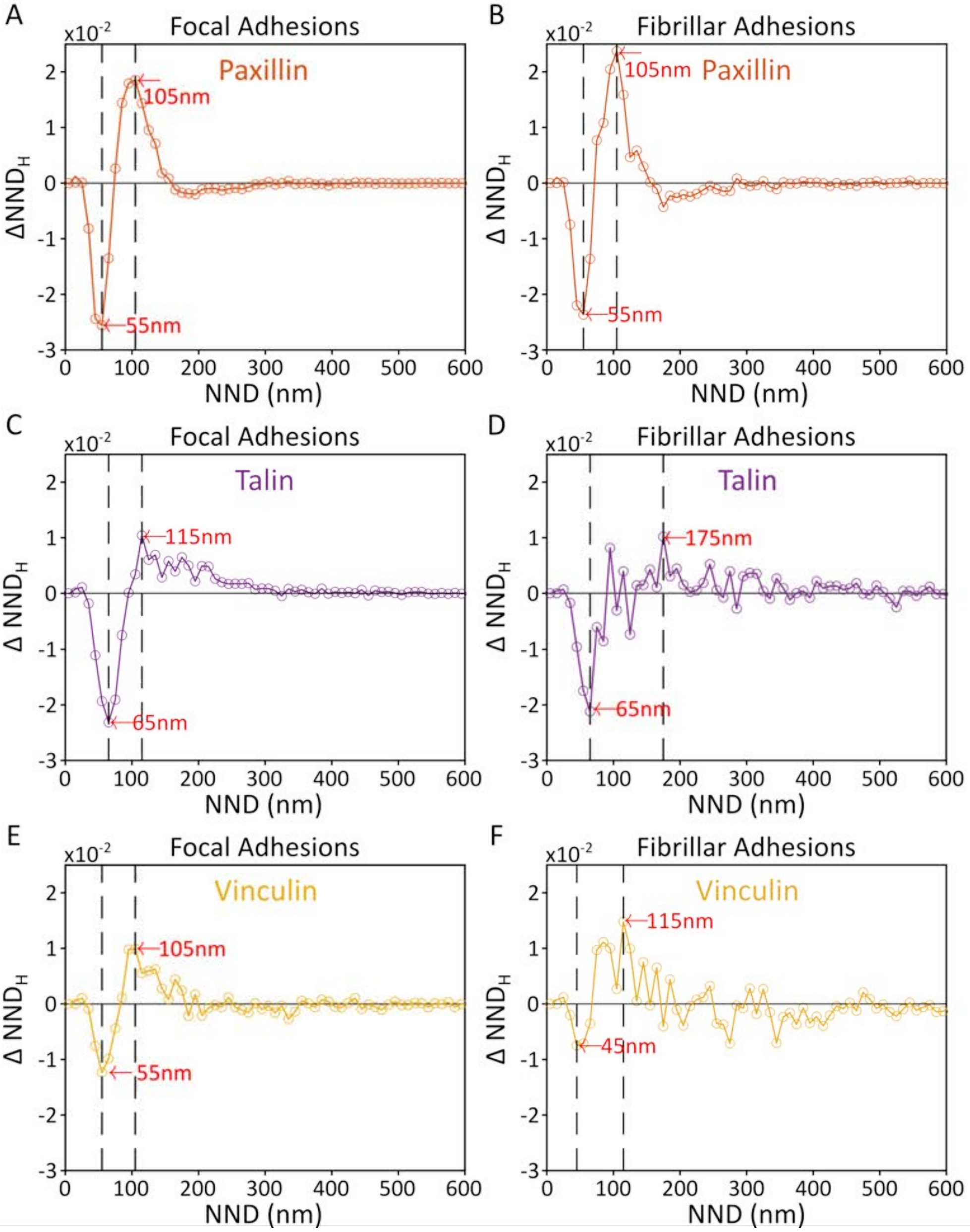

Figure 4.8 *ΔNND_H-plots for adaptor proteins in FAs and fAs after 24 h cell spreading*
(A–F) show the Δ-values (ΔNND_H, see Eq. 4.1) in FAs (A,C,E) and fAs (B,D,F) for the three adaptor proteins, paxillin (A,B), talin (C,D) and vinculin (E,F). Red arrows and numerical values indicate the NND corresponding to the maximum and minimum values of the ΔNND_H histograms.

4.3.5 Effects of the seeding time on the nanocluster organisation in adhesion complexes

In order to gain a greater understanding of the organisation of the protein nanoclusters in adhesions, we ran the same analysis as presented above on STORM images obtained from cells that were allowed to spread for shorter lengths of time (90 min or 3h). Specifically, to investigate whether and how the spreading time affects the distribution of intercluster NNDs, we computed the NND histograms and the ΔNND_H-plots for each protein in FAs and fAs, and plotted them together for each time point (Figure 4.9 to Figure 4.12).

When looking at the NND histograms, we observed that the NND distributions for the integrin clusters in FAs become narrower with spreading time (Figure 4.9 A,C), which is consistent with the observed increase in time of the density of integrin clusters per unit area (Figure 3.9). In contrast, the NND distributions for the adaptors in FAs remained constant and independent of the seeding time (Figure 4.10 A,C,E), again in agreement with the unaltered adaptor cluster density as function of seeding time reported in Chapter 3, Figure 3.9.

Remarkably, the minima and maxima of the ΔNND_H plots for $\alpha_5\beta_1$ and all the adaptor proteins investigated in FAs remain similar and independent of cell seeding time, with positive peaks at around 95–115 nm, and negative troughs at around 45–65 nm. These results indicate that this preferential lateral arrangement, i.e., enrichment and segregation at given distances between the different protein nanoclusters, is already pre-established at early seeding times. Interestingly, in the case of $\alpha_v\beta_3$, the depth of the minima and height of the maxima are quite small at earlier spreading times, and become more pronounced as spreading time progresses (Figure 4.14 D). These results indicate that, in contrast to $\alpha_5\beta_1$, $\alpha_v\beta_3$ lateral ordering is progressively reached at later stages of cell adhesion.

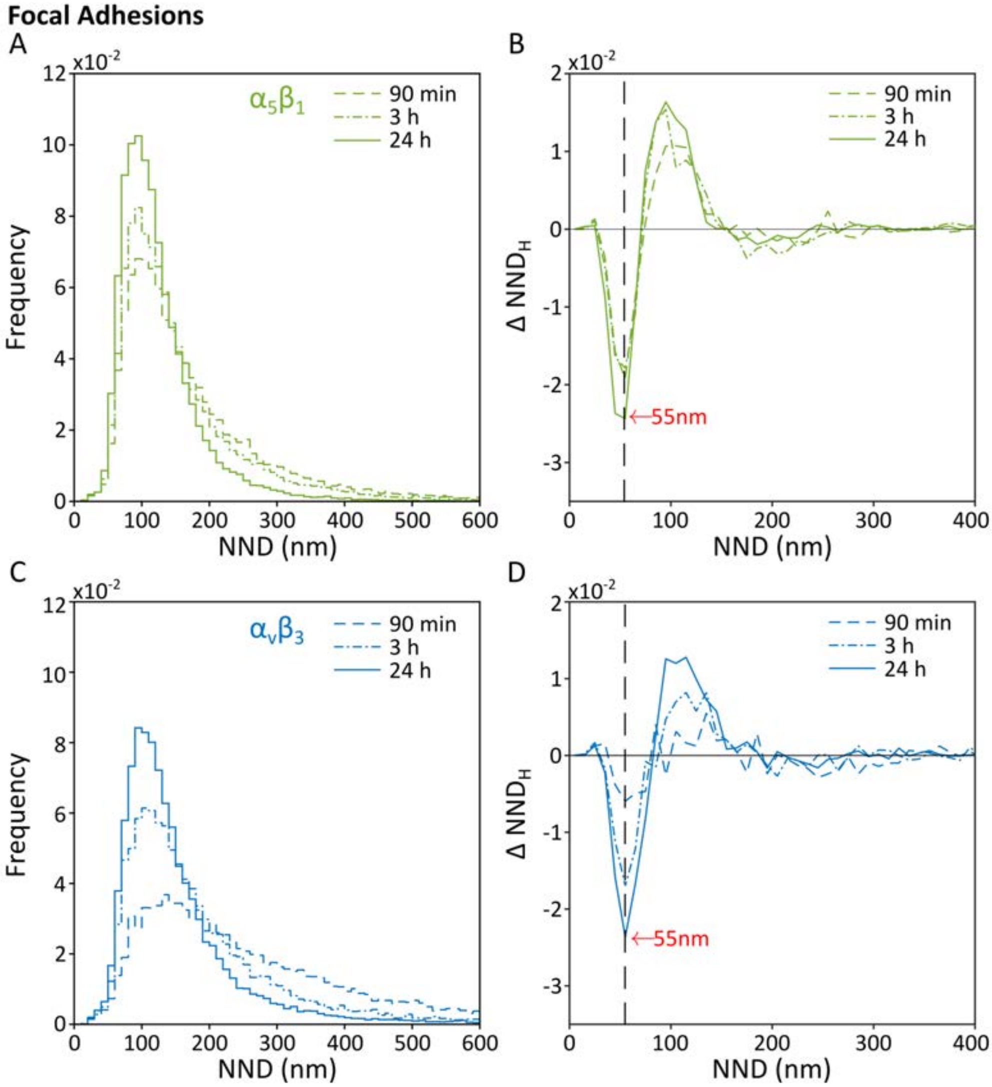

Figure 4.9 The effect of seeding time on intercluster NND distributions for integrins $\alpha_5\beta_1$ and $\alpha_v\beta_3$ in FAs

(A,C) Histograms of the experimental NND distributions for the $\alpha_5\beta_1$ (green) (A) and $\alpha_v\beta_3$ (blue) (C) integrins in FAs for the designated cell spreading times. Histograms for the random simulations have been omitted for the sake of visual clarity. (B,D) ΔNND_H-plots for the subtraction histograms for simulated data from experimental for the $\alpha_5\beta_1$ (green) (B) and $\alpha_v\beta_3$ (blue) (D) integrins in FAs at the three different seeding times (90 min, 3 h and 24 h).

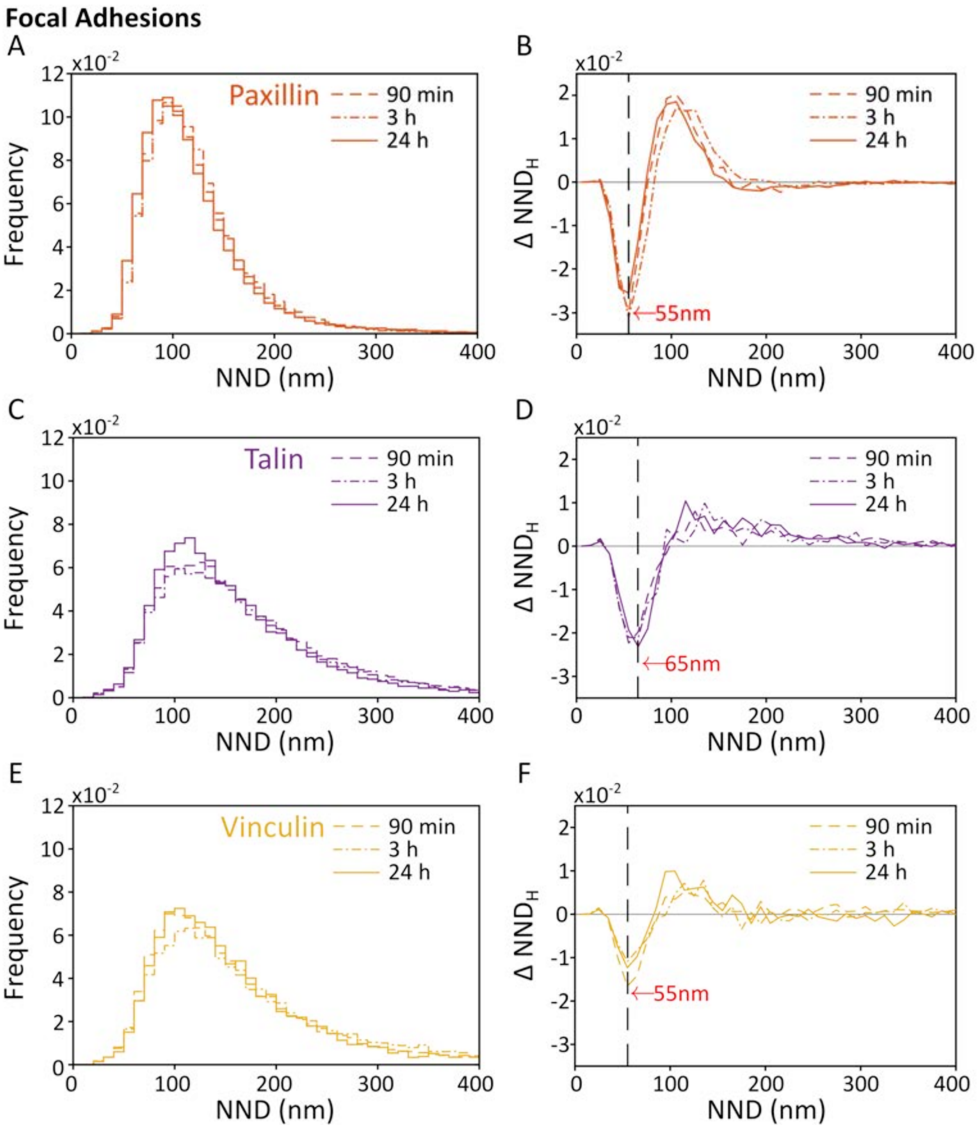

Figure 4.10 *The effect of seeding time on intercluster NND distributions for adaptor proteins in FAs*

(A,C,E) show the histograms for the all the NNDs for the paxillin (orange), talin (purple) and vinculin (yellow) data in FAs for different time points. (B,D,F) are the ΔNND_H plots for the subtraction histograms for simulated data from experimental at the three different seeding times (90 min, 3 h and 24 h).

We next proceeded with the analysis of the NND distributions of the nanoclusters localised on fAs. Our results showed that $\alpha_5\beta_1$ and paxillin maintain the pronounced troughs and peaks, at ~55 nm and ~100 nm, respectively, independent of time (Figure 4.11 A, B and Figure 4.12, A,B). Interestingly, and similar to FAs, the ΔNND_H-plots for $\alpha_v\beta_3$ become better defined and less noisy with spreading time, giving rise

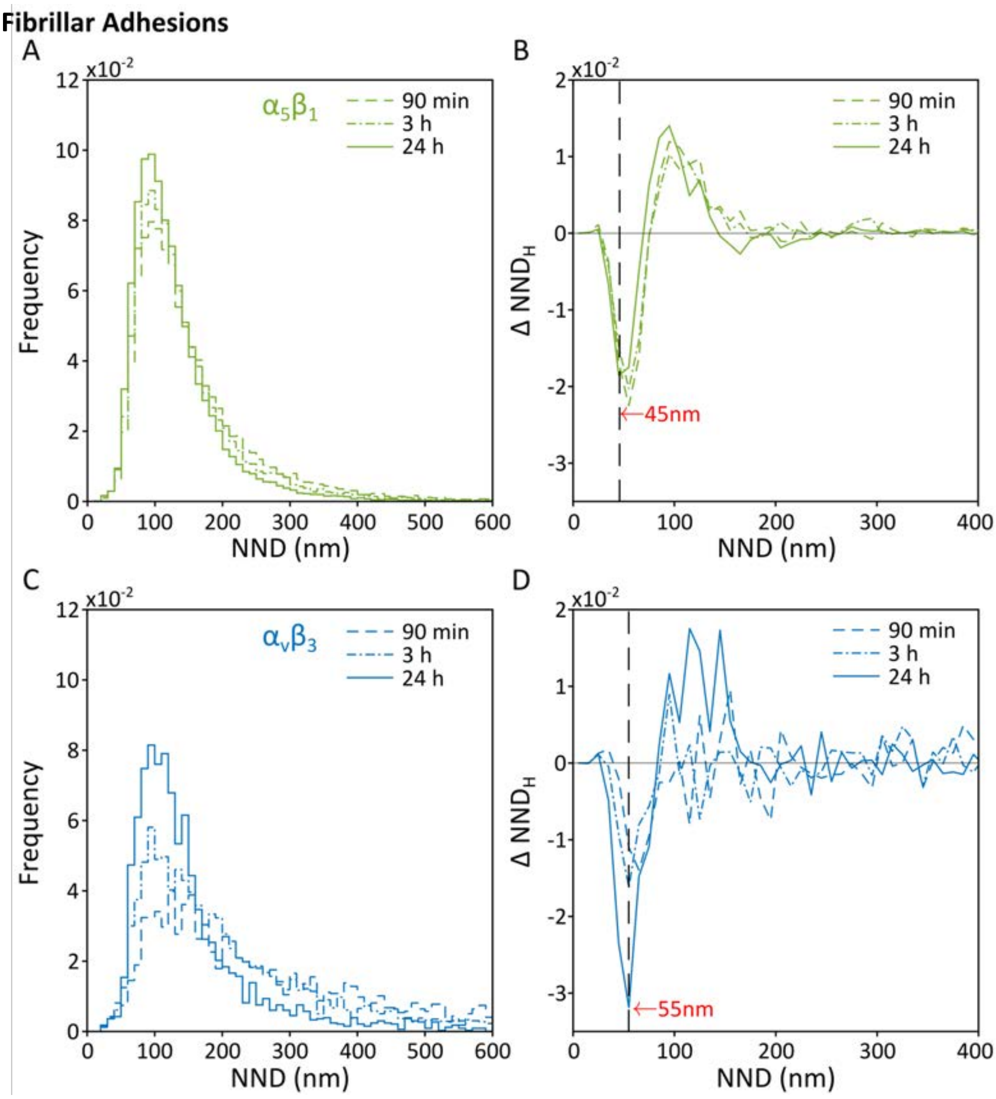

Figure 4.11 *The effect of seeding time on intercluster NND distributions for the two different integrins in fAs*

(A,C) show the histograms for the all the NNDs for the $\alpha_5\beta_1$ (green) and $\alpha_v\beta_3$ (blue) integrins in fA for different spreading times. (B,D) are the ΔNND_H plots at the three different spreading times (90 min, 3 h and 24 h).

to the appearance of a well-defined minima at NND ~55 nm (Figure 4.11 C,D), possibly indicating that the distribution of $\alpha_v\beta_3$ clusters becomes more ordered as cells spread for longer (>3 h) times. The other two adaptors, talin and vinculin, show ΔNND_H plots with a much less pronounced shape and large fluctuations (Figure 4.12 C–F), indicating that their spatial cluster distribution on fAs is much more random than the other proteins and also more random than their own distribution in FAs.

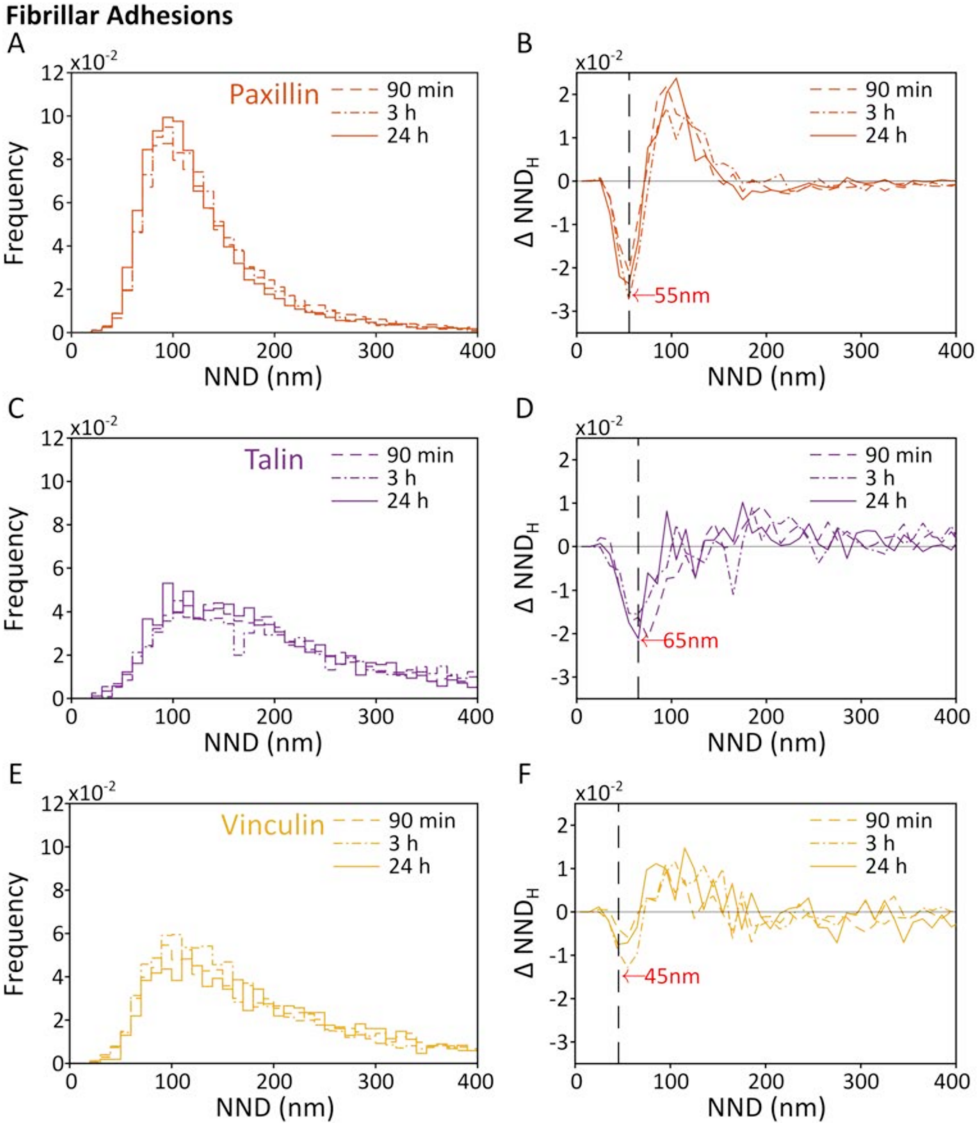

Figure 4.12 *The effect of seeding time on intercluster NND distributions for adaptor proteins in fA*

(A,C,E) show the histograms for the all the NNDs for the paxillin (orange), talin (purple) and vinculin (yellow) data in fAs for different spreading times. (B,D,F) correspond to the ΔNND_H-plots for the three different spreading times (90 min, 3 h and 24 h).

Intriguingly, despite these facts, the negative trough is still present, although less pronounced (Figure 4.12 D,F). Therefore, our results indicate an inherent spatial control of integrin nanoclusters and their adaptor proteins enforcing a preferred minimum lateral spacing between nanoclusters of the same protein.

4.3.6 The progressive lateral ordering of $\alpha_v\beta_3$ integrin nanoclusters with spreading times correlates with increased FA stabilisation

While $\alpha_5\beta_1$integrin nanoclusters establish a lateral spacing at early spreading times, in the case of $\alpha_v\beta_3$ integrin nanoclusters, we found that their lateral distribution is rather random at earlier times and progressively organises reaching a well-defined lateral spacing at 24 h of spreading time. These results suggest once more that $\alpha_5\beta_1$ and $\alpha_v\beta_3$ might be playing different roles during the process of cell adhesion and spreading. Since it has been suggested that $\alpha_v\beta_3$ is mainly responsible for maintaining and stabilising FAs (Roca-Cusachs et al., 2009; Schaufler et al., 2016; Bharadwaj et al., 2017), we hypothesised that the increased lateral ordering of $\alpha_v\beta_3$ along time could contribute to stronger stabilisation of FAs. To address this hypothesis, we determined the fraction of mature FAs as function of cell spreading times (Figure 4.13). Indeed, and as expected, the number of mature FAs per unit area at 24 h is significantly larger than at shorter spreading times, albeit their sizes remain similar.

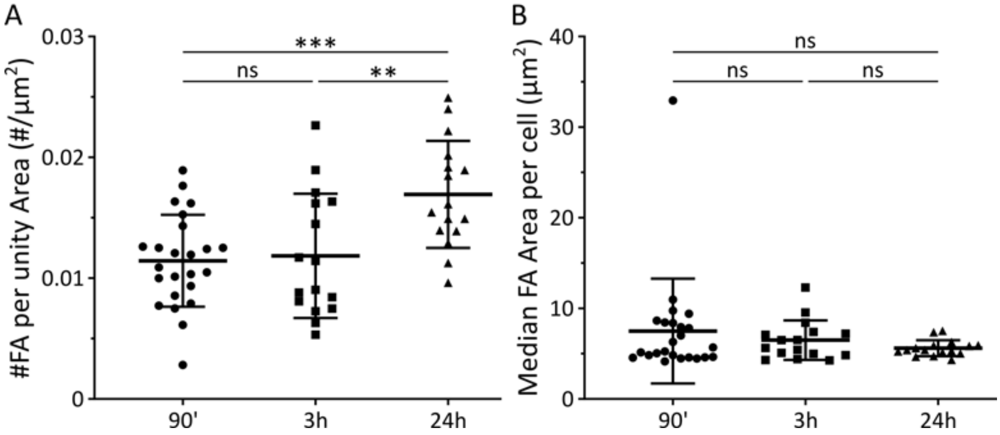

Figure 4.13 *Evaluation of FAs over time*

These plots were generated using paxillin masks from $\alpha_5\beta_1$ and $\alpha_v\beta_3$ experiments and considering areas > 3 µm² to be FAs (Thievessen et al., 2013). (A) shows the number of FAs per unit area per cell, for all three time points. (B) shows the area of FAs over time where each point on the graph is the median FA area per cell. The bars and whiskers show the mean of the distribution over all cells ± the standard deviation. Details of the statistical analysis are described in the methods section along with the details of the statistical tests carried out. One-way ANOVA; ns, $p>0.05$; *, $p<0.05$; **, $p<0.01$; ***, $p<0.001$.

Together with the fold-increase of $\alpha_v\beta_3$ expression (see Chapter 3), its increased lateral ordering in adhesion complexes and increased fraction of FAs as function of cell spreading time, our results fully support the notion that $\alpha_v\beta_3$ is preferentially involved in FA strengthening.

4.4 Discussion

In this chapter, we studied in detail how adhesion protein nanoclusters are spatially organised in focal and fibrillar adhesions. In particular, we examined the distribution of nanoclusters of the same protein within adhesions, aiming at understanding their mesoscopic nanocluster organisation. We first carried out our analyses on fully spread cells at 24 h after seeding, after which we follow on by comparing the data over a time course including shorter spreading times of 90 min and 3 h.

Taken together, our results reveal the existence of a minimum lateral separation between nanoclusters. The negative troughs in all the ΔNND_H-plots of inter-cluster NNDs are indicative of distances that occur less frequently than predicted by simulations of random organisation and could be interpreted to be exclusion zones. This lateral spacing was found at a distance comparable to that of the median diameter of a cluster, where the median diameter was ~43–50 nm, while the negative troughs ranged from 45–65 nm. Our initial understanding was that this finding was obvious and came about due to the NND being measured from centre-to-centre of clusters, therefore, the minimum distance would be the sum of the radii of two clusters, otherwise the clusters would overlap and consequently be considered as a single cluster. However, this should also have been the case for the random data and consequently the ΔNND_H-plots would fluctuate around zero. Therefore, our data suggest the existence of an active mechanism driving the separation of nanoclusters at very short lengths scales (~50 nm). Furthermore, the observation that the maxima of the ΔNND_H plots occur at NNDs within 200 nm raises interesting questions related to the origin of this preferred intercluster separation.

Earlier work showed that integrins are able to sense the lateral spacing of their ligands with the existence of a ligand spacing threshold between 50–70 nm above which cells fail to spread and to form stable adhesions (Arnold et al., 2004; Cavalcanti-Adam et al., 2007; Huang et al., 2009b; Schvartzman et al., 2011). Remarkably, this nanometric ligand spacing is of similar size as the separation distance we have determined by directly visualising the nanoscale organisation of integrin nanoclusters and their adaptors inside adhesion complexes. Thus, our results indicate that the ligand threshold, inferred via cell spreading and adhesion measurements, in fact corresponds to an inherent nanometre scale interspacing of integrin nanoclusters on the cell membrane. Indeed, it has been already suggested that the local density of individual integrin receptors plays an essential role in controlling the dynamics and fate of the adhesive response (Cavalcanti-Adam et al., 2007).

The relevance of this critical ligand spacing has been also investigated by comparing the kinetics of cell spreading on homogenously-coated ligand surfaces and those on nanopatterns separated at different distances (Cavalcanti-Adam et al., 2007). The authors observed no difference in terms of cell spreading area, spreading time and FA turnover and composition as function of seeding time, when comparing homogenous ligand surfaces to 58 nm nanopatterned surfaces. Yet, the average density of RGD molecules on the homogeneous surface has been estimated to be nearly two orders of magnitude larger than on the nanopatterned surfaces (Cavalcanti-Adam et al., 2007) . Based on our findings, we rationalise these observations by the fact that integrin nanoclusters are inherently regulated by the cell with a minimum lateral segregation of ∼55 nm, and thus, a ligand spacing <55 nm would result in a ligand density that would be redundant and not used by the cell to further increase its spreading and/or adhesion. For larger ligand separations above 100 nm, cell spreading and FA turnover are highly compromised (Cavalcanti-Adam et al., 2007). We speculate that the reasons for it might be related not only to the reduced ligand density, leaving an increasing number of integrins unengaged, but also due to the fact that integrins organise in nanoclusters and the larger ligand separations would prevent full nanoclusters from engaging with their ligands. Integrin nanoclustering would also contribute to overcome the single molecule ligand spacing strategy used in these experiments (Arnold et al., 2004; Cavalcanti-Adam et al., 2006, 2007; Huang et al., 2009b; Schvartzman et al., 2011), i.e., single ligands spaced at 50 nm could rapidly re-bind to integrins provided that the latter are sufficiently close to each other, i.e., organised as nanoclusters.

The mechanisms responsible for the spatial sensing of ligands have remained, until now, poorly understood. Our work now shows that this “molecular ruler” is set by the underlying nanoscale distribution of integrin nanoclusters on the cell membrane. Yet, what controls this nanoscale distribution? There are different possible explanations for this, the most obvious being that other proteins act to limit cluster size and to control the separation between nanoclusters. In fact, it has been suggested that a cross-linking adaptor protein of a size comparable to the lateral spacing we have measured might connect integrins to the actin cytoskeleton, acting as a molecular ruler that senses ligand spacing directly (Huang et al., 2009b; Schvartzman et al., 2011). Although this adaptor protein has not yet been identified (being talin the prime suspect), we believe that essentially any adaptor protein nanocluster, in particular paxillin, might serve to physically define integrin lateral spacing (see also Chapter 5).

More recently, the group of Roca-Cusachs has proposed a different physical mechanism based on force loading to regulate the lateral spacing of integrins in cells (Oria et al., 2017). Following their experimental observations on ligand substrates with different rigidities, the authors proposed an expanded molecular clutch model that couples ligand spacing to the elasticity of the substrate. In this way, forces applied to one ligand would also deform its neighbours, incorporating the mechanical coupling between ligands into the model. Forces loading on the molecular clutch (formed by integrins and their adaptors) arise from myosin contractility pulling actin towards the cell centre and being counterbalanced by the elastic resistance of the ligand substrate to deformation. For a given substrate stiffness, the larger the spacing between ligands, the higher the loading force on integrins, such that above a given threshold, the clutches are not able to withstand the force and the adhesion collapses. Thus, according to this model, there is a regulation of molecular force loading that integrins are able to withstand in balance with the forces exerted by the actomyosin machinery. This balance makes that the optimal lateral spacing of integrins in rigid substrates is around 55 nm. Although our data do not currently allow us to favour one mechanism over the other, it would be interesting to perform super-resolution experiments on substrates of different rigidity and/or altering cell contractility to assess whether lateral spacing of integrin nanoclusters is indeed affected.

According to this molecular clutch model, why would $\alpha_v\beta_3$ integrins reach this optimal length scale slower than $\alpha_5\beta_1$ integrins? One possibility is that the engagement with the actomyosin machinery, and thus cell force generation, is lower at earlier seeding times and mainly supported by $\alpha_5\beta_1$ integrins. Indeed, at early seeding times during cell spreading there is a larger number of nascent or intermediate adhesions as they are forming the cell membrane, so that spreading and actin engagement, in the lamellipodium, region is more dynamic (Zimerman et al., 2004; Alexandrova et al., 2008). As time proceeds, cell force generation becomes larger so that $\alpha_5\beta_1$ alone is not able to compensate for, requiring $\alpha_v\beta_3$ integrins to come into play and then re-arranging themselves into this optimal lateral spacing to maintain the force balance.

In summary, the results shown in Chapter 3 and 4 underscore the importance of lateral nanoscale organisation of integrins and their adaptors inside adhesions regulating the activity and function of both integrins in the process of cell adhesion and spreading. First, integrins and their adaptors are inherently nanoclustered maximising rapid re-binding of integrins to fibronectin. Second, the lateral organisation of these nanoclusters is well defined by a lateral segregation of at least

55 nm. In the case of $\alpha_5\beta_1$ integrins and adaptors, this lateral spacing is already defined at 90 min seeding times, while in the case of $\alpha_v\beta_3$ integrins, the lateral ordering occurs progressively. These results are consistent with a role of $\alpha_5\beta_1$ supporting early and stable adhesion and with $\alpha_v\beta_3$ becoming more relevant at later stages, and involved in the re-enforcement of FAs by possibly establishing links with the actin cytoskeleton. The re-enforcement of FAs over time is also consistent with our results showing a larger percentage of FAs at 24 h, where also the fold increase on $\alpha_v\beta_3$ nanocluster density as compared to $\alpha_5\beta_1$ is more than a factor of two larger.

It is interesting to mention that a recent report from the Spatz group also identified the importance of lateral spacing of $\alpha_5\beta_1$ integrins in collective 2D cell migration (Di Russo et al., 2021). In particular, they found that the collective movement of keratinocytes (faster focal adhesion dynamics, better keratinocyte coordination) improves at an optimal $\alpha_5\beta_1$ integrin nanospacing of 50 nm, and being independent of substrate stiffness. The authors reasoned that this integrin spacing is optimal not only for force generation but also for intercellular force transmission mediated by E-cadherin. Thus, nanoscale integrin spacing might not only be present and important for adhesion and migration on isolated cells, but also relevant for collective cell migration and hence, efficient tissue regeneration (Di Russo et al., 2021).

In general, the results of this chapter provide us with interesting new insights into the distribution and organisation of key adhesion complex proteins while also delivering new and exciting questions to approach and answer in the future.

Chapter 5

Lateral distribution of adhesion protein nanohubs at the cell membrane

In the previous chapters, we showed that the lateral organisation of integrins and their main adaptors inside adhesions is highly hierarchical, with the occurrence of nanoclustering for all the proteins investigated, and moreover, a distinct distribution of these nanoclusters inside adhesions which deviate from random. In this chapter, we aim at understanding the lateral organisation of integrin nanoclusters with respect to their different adaptors. For this, we used similar analytical tools as exploited in Chapter 4, but focussing on the lateral relationship between $\alpha_5\beta_1$ *and* $\alpha_v\beta_3$ *to their adaptors, paxillin, talin and vinculin. In the canonical model of integrin activation, protein adaptors are recruited to the sites of integrins, and thus, we were expecting to observe close proximity between integrins and their adaptors. Contrary to these expectations, we found that the distribution of clusters relative to clusters of another protein is close to random, in particular when we compare* $\alpha_5\beta_1$ *and* $\alpha_v\beta_3$ *to talin or vinculin. The only pair that exhibited a distinct variation from random was* $\alpha_5\beta_1$ *and paxillin in FAs and fAs. We explain these unexpected results by considering that only a small subpopulation of integrins is active at a given time point and thus engaged to their adaptor proteins. Capturing these interactions within the full distribution of proteins present in the adhesions is challenging and would require different imaging strategies as to the ones exploited in this research.*

5.1 Introduction

As mentioned in previous chapters, adhesion complexes are dense platforms formed by integrins and many other adhesion adaptors that allow cells to sense their extracellular milieu and to relay this information to the cell interior via the actin cytoskeleton. Although for many years it has been thought that components of adhesion complexes were homogeneously distributed within the membrane, recent literature in the field as well as our results shown in Chapter 3 and 4 demonstrate a much higher level of organisation at the nanoscale. Although we still lack a comprehensive picture of the nanoscale organisation of integrins and their adhesion partners, there exist some reports in the literature that indicate that these proteins segregate at the nanoscale, some of which we briefly review here. Work carried out in the last decade by the Waterman lab, exploited the super-resolution technique known as interferometric photoactivated localisation microscopy (iPALM) to study the axial distribution of adhesion proteins (integrins and their adaptors). This work revealed that these proteins are segregated into functional axial layers (Kanchanawong et al., 2010). Specifically, they described three main layers: the integrin signalling layer (0–50 nm away from the ECM – glass substrate in this case – in the axial direction), composed mainly of integrins and paxillin; the force transduction layer (40 nm separating integrins and actin), with talin and vinculin; and the actin regulatory layer (with a peak of 100 nm away from the ECM), consisting of proteins associated to the maintenance of actin stress fibres, see Figure 1.13 in the introductory chapter. This study provided an invaluable understanding of the organisation of the proteins in the axial direction above the basal cell membrane, but did not provide a map of how these proteins are laterally organised by, potentially, segregating at the nanoscale. The most recent and elucidating study on this topic investigated the clustering of $\alpha_5\beta_1$ integrin in FAs using the super-resolution techniques STED and STORM (Spiess et al., 2018). The authors revealed that active and inactive integrins coexist in FAs as segregated nanoclusters, with talin, kindlin, and vinculin partially colocalising with these integrin nanoclusters.

In the previous two chapters, we demonstrated that each of the adhesion proteins investigated at the nanoscale by means of super-resolution microscopy form nanoclusters. Moreover, these nanoclusters are remarkably similar in terms of sizes and number of molecules, regardless of their partitioning inside or outside adhesions, and independent of cell seeding time. Interestingly, we also observed that all the protein nanoclusters investigated are physically segregated from each other, as opposed to the classical view that FAs are homogeneous patches of fully-colocalising adhesion complex proteins (Humphries et al., 2007). By using dedicated analysis algorithms together with simulations of random organisation we further discovered that integrins and their adaptor proteins maintain a lateral nanoscale segregation between themselves at around 55 nm with an enrichment at ∼100 nm. The notion of a critical lateral spacing between integrins to support cell spreading and adhesion had previously been put forward (Cavalcanti-Adam et al., 2007; Oria et al., 2017) however, to our knowledge, direct observation of this characteristic spacing at the single cell level had never been done before. Moreover, we showed in Chapter 4 that this critical lateral spacing is also followed by all the protein adaptors investigated, i.e., paxillin, talin and vinculin, suggesting that once integrins establish this spacing, the engagement with their adaptors follow a similar lateral distribution.

In this chapter, we focused on the lateral organisation of integrin nanoclusters with respect to their adaptors. We studied how this distance distribution depended on the cell membrane regions (FAs vs fAs), and how it changed over cell spreading time (90 min, 3 h, and 24 h). We further compared our experimental data to simulated random data sets to ascertain if the distributions and changes with time are different as to what we would expect from randomly distributed protein clusters. We find that within the scope of our imaging and analytical tools, the distribution of the clusters relative to clusters of another protein is similar to random.

5.2 Materials and methods

5.2.2 Sample preparation and imaging

Samples were prepared by seeding HFF-1 cells on FN-coated 8-well plates. The cells were allowed to spread for different times (90 min, 3 h, or 24 h), after which they were fixed and then immunolabelled using primary and secondary antibodies as described in detail in Chapter 2.

5.2.3 Image acquisition

All the STORM images analysed in this chapter were taken on a Nikon Eclipse Ti system using a 100x oil objective with NA of 1.49, a 256x256 pixel ROI and a pixel size of 160 nm using TIRF illumination. The system has lasers with wavelengths of 405 nm, 560 nm and 647 nm. For a full description of the image acquisition, see Section 2.4 Chapter 2.

5.2.4 Image reconstruction

Dual-colour STORM image reconstruction was done using Insight3, provided by Bo Huang (UCSF, initially developed in Xiaowei Zhuang's Lab). The analysis was run over the entire data sets but recording only those localisations detected in the second frame of the five-frame cycle, that is the first of the four reporter frames, the localisations can be represented by a cross marking their centres or rendered with a Gaussian profile convoluted with the point. For more detailed description, see Chapter 2 section 2.5.

5.2.5 Image analysis

All the analysis carried out in this chapter was completed using scripts written and developed in house using MATLAB 2019b. We also made use of binary masks defined by manually selecting the adhesions from the dual-colour data sets. These data sets are imported using a Fiji plugin, developed by the group of Melike Lakadamyali during their time at ICFO. The data are analysed using the DBSCAN algorithm (eps=20 nm and N_{min} =3) to detect clusters of proteins. This algorithm then provides the CoM of each cluster (along with other properties as described in Chapters 2 and 3).

Nearest neighbour distances (NND) computation

To establish how the integrin nanoclusters are distributed relative to their partners, we used the MATLAB function *knnsearch* to compute the NND between the centres of mass of nanoclusters of different paired proteins, NND_{A-B} and NND_{B-A}. The distributions of NND_{A-B} provide a quantitative measure of the proximity between the nanoclusters of different proteins, which can be used as an indirect indication of possible protein-protein interactions.

Computational generation of random nanocluster distributions

To assess whether the NND distributions obtained from the experimental data correspond to a preferential type of organisation or to random, we further performed simulations by generating *in silico* NND histograms of randomly distributed nanoclusters inside the adhesion structures, both FAs and fAs. In order to proceed, we essentially needed two ingredients: *First,* to extract from the experimental data the exact number of nanoclusters per adhesion; *Second*, to distribute the same number of nanoclusters in a random fashion within the adhesions, while excluding their spatial overlapping. For detailed description on how the *in silico* histograms were generated see Chapter 2 section 2.6.5.

Fitting model for NND between clusters of different proteins

To extract meaningful information from distributions of NND between protein clusters there are a number of quantities one can use: the peak value position of the histogram, the mean, the median, and the full width at half maximum (FWHM), to name just a few. In order to extract the peak value position from the NND histogram between clusters of different proteins it was necessary to fit a smooth curve because the histograms of the binned experimental data do not normally show a well-defined peak due to the discrete nature of the data. The model we used builds upon the analytical distribution of NND for randomly localised points (Poisson point process), modified to account for different point densities in the different adhesions, which we show follow a normal distribution in Figure 5.1 B.

Let us now derive the mathematical function that describes such a distribution. We start by considering a finite flat two-dimensional region of arbitrary shape and area, A (Figure 5.1 A, blue ellipse), containing a finite number of protein clusters, N (Figure 5.1 A, red crosses, indicating the CoM of the clusters), resulting in a density of points per unit area, φ,

$$\varphi = \frac{N}{A}. \qquad (5.1)$$

We first develop the mathematical description of the distribution of NND between randomly localised points. For an arbitrary point j, the probability, p(r), that its closest point is located at a distance r is given by the probability that no other point is closer than r , multiplied by the probability that at least one other point is in the infinitesimal circular ring of radii [r, r+dr]:

$$p(r)dr = \left(1 - \int_0^r p(x)dx\right) \cdot \frac{(N-1)2\pi r dr}{A}. \qquad (5.2)$$

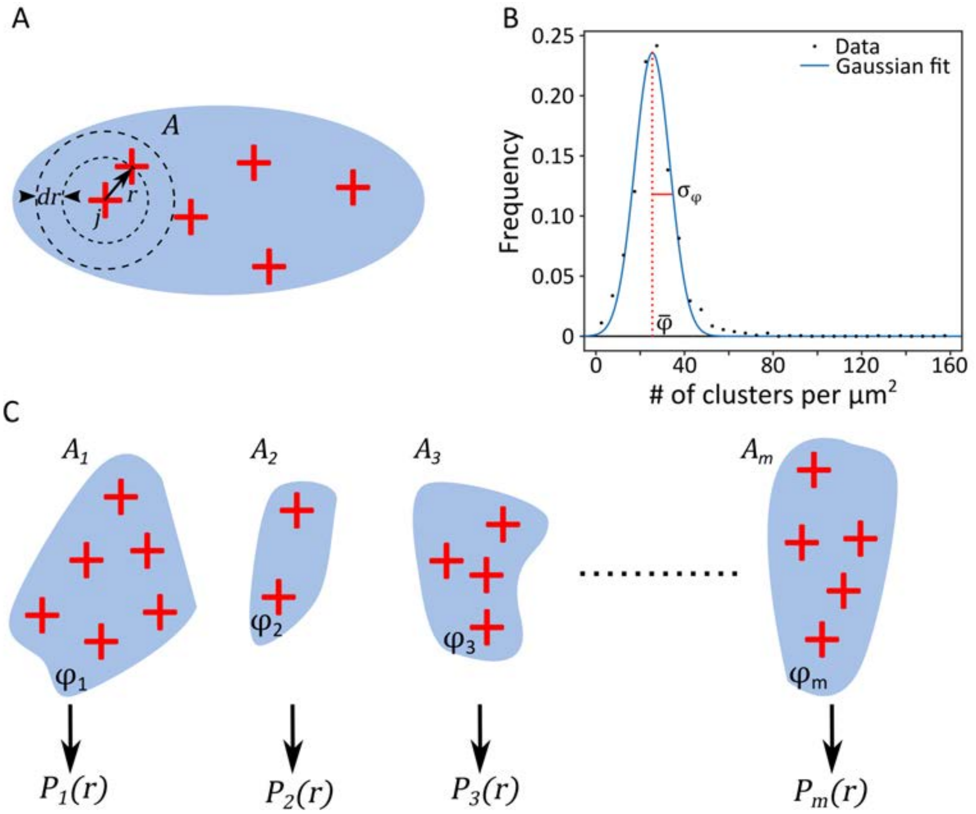

Figure 5.1 *Schematic of the mathematical model used to describe the distribution of NND between clusters of two different proteins*

Schematic representation of an adhesion with six clusters (whose CoM are represented by the red crosses). (B) Distribution of number density of clusters per unit area for a representative cell (black dots) and corresponding fit with a Gaussian (blue line), with mean ,$\bar{\varphi}$, and standard deviation, σ_φ, are marked. (C) Schematic representing a number of different areas (e.g., different FAs) with different density of clusters and therefore different probability distributions, $P_m(r)$.

This estimation does not include edge effects because we assume that the area is greater than the typical NND squared (i.e., A>>r2) and therefore that the number of clusters is much larger than 1, N>>1:

$$\frac{(N-1)2\pi r dr}{A} \approx \varphi 2\pi r dr \qquad : N \gg 1. \tag{5.3}$$

With this approximation, we can integrate Eq. (5.2) as

$$p(r) = 2\pi r\varphi\left(1 - \int_0^r p(x)dx\right). \tag{5.4}$$

Taking the derivate of both sides of this equation with respect to r leads to

$$\frac{dp(r)}{dr} = 2\pi\varphi\left(1 - \int_0^r p(x)dx\right) + 2\pi r\varphi\left(-\frac{d}{dr}\int_0^r p(x)dx\right). \tag{5.5}$$

Then, using the fact that Eq. (5.4) can be rewritten as

$$\left(1 - \int_0^r p(x)dx\right) = \frac{p(r)}{2\pi r\varphi}\,, \tag{5.6}$$

and applying the Leibniz integral rule,

$$\left(-\frac{d}{dr}\int_0^r p(x)dx\right) = -p(r)\,, \tag{5.7}$$

we can express Eq. (5.5) as

$$\frac{dp(r)}{dr} = \frac{p(r)}{r} - 2\pi r\varphi p(r) = \left(\frac{1}{r} - 2\pi r\varphi\right)p(r). \tag{5.8}$$

After some algebra, we can find the analytical expression for p(r) as

$$\frac{dp(r)}{p(r)} = \left(\frac{1}{r} - 2\pi r\varphi\right)\mathrm{dr}\,, \tag{5.9}$$

$$\int \frac{dp(r)}{p(r)} = \int \left(\frac{1}{r} - 2\pi\varphi r\right)dr\,, \tag{5.10}$$

$$ln\, p(r) = ln\, r - \pi\varphi r^2 + ct\,, \tag{5.11}$$

$$p(r) = k \cdot re^{-\pi\varphi r^2}\,. \tag{5.12}$$

Using the normalisation condition, we can find the value of the integration constant, k, as

$$\int_0^\infty p(r)dr = 1 \Rightarrow k\int_0^\infty re^{-\pi\varphi r^2}dr = 1 \Rightarrow k\left(\frac{-1}{2\pi\varphi}\right)\, e^{-\pi\varphi r^2}\Big|_0^\infty = 1$$

$$\Rightarrow \frac{k}{2\pi\varphi} = 1 \Rightarrow k = 2\pi\varphi\,. \tag{5.13}$$

Altogether, the Poisson point process distribution of NND for randomly distributed points in a two-dimensional space is given by

$$p(r) = 2\pi\varphi \cdot r \cdot e^{-\pi\varphi r^2}. \tag{5.14}$$

We next expand on this distribution function by considering different regions with different point densities. This situation corresponds to our experimental conditions, where the density of protein clusters per unit area varies amongst adhesions (Figure 5.1 C). We assumed a normal distribution of densities amongst adhesions, which we showed is a reasonable approximation of the actual density distribution in our data (Figure 5.1 B). Hence, the point density φ follows a probability distribution w(φ) as

$$w(\varphi) \sim exp\left(-\frac{(\varphi-\overline{\varphi})^2}{2\,\sigma_\varphi^2}\right) : \varphi > 0, \tag{5.15}$$

Where $\overline{\varphi}$ and σ_φ are two fitting parameters describing the density distribution. Next, by convolving p(r) with $w(\varphi)$, and integrating over all possible values of $\varphi > 0$, we obtain the new modified NND probability, P(r, $\overline{\varphi}$,σ_φ), as

$$P(r,\bar{\varphi},\sigma_\varphi) \sim \int_0^\infty p(r)\cdot w(\varphi)d\varphi,$$

$$P(r,\bar{\varphi},\sigma_\varphi) =$$

$$C\cdot\int_0^\infty 2\pi\varphi\cdot r\cdot e^{-\pi\varphi r^2}\cdot exp\left(-\frac{(\varphi-\bar{\varphi})^2}{2\sigma_\varphi^2}\right)d\varphi\,. \tag{5.16}$$

Imposing normalisation:

$$\int_0^\infty P(r,\bar{\varphi},\sigma_\varphi)\,dr = 1 \Rightarrow \mathrm{C} = \frac{\sqrt{2/\pi}}{\sigma_\varphi\left(1+\mathrm{erf}\left(\frac{\bar{\varphi}}{\sqrt{2}\cdot\sigma_\varphi}\right)\right)}\ , \tag{5.17}$$

results in,

$$P(r,\bar{\varphi},\sigma_\varphi) = 2e^{-\frac{\bar{\varphi}^2}{2\sigma_\varphi^2}}\cdot r\,\frac{\mathrm{V(r)}}{1+erf\left(\frac{\bar{\varphi}}{\sqrt{2}\sigma_\varphi}\right)}, \tag{5.18}$$

where

$$V(r) = \left[\sqrt{2\pi}\sigma_\varphi - \pi\left(\pi\sigma_\varphi^2 r^2-\bar{\varphi}\right)\cdot\left(1-erf\left(\frac{\pi\sigma_\varphi^2 r^2-\bar{\varphi}}{\sqrt{2\pi}\sigma_\varphi}\right)\right)e^{\frac{\left(\bar{\varphi}-\pi\sigma_\varphi^2 r^2\right)^2}{2\sigma_\varphi^2}}\right], \tag{5.19}$$

and erf(x) is the error function:

$$\mathrm{erf(x)} = \frac{2}{\sqrt{\pi}}\int_0^x e^{-t^2}dt\ . \tag{5.20}$$

We finally obtain an analytical description of this probability distribution,

$$P(r,\bar{\varphi},\sigma_\varphi) =$$

$$\frac{2e^{-\frac{\bar{\varphi}^2}{2\sigma_\varphi^2}}\cdot r\left[\sqrt{2\pi}\sigma_\varphi-\pi\left(\pi\sigma_\varphi^2 r^2-\bar{\varphi}\right)\cdot\left(1-erf\left(\frac{\pi\sigma_\varphi^2 r^2-\bar{\varphi}}{\sqrt{2}\,\sigma_\varphi}\right)\right)\cdot e^{\frac{\left(\bar{\varphi}-\pi\sigma_\varphi^2 r^2\right)^2}{2\sigma_\varphi^2}}\right]}{1+erf\left(\frac{\bar{\varphi}}{\sqrt{2}\sigma_\varphi}\right)}. \tag{5.21}$$

With this nonlinear mathematical model for the distribution of clusters, we manually selected seed values such that by fitting using the Newton's method for nonlinear fitting (computed using Wolfram Mathematica 9) we achieve an r^2 of at least 0.95, if the fitting was possible. When fitting the simulated data, a high r^2 value (usually>0.99) was always achievable, as we generated 10x more data per condition to achieve a random simulation. However, occasionally due to the nature of some of the experimental data this was more challenging. Figure 5.2 shows a representative image of our fitting in the case of experimental and simulated data for the $\alpha_5\beta_1$-to-paxillin at 24 h condition.

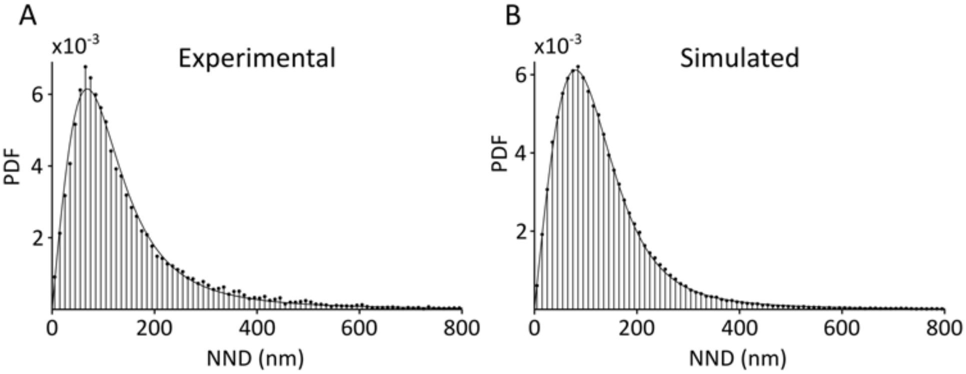

Figure 5.2 *Examples of experimental and simulated data fitted using the model*
(A,B) are representative histograms for experimental and simulated NND data between clusters of $\alpha_5\beta_1$ and paxillin. These histograms were fitted with a curve from the model described above. Bin width= 20 nm.

Data representation with GraphPad Prism

The median value per cell is calculated from the cluster analysis per cell. These values are represented using the box-and-whisker plots in GraphPad Prism, version 9.1.2, where the line shows the median over all cells, the box extends to the 1st and 3rd quartiles and the whiskers show the max to min range over the distribution of the cells for each protein. All box-and-whisker plots in this chapter will follow these limits.

Statistical analysis with GraphPad Prism

We performed paired t-tests between experimental and simulated data for each of the proteins in FAs and fAs. With a confidence level of 95%; ns, $p>0.05$;*, $p<0.05$; **, $p<0.01$; ***, $p<0.001$.

5.3 Results

5.3.2 Super-resolution microscopy reveals the lateral segregation between nanoclusters of different adhesion complex components

As already mentioned in Chapter 2, most of the super-resolution images collected in this thesis were performed in two colours, i.e., always labelling one of the integrins as reference with the second colour being either paxillin, talin or vinculin. Some representative dual-colour images are shown in Figure 3.1, Figure 5.3 and Figure 5.4. After visual inspection of the STORM images taken in HFF-1 cells that spread for 24 h, we noticed that integrin nanoclusters appear to be in close proximity to those of the adaptor proteins. However, despite this proximity between nanoclusters of different proteins, we rarely observed colocalisation events, meaning that the nanoclusters remain segregated from each other. To substantiate these observations with quantitative information, we started by reconstructing the dual-colour images using only the localisations found to form nanoclusters and identifying their centre-of-mass (CoM) positions (Figure 5.3 and Figure 5.4). These dual-colour images were taken in a pairwise manner such that they always included an integrin – either $\alpha_5\beta_1$ (Figure 5.3) or $\alpha_v\beta_3$ (Figure 5.4) – together with an adaptor protein – paxillin (Figure 5.3 A, Figure 5.4 A), talin (Figure 5.3 B, Figure 5.4 B), or vinculin (Figure 5.3 C, Figure 5.4 C). Observing on the scale of a reconstructed image of a whole cell, it is difficult to draw any conclusions about the nanoscale organisation of the protein clusters relative to each other. However, we can zoom in on these reconstructions and reveal individual clusters (insets (i) in Figure 5.3 and Figure 5.4) or zoom even further still to observe the localisations within these clusters (insets (ii) of Figure 5.3 and Figure 5.4). It is then at the level of nanoclusters that we observed with enhanced detail on how these pairs of proteins are distributed relative to each other.

Despite the high densities of proteins in adhesions, the overlap or colocalisation of clusters of two different proteins is rarely observed. We noticed that for the integrins $\alpha_5\beta_1$ and $\alpha_v\beta_3$ the nanoclusters seem to occur in pairs with talin or vinculin (see inset B(ii) and C(ii) of Figure 5.3 and Figure 5.4, where integrins are magenta and adaptors are in green) but with no clear overlap occurring. We also noticed that despite that high density of paxillin, the clusters appear to have very low colocalisation with either integrin (see inset A(ii) of Figure 5.3 and Figure 5.4) although the occurrence of clusters in close proximity appears to be high especially for $\alpha_5\beta_1$ near the edge of the adhesions (see inset A(ii) of Figure 5.3). With these intriguing observations noted, it became clear that we require extensive quantitative analysis in order to understand the details of how clusters of different proteins are distributed and interact with each other.

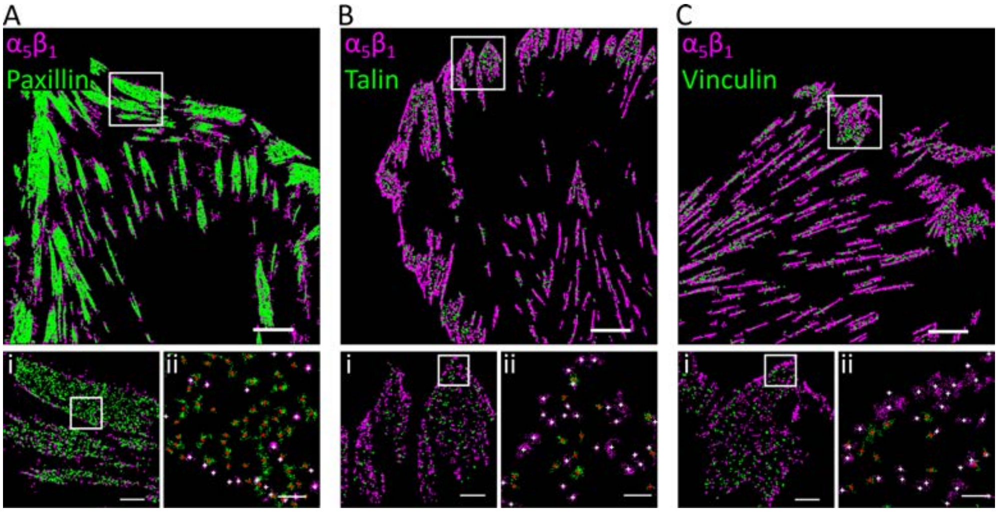

Figure 5.3 *Integrin $\alpha_5\beta_1$ and adaptor proteins nanocluster distribution in adhesion complexes on HFF-1 cells at 24 h of seeding*

The images show the individual localisations belonging to clusters of $\alpha_5\beta_1$ (in magenta) and the adaptor proteins paxillin (A), talin (B), or vinculin (C) (in green). Cluster detection on the STORM data was performed using the DBSCAN algorithm (final threshold of at least 10 localisations per cluster). Subpanels labelled as (i) show the zoomed-in regions corresponding to individual FAs (marked by a white square in the left panels). Subpanels labelled as (ii) show subsequent zoomed-in regions (of the regions marked by white squares in subpanels (i)), where the white and red crosses indicate the CoM of each $\alpha_5\beta_1$ and adaptor protein cluster, respectively. Scale bar = 5 µm (large ROIs), 1 µm (i), and 200 nm (ii).

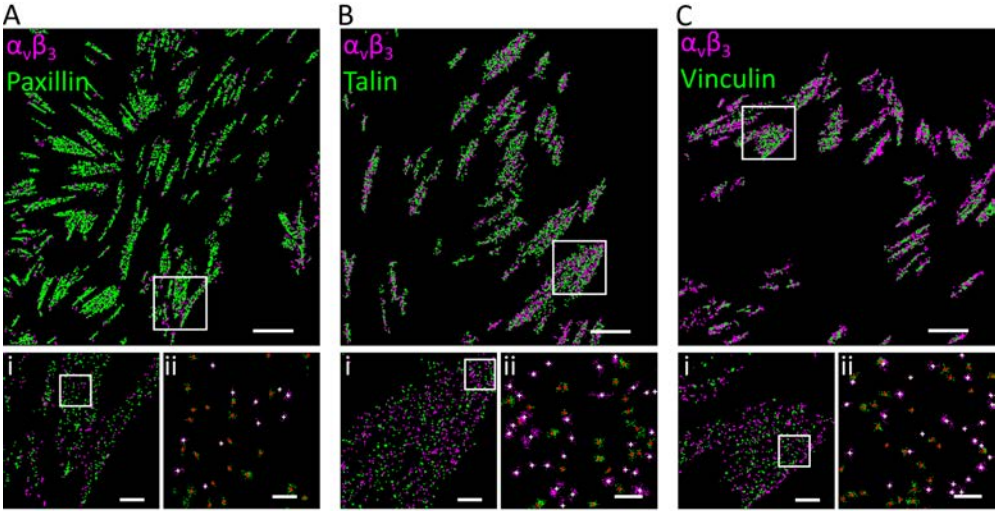

Figure 5.4 *Integrin $\alpha_v\beta_3$ and adaptor proteins nanocluster distribution in adhesion complexes on HFF-1 cells at 24 h of seeding*

The images show the individual localisations belonging to clusters of $\alpha_v\beta_3$ (in magenta) and the adaptor proteins paxillin (A), talin (B), or vinculin (C) (in green). Cluster detection on the STORM data was performed using the DBSCAN algorithm (final threshold of at least 10 localisations per cluster). Subpanels labelled as (i) show the zoomed-in regions corresponding to individual FAs (marked by a white square in the left panels). Subpanels labelled as (ii) show subsequent zoomed-in regions (of the regions marked by white squares in subpanels (i)), where the white and red crosses indicate the CoM of each $\alpha_v\beta_3$ and adaptor protein cluster, respectively. Scale bar = 5 µm (large ROIs), 1 µm (i), and 200 nm (ii).

5.3.3 Quantification of lateral distances between nanoclusters of different adhesion proteins in cells spreading for 24 h

We visually observed instances of nanoclusters of two different proteins being in close proximity to each other (Figure 5.3 and Figure 5.4). Motivated by these observations, we performed a rigorous quantitative analysis to report on the preferred distances between the clusters of the different adhesion protein pairs. As described in the Chapter 2, section 2.6.5, we computationally generated sets of data representing a random distribution of nanoclusters in the adhesions. This allowed us to relate the experimental distributions of nearest neighbour distances (NND) between the CoM of clusters of two different proteins (see red and white crosses in Figure 5.3 and Figure 5.4, inset (ii)), to the expected NND distributions from a random nanocluster distribution, as obtained in our simulated data sets. Importantly, it has to be noted that the NND between two different protein clusters is not symmetric, meaning that the distance from an integrin cluster to its nearest adaptor cluster is not necessarily the same as the distance from an adaptor cluster to its nearest integrin cluster. The reason for this disparity is essentially given by the fact that integrin nanoclusters and their adaptor nanoclusters have different densities. Taking all this into account, we studied the distributions of NNDs in the case of each protein, for the different regions of the cell membrane (FAs, fAs, and outside adhesions). We first focussed on HFF-1 cells seeded on FN that were allowed to spread for 24 h.

We computed the full distributions for the NNDs from the CoM of protein A to protein B (where protein A is $\alpha_5\beta_1$ or $\alpha_v\beta_3$, and protein B is paxillin, talin, or vinculin), and compared them to the random distributions for clusters in FAs (Figure 5.5), fAs (Figure 5.6), or outside adhesions (Figure 5.7). We observed that the experimental and the simulated random NND distributions have very similar shapes for clusters inside adhesions (Figure 5.5 and Figure 5.6). Intriguingly, when we examined the NND distributions for clusters outside of adhesions, the experimental distribution showed a shift to smaller distances as compared to the simulated random distributions for all instances except vinculin to integrins (Figure 5.7). This initial analysis suggests that, while the clusters in the high-density adhesion complexes (both FAs and fAs) seem to be randomly distributed with respect to their partners, the clusters found outside the adhesions are in closer proximity to their partner clusters compared to what would be expected if they were randomly distributed.

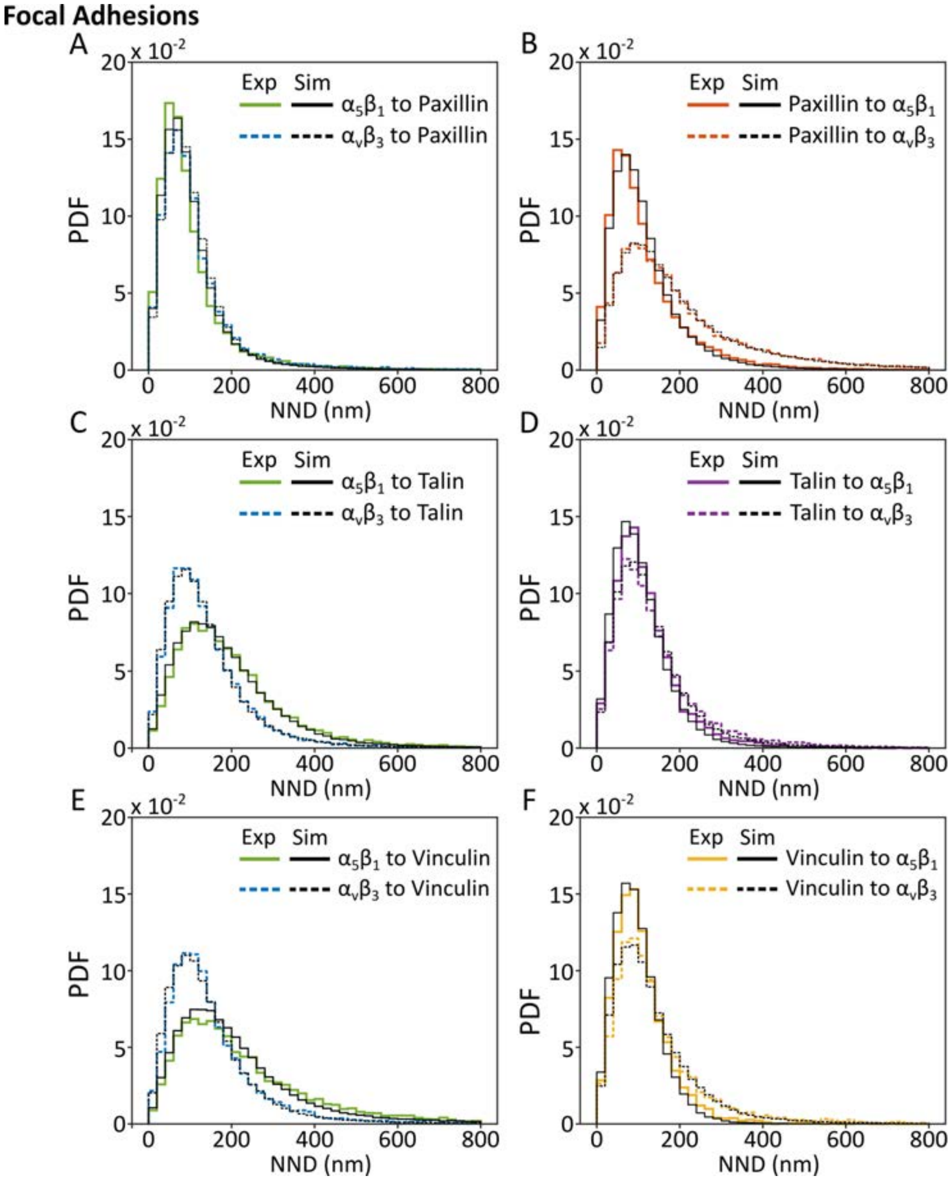

Figure 5.5 *Distribution of NNDs between integrins and adaptor protein clusters in FAs at 24 h*
Each histogram consists of the NNDs between clusters of the different proteins over all cells (see Table 2.7 for $\alpha_5\beta_1$ data and Table 2.8 for $\alpha_v\beta_3$ data). Left panels (A,C,E) show the experimental (Exp) NND distributions for each integrin ($\alpha_5\beta_1$, solid green lines; $\alpha_v\beta_3$, dashed blue lines) to its adaptor (paxillin, A; talin, C; vinculin, E). The corresponding simulated (Sim) random distributions are shown in black (solid and dashed lines for the random simulations of $\alpha_5\beta_1$ and $\alpha_v\beta_3$, respectively). The right panels (B,D,F) show the NND distributions for each adaptor (paxillin, B; talin, D; vinculin, F) to clusters of one of the two integrins. Continuous and dashed lines show distributions from adaptors to $\alpha_5\beta_1$ and $\alpha_v\beta_3$, respectively. Orange, purple and yellow denote experimental data for the adaptors, paxillin, talin and vinculin, respectively, and black corresponds to the simulated data for each panel. The simulated data sets have ten times as many data points as the experimental ones. The bin width is 20 nm.

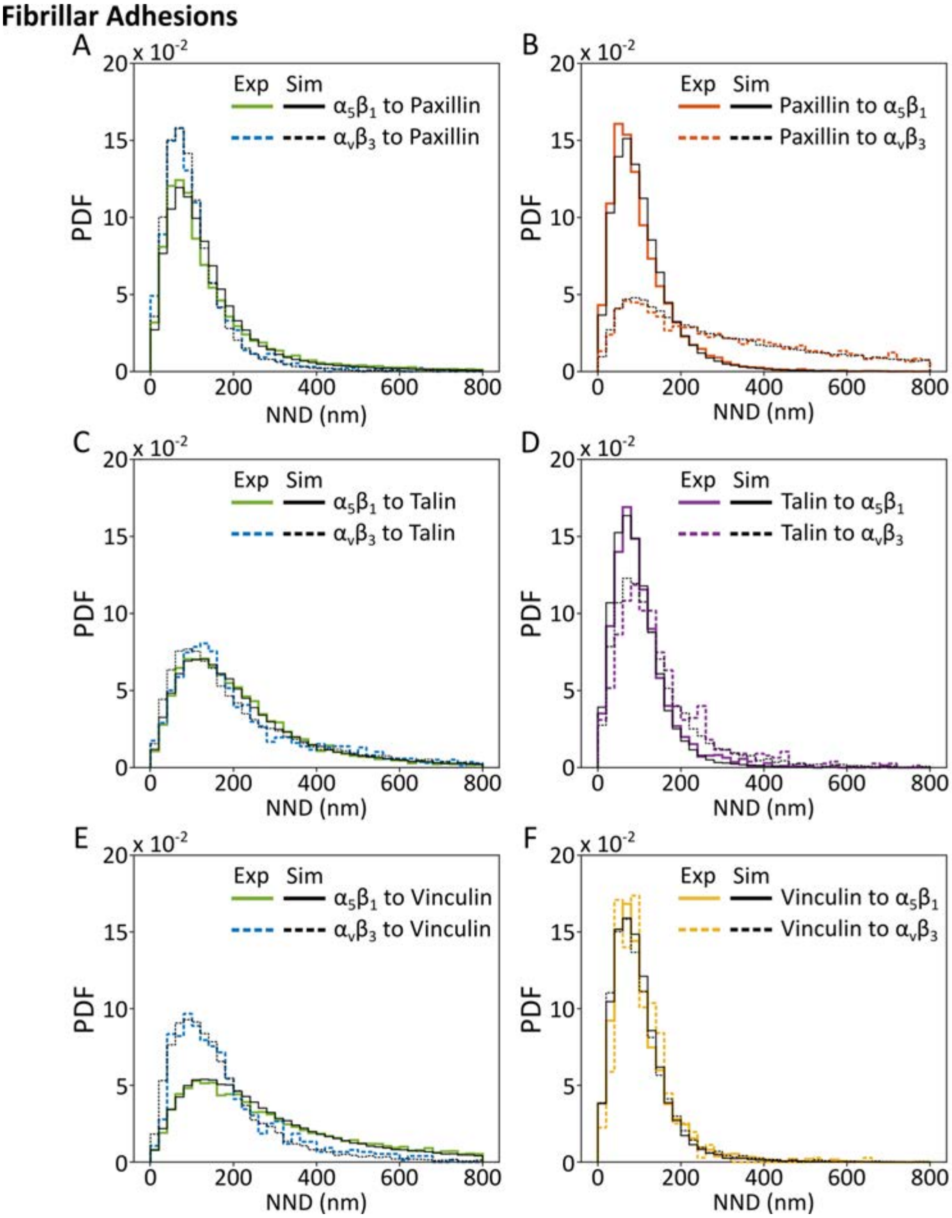

***Figure 5.6** Distribution of NNDs between integrins and adaptor proteins in fAs at 24 h*

Each histogram consists of the NNDs between clusters of the different proteins over all cells (see Table 2.7 for $\alpha_5\beta_1$ data and Table 2.8 for $\alpha_v\beta_3$ data) and compared to the NND values obtained from simulations of random organisation. The explanation of the colours and lines used are similar to the previous figure (see also the legends on the corresponding panels).

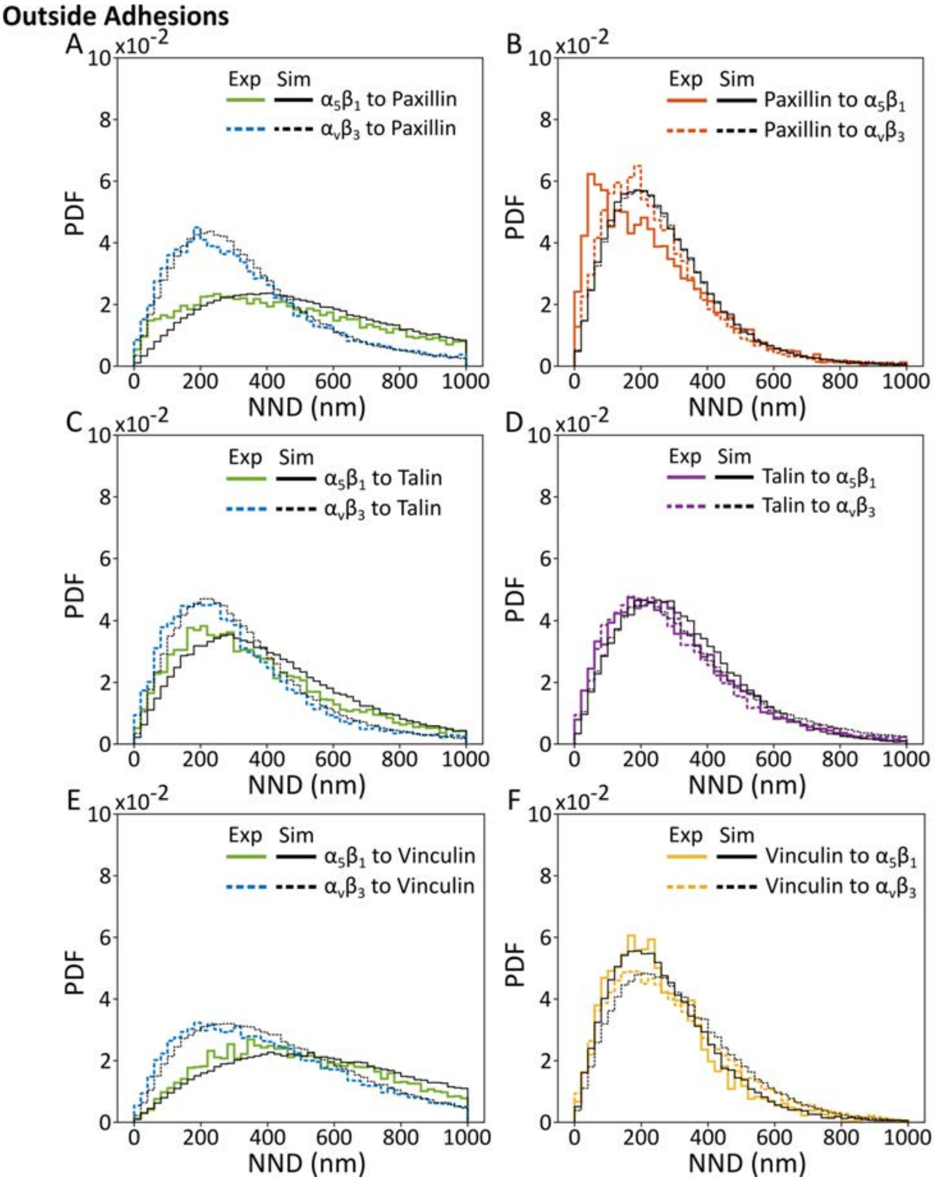

Figure 5.7 Distribution of NNDs between integrins and adaptor proteins outside adhesions at 24 h

Each histogram consists of the NNDs between clusters of the different proteins over all cells (see Table 2.7 for $\alpha_5\beta_1$ data and Table 2.8 for $\alpha_v\beta_3$ data) and compared to the NND values obtained from simulations of random organisation. The explanation of the colours and lines used are similar to Figure 5.5 (see also the legends on the corresponding panels).

These data hint towards the intriguing possibility of a direct or indirect interaction between integrin and adaptor protein clusters of paxillin and talin outside adhesions, which could serve to bring those protein clusters together to form the so-called nascent adhesions, which act as seeding points for adhesion complex formation.

In order to gain better understanding of the relative organisation between these protein pairs, and to assess whether their distributions are different from random, we implemented a fitting model to describe the NND distributions per cell (see methods section 5.2.5 for details). With this fitting model we can obtain numerical estimations for different distribution descriptors, such as the peak NND value per cell, for both the experimental and the simulated random distributions. From these values, we calculated the relative difference between the experimental peak NND, $\mathrm{PeakNND_{exp}}$, and the random peak NND, $\mathrm{PeakNND_{sim}}$, which we named $\delta\mathrm{NND_{peak}}$,

$$\delta NND_{peak} = \frac{PeakNND_{exp} - PeakNND_{sim}}{PeakNND_{sim}}\,. \tag{5.22}$$

This value indicates how the peaks of the experimental NND distributions per cell vary from random, with negative values indicating that the peak of the experimental data is at a shorter distance than the simulated one, and positive values representing a separation between clusters that cannot be accounted for by a random distribution of clusters. Interestingly, the mean values of $\delta\mathrm{NND_{peak}}$ for $\alpha_5\beta_1$ to paxillin and vice versa (Figure 5.8) resulted negative in all regions (FAs, fAs and outside adhesions), implying that the most common distance between $\alpha_5\beta_1$ and paxillin clusters is shorter than if the two proteins were distributed randomly, regardless of the region of the cell membrane. In contrast, the mean values of $\delta\mathrm{NND_{peak}}$ for $\alpha_v\beta_3$ to paxillin and vice versa were close to zero in FAs and fAs, indicating no preferred organisation between them. In the case of talin with respect to both integrins, the mean $\delta\mathrm{NND_{peak}}$ resulted close to zero on FAs, but positive in the case of fAs, suggesting that on these types of adhesions, integrins and talin are actively separated from each other. Finally, in the case of vinculin and integrins, no preferential organisation was found both of FAs and fAs. Strikingly, for all the protein combinations studied, the mean $\delta\mathrm{NND_{peak}}$ resulted negative outside adhesions.

As discussed during the analysis of the NND between clusters of the same protein (Chapter 4), summarising a full set of data by a single value does not provide a complete picture for how the protein clusters are spatially organised. Therefore, we also generated $\Delta\mathrm{NND_H}$-plots where we subtracted the random simulated NND distribution from the experimental data NND distribution, to highlight any subtle differences between the two distributions. This analysis was done for the clusters specifically localised in each of the three regions the cell membrane (FAs, Figure 5.9; fAs, Figure 5.10; and outside adhesions, Figure 5.11). Although these plots show the detailed differences per bin of the histogram, they reveal a similar trend as the variation of the peak NND (Figure 5.8). Interestingly, the trend of paxillin being closer to $\alpha_5\beta_1$ and vice versa is maintained in the ΔNND_H plots, with a maximum difference at 50 nm for both paxillin to $\alpha_5\beta_1$ and $\alpha_5\beta_1$ to paxillin and in all three regions. However, this preferred distance is not observed for the $\alpha_v\beta_3$ to paxillin plots in FAs or fAs. In the case of the clusters outside adhesions, there appears to be a positive peak at ∼70 nm for $\alpha_v\beta_3$ to paxillin (Figure 5.11 A) and a peak at ∼110 nm for paxillin to $\alpha_v\beta_3$ (Figure 5.11 B). Furthermore, the ΔNND_H-plots for talin and vinculin with respect to either integrin maintained the predominantly random trend observed when we considered only the peak NND in FAs and fAs (Figure 5.8). Additionally, the analysis of clusters outside of the adhesions shows a slight positive trend for distances less than 200 nm for talin data (Figure 5.11 C, D), and it is reduced and noisier when we consider vinculin (Figure 5.11 E, F).

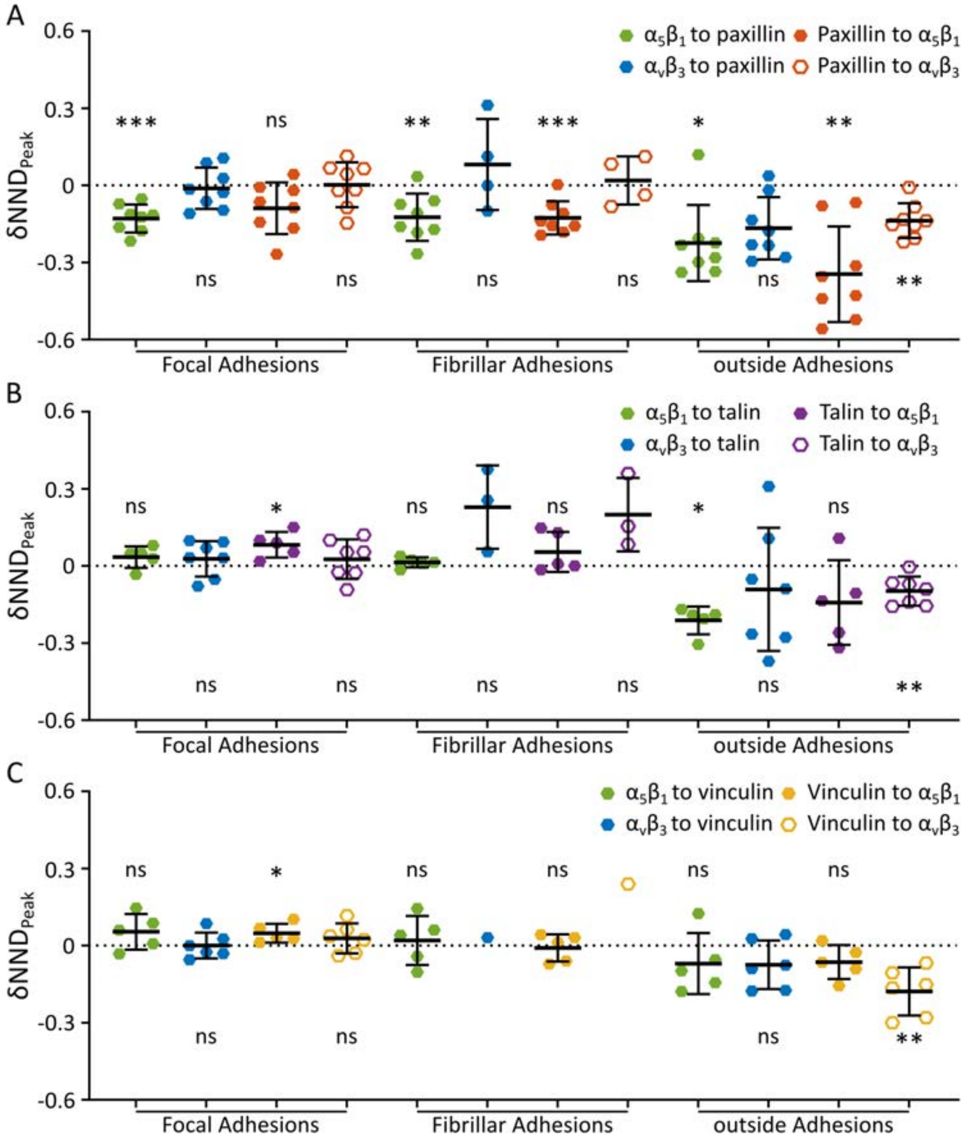

Figure 5.8 *Relative difference between peak values for experimental and simulated data (δNND_{peak}) per cell imaged at 24 h*

Each point on the graphs represents the relative difference between the experimental and simulated peak NND values per cell, for distances from integrin nanoclusters to paxillin (A), talin (B), or vinculin (C) and vice versa. Each graph has data for FA, fAs and outside adhesions. The bar marks the mean and the whiskers show the standard deviation over the cells. The single dots on panel C correspond to a single cell, because of the six cells imaged at 24 h for $\alpha_v\beta_3$ and vinculin only one cell had fibrillar adhesions.

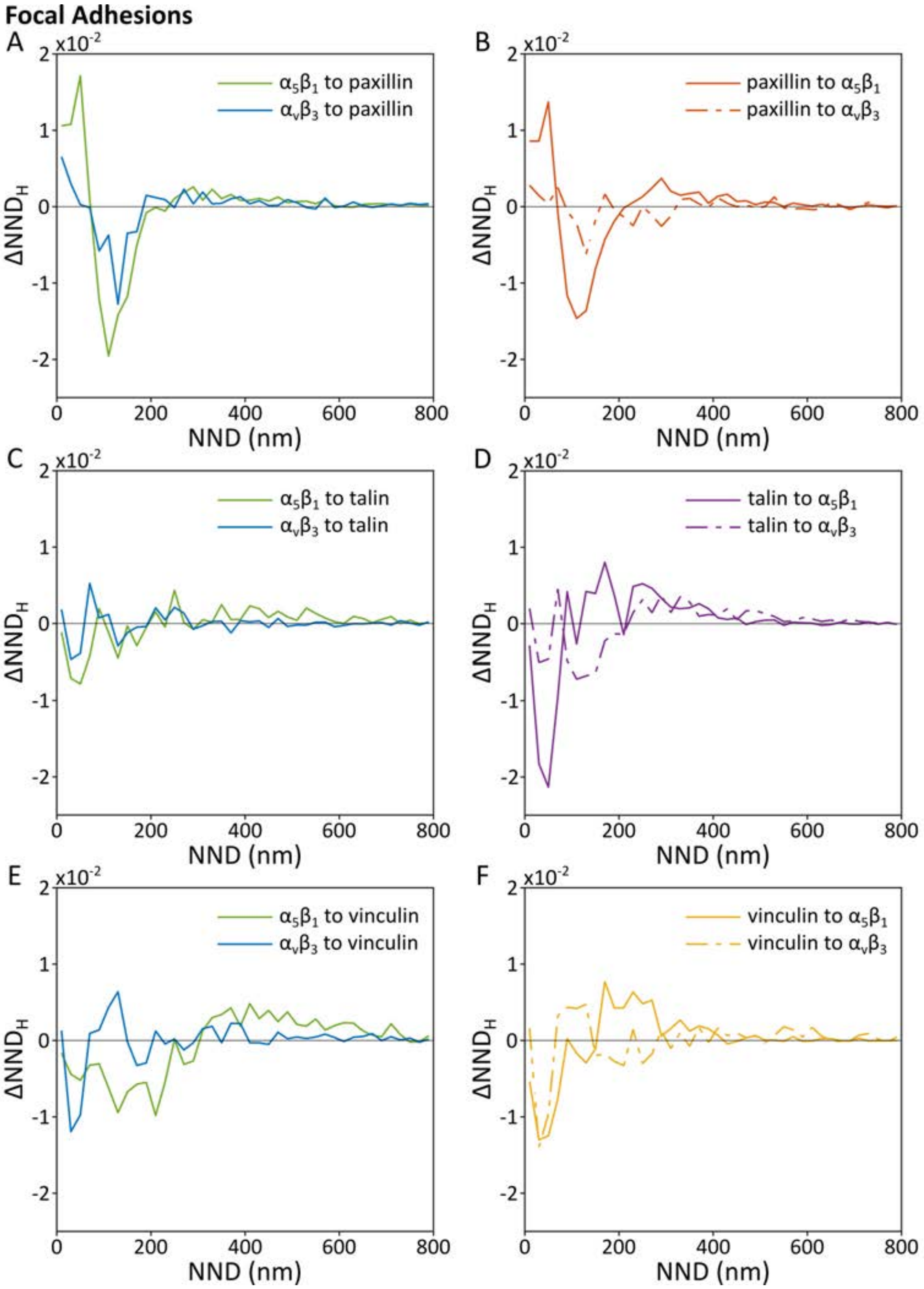

Figure 5.9 *ΔNND$_H$-plots between clusters of different proteins in FAs after 24 h spreading* (A–F) show the ΔNND$_H$-plots for the FA data in Figure 5.5. The left panels (A,C,E) show Integrins, $\alpha_5\beta_1$ (green) and $\alpha_v\beta_3$ (blue), to adaptors. The right panels (B,D,F) show data from adaptors (paxillin, orange, talin, purple, vinculin, yellow) to integrin ($\alpha_5\beta_1$, continuous line, and $\alpha_v\beta_3$, broken line).

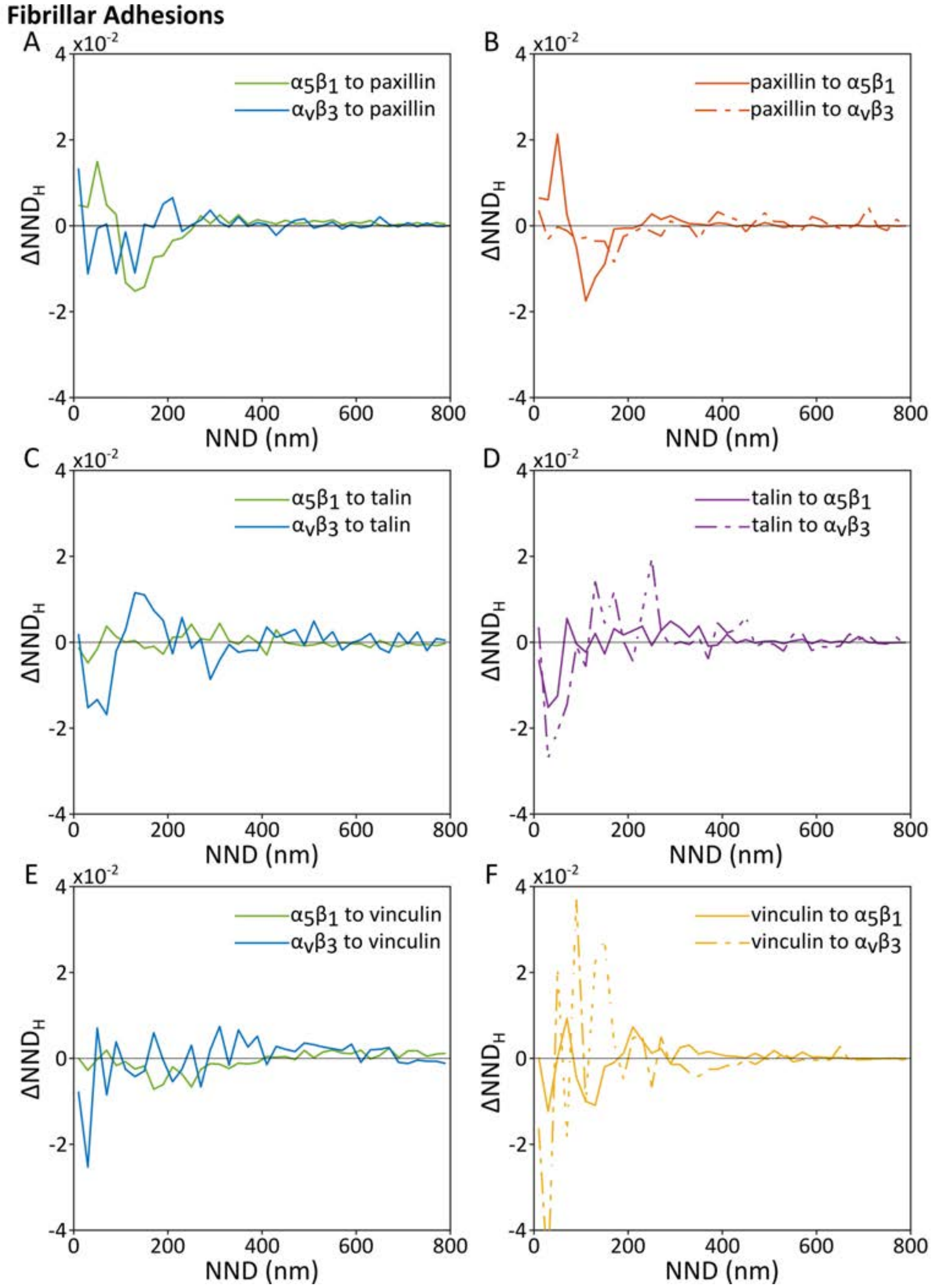

Figure 5.10 ΔNND$_H$-plots between clusters of different proteins in fAs after 24 h spreading
(A–F) show the ΔNND$_H$-plots for the fA data in Figure 5.6. The left panels (A,C,E) show Integrins, $\alpha_5\beta_1$ (green) and $\alpha_v\beta_3$ (blue), to adaptors. And the right panels (B,D,F) show data from adaptors (paxillin, orange, talin, purple, vinculin, yellow) to integrin ($\alpha_5\beta_1$, continuous line, and $\alpha_v\beta_3$, broken line).

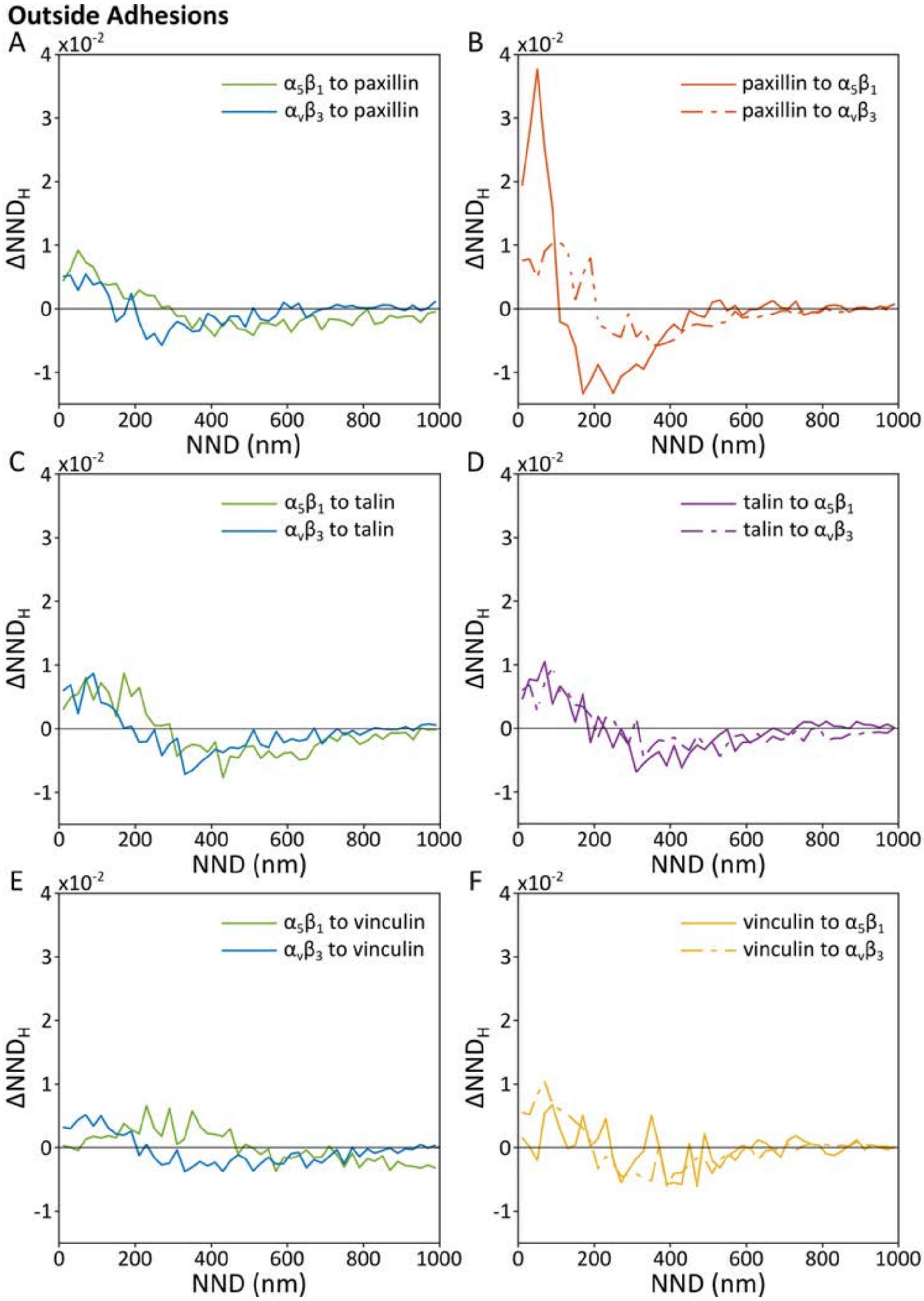

Figure 5.11 *ΔNND_H-plots between clusters of different proteins outside adhesions after 24 h spreading*

(A–F) show the ΔNND_H -plots for the outside adhesion data in Figure 5.7. The left panels (A,C,E) show integrins, $\alpha_5\beta_1$ (green) and $\alpha_v\beta_3$ (blue), to adaptors. And the right panels (B,D,F) show data from adaptors (paxillin, orange, talin, purple, vinculin, yellow) to integrin ($\alpha_5\beta_1$, continuous line, and $\alpha_v\beta_3$, broken line).

5.3.4 *Quantification of lateral distances between nanoclusters of different adhesion proteins in cells as a function of spreading time*

In Sections 5.3.2 and 5.3.3, we have presented results from experiments carried out on cells fixed 24 h after seeding, when the cells have reached a steady state in terms of spreading and adhesion complex formation. Despite the importance of understanding the spatial organisation of adhesion protein nanoclusters at steady state, these data cannot provide us with a dynamic view on cluster organisation during cell attachment to the substrate and spreading. To tackle this question, we investigated how adhesion protein nanoclusters are distributed relative to each other at earlier times after seeding (90 min and 3 h), and compared them to the steady state distributions at 24 h after seeding. Specifically, from the STORM images we collected on cells fixed at these different spreading times (90 min, 3 h, or 24 h), we studied the lateral distribution of integrin ($\alpha_5\beta_1$ or $\alpha_v\beta_3$) clusters with respect to those formed by the adaptors (paxillin, talin, or vinculin), in the three previously defined basal membrane regions.

Our main observations from previous section on the 24 h data hold true for the earlier time points. Our results indicate that the relative distribution between $\alpha_5\beta_1$ and paxillin clusters is maintained in time, with little to no variation seen with time when considering the data from $\alpha_5\beta_1$ to paxillin (Figure 5.12 and Figure 5.13 A). When we considered the reverse case, i.e., from paxillin to $\alpha_5\beta_1$, we observed a modest increase in the variation with time for FAs (Figure 5.12 B), no change with time for fAs (Figure 5.13 B) and a reduction in the variation with time for the clusters found outside adhesions (Figure 5.14 B). Interestingly, for this protein pair, the highest variation from random for the three time points in the three regions is always found at distances of ~50–70 nm. Although the data for $\alpha_5\beta_1$ with respect to talin or vinculin showed less variation from random, it is possible to appreciate a trend suggesting that talin and vinculin clusters in FAs are excluded at shorter distances from $\alpha_5\beta_1$ clusters (Figure 5.12 D and F). The $\alpha_5\beta_1$ to talin or vinculin data in fAs (Figure 5.13 C, E), as well as the talin to $\alpha_5\beta_1$ (Figure 5.13 D), fluctuate around zero and appear to resemble a random distribution. Notably, when looking at the distribution of vinculin and $\alpha_5\beta_1$ clusters in fAs (Figure 5.13 F), the ΔNND_H-plots resemble those obtained in FAs at early time points (Figure 5.12) – with troughs in a range of 30–70 nm –, while the data at 24 h appear indistinguishable from random.

Interestingly, when we analysed how $\alpha_v\beta_3$ clusters found in FAs and fAs are spatially distributed with respect to the three different adaptor proteins, our results showed that they generally follow a random distribution for all studied spreading times (90 min, 3 h, and 24 h) (Figure 5.15 and Figure 5.16). The most notable difference is that at 90 min after seeding, $\alpha_v\beta_3$ showed negative troughs (i.e., exclusion) at short distances for all three adaptor proteins in FAs and fAs, which transitioned to a random distribution at 24 h (Figure 5.15 and Figure 5.16).

Finally, we analysed the distribution of clusters found on the cell membrane outside of the adhesion complexes for experiments with $\alpha_5\beta_1$ (Figure 5.14) and $\alpha_v\beta_3$ (Figure 5.17). We observed that for paxillin to either of the integrins, there was a peak in the ΔNND_H-plots at shorter distances (<200 nm), although the peak was much more pronounced for paxillin to $\alpha_5\beta_1$ (Figure 5.14 B) than for paxillin to $\alpha_v\beta_3$ (Figure 5.17 B) (with a ~six-fold difference), and this was true at all time points. For the ΔNND_H-plots of talin to $\alpha_5\beta_1$ (Figure 5.14 D) the peak was found to be approximately three times less than the peak seen for paxillin to $\alpha_5\beta_1$. Furthermore, we also noted that the ΔNND_H value for talin to $\alpha_5\beta_1$ was influenced by time, where the peak at 3 h was twice that of the peaks at 90 min or 24 h (Figure 5.14 D). When we did the same analysis for talin to $\alpha_v\beta_3$ we saw a much-reduced peak (Figure 5.17 D) similar to that found for vinculin (Figure 5.17 F) and very close to random. When we considered the distances from $\alpha_5\beta_1$ to paxillin (Figure 5.14 A) the peaks were not varying with time, however the peak values were reduced to approximately a sixth of the peaks found for paxillin to $\alpha_5\beta_1$. The trend observed from $\alpha_5\beta_1$ to talin (Figure 5.14 C) resembled that of its counterpart, talin to $\alpha_5\beta_1$, including the enhanced peak seen at 3 h after seeding. When considering the remaining plots of $\alpha_5\beta_1$ to vinculin, the trend was random with no discernible peaks at short distances (Figure 5.14 E). Finally, when we considered $\alpha_v\beta_3$ to adaptors the trend was the same: there was no variation with time and only a subtle positive peak below 200 nm, resembling a very close to random distribution at all time points.

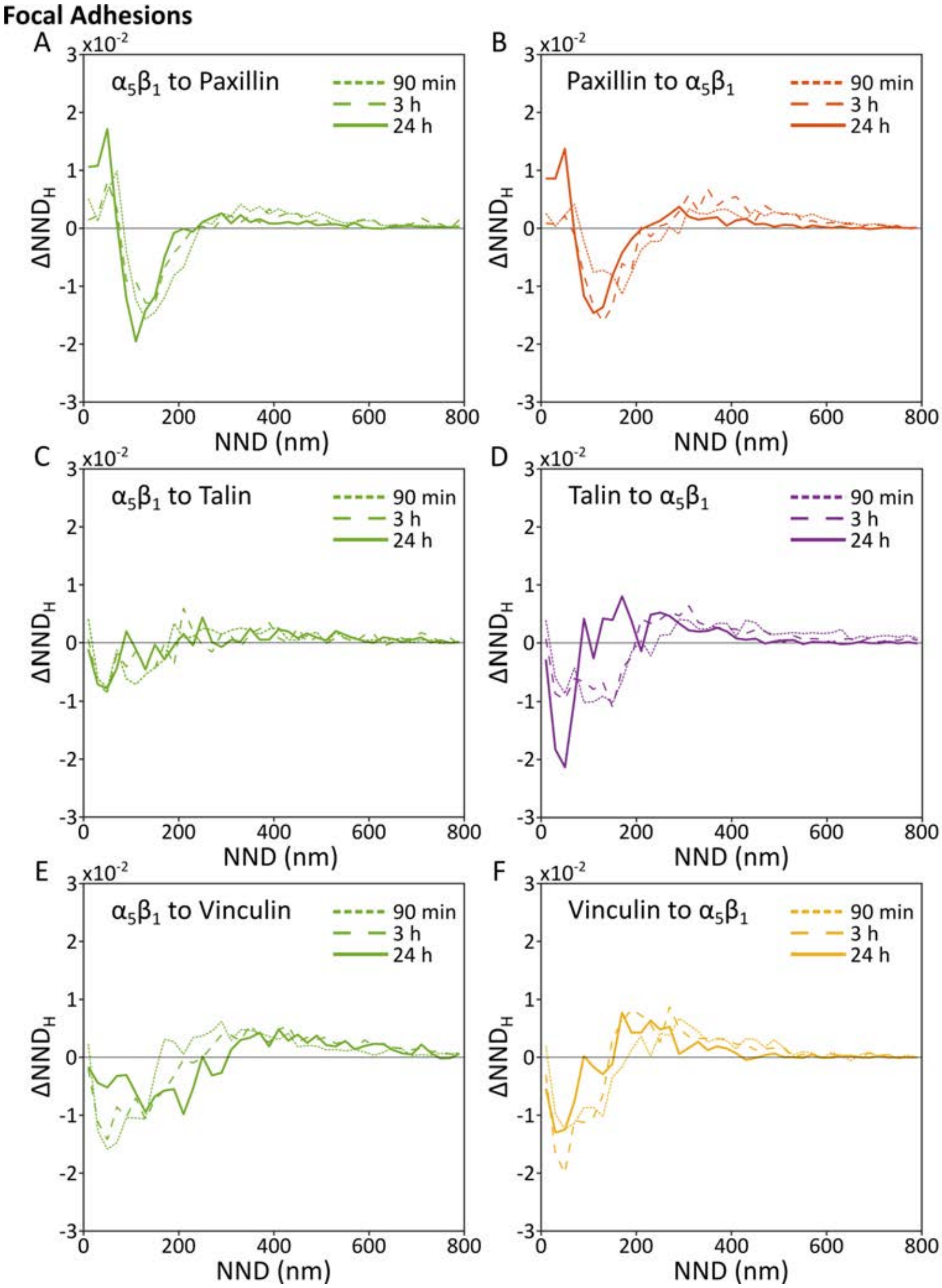

Figure 5.12 The effect of seeding time on NND distributions for experiments with $\alpha_5\beta_1$ and adaptor proteins in FAs

(A,C,E) show the ΔNND$_H$-plots for $\alpha_5\beta_1$ to adaptors, paxillin (A), talin (C) and vinculin (E) with time. (B,D,F) show the ΔNND$_H$-plots from an adaptor, paxillin (orange), talin (purple) or vinculin (yellow), to an $\alpha_5\beta_1$ cluster with time. For three different time points, 90 min, 3 h and 24 h, as shown in figure legend.

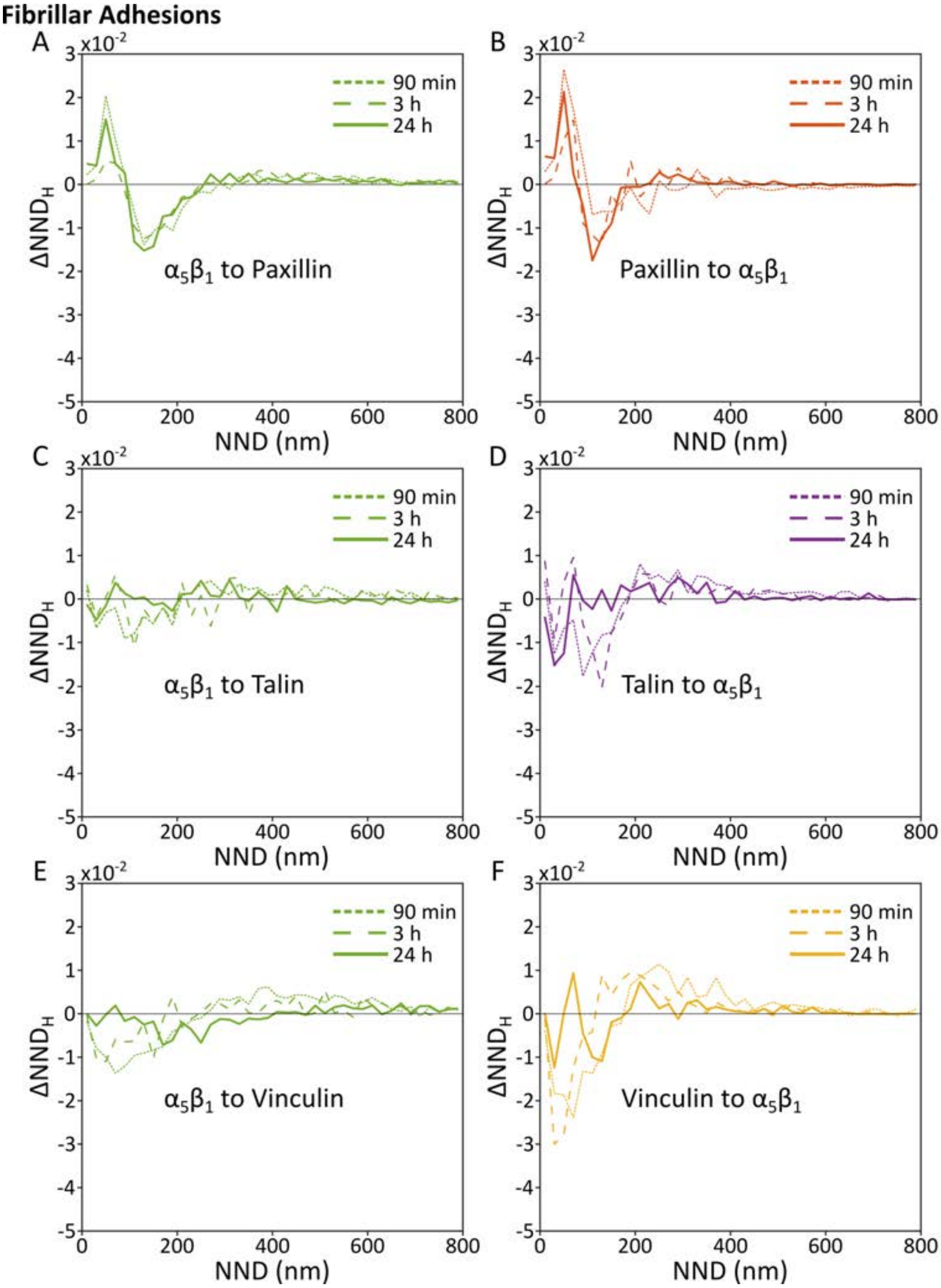

Figure 5.13 *The effect of seeding time on NND distributions for experiments with $\alpha_5\beta_1$ and adaptor proteins in fAs*

(A,C,E) show the ΔNND_H -plots for $\alpha_5\beta_1$ to adaptors, paxillin (A), talin (C) and vinculin (E) with time. (B,D,F) show the ΔNND_H -plots from an adaptor, paxillin (orange), talin (purple) or vinculin (yellow), to an $\alpha_5\beta_1$ cluster, with time. For three different time points, 90 min, 3 h and 24 h, as shown in figure legend.

Outside Adhesions

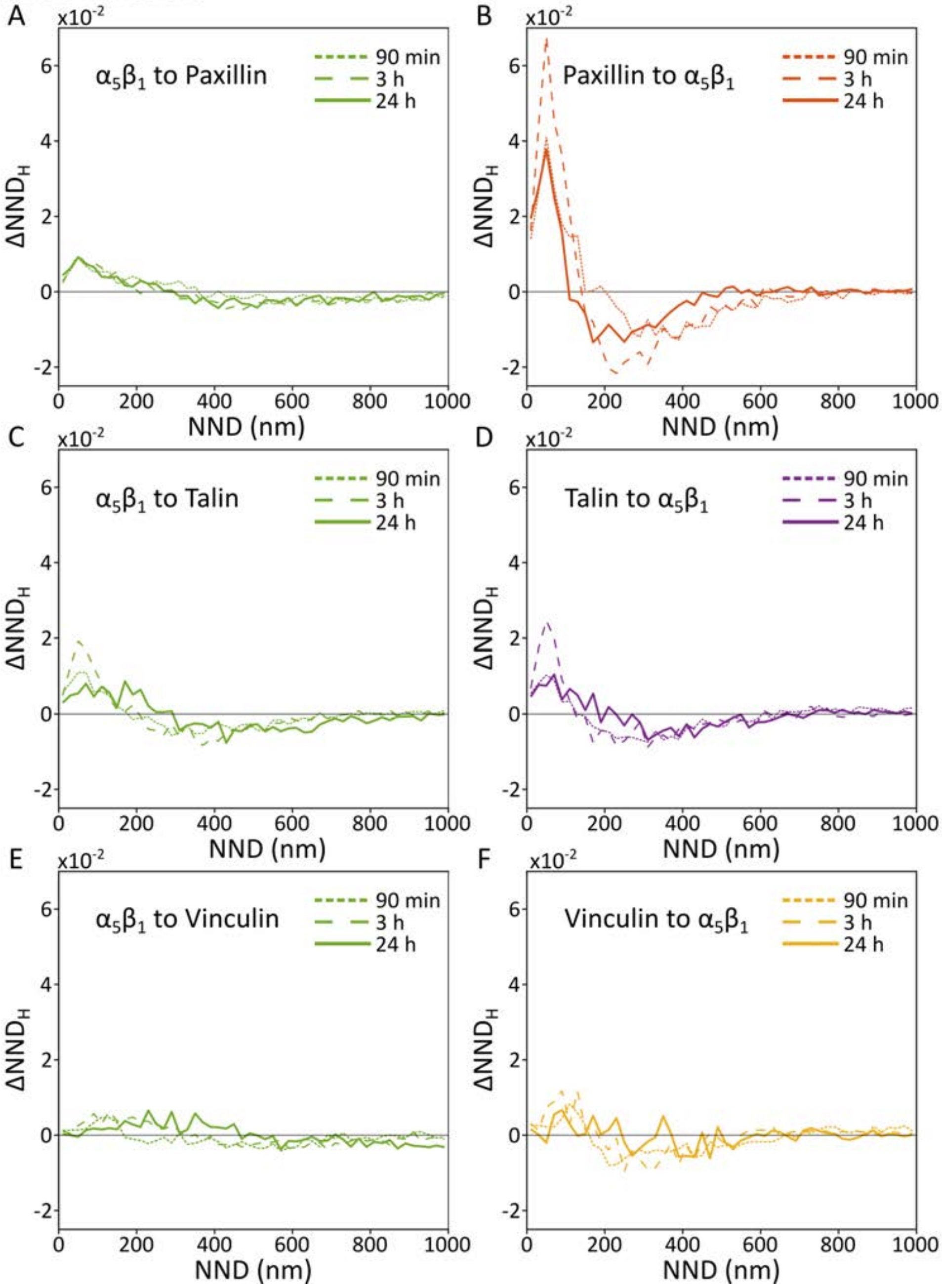

Figure 5.14 *The effect of seeding time on NND distributions for experiments with $\alpha_5\beta_1$ and adaptor proteins outside adhesions*

(A,C,E) show the ΔNND_H -plots for $\alpha_5\beta_1$ to adaptors, paxillin (A), talin (C) and vinculin (E) with time. (B,D,F) show the ΔNND_H -plots from an adaptor, paxillin (orange), talin (purple) or vinculin (yellow), to an $\alpha_5\beta_1$ cluster, with time. For three different time points, 90 min, 3 h and 24 h, as shown in figure legend.

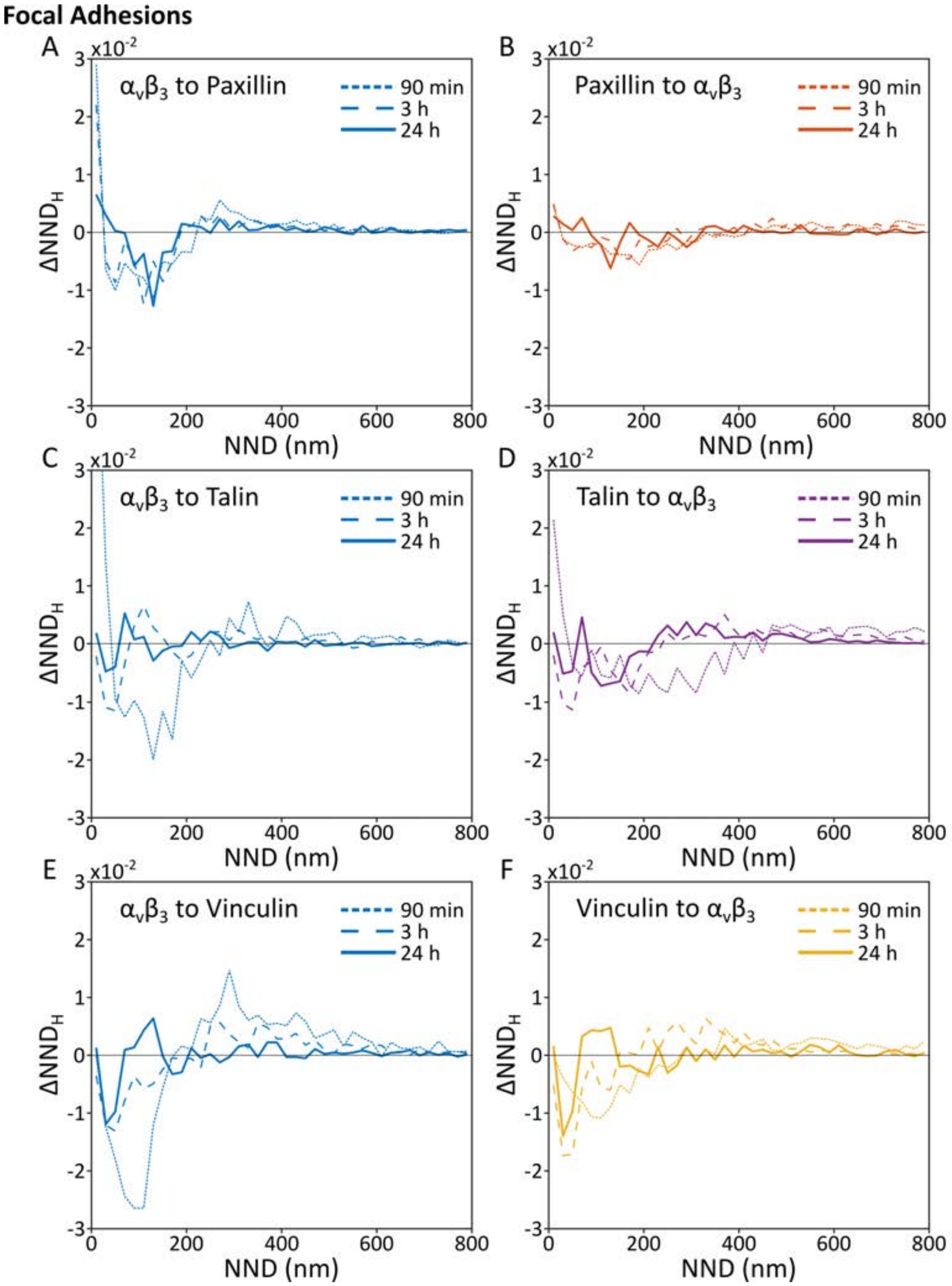

Figure 5.15 *The effect of seeding time on NND distributions for experiments with $\alpha_v\beta_3$ and adaptor proteins in FAs*

(A,C,E) show the ΔNND_H -plots for $\alpha_v\beta_3$ to adaptors, paxillin (A), talin (C) and vinculin (E) with time. (B,D,F) show the ΔNND_H -plots from an adaptor, paxillin (orange), talin (purple) or vinculin (yellow), to an $\alpha_v\beta_3$ cluster, with time. For three different time points, 90 min, 3 h and 24 h, as shown in figure legend.

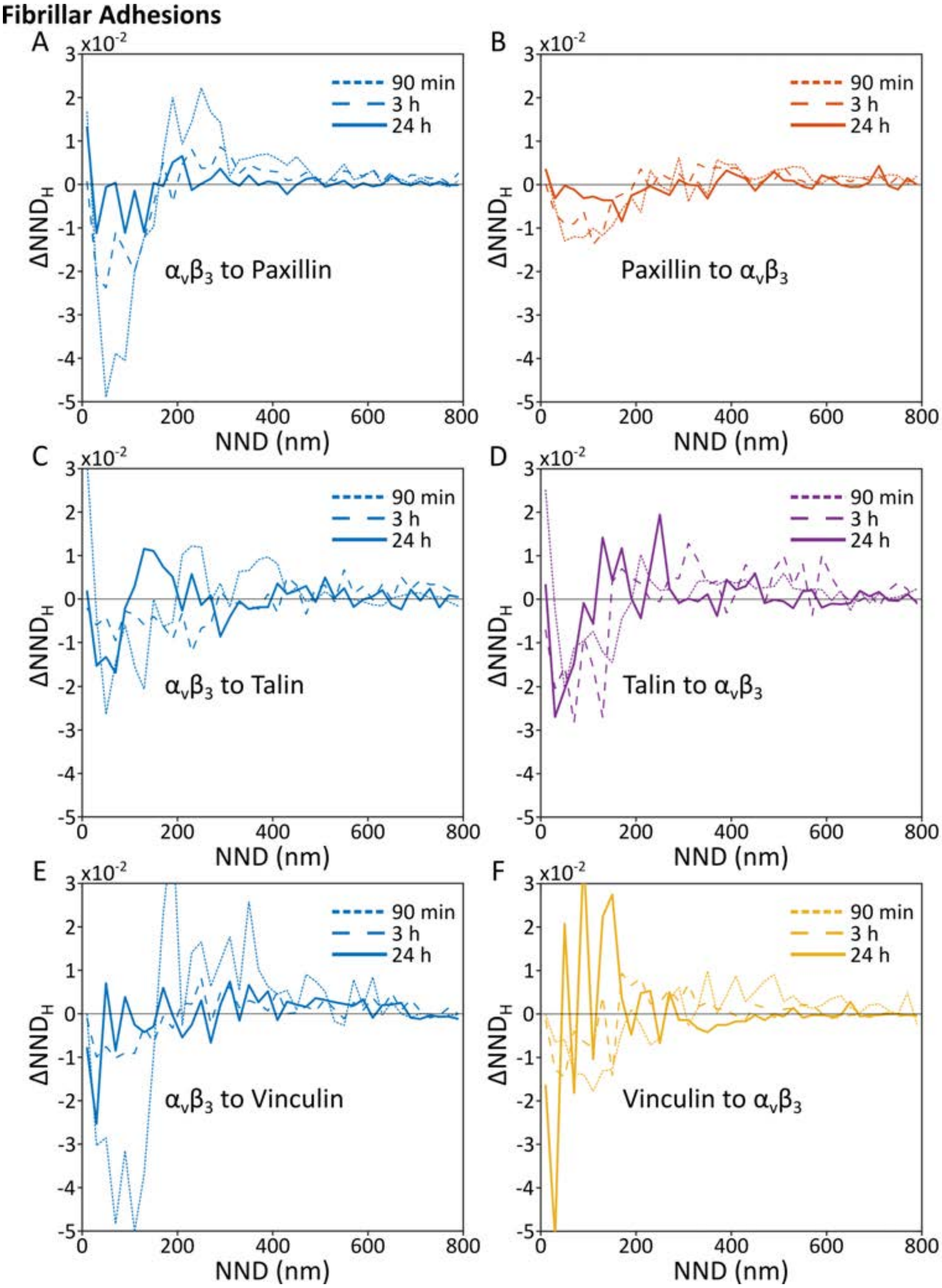

Figure 5.16 *The effect of seeding time on NND distributions for experiments with $\alpha_v\beta_3$ and adaptor proteins in fAs*

(A,C,E) show the ΔNND_H-plots for $\alpha_v\beta_3$ to adaptors, paxillin (A), talin (C) and vinculin (E) with time. (B,D,F) show the ΔNND_H-plots from an adaptor, paxillin (orange), talin (purple) or vinculin (yellow), to an $\alpha_v\beta_3$ cluster, with time. For three different time points, 90 min, 3 h and 24 h, as shown in figure legend.

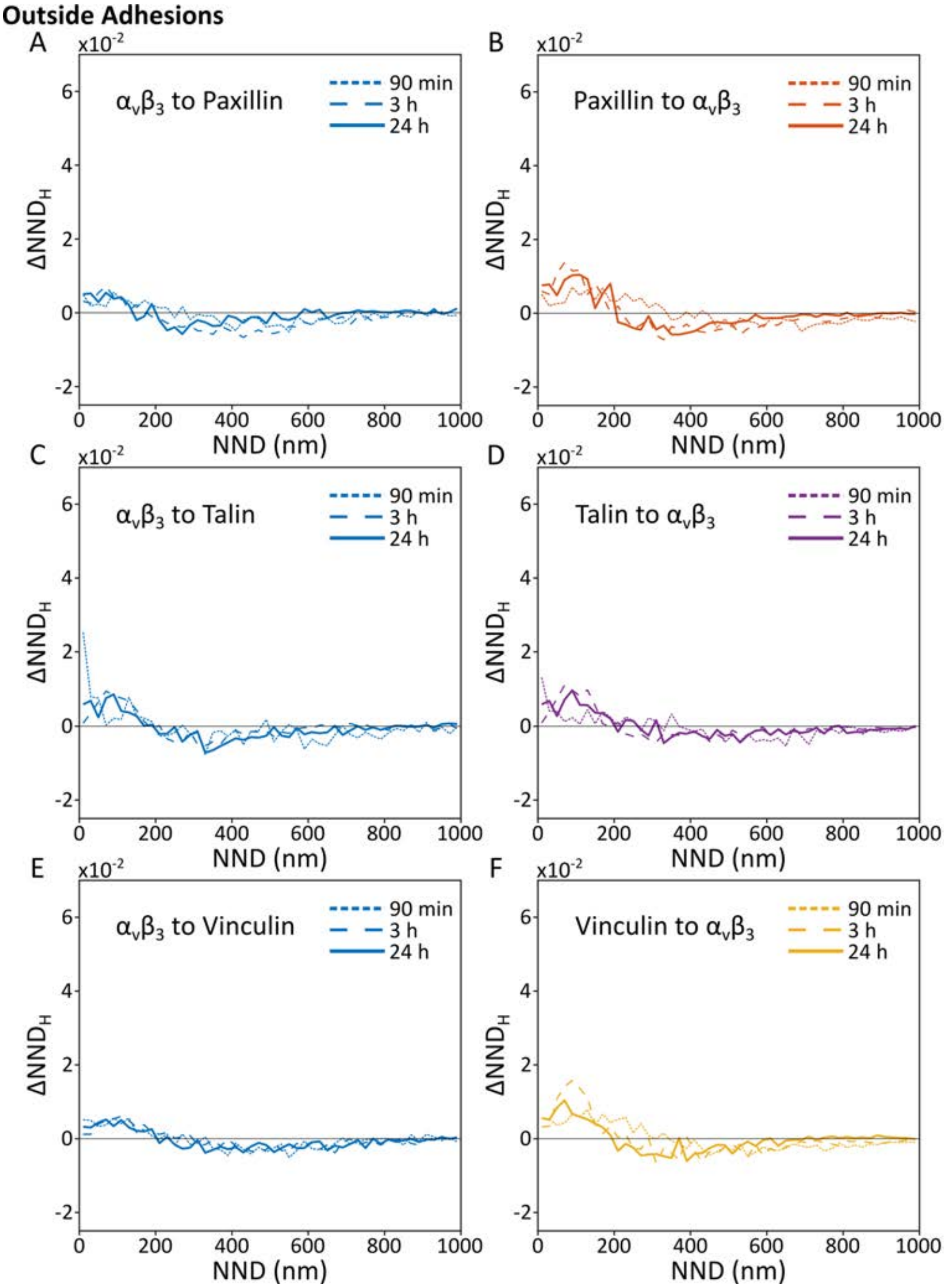

***Figure 5.17** The effect of seeding time on NND distributions for experiments with $\alpha_v\beta_3$ and adaptor proteins outside adhesions*

(A,C,E) show the ΔNND_H -plots for $\alpha_v\beta_3$ to adaptors, paxillin (A), talin (C) and vinculin (E) with time. (B,D,F) show the ΔNND_H -plots from an adaptor, paxillin (orange), talin (purple) or vinculin (yellow), to an $\alpha_v\beta_3$ cluster, with time. For three different time points, 90 min, 3 h and 24 h, as shown in figure legend.

Interestingly, and perhaps surprisingly, taken together, our data suggest that the distribution relationship between integrins and their partners is not as we had initially thought. Because direct or indirect binding of these adaptor proteins to the integrins impact the formation of FAs (Turner et al., 1990; Ripamonti et al., 2021; Gingras et al., 2008; Tanentzapf and Brown, 2006; Calderwood et al., 1999; Humphries et al., 2007; Zhang et al., 2008; Yao et al., 2015), we naively expected the existence of a preferred distance between clusters of each pair of proteins. However, our data shows that only $\alpha_5\beta_1$ and paxillin have this preferential separation in all regions of the membrane, and that a random distribution between protein clusters is found for talin and vinculin with respect to the integrins $\alpha_5\beta_1$ or $\alpha_v\beta_3$ in adhesions. Unexpectedly, we found that there is a preference for short distances between clusters outside the adhesions. Given that this is a membrane region of very low cluster density, our finding that those clusters are not randomly distributed with respect to one another points towards the existence of a cluster-cluster attraction/interaction mechanism outside adhesion complexes.

5.4 Discussion

In this chapter, we focused on how nanoclusters of different proteins are organised with respect to each other, with the aim of investigating the interactions between integrins and some of their key adaptor proteins. We first carried out our analyses on fully spread cells that were fixed 24 h after seeding, after which we end up by comparing the data over a time course including shorter spreading times of 90 min and 3 h.

Our results of NND between nanoclusters of $\alpha_5\beta_1$ and paxillin showed a preferential proximity of ~50–70 nm between them and being maintained on the three regions of the membrane investigated, FAs, fAs, and outside adhesions. This preferential proximity moreover, remained constant as function of seeding time. In strong contrast, the relative organisation in FAs and fAs of integrin nanoclusters ($\alpha_5\beta_1$ or $\alpha_v\beta_3$) with respect to the adaptor proteins talin or vinculin appeared to be random, as shown by comparing the peaks of the experimental and simulated distributions (Figure 5.8) and the ΔNND_H-plots (Figure 5.9 and Figure 5.10). As we have already touched upon earlier, it seemed reasonable to expect a certain level of organisation between these pairs in adhesion complexes, where integrin and adaptor proteins functionally interact and are therefore often acting as engaged pairs (Calderwood and Ginsberg, 2003; Tanentzapf and Brown, 2006; Ripamonti et al., 2021). In this scenario, the relative distribution between these partners should vary from random. However, the correct interpretation of our data requires a more careful consideration for two reasons. First, in our work, we evaluated a snapshot of a dynamic process, where we imaged just two proteins at a time. Second, talin can bind to both integrins (Calderwood et al., 1999; Cluzel et al., 2005; Liu et al., 2015) and integrins can dynamically transit between active and inactive conformations (Li et al., 2017; Sun et al., 2019). Hence, the dynamic and transient nature of integrin activation and inactivation (Bakker et al., 2012; Rossier et al., 2012; Rossier and Giannone, 2016; Tsunoyama et al., 2018) would lead to rapid engagement and disengagement of the adaptor proteins. A random distribution of adaptor nanoclusters with respect to the integrins would then allow for an efficient re-engagement of free adaptors. It is also important to note that integrins have a higher density of nanoclusters as compared to talin or vinculin, as shown in Chapter 3. Therefore, if a talin molecule becomes disengaged there is a high probability that there would be an available integrin nanocluster in close proximity to re-engage talin and to maintain the overall homeostasis of the FA. By this reasoning, one could argue that we could then expect to see a level of organisation when we study the ΔNND_H from talin to a given integrin. However, here we studied only a subpopulation, i.e., talin to $\alpha_5\beta_1$ or talin to $\alpha_v\beta_3$. We would need to image all three proteins together or silence the expression of one of the integrins in order to gain a better understanding of the organisation of talin with respect to the integrins. This argument also holds for vinculin, as the presence of vinculin to reinforce the integrin-talin-actin bond is dependent on its ability to bind talin and actin and so is independent of which integrin is in the complex (Humphries et al., 2007; Hirata et al., 2014), and so a random distribution of vinculin with respect to the integrins agrees with the currently accepted biological models. To gain a better understanding of these interactions following a microscopy-based approach as the one we used in this thesis, will require further imaging. Going forward with the knowledge we have gained in this study we now have a number of avenues to explore. One possibility is to use antibodies targeting only active integrins. Additionally, increasing the number of proteins that can be simultaneously imaged would allow investigating the relative distribution of up to three proteins, e.g., the two integrins together with an adaptor such as talin. The results of these experiments would provide us with further insight and will hopefully be part of the future work in our group.

Finally, we would like to discuss the finding that, on the membrane regions outside adhesions, there are clusters of different proteins found at shorter distances than predicted by a random distribution (Figure 5.11, Figure 5.14, and Figure 5.17). To us this was remarkable, as the area of the cell membrane outside adhesions is large and the density of adhesion protein clusters is relatively low, <10 clusters/µm^2 (Figure 3.9). Because of this low density, we would have expected that the protein clusters would be further away from one another and the existence of occasional short distances between the clusters would follow a random distribution. Intriguingly, the observed peak at short NND is more pronounced when looking at the NND from adaptor proteins, such as paxillin and talin, to integrins than vice versa (Figure 5.14 and Figure 5.17). One way to interpret these results is to consider the proteins in question: integrins are membrane proteins that remain inserted into the membrane, however paxillin, talin, and vinculin are soluble proteins and therefore only remain at the cell membrane when anchored to another membrane component. Therefore, the more pronounced peak from paxillin or talin to integrin $\alpha_5\beta_1$ could be due to the fact that all the adaptor clusters found at the membrane are engaged with an integrin that tethers them to the membrane preventing them to diffuse away to the cytosol. When considering the integrins to the adaptors, we see a reduced or no peak as they are membrane proteins that do not need to be engaged to remain at the surface. We suggest that our data provide information on the elusive and transient nascent adhesions, which form on low adhesion protein density regions of the basal membranes. Nascent adhesions form independent of the surface rigidity (Changede et al., 2015) and act as nucleating points for adhesions formation (Choi et al., 2008). They have been shown in previous studies using diffraction-limited microscopy to be short-lived and found to account for ∼60% of the adhesions formed in the cells. Only a mere ∼30% of those resulted in midsize adhesions and a remarkable low percentage, i.e., ∼5% form the fully mature force-dependent FAs (Thievessen et al., 2013). Future studies focusing at imaging multiple proteins simultaneously with super-resolution microscopy will complement recent findings from Han *et al.* (Han et al., 2021) that indicated that the fate of the nascent adhesions depends on the arrival of the adaptors, which form the initial nucleating point and thereby dictate whether maturation to FAs occurs or not. Our data may agree with this new publication as we detect a population of talin and paxillin that is in close proximity to the integrin $\alpha_5\beta_1$. Nevertheless, this recent work showed a dependence on all three adaptors at the nascent adhesion sites while we have only detected a very subtle peak for vinculin to $\alpha_v\beta_3$ and an apparent random association to $\alpha_5\beta_1$.

In general, the results of this chapter provide us with interesting new insights into the distribution and organisation of key adhesion complex proteins while also delivering new and exciting questions to approach and answer in the future.

Chapter 6

Integrin $\alpha_5\beta_1$ nanoclusters are distributed preferentially on the edge of focal adhesions

So far, the research presented in this thesis has focused on the characterisation of adhesion protein nanoclusters (Chapter 3), how they are organised considering the spatial distribution of nanoclusters of the same protein (Chapter 4), and the relative distribution between nanoclusters of different proteins (Chapter 5). In this chapter, we assessed the organisation of the nanoclusters with respect to the adhesion complexes themselves. We show that $\alpha_5\beta_1$ *integrin nanoclusters are preferentially found on the edges of FAs. Interestingly, this characteristic arrangement is strengthened at longer cell spreading times. In contrast,* $\alpha_v\beta_3$ *shows no obvious preferential organisation within adhesions upon visual inspection. However, interestingly, at early time points our data show a small population of* $\alpha_v\beta_3$ *clusters that exhibit an organisation different to random, which was lost after 24 h. We further combined the analysis presented in Chapter 5 (the NND distribution between different protein clusters), with the distance to the adhesion edge computed in this chapter. Using this approach, we found that those* $\alpha_5\beta_1$ *nanoclusters enriched on the edge of FAs are also close to their nearest neighbour adaptor cluster. Our data together with data in earlier publications are consistent with the hypothesis that* $\alpha_5\beta_1$ *and* $\alpha_v\beta_3$ *play different roles in FAs, and with* $\alpha_5\beta_1$ *itself having distinct roles depending on its tensioned state. We therefore propose a model where* $\alpha_5\beta_1$ *in the ring around the adhesion edge is functionally engaged with adaptors such as talin and paxillin for maintaining cell attachment, whereas* $\alpha_5\beta_1$ *and* $\alpha_v\beta_3$ *in the central region of the adhesions synergise together for mechanosensing and mechanotransduction.*

6.1 Introduction

The adhesion complexes, which form between the extracellular matrix (ECM) and the cell's cytoskeleton, have been studied extensively since their discovery 50 years ago (Abercrombie et al., 1971). In the half a century since, the development of imaging techniques and biochemistry tools have allowed us to gain a better understanding of these complexes, from the seemingly straightforward question of the protein players involved, to their role in processes such as cell migration and, more recently, the details of how mechanosensing and mechanotransduction work. While many questions have been answered, many uncertainties still remain for us to explore. The canonical view until recently was that the proteins of the adhesion complex were uniformly distributed throughout the adhesion. Since the development of super-resolution microscopy over 15 years ago (Huang et al., 2009a), we have achieved a more detailed view of how adhesion complex proteins are spatially organised at the nanometre scale. In particular, Kanchanawong et al. showed that a number of key adhesion proteins are axially stratified in different layers above the basal membrane of the cell (Kanchanawong et al., 2010), whereas other studies showed that a number of these proteins form nanoclusters at the cell membrane (Shroff et al., 2007; van Zanten et al., 2009; Spiess et al., 2018).

Integrins are the central protein family forming these adhesion platforms as they are transmembrane proteins that link the ECM with the cell’s cytoskeleton. The two main integrins forming adhesion complexes on FN substrates are $\alpha_5\beta_1$ and $\alpha_v\beta_3$ (Kumar, 1998; Schiller et al., 2013). Understanding their specific roles has been the aim of extensive research in the past years, which still remains a challenging task due to the seemingly symbiotic relationship between these two integrins. Despite this, already back in 2009 it was suggested that $\alpha_5\beta_1$ determines adhesion strength whereas $\alpha_v\beta_3$ plays a role in mechanotransduction (Roca-Cusachs et al., 2009). An example of the signalling crosstalk between these two integrins was shared in 2013, when it was shown that cells that express α_v-class integrins activate the RhoA signalling pathway without a positive read-out for phosphorylated myosin light chain (pMLC) (Schiller et al., 2013). The authors further suggested that $\alpha_5\beta_1$ was the beneficiary of this RhoA signally cascade. In more recent work from the Fässler and Müller labs, it was shown that cells expressing only the $\alpha_5\beta_1$ integrin formed strong adhesion bonds with FN, which were reduced in cells expressing both $\alpha_5\beta_1$ and $\alpha_v\beta_3$, likely due to talin equivalently binding to either integrin (Bharadwaj et al., 2017). They also showed that by specifically activating $\alpha_v\beta_3$ using a VN-coated cantilever, the strength of the bonds formed between $\alpha_5\beta_1$ and FN was enhanced. In summary, the study by Bharadwaj et al. underscored how these two integrins work closely together to control cell adhesions.

Another important finding in the field has been that $\alpha_5\beta_1$ can be found in adhesions in two different mechanical states: relaxed or tensioned (Friedland et al., 2009). The authors showed that the tensioned state of $\alpha_5\beta_1$ is myosin-dependent. Moreover, they found that in the presence of a myosin inhibitor, the tensioned state could be recovered by the application of an external force to the cell. The study also showed that the FN bonds formed in the different states were biochemically distinct: relaxed $\alpha_5\beta_1$ requires the RGD motif of FN, whereas tensioned $\alpha_5\beta_1$ binds FN depending on the synergy sites (see also Chapter 1 for further details).

The cytosolic family of proteins known as Kank proteins are a relatively new adhesion protein family (Chen et al., 2018), which in vertebrates is formed by four paralogues (Kank1–4). Of these, Kank2 has been shown to be present in FAs, and it can bind β_1 and β_3 integrin tails equally well. Interestingly, Kank2 has been shown to form a ring or FA belt on the edge of FAs (Sun et al., 2016b). That particular study also showed that Kank2 has the ability to induce adhesion sliding, where they showed with live cell microscopy that Kank2 and paxillin form thin elongated structures from the proximal border of FAs into the centre. The similarity of these elongated central structures and the fact that they showed that Kank2 regulated the tensions state of $\alpha_5\beta_1$ and induced bond slippage for $\alpha_5\beta_1$ and FN indicates to us that this ring on the periphery of a FA might act as a precursor to fA formation where $\alpha_5\beta_1$ is the main integrin.

Thus, despite an enormous amount of literature in the field, the specific roles of both integrins in the processes of adhesion, migration and mechanosensing remain unclear. We hypothesised that the versatility in terms of function of both integrins binding to the same ligand might be accomplished by their different nanoscale distributions inside FAs. Thus, in this chapter we quantified the nanocluster distribution of both integrins and their adaptors with respect to the edge of adhesions. Our results revealed that $\alpha_5\beta_1$ integrin nanoclusters are preferentially enriched on the edge of FAs/adhesion complexes, as compared to other adhesion proteins. Moreover, we find a region close to the adhesion edges (<100 nm from the edge) where the population of $\alpha_5\beta_1$ is close to and potentially engaged with paxillin and talin nanoclusters. By contrast, $\alpha_v\beta_3$ clusters lack this organisation with respect to the edge of adhesions and its nearest neighbour adaptor proteins, and they instead exhibit a random distribution throughout the adhesions. These data, together with all those from preceding publications, have allowed us to propose a model for the lateral organisation of proteins in FAs.

6.2 Materials and methods

6.2.2 Sample preparation and imaging

Samples were prepared by seeding HFF-1 cells on FN coated 8-well plates. The cells were allowed to spread for different times (90 min, 3 h and 24 h), after which they were fixed and then immunolabelled as described in detail in Chapter 2 section 2.2.

6.2.3 Image acquisition:

All the images analysed in this chapter were taken on a Nikon Eclipse Ti system using a 100x oil objective with NA 1.49 a 256x256 pixel ROI and a pixel size of 160 nm using TIRF illumination. The system has lasers with wavelengths of 405 nm, 560 nm and 647 nm. For a full description of the image acquisition see Chapter 2, Section 2.4.

6.2.4 Image reconstruction

Dual-colour STORM image reconstruction was done using Insight3, provided by Bo Huang (UCSF, initially developed in Xiaowei Zhuang's Lab). The analysis was run over the entire data sets but recording only those localisations detected in the second frame of the five-frame cycle, that is the first of the four reporter frames, the localisations can be represented by a cross marking their centres or rendered with a Gaussian profile convoluted with the point. For more detailed description, see Chapter 2 section 2.5.

6.2.5 Image analysis

The majority of our analysis carried out in this chapter were completed using scripts written and developed in house, using MATLAB 2019b. We also incorporate already existing algorithms such as DBSCAN (Ester et al., 1996) into our scripts. DBSCAN was the initial analysis to identify clusters of our proteins of interest.

We then used the inbuilt MATLAB function '*bwboundaries*' to identify the adhesion boundaries. This function identifies the pixel coordinates where the binary mask switches from 0 to 1. This function output is a list of coordinates that correspond to the centres of the pixels around the inner edge of the structure.

We also made use of the MATLAB function '*knnsearch*' to find the shortest distance from the cluster CoM to the edge of an adhesion. In a similar way to the previous chapters, we use an algorithm developed in house to generate a random distribution of nanoclusters in adhesions. A detailed description of the steps we used can be found in Chapter 2.

Data representation with GraphPad Prism

Median values for the distance-to-edge per cell were calculated from the full distributions of the experimental and simulated data. We then found the relative difference and these values are represented as scatter plots using GraphPad Prism (version 9.1.2), where the lines and the whiskers show the mean value and the standard deviation, respectively, of the distribution of median values for each cell.

Statistical analysis with GraphPad Prism

The statistical analysis used in this chapter to assess the statistical significance of the variation of the median distance-to-edge per cell was carried out using GraphPad Prism (version 9.1.2). Specifically, when testing the statistical significance of the differences between the distribution mean values, we ran one-way ANOVA tests or paired Student's t-test when comparing the experimental with simulated distributions of median distances to the edge for each protein. The confidence interval was 95%.

6.3 Results

6.3.2 Super-resolution microscopy reveals that clusters of $\alpha_5\beta_1$ are enriched on the edge of FAs

In here we focus on investigating the distribution of adhesion protein nanoclusters relative to the overall structure of the adhesions they form. This study was motivated by the observation that $\alpha_5\beta_1$ nanoclusters appeared to be enriched at the edges of FAs, as seen in our multicolour STORM images (Figure 6.1). The images qualitatively indicate that, regardless of the adaptor it was paired with, $\alpha_5\beta_1$ nanoclusters are enriched around the edges of the FAs while the associated adaptor clusters appear more homogeneously distributed across the FAs (Figure 6.1, inset (i) for each panel). As the structures of fAs are, by their nature, very narrow and elongated, the possible enrichment of $\alpha_5\beta_1$ clusters around the adhesion edge was not so obvious (Figure 6.1, inset (ii) for each panel).

In contrast, visual inspection of the reconstructed STORM images of $\alpha_v\beta_3$, did not reveal any obvious organisation of $\alpha_v\beta_3$ with respect to the adhesion (FA or fA) edges (Figure 6.2). Moreover, in agreement with the multicolour STORM images of $\alpha_5\beta_1$ and the adaptors (Figure 6.1), the nanoclusters of the adaptor proteins, when imaged together with $\alpha_v\beta_3$, appear to be homogenously distributed both in FAs and fAs, thus providing an extra layer of validation of our multicolour super-resolution microscopy approach.

In summary, our qualitative observation of multicolour STORM images suggests that $\alpha_5\beta_1$ nanoclusters are enriched at the edge of FAs, whereas $\alpha_v\beta_3$, paxillin, talin and vinculin clusters seem to be uniformly distributed across the adhesions.

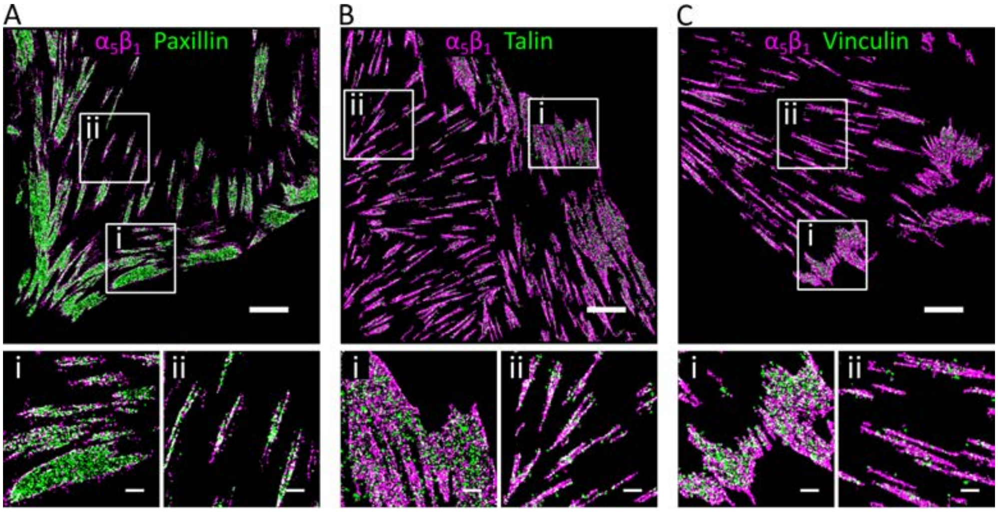

Figure 6.1 *Multicolour STORM images of $\alpha_5\beta_1$ and its adaptor proteins in HFF-1 cells plated for 24 h on FN*

Rendered STORM images of all the localisations of $\alpha_5\beta_1$ (in magenta) with the different adaptors (in green): paxillin (A), talin (B), or vinculin (C). Bottom row shows zoom-in regions of FAs (panels i) and fAs (panels ii) for each protein pair. Scale bars of main images are 5 µm and of zoom-ins are 1 µm.

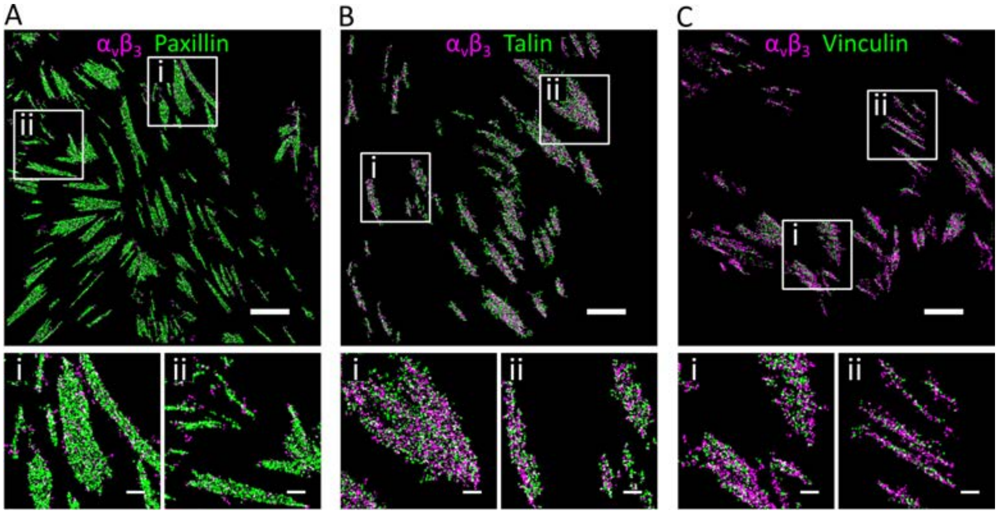

Figure 6.2 *Multicolour STORM images of $\alpha_v\beta_3$ and its adaptor proteins in HFF-1 cells plated for 24 h on FN*

Rendered STORM images of all the localisations of $\alpha_v\beta_3$ (in magenta) with the different adaptors (in green): paxillin (A), talin (B), or vinculin (C). Bottom row shows zoom-in regions of FAs (panels i) and fAs (panels ii) for each protein pair. Scale bars of main images are 5 µm and of zoom-ins are 1 µm.

6.3.3 Integrin $\alpha_5\beta_1$ clusters are preferentially found on the edge of FAs at 24 h of cell seeding

The observed difference between the organisation of the nanoclusters of the two integrins, $\alpha_5\beta_1$ and $\alpha_v\beta_3$, struck us as potentially very interesting as it may point to the different roles that these two integrins have in the adhesion complex. In order to analyse quantitatively this preference of $\alpha_5\beta_1$ nanoclusters to accumulate at the edge of FAs, we developed novel analytical tools, based on NND computations, to compute the distance from the adhesion protein nanoclusters to the edge of the adhesion they form. Building on the analysis carried out in previous chapters, we performed the distance-to-edge computations on an adhesion-by-adhesion basis, using built-in MATLAB functions (see Methods section 6.2.5 of this chapter). In brief, we first found the edges of the adhesion areas in the binary mask (Figure 6.3, blue boundary). We then computed the NND between the CoM of each nanocluster and the centre of the edge pixel. This distance, which we call distance-to-edge, corresponds to the minimum distance from a nanocluster to the adhesion edge. The proximity to the edge of $\alpha_5\beta_1$ nanoclusters is illustrated in Figure 6.3 C, where we show a representative image of a FA, where the CoM of the $\alpha_5\beta_1$ clusters (shown in magenta) appear to be preferentially localised closer to the adhesion edges (shown in blue), and where paxillin clusters (shown in green) appear more uniformly distributed across the adhesion.

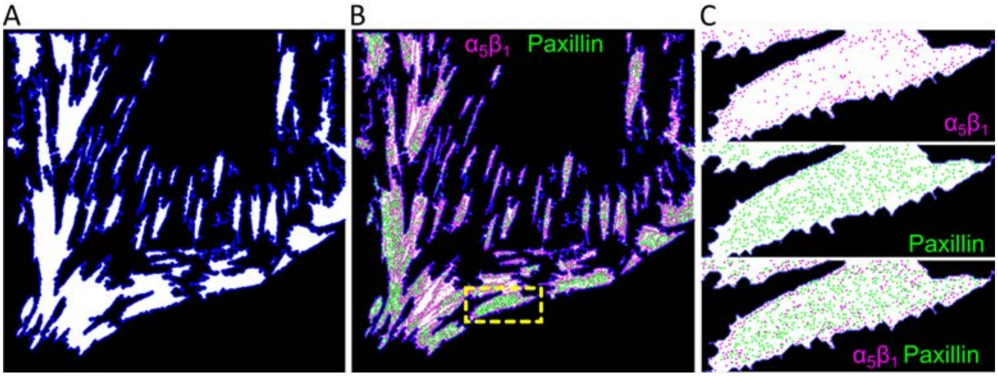

***Figure 6.3** Definition of adhesion edge for distance-to-edge analysis*

(A) Binary mask of the manually selected adhesions with the edges detected by MATLAB (blue). (B) Image of the mask with adhesion edges in blue, as shown in (A), together with the localisations of the CoM of the clusters of $\alpha_5\beta_1$ (magenta) and paxillin (green). (C) Zoom-in of the yellow dashed box in (B), where the top panel shows the CoM of $\alpha_5\beta_1$ clusters inside the adhesion with edges marked by blue points, the middle panel shows the CoM of paxillin clusters, and the bottom panel shows the CoM of both $\alpha_5\beta_1$ and paxillin clusters together with adhesion edges.

Using this approach, we computed the distance-to-edge for the nanoclusters of the different adhesion proteins, in an adhesion-by-adhesion basis, for both experimental and simulated data. In general, if the nanoclusters are uniformly distributed, one would expect that the probability of finding a cluster at a specific distance-to-edge decreases with increasing distance from edge. This occurs because there is a larger area along the perimeter of a shape, e.g. for a circular shape this decrease is linear with the distance to the edge. We found that our experimental and simulated data indeed exhibit this behaviour (Figure 6.4 for FAs and Figure 6.5 for fAs). These results reveal that the nanoclusters of all studied adhesion proteins follow, in terms of their spatially distribution with respect to the adhesion edge, a similar distribution to the random situation. However, and despite the similarity between the experimental and random distributions, we could observe subtle but significant differences that indicate an increase in the probability of finding $\alpha_5\beta_1$ clusters very close to FA edges as compared to the random distribution (Figure 6.4 A). A similar trend was also detected in the case of talin nanoclusters, although the effect was less pronounced (Figure 6.4 D). By contrast, and in line with our visual inspection, $\alpha_v\beta_3$ nanoclusters do not appear to be preferentially positioned at the edges of FAs, but instead they appear to be partially excluded from the adhesion edges (Figure 6.4 B). This exclusion from the FA edges was also observed for the clusters of the adaptor proteins paxillin and vinculin (Figure 6.4 C and E). Another observation made from the experimental histograms was the presence of a small shoulder, indicating deviation from the random distribution, with a higher probability to find clusters at distances between 40 and 100 nm from the edge, in particular for $\alpha_5\beta_1$, paxillin, and talin (Figure 6.4 A, C, and D, respectively). This shoulder was less pronounced for $\alpha_v\beta_3$ (Figure 6.4 B) and with vinculin showing a distribution essentially indistinguishable from random (Figure 6.4 E).

We next performed the same analysis for the adhesion protein clusters on fAs. Our results show that the trend is generally more similar to random (Figure 6.5), which likely results as a consequence of the elongated shape of fAs themselves. The distance-to-edge of clusters of $\alpha_v\beta_3$ (Figure 6.5 B), talin (Figure 6.5 D), and vinculin (Figure 6.5 E), appeared to follow similar distributions as their random counterparts. By contrast, the data for $\alpha_5\beta_1$ (Figure 6.5 A), and paxillin (Figure 6.5 C), show a shoulder (frequency higher than random) for those clusters located at around 40–100 nm from the fA edge, similar to that seen in the case of FAs, albeit the extent of this shoulder was less pronounced (Figure 6.4 A, C). Taken together, although we observe small differences between experimental and simulated data for some adhesion proteins, this type of analysis might seem to essentially suggest that adhesion protein nanoclusters are randomly distributed with respect to the fA edges.

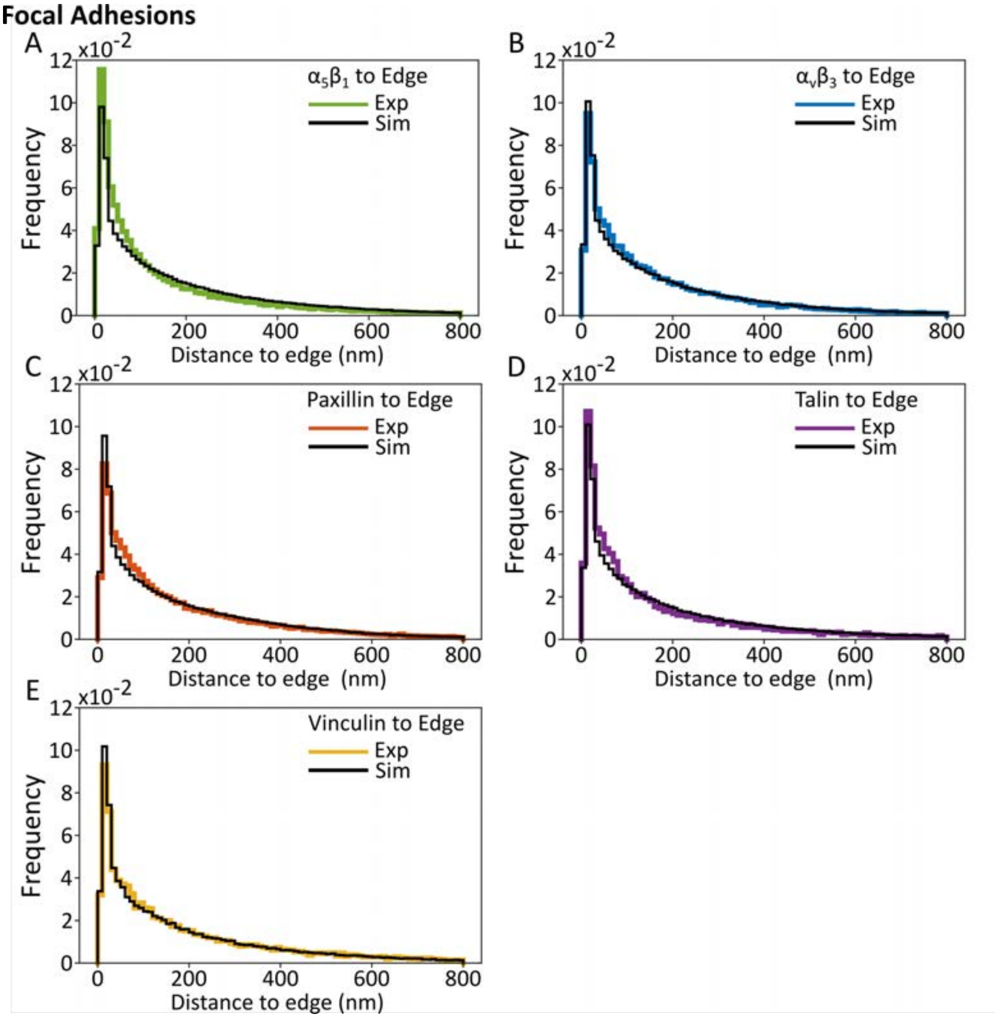

Figure 6.4 *Histograms of distance-to-edge distribution of adhesion protein clusters on FAs*
Distance-to-edge distributions obtained from DBSCAN-analysed STORM images of HFF-1 cells fixed 24 h after seeding. Each histogram represents the frequency distribution over all cells of the cluster distance-to-edge, that is, the NND between the cluster CoM and the FA edges. Experimental (Exp) data sets are shown as the coloured histograms in each panel, corresponding to $\alpha_5\beta_1$ (A, green), $\alpha_v\beta_3$ (B, blue), paxillin (C, orange), talin (D, purple), and vinculin (E, yellow), whereas the simulated random distributions (Sim) are respectively shown as black histograms in each panel. Bin width=10 nm.

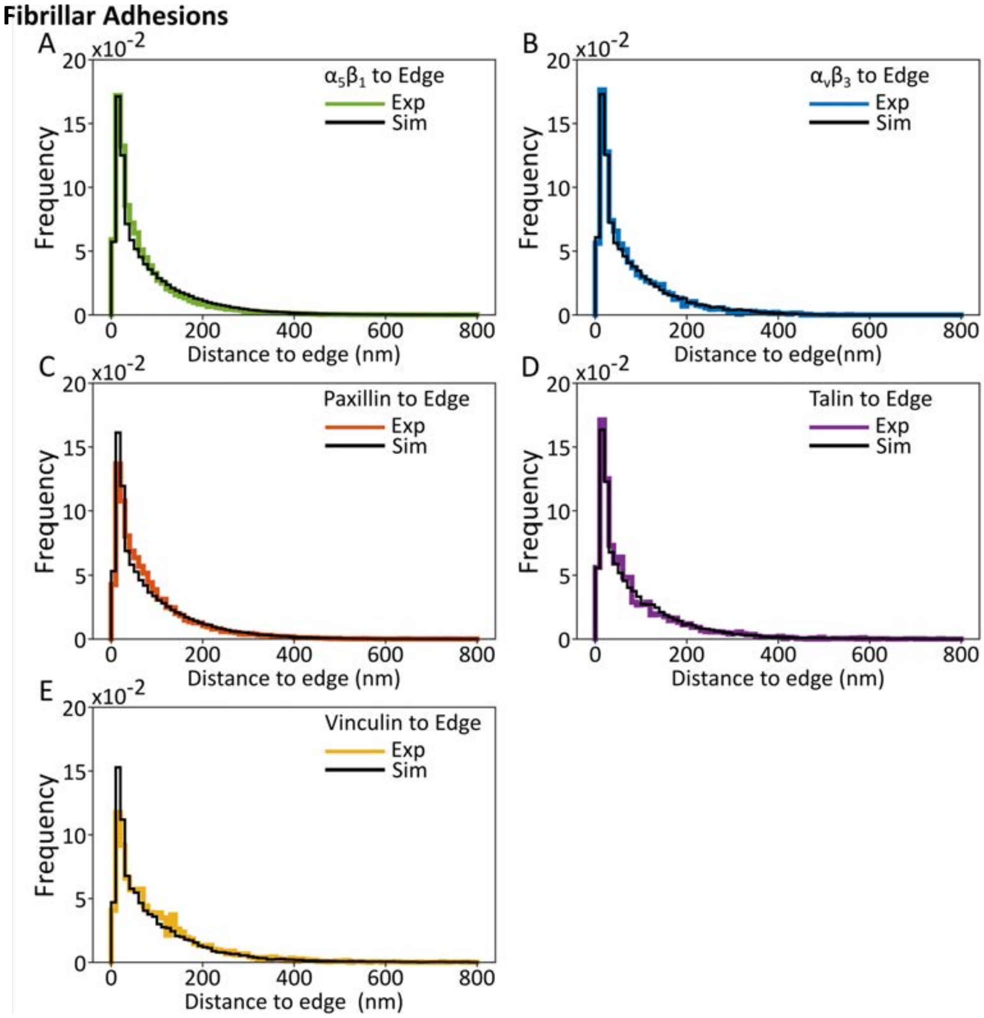

***Figure 6.5** Histograms of distance-to-edge distribution of adhesion protein clusters on fAs*

Distance-to-edge distributions obtained from DBSCAN-analysed STORM images of HFF-1 cells fixed 24 h after seeding. Each histogram represents the frequency distribution over all cells of the cluster distance-to-edge, that is, the NND between the cluster CoM of and the fA edges. Experimental (Exp) data sets are shown as the coloured histograms in each panel, corresponding to $\alpha_5\beta_1$ (A, green), $\alpha_v\beta_3$ (B, blue), paxillin (C, orange), talin (D, purple), and vinculin (E, yellow), whereas the simulated random distributions (Sim) are respectively shown as black histograms in each panel. Bin width=10 nm.

As mentioned above, representing the entire data distributions as histograms provides us with a very general overview of how the nanoclusters are distributed with respect to the adhesion edges. In order to investigate the details of these distributions and to allow us to carry out statistical analyses, we looked for single parameters that can globally characterise the population. We first computed the median values of the distance-to-edge per cell of both the experimental ($med(D2E_{exp})$) and simulated ($med(D2E_{sim})$) data sets, from which we calculated the relative difference between the medians, which we term the edge proximity factor (EPF) defined as:

$$EPF = \frac{(med(D2E_{exp}) - med(D2E_{sim}))}{med(D2E_{sim})}. \tag{6.1}$$

We calculated the EPF of each protein per cell in both FAs or fAs, Figure 6.6. With this data we aimed to establish two things: *(i)* if the distribution of nanoclusters for each protein was significantly different from random; and *(ii)* if our visual assessment that $\alpha_5\beta_1$ was more prone to being located on the edge of adhesions, compared the other four proteins analysed, was found to be quantitively significant. To test whether the distribution of EPF values was different from zero (the EPF value expected form a random distance-to-edge distribution), firstly, we ran a paired Student's t-test for each protein comparing the distance-to-edge distributions for the experimental data with the corresponding simulated data, see significance markers over each condition in Figure 6.6. Following that, having established that the median distance to the edge for clusters of $\alpha_5\beta_1$ was significantly shorter than predicted by random, we then ran a one-way ANOVA test on the EPF distributions for the five components, separating the cluster data depending on if they are from FA or fAs. This analysis provided us information about the differences between the distributions for each protein. However, we were only interested in how the four proteins $\alpha_v\beta_3$, paxillin, talin and vinculin, varied with respect to $\alpha_5\beta_1$, which was found to be closest to the edge. Therefore, from the final analysis we only show the significance of the variation for $\alpha_5\beta_1$ to each other protein, Figure 6.6.

This analysis showed that $\mathrm{EPF}\sim$-0.3 for $\alpha_5\beta_1$ clusters in FAs (green circles, Figure 6.6), meaning that the median distance from $\alpha_5\beta_1$ clusters to the edge of an FA was shorter than the one expected from a uniform distribution of clusters throughout the FA. Interestingly, we found that all the different proteins in FAs, with the exception of vinculin, exhibited negative median EPF values. These results thus indicate that both integrins, paxillin and talin preferentially locate close to FA edges, with $\alpha_5\beta_1$ being the most noticeable one. In the case of fAs, we found more variation across proteins: whereas $\alpha_5\beta_1$ and talin showed significant proximity to the fA edges, paxillin and vinculin appeared to be actively away from the edges, and $\alpha_v\beta_3$ was randomly distributed in fAs. Nevertheless, it is worth mentioning that the larger variations found across proteins in fAs might be partly due to their narrow and long shapes making the analysis more challenging.

We further assessed how each protein differed from the others, with a particular focus on the variation between $\alpha_5\beta_1$ and the other four proteins (Figure 6.6). We found that, although integrins, paxillin and talin were significantly closer to the edge than simulated data, the extent of the difference was significantly larger for $\alpha_5\beta_1$ as compared to the other proteins in FAs. We also found that the differences for clusters in fAs was less pronounced with a significant difference found between $\alpha_5\beta_1$ and paxillin and vinculin, both of which were found to be further away from the edges than predicted by simulations of random organisation. In addition, the difference for $\alpha_5\beta_1$ with $\alpha_v\beta_3$ or with talin were not significant (Figure 6.6, median value over the different cells, Table 2.6).

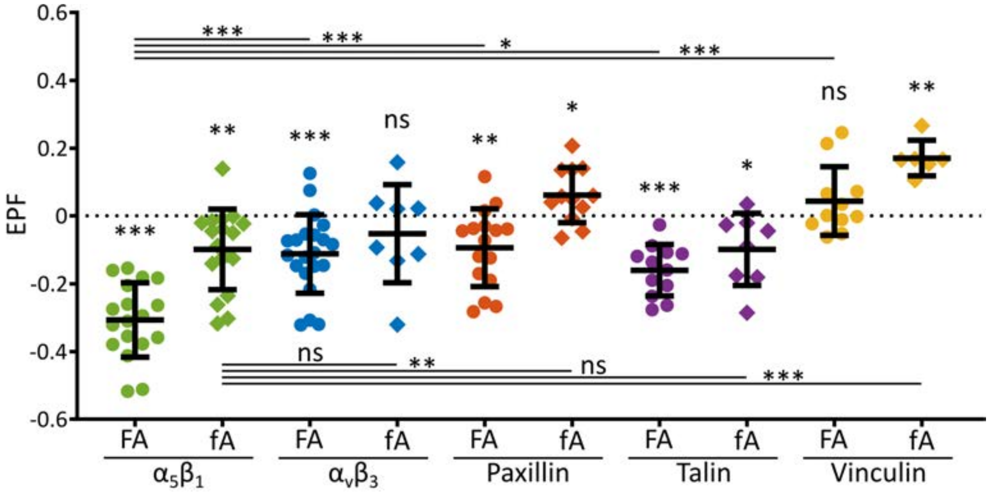

Figure 6.6 *The edge proximity factor (EPF) per cell imaged at 24 h after cell seeding*

EPF per cell for each of the proteins investigated, considering if they are in FAs or fAs. Data are shown as individual median values per cell together with the mean ± stdev superimposed in black. Statistical significance between different adhesion types and between different protein clusters was tested using a one-way ANOVA test (significance symbols shown on top of the bars connecting the different conditions) (see Methods section 6.2.5 for the details), whereas to test whether the experimental distribution is statistically different from a random distribution, i.e. if the EPF is statically different to zero, we used a paired Student's t-test to compare the experimental and simulated distributions of median distances to the edge (med(d2e)) (significance symbols shown on top of each EPF distribution), where ns = not significative, $p>0.05$; *, $p<0.05$; **, $p<0.01$; ***, $p<0.001$.

The data in Figure 6.6 indicates whether a protein's distribution is different from random and also whether that means clusters are enriched closer to (negative EPF) or further from (positive EPF) the adhesion edge, but this analysis does not provide us with information regarding the actual distances to the edge. In order to explore with more detail whether our experimental data differs from random and how that difference changes as a function of the distance-to-edge, we generated once more Δ-plots, which correspond to the difference between the shortest distance-to-edge (d2e) histograms of experimental and simulated data sets for each protein,

$$\Delta d2e = H_{exp}(d2e) - H_{sim}(d2e)\ . \tag{6.2}$$

In these plots, positive values indicate a larger population of nanoclusters at a given distance, compared to random organisation. The Δd2e plots conclusively show that the highest, positive peak appears for $\alpha_5\beta_1$ data at short distances from the edge (Figure 6.7). In the case of FAs, the most proximal distance where $\alpha_5\beta_1$ nanoclusters are enriched occurs at ∼20 nm, while for fAs this value is ∼40 nm (Figure 6.7 A). This analysis also showed that $\alpha_v\beta_3$, paxillin and talin clusters in FAs have distributions that vary from random (Figure 6.7 B,C,D), which according to the statistical tests ran on the EPF are significant, Figure 6.6. However, the Δd2e plots for $\alpha_v\beta_3$, paxillin and talin show very different shapes compared to the well-defined peak of $\alpha_5\beta_1$ data. With the Δd2e-plots it is now revealed that although the median distance-to-edge per cell, for $\alpha_v\beta_3$ and paxillin, was found to be shorter than what was predicted by random simulations the clusters are in fact excluded from the immediate adhesion edge. Instead, these Δd2e-plots reveal that the clusters populate a region between 40–100 nm from the edge. These Δd2e-plots provided additional information as compared to the plot of the relative difference between median distance to edge (Figure 6.6), they give us access to finer details, in terms of the preferred distances involved. For paxillin, our data shows the appearance of a negative trough at distances below 50 nm for both FAs and fAs. This negative trough indicates an exclusion of clusters from the edge of the adhesion with an enrichment at a distance of 50–100 nm. The data for vinculin, Figure 6.7 E, shows an apparent exclusion from the edge of adhesion with the negative values <50 nm. In the case of the vinculin plot for FA data we see that it fluctuates around zero indicating a random distribution which is also what we saw for EPF of vinculin in FAs, Figure 6.6.

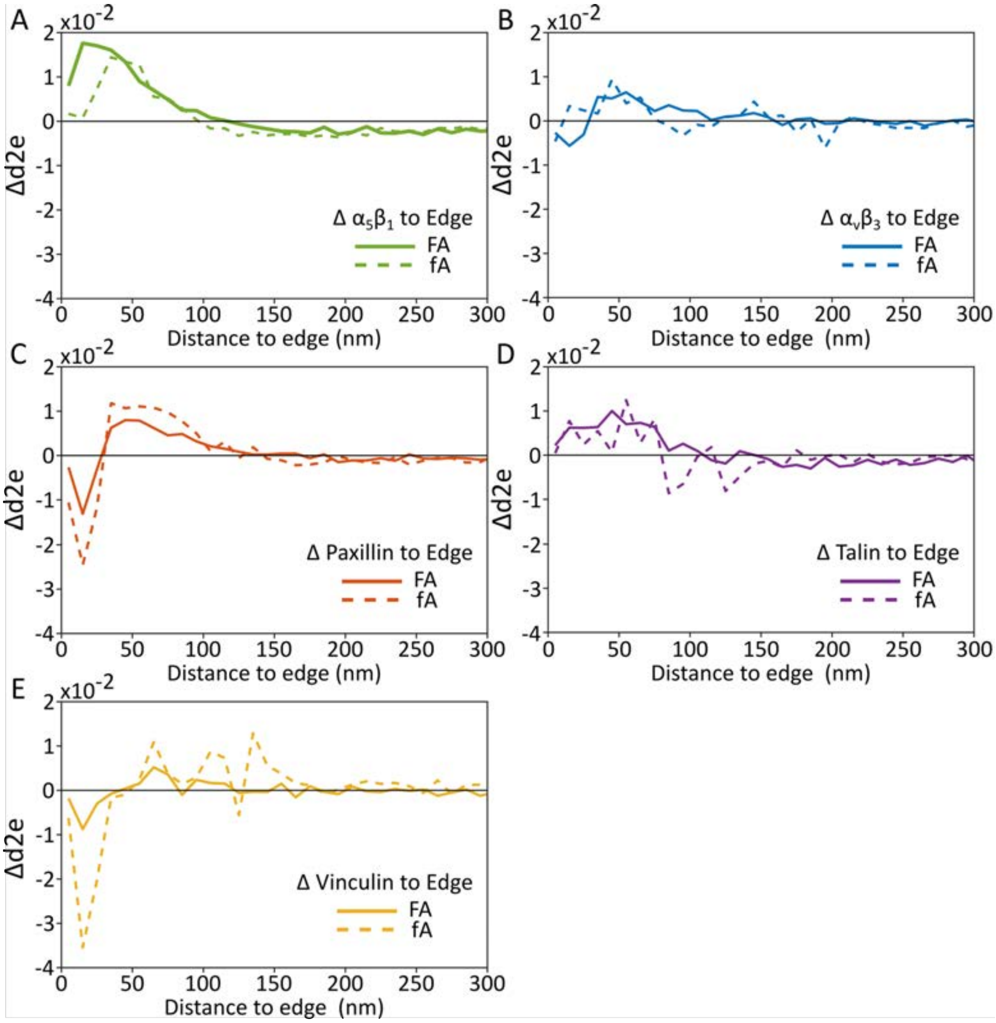

Figure 6.7 *Δd2e-plots for NND between nanoclusters and the edge of FAs or fAs in HFF-1 cells imaged at 24 h after plating*

Δd2e-plots for the FA (solid lines) and fA (dashed lines) computed from the data in Figure 4.3 and Figure 6.5, respectively. These plots show the variation from random in the distribution of distances to the edge for clusters of each of the proteins: $\alpha_5\beta_1$ (A, green), $\alpha_v\beta_3$ (B, blue), paxillin (C, orange), talin (D, purple), and vinculin (E, yellow).

6.3.4 Distance-to-edge of adhesion protein clusters as a function of spreading time

In the previous section, we investigated how adhesion protein nanoclusters are spatially organised with respect to the adhesion edges after 24 h of cell seeding. At that specific time point, cells reached a steady state characterised by full attachment and spreading. We next aimed at uncovering if and how the distribution and organisation of adhesion protein nanoclusters inside the adhesions evolved as a function of spreading time. To this end, we expanded our distance-to-edge analysis

(Δd2e-plots) in HFF-1 cells fixed at earlier time points after seeding (90 min and 3 h), and compared those results to the 24 h steady state condition (Figure 6.8).

We start by describing the Δd2e-plots corresponding to the nanocluster distribution on FAs (Figure 6.8 A, C, E). These results confirm that $\alpha_5\beta_1$ nanoclusters show the greatest level of mesoscopic re-organisation during the dynamic evolution of cell spreading, exhibiting the largest positive peaks amongst all the studied adhesion proteins (Figure 6.8 A, C, E). Notably, the position of this peak for $\alpha_5\beta_1$ nanoclusters shifts from being at ~50 nm from the edge at 90 min spreading time towards shorter distances (~15 nm) at 3 h and 24 h. We interpret this very short distance-to-edge as the clusters of $\alpha_5\beta_1$ being on the very edge of the FA delineating its boundary. Although our data show that $\alpha_v\beta_3$ clusters are slightly enriched at the edge at 90 min time point (Figure 6.8 A), this Δd2e-plot is quite noisy. Furthermore, at 3 h and 24 h this peak is not discernible and the positive values are much smaller than those for $\alpha_5\beta_1$ (Figure 6.8 C, E). The behaviour of paxillin observed in the 24 h condition (Figure 6.7 C) – exclusion of clusters from the very edge of FAs and a concomitant enrichment at distances of ~50 nm from the edge –, was maintained during the entire time evolution after cell seeding (Figure 6.8 A, C, E, orange lines).

We next analysed the Δd2e-plots for all the proteins in fAs. Notably, the Δd2e-plots of paxillin and vinculin consistently show the presence of a negative trough for distances to the edge below 50 nm (Figure 6.8 B, D, F, orange and yellow curves, respectively). These results indicate that these protein nanoclusters are partially depleted from the adhesion edges during the entire spreading process (from 90 min to 24 h after seeding). In addition, paxillin, vinculin, talin, and $\alpha_5\beta_1$ all exhibit a positive peak at ~40–75 nm from the edge (Figure 6.8 B, D, F). The Δd2e-plots for talin and $\alpha_v\beta_3$ in fAs show a noisier behaviour and show greater variation over time. In particular, the highest positive peak at ~25–30 nm from the edge is found at 3 h of cell spreading (Figure 6.8 D, purple and blue curves, respectively), and then vanish after 24 h of cell spreading (Figure 6.8 F).

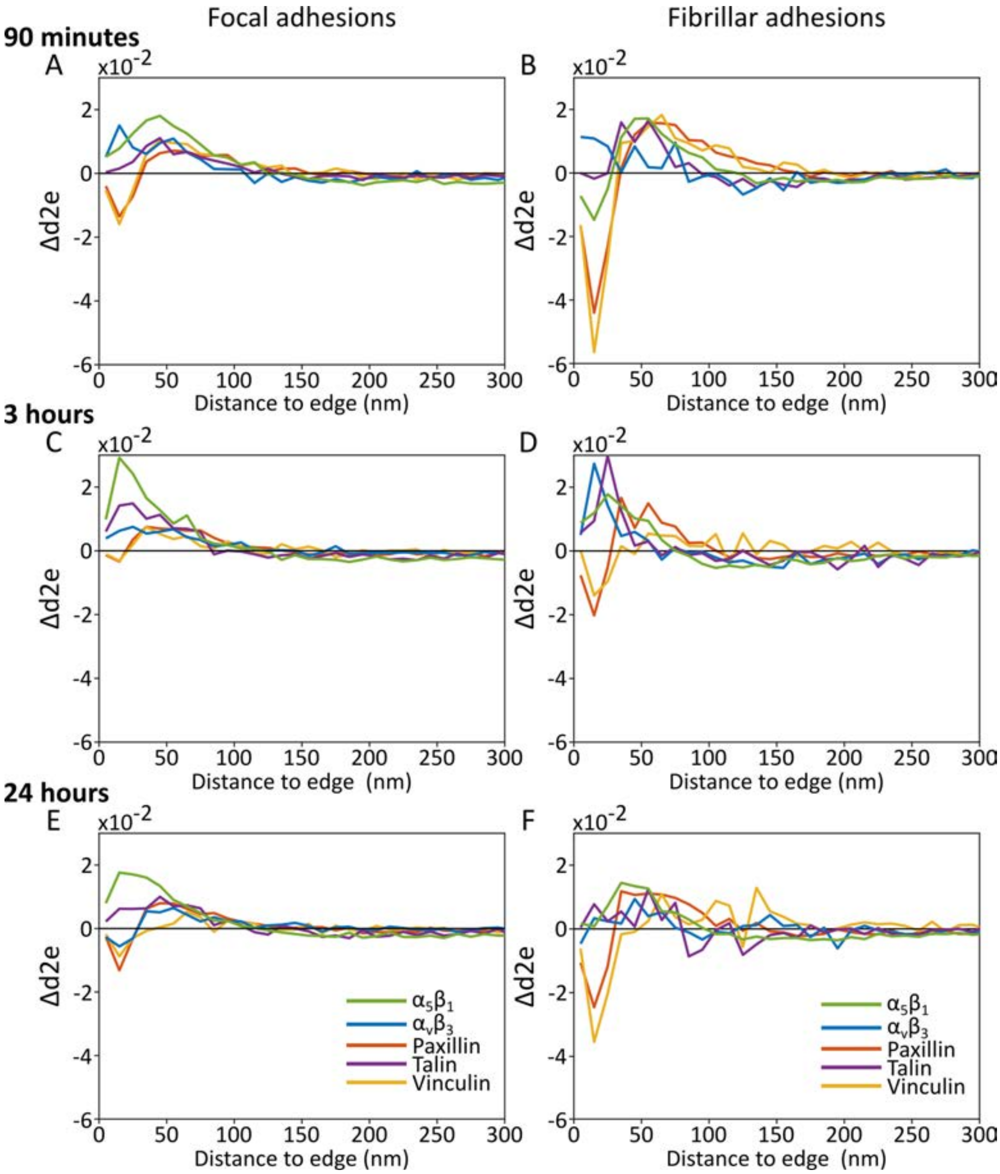

Figure 6.8 *Δd2e-plots for NND between nanoclusters and the edge of FAs or fAs in HFF-1 cells imaged at 90 min, 3 h and 24 h after plating*

Δd2e-plots for nanoclusters in FAs (A, C, E) or fAs (B, D, F) for each adhesion protein: $\alpha_5\beta_1$ (green), $\alpha_v\beta_3$ (blue), paxillin (orange), talin (purple), and vinculin (yellow). Cells were fixed and imaged by STORM at 90 min (A, B), 3 h (C, D), or 24 h (E, F) after seeding them on FN-coated coverslips.

Taken together, the results of our analysis at different times after cell seeding indicate that there is a non-random mesoscopic organisation of adhesion protein nanoclusters within adhesions. In particular, this degree of spatially non-uniform cluster organisation is most pronounced for the integrin $\alpha_5\beta_1$ in FAs, where it is found preferentially distributed on the edge of the adhesions, and for paxillin nanoclusters, which appeared to be enriched at regions between 50 and 100 nm away from FA edges. The Δd2e-plots for fAs show larger variations and fluctuations as function of cell seeding times. Since the analysis on fAs might be influenced by the elongated shape of these adhesion structures, making a distance-to-edge measurement difficult to interoperate, we restricted our next analyses solely to FA data.

6.3.5 *Distance-to-edge of adhesion protein nanoclusters as a function of intercluster distance*

Based on the results presented in the last two sections, we sought to investigate whether there is a correlation between the intercluster distances of different adhesion proteins and their location with respect to the adhesion edges in FAs. We hypothesised that nanoclusters found in close proximity to each other are likely to be engaged or interacting with one another in a functional manner. In order to define a "possible interacting distance" between nanoclusters, we took advantage of our data presented in Chapter 5 (section 5.3.4), which showed that the preferential distance between $\alpha_5\beta_1$ and paxillin nanoclusters is ∼70 nm (Figure 5.9). Therefore, we used a conservative threshold distance of 100 nm to separate "possibly interacting clusters" (with intercluster distances <100 nm) from un-engaged, non-interacting clusters (with interclusters distances >100 nm). This threshold distance allowed us to split our data in two groups of nanoclusters and separately analyse the distance-to-edge distributions for each subset. In this way, the analysis provides a means to test the possibility of a preferential positioning of proximal or engaged nanoclusters with respect to the adhesion edges.

We carried out the analysis for each pair of proteins imaged on FAs at three different spreading time points. We generated Δd2e-plots where we now consider separately those clusters with a partner protein nearest neighbour (NN) closer than 100 nm ("proximal to NN", light shaded bars of Figure 6.9–Figure 6.14) and the remaining clusters ("far from NN", dark shaded bars of Figure 6.9–Figure 6.14). Our results from the previous section showed a population of $\alpha_5\beta_1$ nanoclusters close to the FA edges (Figure 6.8 A, C, and E). We now realise that this population close to the edge is a mixture of $\alpha_5\beta_1$nanoclusters close to their NN and far away from their NN, regardless of the investigated adaptor (Figure 6.9–Figure 6.11, left panels). Moreover, when we considered the distance to the edge of the different adaptor proteins taking into account their proximity to $\alpha_5\beta_1$, we observed some interesting trends.

First, we found a population of paxillin nanoclusters in close proximity to their $\alpha_5\beta_1$ neighbours within a region of 30–130 nm to the FA edge (Figure 6.9). Moreover, these proximal $\alpha_5\beta_1$–paxillin nanoclusters shifted to regions closer to the FA edge as function of seeding time, being around ~85 nm at 90 min and ~55 nm, and 3 h respectively. It was then seen that at 24 h there was a reduction of this peak. Second, at 90 min and 3 h, talin nanoclusters found close to FA edges had a similar probability for being proximal or not, to $\alpha_5\beta_1$ nanoclusters (Figure 6.10). Interestingly, at 24 h, all the talin nanoclusters close to the FA edges are also proximal to $\alpha_5\beta_1$ nanoclusters. We found that the talin population close to their $\alpha_5\beta_1$ neighbour had a peak preferred distance to the edge of ~55 nm at 24 h, with the $\alpha_5\beta_1$ close to talin showing approximately the same peak. Finally, when $\alpha_5\beta_1$ was analysed together with vinculin, we detected a less dominant population of $\alpha_5\beta_1$ nanoclusters close to its vinculin NN, as compared to the other adaptors (Figure 6.11). When we considered the distance-to-edge for vinculin clusters, we saw an exclusion of nanoclusters from the immediate edge, (30–50 nm), at all three time points, regardless of their proximity to $\alpha_5\beta_1$. We also detected a population of proximal $\alpha_5\beta_1$-vinculin nanoclusters at ~45–135 nm from the FA edges at 90 min and 3 h, that reduced closed to zero at 4h after cell seeding.

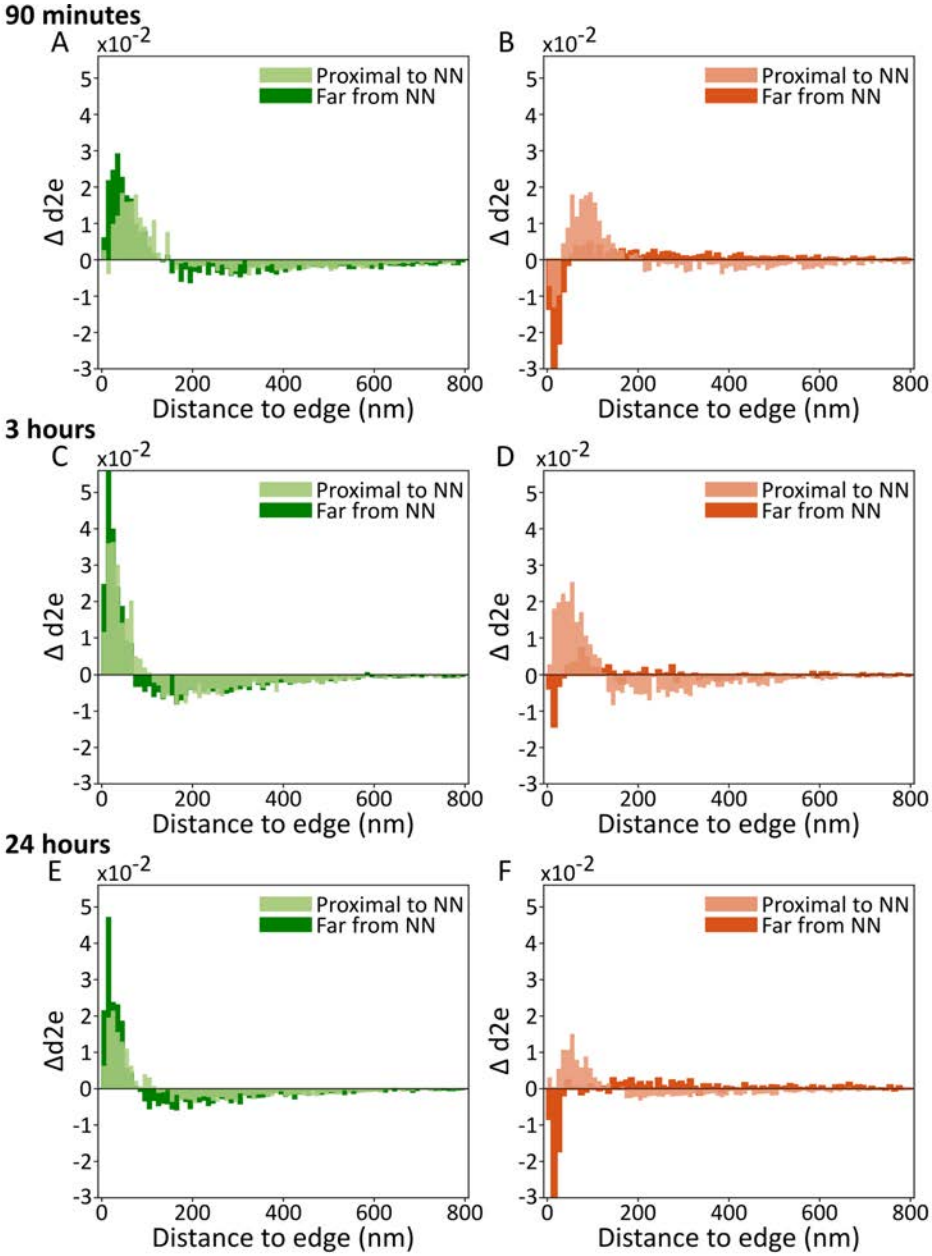

Figure 6.9 Δd2e-plots for the minimum distance to the edge of FAs of the $\alpha_5\beta_1$ and paxillin clusters, splitting the data between clusters that are proximal vs. far to its nearest neighbour (NN) partner protein cluster, for cells seeded for different times

Δd2e-plots of the distance-to-edge for clusters proximal to their partner NN, ($NND_{A\text{-}B}$ <100 nm; light-coloured bar plots) and for clusters far from their partner NN ($NND_{A\text{-}B}$ >100 nm; dark-coloured bar plots). (A,C,E) show distance-to-edge Δd2e-plots for $\alpha_5\beta_1$ clusters in FAs (green), considering their proximity to paxillin clusters. (B, D, F) show distance-to-edge Δd2e-plots for paxillin clusters in FAs (orange), considering their proximity to $\alpha_5\beta_1$ clusters. HFF-1 cells were fixed and imaged at 90 min (A,B), 3 h (C, D), or 24 h (E, F) after seeding on FN-coated glass.

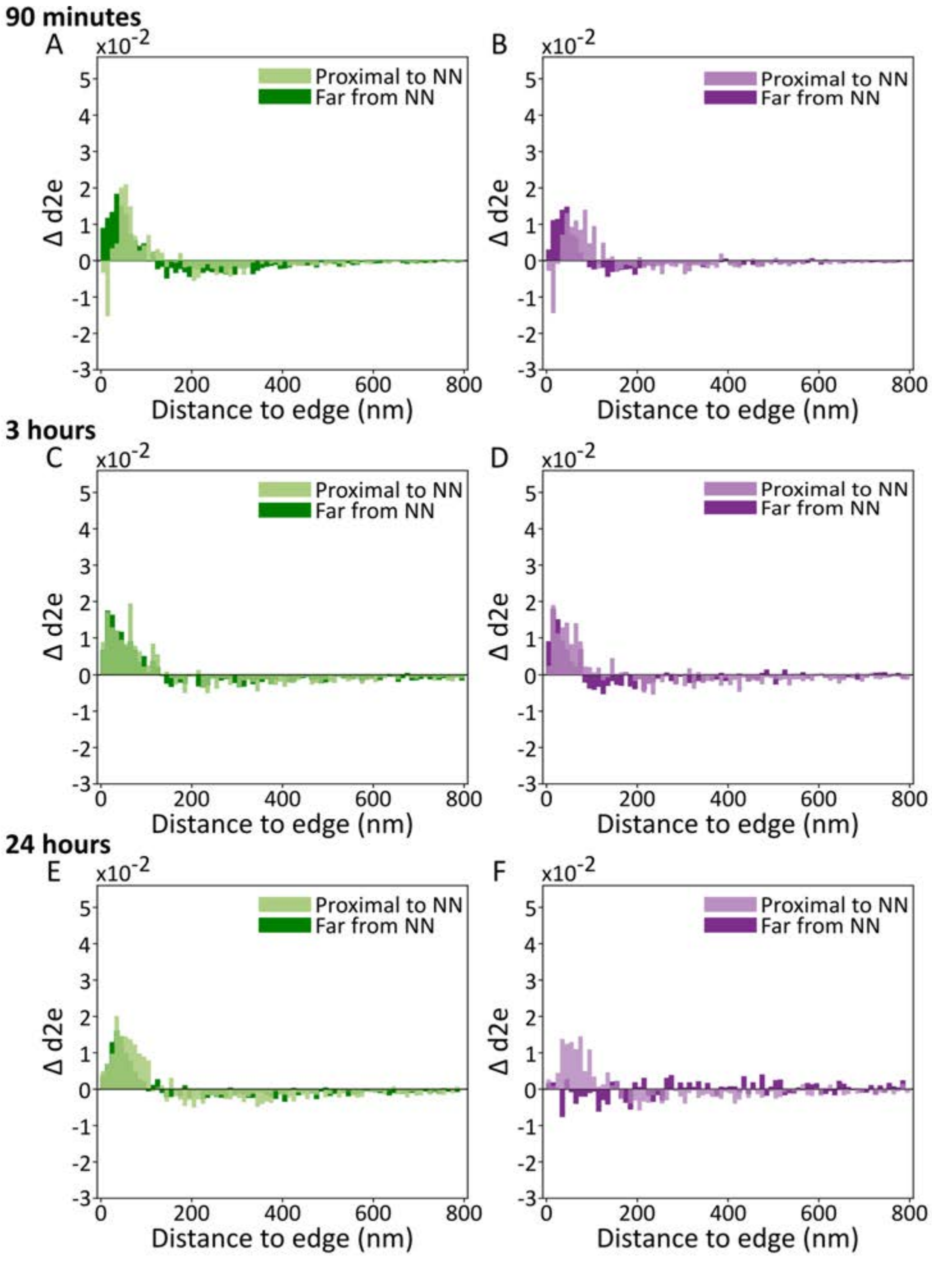

Figure 6.10 *Δd2e-plots for the minimum distance to the edge of FAs of the $\alpha_5\beta_1$ and talin clusters, splitting the data between clusters that are proximal vs. far to its nearest neighbour (NN) partner protein cluster, for cells seeded for different times*

Δd2e-plots of the distance-to-edge for clusters proximal to their partner NN, ($NND_{A\text{-}B}$ <100 nm; light-coloured bar plots) and for clusters far from their partner NN ($NND_{A\text{-}B}$ >100 nm; dark-coloured bar plots). (A,C,E) show distance-to-edge Δd2e-plots for $\alpha_5\beta_1$ clusters in FAs (green), considering their proximity to talin clusters. (B, D, F) show distance-to-edge Δd2e-plots for talin clusters in FAs (purple), considering their proximity to $\alpha_5\beta_1$ clusters. HFF-1 cells were fixed and imaged at 90min (A,B), 3 h (C, D), or 24 h (E, F) after seeding on FN-coated glass.

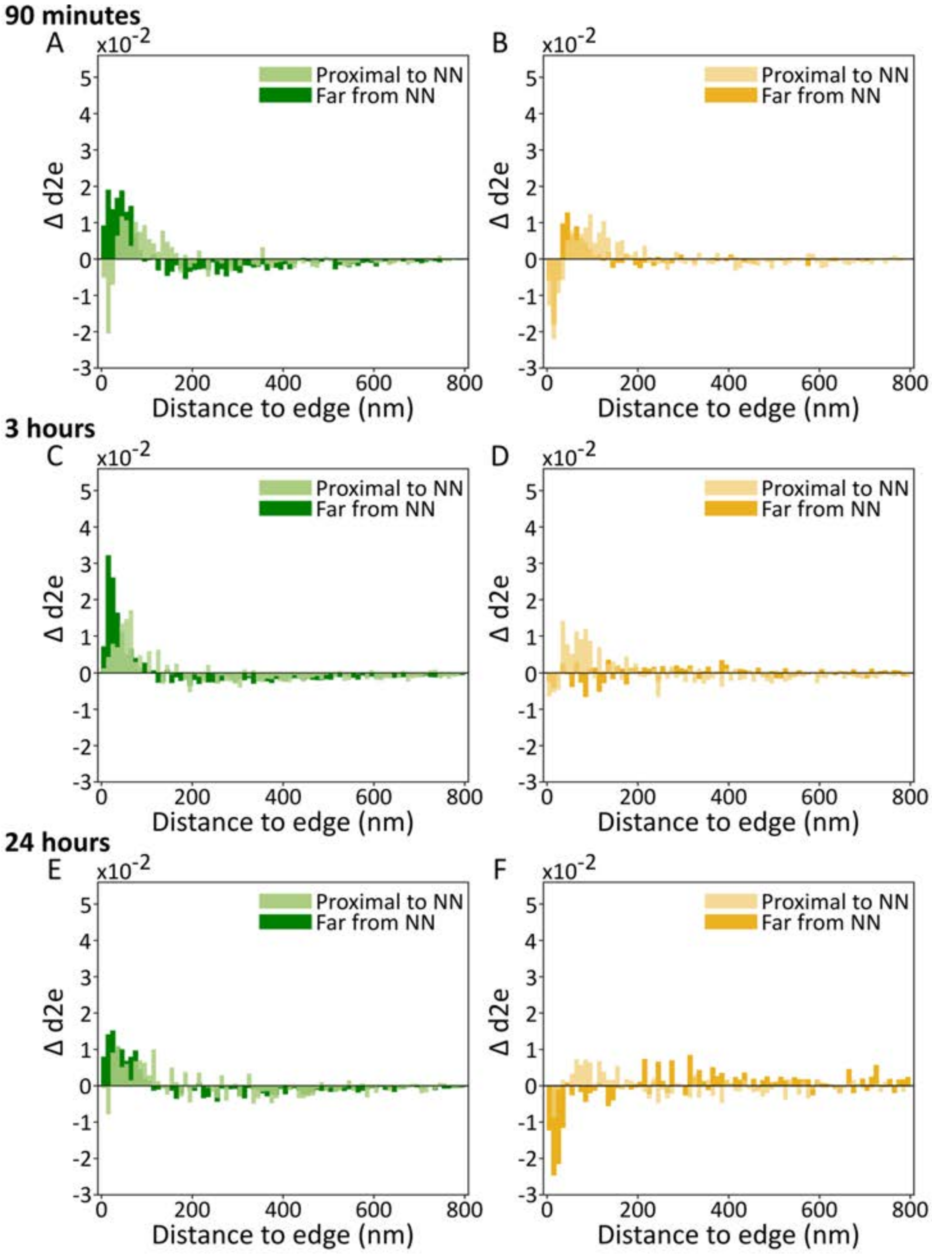

Figure 6.11 Δd2e-plots for the minimum distance to the edge of FAs of the $\alpha_5\beta_1$ and vinculin clusters, splitting the data between clusters that are proximal vs. far to its nearest neighbour (NN) partner protein cluster, for cells seeded for different times

Δd2e-plots of the distance-to-edge for clusters proximal to their partner NN, ($NND_{A\text{-}B}$ <100 nm; light-coloured bar plots) and for clusters far from their partner NN ($NND_{A\text{-}B}$ >100 nm; dark-coloured bar plots). (A,C,E) show distance-to-edge Δd2e-plots for $\alpha_5\beta_1$ clusters in FAs (green), considering their proximity to vinculin clusters. (B, D, F) show distance-to-edge Δd2e-plots for vinculin clusters in FAs (yellow), considering their proximity to $\alpha_5\beta_1$ clusters. HFF-1 cells were fixed and imaged at 90min (A,B), 3 h (C, D), or 24 h (E, F) after seeding on FN-coated glass.

In the case of $\alpha_v\beta_3$, we already showed in the previous sections that these nanoclusters had a reduced tendency to be enriched on the edge of adhesions, as compared to $\alpha_5\beta_1$ clusters. Yet, we aimed at establishing whether there are preferred regions within the adhesions where adaptors and $\alpha_v\beta_3$ clusters are found to be in close proximity, possibly engaging with one another. This analysis indicated that the majority of the $\alpha_v\beta_3$ integrin nanoclusters proximal to their NN adaptors were randomly distributed throughout the adhesion. Instead, the population of $\alpha_v\beta_3$ nanoclusters far from their NN were preferentially closer to the adhesion edges, in particular at early time points, 90 min and 3 h (Figure 6.12–Figure 6.14). Furthermore, paxillin clusters were preferentially found around 40–100 nm from the edge, regardless of their proximity to $\alpha_v\beta_3$ nanoclusters and seeding times (Figure 6.12). In the case of talin nanoclusters, our data indicated a higher preference for talin clusters non-proximal to $\alpha_v\beta_3$ to be at the very edge of FAs, at 3 h or 24 h time points (Figure 6.13 D, F, dark purple). By contrast, the talin clusters proximal to $\alpha_v\beta_3$ showed a close to random distribution in the FAs at early spreading times (90 min, 3 h) (Figure 6.13 B, D, light purple), which at 24 h evolved into a distribution with a higher preference for clusters to be in the region between 40–100 nm from the edge (light purple Figure 6.13 F). This trend is similar to that observed with the $\alpha_5\beta_1$-talin data (Figure 6.10 F, light purple). Finally, when we considered the vinculin-$\alpha_v\beta_3$ pair, our results most notably show that, while at 3 h and 24 h the Δd2e-plot distributions were noisy and close to random (Figure 6.14 C–F), at 90 min there was a population of both $\alpha_v\beta_3$-vinculin clusters enriched in the region between 40–140 nm from the edge (Figure 6.14 B), regardless of the proximity from vinculin to the integrin. Furthermore, $\alpha_v\beta_3$ also had a population close to the edge at 90 min (Figure 6.8 A, blue curve) and now we show that a larger population of these clusters, is distant from, and hence probably not engaged with, its vinculin NN (Figure 6.14 A, dark blue). In summary, when comparing the $\alpha_v\beta_3$ data with $\alpha_5\beta_1$ data we can state that $\alpha_v\beta_3$ clusters are generally distributed in a more random fashion. Moreover, the small population of $\alpha_v\beta_3$ clusters found close to FA edges did not appear to be in close proximity to any of the adaptor proteins investigated.

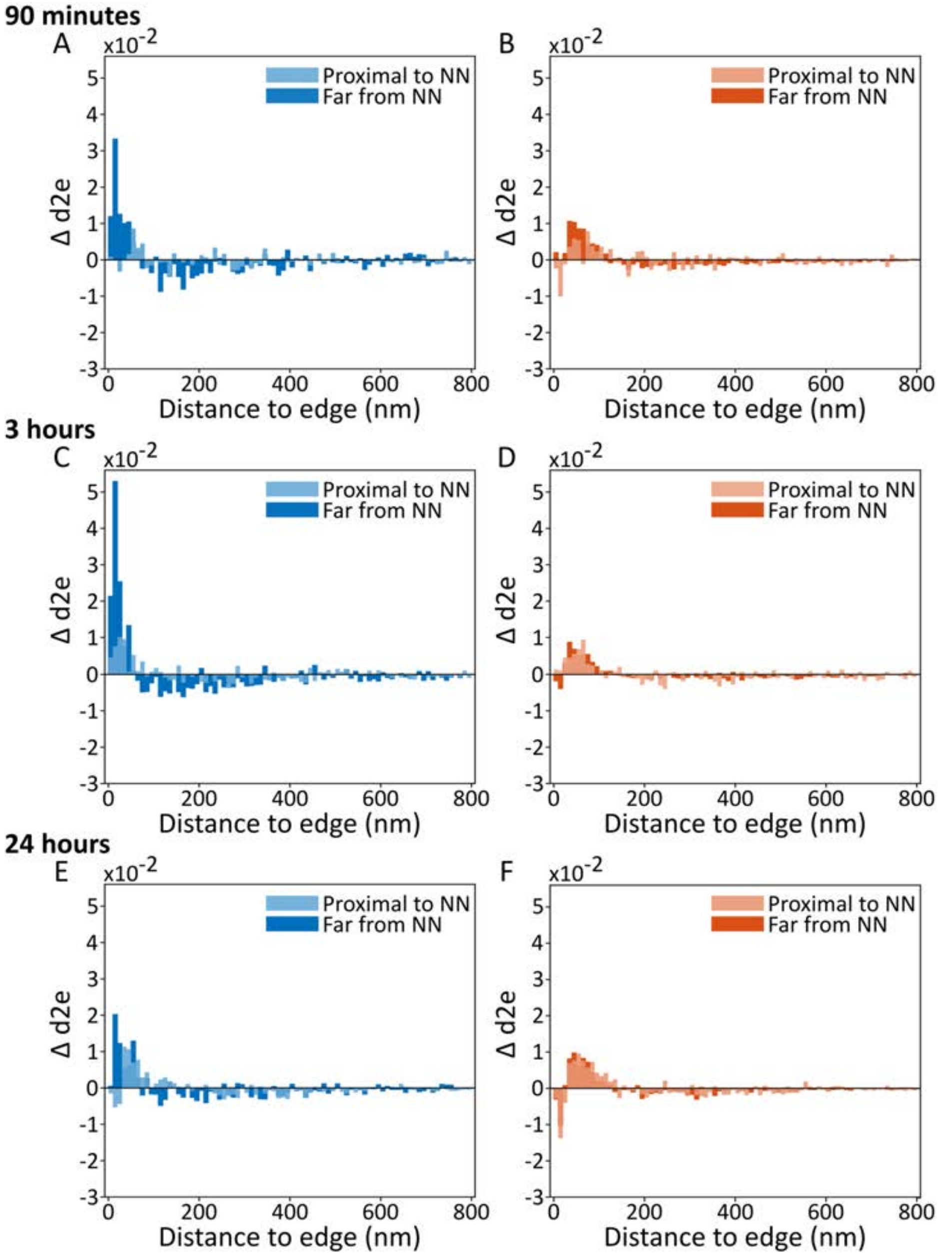

Figure 6.12 Δd2e-plots for the minimum distance to the edge of FAs of the $\alpha_v\beta_3$and paxillin clusters, splitting the data between clusters that are proximal vs. far to its nearest neighbour (NN) partner protein cluster, for cells seeded for different times

Δd2e-plots of the distance-to-edge for clusters proximal to their partner NN, ($NND_{A\text{-}B}$ <100 nm; light-coloured bar plots) and for clusters far from their partner NN ($NND_{A\text{-}B}$ >100 nm; dark-coloured bar plots). (A,C,E) show distance-to-edge Δd2e-plots for $\alpha_v\beta_3$ clusters in FAs (blue), considering their proximity to paxillin clusters. (B, D, F) show distance-to-edge Δd2e-plots for paxillin clusters in FAs (orange), considering their proximity to $\alpha_v\beta_3$ clusters. HFF-1 cells were fixed and imaged at 90 min (A,B), 3 h (C, D), or 24 h (E, F) after seeding on FN-coated glass.

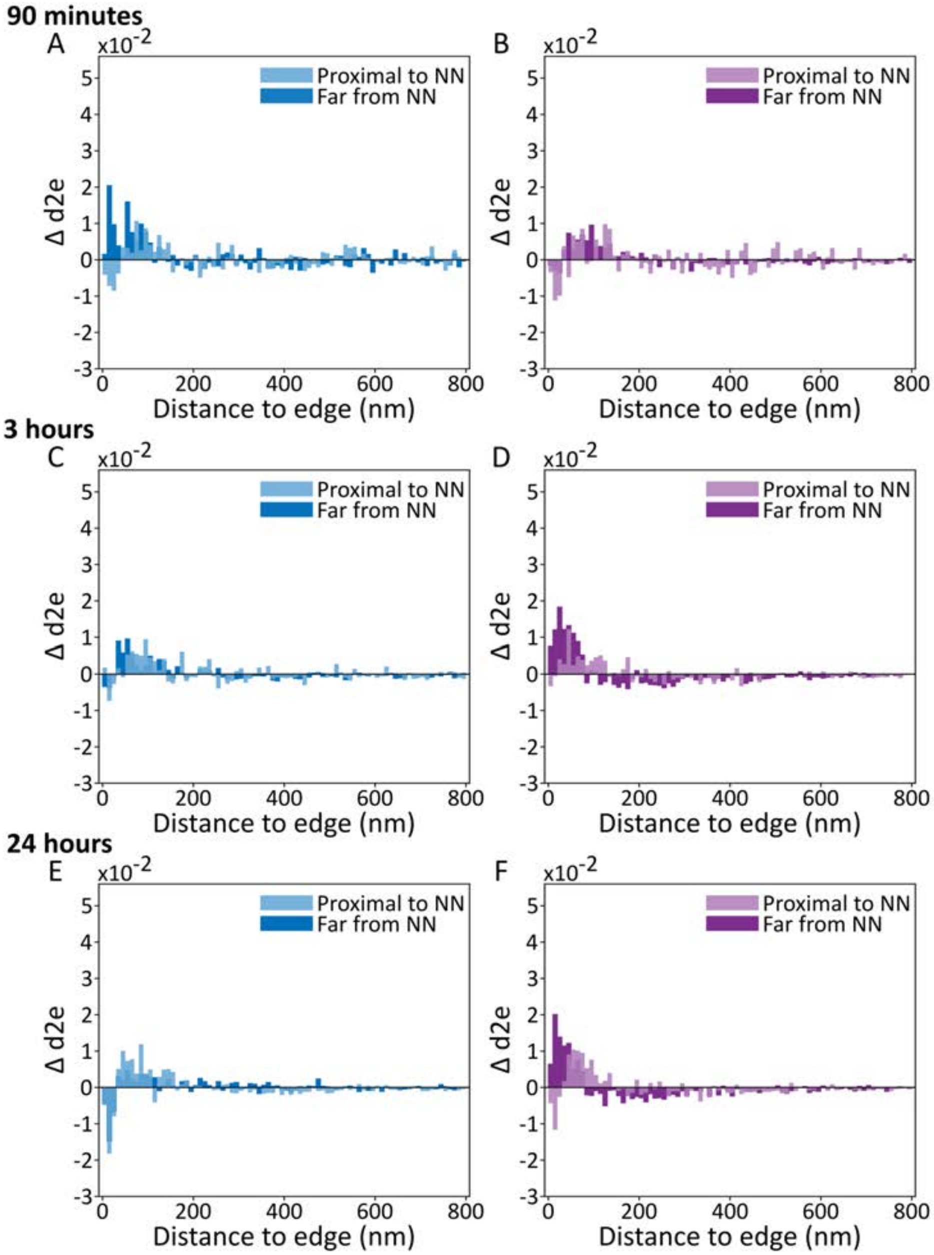

Figure 6.13 Δd2e-plots for the minimum distance to the edge of FAs of the $\alpha_v\beta_3$and talin clusters, splitting the data between clusters that are proximal vs. far to its nearest neighbour (NN) partner protein cluster, for cells seeded for different times

Δd2e-plots of the distance-to-edge for clusters proximal to their partner NN, ($NND_{A\text{-}B}$ <100 nm; light-coloured bar plots) and for clusters far from their partner NN ($NND_{A\text{-}B}$ >100 nm; dark-coloured bar plots). (A,C,E) show distance-to-edge Δd2e-plots for $\alpha_v\beta_3$ clusters in FAs (blue), considering their proximity to talin clusters. (B, D, F) show distance-to-edge Δd2e-plots for talin clusters in FAs (purple), considering their proximity to $\alpha_v\beta_3$ clusters. HFF-1 cells were fixed and imaged at 90 min (A,B), 3 h (C, D), or 24 h (E, F) after seeding on FN-coated glass.

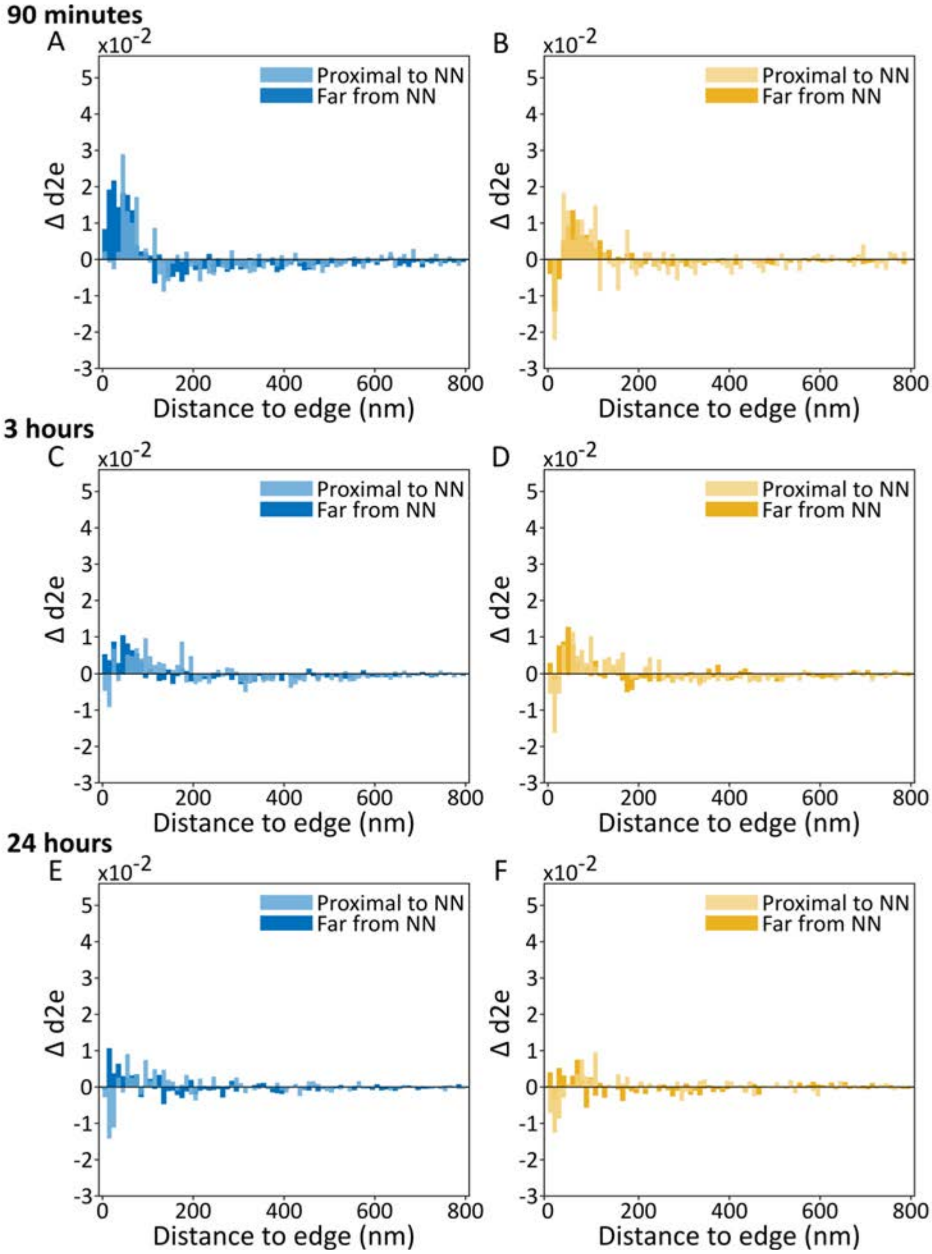

Figure 6.14 *Δd2e -plots for the minimum distance to the edge of FAs of the $\alpha_v\beta_3$ and vinculin clusters, splitting the data between clusters that are proximal vs. far to its nearest neighbour (NN) partner protein cluster, for cells seeded for different times*

Δd2e-plots of the distance-to-edge for clusters proximal to their partner NN, ($NND_{A\text{-}B}$ <100 nm; light-coloured bar plots) and for clusters far from their partner NN ($NND_{A\text{-}B}$ >100 nm; dark-coloured bar plots). (A,C,E) show distance-to-edge Δd2e-plots for $\alpha_v\beta_3$ clusters in FAs (blue), considering their proximity to vinculin clusters. (B, D, F) show distance-to-edge Δd2e-plots for vinculin clusters in FAs (yellow), considering their proximity to $\alpha_v\beta_3$ clusters. HFF-1 cells were fixed and imaged at 90 min (A,B), 3 h (C, D), or 24 h (E, F) after seeding on FN-coated glass.

Overall, in this section we showed that there is a greater level of spatial organisation of the integrin $\alpha_5\beta_1$ together with its adaptors than that observed for $\alpha_v\beta_3$. The adaptor proteins proximal to their $\alpha_5\beta_1$ NN were found to be preferentially in a region 40–100 nm away from the FA edges. Furthermore, the fraction of $\alpha_5\beta_1$ nanoclusters proximal to their adaptors were located at ~50 nm from the FAs. In strong contrast, $\alpha_v\beta_3$ nanoclusters exhibited a more random distribution within FAs, with only a very modest fraction being close to the FA edges and without any preference for being proximal to any of their adaptors.

6.4 Discussion

The results presented in this chapter provide strong evidence of a non-uniform mesoscopic organisation of adhesion protein nanoclusters in FAs, and that this organisation is distinct for the integrins $\alpha_5\beta_1$ and $\alpha_v\beta_3$. These findings, which to the best of our knowledge have not been reported before, may shed some light on the long-standing debate of the different roles of the two main FA integrins, $\alpha_5\beta_1$ and $\alpha_v\beta_3$. The first indication of this difference in organisation came from our findings that $\alpha_5\beta_1$ nanoclusters preferentially localise on the edge of FAs, where they form a ring-like structure similar to that observed for the adhesion protein Kank2 (Sun et al., 2016b). We first showed that the spatial organisation of $\alpha_5\beta_1$ nanoclusters in FAs is different from a random cluster distribution. Indeed, the median value of the distribution of distances between $\alpha_5\beta_1$ nanoclusters and the edge of the adhesion was significantly smaller than the corresponding value obtained from simulated data of random organisation. Moreover, this marked difference between the experimental and the simulated data for $\alpha_5\beta_1$ nanoclusters was significantly larger than the variation seen for other adhesion proteins or between nanoclusters in FAs and fAs (Figure 6.6). We next exploited the power of our quantitative analysis tools on STORM data to investigate in more detail how the different adhesion proteins organise in FAs and fAs. To that end, we computed Δd2e-plots – which characterise the deviation from a random distribution of clusters – of the different adhesion proteins in FAs and fAs in cells plated for 24 h on FN (Figure 6.7). The results of this analysis indicated that the comparison of random and simulated data for $\alpha_v\beta_3$, talin, and vinculin nanoclusters was not dependent of the type of adhesion (FAs or fAs). We saw that they had broader spreads and reduced peaks indicating that they are distributed in a close-to-random fashion (Figure 6.7 B, D, E). In contrast, the Δd2e-plots for paxillin and $\alpha_5\beta_1$ indicated a certain level of non-random cluster organisation. On the one hand, paxillin appeared to be excluded from the immediate edge in both FAs and fAs, with an enrichment of clusters in the region ~30–100 nm from the edge. On the other hand, we detected again a tendency for $\alpha_5\beta_1$ clusters to be more densely distributed on the edge of FAs (the region between 0–100 nm from the FA edge), with the highest abundance at 25–35 nm, or 35–45 nm from the edge of FAs or fAs, respectively. These observations have led us to propose that $\alpha_5\beta_1$ nanoclusters may define the edge of an adhesion as, the variation from random peaks at values ~25 nm from the edge, which corresponds to the median cluster radius, as described in Chapters 3.

$\alpha_5\beta_1$ has been shown to be the main integrin involved in the formation of fAs , which in turn have a characteristic linear organisation (Schaufler et al., 2016; Barber-Pérez et al., 2020). This idea agrees with our observations of the variation from random of $\alpha_5\beta_1$ clusters (with a peak distance at ~35 nm), because a random organisation of clusters seems unlikely due to the nature of the adhesions. Interestingly, when we investigated how the organisation of adhesion protein clusters evolved as a function of the spreading time, we found an opposite behaviour of the two integrins: while $\alpha_5\beta_1$ was found to be closer to the edge of FAs with time, $\alpha_v\beta_3$ transitioned to a more random distribution. We showed that the adaptors follow the same trend at $\alpha_v\beta_3$ with time, with the exception of talin, which appears to follow the trend of $\alpha_5\beta_1$ but to a somewhat lesser extent. These data allow us to suggest the possibility that the non-uniform organisation of $\alpha_5\beta_1$ in FAs is already established at early time points, when cells begin to establish strong adhesions with the substrate and are actively spreading, to then shift in a more pronounced manner towards the edge of the adhesion with time. By contrast, $\alpha_v\beta_3$ clusters lose the somewhat peripheral distribution in adhesions and become more randomly distributed with the progression of time after seeding. These results, in combination with previously published reports from other groups (Roca-Cusachs et al., 2009; Bharadwaj et al., 2017), strongly support the model in which these two integrins perform different roles in the adhesion complexes, where the function of $\alpha_5\beta_1$ requires a certain level of organisation and accumulation at the edge of FAs, in contrast to that of $\alpha_v\beta_3$, which is randomly organised, following a uniform distribution across the FAs.

In the final section of this chapter, we investigated possible correlations between the proximity of clusters of different proteins in relation to their spatial location within adhesions. The aim was to understand if there was a hierarchical, multi-level organisation of adhesion protein nanoclusters relative to each other and relative to the entire adhesion. Our data point towards the existence of a region within the first 100 nm from the adhesion edges – akin to the "FA belts" proposed by Fässler and colleagues (Sun et al., 2016b) – where clustered $\alpha_5\beta_1$ molecules are able to functionally interact with paxillin, talin, and, to a lesser extent, vinculin. We showed (Figure 6.9–Figure 6.14) that clusters of $\alpha_5\beta_1$, paxillin, talin and vinculin, are close to each other and more densely populating the 100 nm-wide FA belt. However, this trend is diminished or lost completely when considering the adaptors paired with $\alpha_v\beta_3$. We interpreted these data as an indication that $\alpha_5\beta_1$ together with its adaptors are forming a ring around the edge of adhesions where they are engaged. We propose that this is contributing to the cellular capacity to attach to the substrate in a similar way to the mechanism utilised by certain cell types – such as endothelial cells, osteoclasts, invasive cancer cells, or immune cells – in the formation of podosomes, actin-rich structures used by these cells to attach to their environment (Linder and Aepfelbacher, 2003; van den Dries et al., 2013). However, instead of the protrusion that is formed in the podosome core (Figure 6.15), we propose that $\alpha_v\beta_3$ together with a subpopulation of $\alpha_5\beta_1$ are found throughout the adhesion core to function in mechanosensing of the environment and in mechanotransduction, while a second population of $\alpha_5\beta_1$ forms this ribbon-shaped region at the periphery of the adhesions to enable firm attachment to the substrate (Figure 6.16). We hypothesise that this is made possible by the existence of $\alpha_5\beta_1$ in two distinct tensional states (Friedland et al., 2009) along with the different signalling cascades that lead to

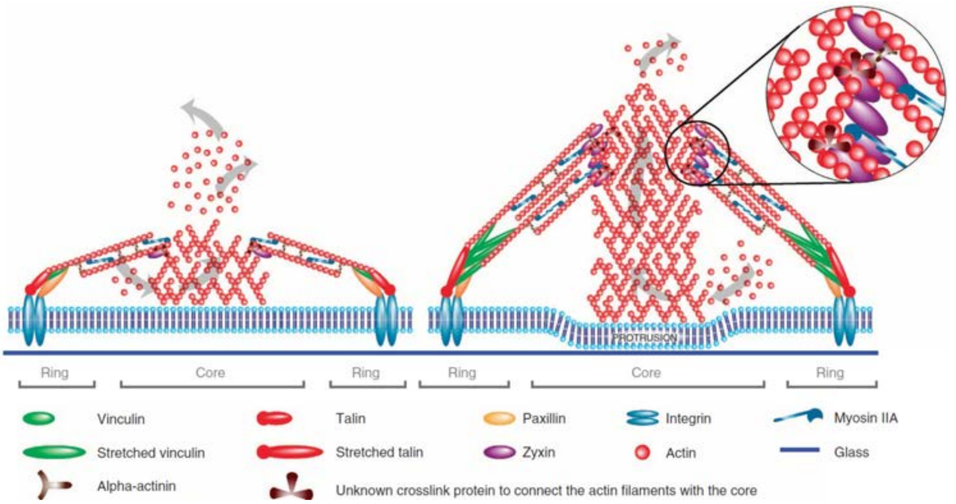

Figure 6.15 Model depicting the interplay of the actin network and myosin IIA at podosomes
Left podosome is in early stages of formation with paxillin and talin already at their maximum levels in the ring, while vinculin is at relatively low levels with the tension across the actin network. Zyxin is depicted as a linker between the core branched actin and the actomyosin machinery in the ring. Polymerisation of the branched actin is shown to occur close to the membrane while and in early stage the polymerisation at the membrane and depolymerisation at the other end, (depicted with grey arrows) at in a state where there is less polymerisation than depolymerisation. As the podosome matures and grows (right) the polymerisation of actin at the membrane is increased forcing the membrane down into the substrate, due to the stiff glass substrate here the branched actin is forced up transmitting force across the actomyosin and adaptors. This force induces increased recruitment of proteins such as vinculin and zyxin, figure was adapted from *van den Dries et al., 2013*.

myosin-dependent or independent force generation (Schiller et al., 2013). The study by Schiller et al. underscored the importance of regulating the two integrins in FAs. This has been studied by blocking one or other of the integrins and measuring aspects such as cell speed, directionality, cell area and FA area. It was shown that if either integrin is blocked a cell's speed increases however the directionality decreases. It was also shown that with only $\alpha_5\beta_1$ engaged, due to the blocking of $\alpha_v\beta_3$, the FA area was seen to be significantly larger than if neither integrin is blocked or only $\alpha_5\beta_1$ is blocked (Missirlis et al., 2016).

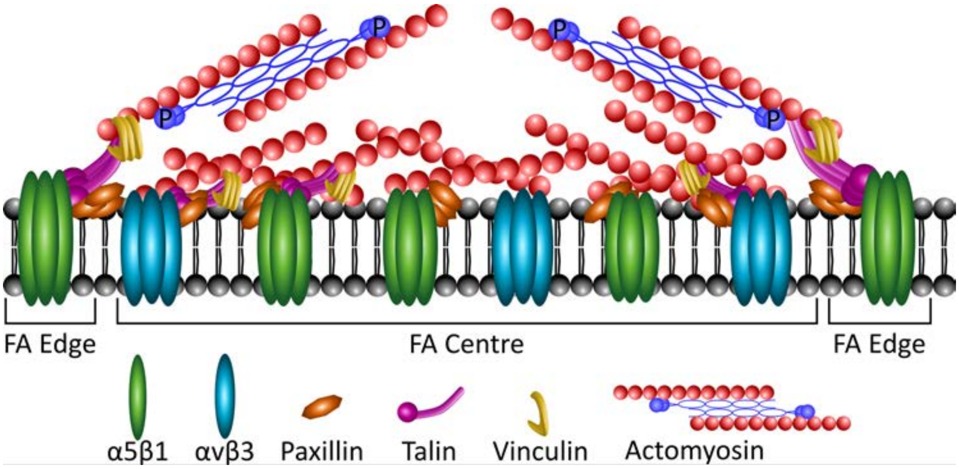

Figure 6.16 *Our working model for the organisation of integrin nanoclusters in adhesion complexes*

Schematic representation of a FA, showing the ring around the edge of the adhesion with clusters of $\alpha_5\beta_1$ (green) under tension due to the actomyosin machinery attached via paxillin (orange), talin (magenta), and vinculin (yellow). The core of the FA contains both $\alpha_5\beta_1$ and $\alpha_v\beta_3$, where in our model $\alpha_5\beta_1$ is in its relaxed, FN-bound state functioning in mechanosensing. Although, we have no direct evidence we consider the possibility that the core region contains actin possibly assembled via formins and or Arp2/3. Image based on *van den Dries et al., 2013*.

Although our current hypothesis is based on a number of different analyses, further experimental work will be required to test the predictions of our model. As a first step, we propose that simultaneous STORM imaging of the two integrins, $\alpha_5\beta_1$ and $\alpha_v\beta_3$, will serve to conclusively assess whether $\alpha_5\beta_1$ is the protein establishing the edges of the focal adhesion. By expanding this approach with the use of specific antibodies against active or inactive integrins, we will be able to decisively monitor which fraction of the proteins forming the ring are active and engaged. Secondly, we propose to further investigate the mechanisms of actin filament polymerisation involved in the process, which could be done by imaging myosin and mDia or other formins. If our reasoning is correct, we predict that we would see a greater tendency for phosphorylated myosin light chain, pMLC, to be found at the $\alpha_5\beta_1$ rings, whereas formins would be mainly present in the central areas of the adhesions. Another approach we can use to visualise actin is the recently developed polar-STORM technique, which combines in-plane single-molecule orientation measurements with super-resolution STORM imaging (Cruz et al., 2016). With polarisation sensitive imaging of actin, we should be able to identify different actin structures. If our hypothesis is true, with this technique, we would expect to see aligned actin filaments on the edge of FAs and disordered or branched actin in the central regions.

Chapter 7

Conclusions and Outlook

The overarching goal of this thesis has been to contribute to the understanding of the nanoscale lateral organisation of key proteins involved in adhesion complexes. For this, we exploited super-resolution STORM imaging and visualised with ultrahigh spatial resolution the lateral nanoscale organisation of five key components involved in adhesion complexes: the two integrins, $\alpha_5\beta_1$ and $\alpha_v\beta_3$, and three adaptor proteins, paxillin, talin, and vinculin. Along with extensive imaging, we also applied and developed different types of data analysis algorithms to bring quantitative understanding on the organisation of these adhesion proteins on different adhesive structures, in particular, focal adhesions and fibrillar adhesions. In this final chapter, we summarise our findings and discuss our working model, already proposed in Chapter 6, by placing it in the context of our own findings and pre-existing research in the field. Finally, we look to the future of research in our field and propose ways to build on our experimental results in order to gain a greater understanding on the biological mechanisms responsible for the control and organisation of cell-ECM adhesion complexes.

7.1 Main findings of our research

Despite the immense amount of work carried out over the last decades in the converging fields of integrin biology, adhesion complexes, and mechanobiology, we are still uncovering new fundamental details of how these topics are intertwined. The experiments and analyses presented in this thesis are our contribution towards a better understanding of these intricate biological processes. We believe that our work contributes to a more detailed insight of how the nanoscale organisation of integrins and their adaptor proteins influence the adhesion complexes and their role in mechanobiology. When we viewed our research in the context of prior publications, we found that our results agree and significantly expand on those earlier findings, allowing us to develop new hypotheses and to suggest potential lines for future research.

The first major finding of this thesis is that the five adhesion complex components we chose to study, $\alpha_5\beta_1$, $\alpha_v\beta_3$, paxillin, talin, and vinculin, all formed nanoclusters at the basal membrane of human fibroblast cells. We showed that these nanoclusters were of similar size (cluster area 1500–2000 nm^2) and it was maintained regardless of the time allowed for cell spreading. It has been recently shown that $\alpha_5\beta_1$ integrins are found as distinct active and inactive nanoclusters in FAs (Spiess et al., 2018). Our data, despite being carried out on the full integrin population, is in agreement with the findings of Spiess et al., in terms of the existence of nanoclustered integrins on the cell membrane and also their physical sizes. Our new findings in terms of the apparent independence of cluster sizes with cell seeding times, and the prevalence of nanoclustering for all the proteins investigated, suggest that these proteins form universal nanohubs that can serve for the efficient engagement to the extracellular matrix (ECM) in the adhesion complex.

Due to the similarities in the cluster sizes, we sought out other features that could reveal what influences the different roles of the key proteins in controlling cellular behaviour. Interestingly, we found that the number of nanoclusters per unit area (density of nanoclusters) increased with seeding time for $\alpha_5\beta_1$ and $\alpha_v\beta_3$ integrins – but not for the adaptor proteins – in both focal (FAs) and fibrillar (fAs) adhesions. Additionally, we found that at 90 min after cell seeding, there were twice as many clusters per unit area for $\alpha_5\beta_1$ as compared to $\alpha_v\beta_3$. We found the discrepancy between the density of the clusters of these two integrins interesting, as it suggests that, at earlier time points while the cell is still spreading uniformly, the role of $\alpha_5\beta_1$ seems to be dominant. Furthermore, our data showed that the density of $\alpha_v\beta_3$ nanoclusters increase by four-fold between 90 min and 24 h, which might indicate a functional switch for this integrin as the cell transitions from a uniformly-spreading state to the more elongated, polarized phenotype that is associated to migrating cells (Cavalcanti-Adam et al., 2007; Seetharaman and Etienne-Manneville, 2018). Thus, our results indicate that the relative nanoclustering density between both integrins as function of cell seeding times are strongly related to the cell state, i.e., from uniform cell spreading and adhesion, requiring a larger contribution from $\alpha_5\beta_1$ integrins, to polarisation and migration, where the role of $\alpha_v\beta_3$ becomes more important.

Regarding the adaptor proteins, the fact that they form nanoclusters at a constant density within adhesions regardless of the spreading time is intriguing, especially in view of the varying integrin cluster density data and the steady-state of the cell. A main role of the adaptor proteins is to engage with integrins to trigger signalling (Turner, 2000; Humphries et al., 2019) and to link and reinforce the linkage with the actin cytoskeleton (Humphries et al., 2007; Atherton et al., 2015). Our experimental data show that talin and vinculin both have a similar cluster density in adhesions (~10 clusters/μm^2) that is well-preserved across all spreading time points, which agrees with the idea that they work together to anchor integrins to actin and reinforce this link to withstand greater forces (Humphries et al., 2007; Zhang et al., 2008; Case et al., 2015; Rothenberg et al., 2018; Boujemaa-Paterski et al., 2020). Therefore, we suggest that the ratio of integrin to adaptor protein clusters can be interpreted as an indicator of the switch in cell behaviour. At early seeding times (90 min after plating), we found a ~1:1 ratio in the numbers of nanoclusters of integrins:talin (or vinculin), whereas at later time points (24 h), the ratio increases to ~3:1. We can rationalise these results by considering that, at any given time point, integrins can exist as active and inactive nanoclusters within adhesion complexes (Spiess et al., 2018). At early times after seeding (90 min) – when the cells are uniformly spreading (Figure 7.1 A) –, there would be a large adhesion-related activity that requires engagement with adaptors and, as a consequence, integrin activation. It therefore seems reasonable to expect that the ratio of active-to-inactive integrins is high, requiring full engagement of the adaptor proteins. By contrast, at later time points (our 24 h condition) (Figure 7.1 C) – when the cells are in a promigratory, polarised state – the FA formation is in a steady state, where new adhesions are formed in the leading edge while FAs are disassembled at the rear of the cell (Webb et al., 2002). Under such steady conditions, cells might undergo more dynamic transitions between engaged (active) and disengaged (inactive) integrins and therefore the ratio between active-inactive integrin clusters should decrease. Hence, it seems plausible that, although the total integrins:adaptor proteins ratio increases with time, the ratio between active integrins:adaptor proteins would remain approximately unaltered.

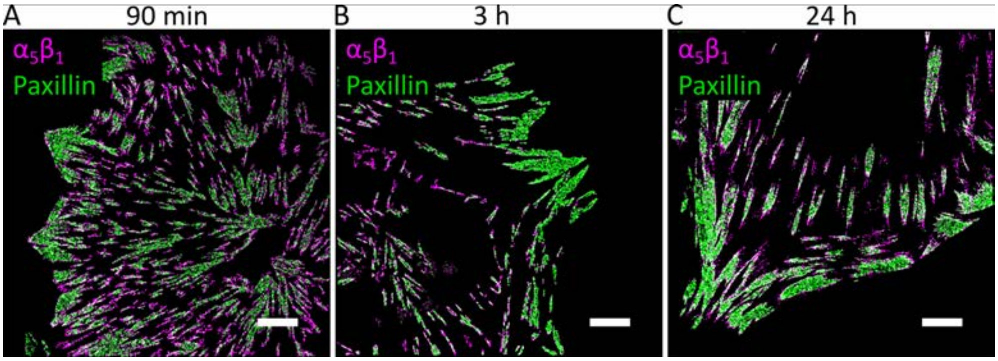

Figure 7.1 *Representative STORM images of fibroblasts at the different times after plating them on FN-coated glass*

STORM images of HFF-1 cells plated on FN-coated glass, and fixed at different times after seeding: 90 min (A), 3 h (B), and 24 h (C). The cells were stained for $\alpha_5\beta_1$ (magenta) and paxillin (green). At 90 min and 3 h, cells spread well and uniform. At 24 h, cell show clear polarisation. Scale bars: 5 µm.

There are numerous studies that used genetic approaches to investigate how key adhesion proteins and their mutual interactions control the integrity of FAs, the assembly stability and disassembly. To elucidate the specific roles of $\alpha_5\beta_1$ and $\alpha_v\beta_3$ integrins, Schiller et al. generated immortalized mouse kidney fibroblasts that were knocked-out for all integrins (pan-knock-outs), which they then transduced with individual integrins. Using this approach, they found that cells that only express $\alpha_5\beta_1$ spread very well, have more nascent adhesions and less FAs, whereas vice versa was seen for cells expressing only $\alpha_v\beta_3$ (Schiller et al., 2013). When both integrins were expressed, there was a middle ground indicating that the two integrins work together to maintain an equilibrium in terms of the numbers of nascent adhesions and FAs (Schiller et al., 2013). Interestingly, vinculin and its interaction with actin also play a role in controlling the maturation of adhesions, because vinculin knock-out cells present a reduced number of nascent adhesions and a significant increase in mature adhesions, leading to adhesion growth up to at least the intermediate adhesion phase (Thievessen et al., 2013). Other studies showed that even after the depletion of talin2 in talin1-null cells, cells undergo an initial phase of uniform spreading after seeding. However, when those talin-depleted cells are allowed to spread for 90 min, they stop spreading and instead, they round up (Zhang et al., 2008). These publications are some prime examples that highlight how important the balance between these proteins and their interactions is to control cell spreading and the interaction with the environment.

In Chapter 3, we also briefly explored potential mechanisms that could lead to the increased nanoclustering density of $\alpha_5\beta_1$ and $\alpha_v\beta_3$ in FAs as a function of spreading time. Amongst others, we particularly ruled out diffusion of integrins from the outside to the inside of adhesions. Although single particle tracking (SPT) studies have shown that integrins can freely diffuse outside adhesions and can enter adhesions to then become immobilised (Rossier et al., 2012; Rossier and Giannone, 2016; Tsunoyama et al., 2018), our STORM data on fixed cells do not support such mechanism as the primary one to increase integrin density in adhesions. Instead, our data are more consistent with the recruitment of integrins either from another region of the membrane (apical cell membrane) or from other cellular organelles, such as the endosomes – through which integrins recycle –, or the Golgi apparatus – from where newly-synthesised integrins are trafficked to the membrane (Moreno-Layseca et al., 2019). In the future, we think that working out the exact route and mechanism for the delivery of these integrins will be an important and interesting area of research. Along these lines, it has been shown that integrins are endocytosed by a number of different routes, such as by clathrin-mediated endocytosis during FA disassembly (Chao and Kunz, 2009), but also by clathrin-independent routes (Lakshminarayan et al., 2014), and that microtubules and their transport capabilities are involved in the stabilisation of adhesions localised at the trailing edge of migrating cells (Theisen et al., 2012). These earlier contributions provide specific targets to guide future work aimed at understanding how these proteins are delivered to the desired region of the cell membrane as the cell spreads and migrates.

In subsequent chapters, we exploited our DBSCAN cluster data by implementing a number of analytical tools to study nanocluster distributions and their organisation in adhesion complexes. Interestingly, we found that integrin nanoclusters and their adaptors are laterally segregated at a characteristic distance of at least ~55 nm inside adhesions, at each time point. These results led us to recall previous publications that focused on the importance of ligand spacing for efficient cell spreading. The results presented in those publications suggested the existence of a yet-to-be-identified molecular ruler that cells use to sense ligand spacing (Cavalcanti-Adam et al., 2006, 2007). More recently, the group of Roca-Cusachs proposed a different mechanism based on force loading on integrins to explain this critical ligand spacing (Oria et al., 2017). In this thesis, we have uncovered a similar lateral spacing trend but this time by directly studying the lateral organisation of the actual integrins on cells spread on surfaces homogeneously-coated with the ligand (FN). Although the mechanisms that determine the integrin cluster size and their intercluster separation remain poorly understood, we believe that the force balance between actomyosin contractility and substrate rigidity sensed by integrins could determine their critical lateral spacing, along the lines of the proposed model by Oria et al. Below this critical separation, the presence of integrins would be redundant and of no utility to the cell, and above that, FA and mechanotransduction would be compromised. It would be therefore particularly interesting to perform STORM imaging on cells seeded on substrates with different rigidity (or viscosity) and to address whether integrin spacing is indeed dependent on force sensing. An alternative mechanism of integrin spacing (along the lines of the existence of a molecular ruler) might involve the presence of GPI-anchored proteins inside adhesions. Indeed, it has been proposed that GPI-anchored proteins could influence integrin clustering in adhesions via vinculin and inner-leaflet phospholipids (Kalappurakkal et al., 2017). Dual-colour STORM imaging of integrins together with GPI-APs could directly address this hypothesis.

During the course of this research, we also studied the distribution of nanoclusters of different proteins with respect to each other. Strikingly, we found that adhesion protein nanoclusters distribute in a random fashion with respect to the clusters of the other adhesion proteins, with the exception of the $\alpha_5\beta_1$ and paxillin pair (Figure 5.9 – Figure 5.11). These data suggest that these two proteins can be closely interacting to trigger downstream signalling pathways. However, the random distribution of integrin $\alpha_5\beta_1$ and $\alpha_v\beta_3$ clusters with respect to talin and vinculin was surprising as we would have expected a closer proximity of these partners within adhesions. To rationalise these results, we must consider a number of factors related to integrins and the adaptor proteins, as well as our imaging conditions. From the side of the integrins, we know that integrins dynamically transit between different conformational states (Rossier et al., 2012), and they can be either active or inactive within the FAs (Spiess et al., 2018). Moreover, we also know from our own data that there is a lower nanocluster density of talin and vinculin as compared to the integrin availability inside adhesions, consistent with the results of Rossier et al. and Spiess et al. Thus, if at a given time, only a sub-population of integrins are actively engaged to their adaptor partners, the effective pool of active, and thus fully engaged integrins, could be washed out within the full distribution of proteins so that we are not able to detect a preferred proximity. In addition, we must also consider that we image just a single integrin species at the time together with one of the adaptors and, importantly, that we used pan-specific antibodies that label all integrin conformations. Together, these would further reduce our probability of detecting fully engaged integrins. We propose to overcome these limitations in the future by means of three different approaches. One, we could increase the specificity of our integrin labelling, by either using conformation-specific antibodies (that selectively detect active integrins) or cation treatments to increase the levels of activated integrins (Luo et al., 2007; Bakker et al., 2012; Rossier et al., 2012). Two, we could use cells that specifically express different mutants, resulting in dominant active forms of proteins such as talin and vinculin enabling us to evaluate how the conformational form of these proteins influences their distribution with respect to integrins. A third possibility would be to perform three-colour super-resolution imaging of the two integrins with a given adaptor. However, this still remains technically challenging, especially for STORM imaging, so we would have to consider other super-resolution techniques such as STED microscopy.

Finally, we focused on defining the distribution of protein nanoclusters with respect to the edges of adhesions, first by considering each protein independently, and second by studying if the distance between clusters of different protein pairs depended on their location within the adhesions. We showed that $\alpha_5\beta_1$ clusters were preferentially located at shorter distances to the adhesion edges. Interestingly, our data revealed that, as cells were settling on the substrate and spreading time progressed, there was a larger population of $\alpha_5\beta_1$ clusters closer to the edge, while $\alpha_v\beta_3$ clusters became more randomly distributed. Strikingly, we revealed a region, located at the periphery of FAs, where a relatively large population of $\alpha_5\beta_1$ clusters – but not of $\alpha_v\beta_3$ clusters – is in close proximity to the adaptor proteins talin, paxillin, and, to a lesser extent, vinculin. Thus, our results reveal the existence of a protein "ring" around FAs enriched with $\alpha_5\beta_1$, paxillin, talin, and vinculin nanoclusters and a more random distribution of all of these proteins in the central regions of FAs.

7.2 Working model

Before presenting our working model it is important to consider a number of key publications related to the crosstalk between integrins as well as the types and strengths of the bonds formed by integrins and their ligands (Li et al., 2003; Kong et al., 2009; Roca-Cusachs et al., 2009; Litvinov et al., 2011, 2019; Elosegui-Artola et al., 2016; Bharadwaj et al., 2017; Chen et al., 2017). In particular, single-molecule studies showed that the catch bonds formed between $\alpha_5\beta_1$ and FN and between $\alpha_v\beta_3$ and FN have different characteristics. While $\alpha_5\beta_1$ forms a catch bond with FN in the range of 10–30 pN with the peak lifetime at 7 s and a slip bond behaviour above that (Kong et al., 2009), $\alpha_v\beta_3$ and FN show a catch bond behaviour for relatively smaller forces, between 5–25 pN, with the peak life time at 5–6 s (Elosegui-Artola et al., 2016). The different behaviour of these molecular bonds could influence the specific roles of these two integrins in the adhesion. In addition, $\alpha_5\beta_1$ has been shown to exist in two active states, relaxed and tensioned, and the transition between these states is triggered upon force exertion either by myosin II or by external forces (Friedland et al., 2009). In the context of our results, this could indicate that $\alpha_5\beta_1$ has potentially two roles: a myosin II-dependent role, preferentially occurring at the edge of the FAs, and a myosin II-independent role located at the centre of the FAs. Also in 2009, Roca-Cusachs et al. presented evidence supporting the idea that $\alpha_5\beta_1$ plays a greater role in cell attachment while $\alpha_v\beta_3$ works together with talin to enable mechanotransduction (Roca-Cusachs et al., 2009). Furthermore, genetically-modified cells engineered to express only α_v-class integrins with β_1, only α_v-class, or only $\alpha_5\beta_1$, portrayed different cell attachment strengths after being in contact for 120 s with a functionalized surface: $\alpha_5\beta_1$ showed the largest detachment force (7 nN), whereas α_v-class-only-expressing cells showed the lowest force (3 nN), and the force in cells with α_v-class integrins in combination with β_1 lay in a middle ground (~4 nN) (Bharadwaj et al., 2017). Thus, putting all together, we suggest that the roles of $\alpha_5\beta_1$ and $\alpha_v\beta_3$ are influenced by their lateral organisation within the FA: $\alpha_5\beta_1$ on the edges of adhesions with a primary role in adhesion strengthening and $\alpha_v\beta_3$ randomly distributed throughout to enable efficient mechanosensing and mechanotransduction. Three pieces of information work well together to point towards $\alpha_v\beta_3$ having a primary role in mechanosensing and mechanotransduction: *(i)* the lower force threshold found for molecules of $\alpha_v\beta_3$ (Elosegui-Artola et al., 2016); *(ii)* as well as in FN-seeded cells that only express $\alpha_v\beta_3$ (Bharadwaj et al., 2017); and *(iii)* our results showing that $\alpha_v\beta_3$ is distributed throughout the adhesion in a random manner.

Interestingly, high-resolution time-lapse traction force microscopy has been used to characterise the distribution and dynamics of cell-generated forces exerted by individual mature FAs of cells seeded on a FN-coated polyacrylamide substrate (Plotnikov et al., 2012). Those results indicated the existence of two different types of force: a dynamic tugging traction and a stable traction. These forces localise differently inside FAs, with the stable traction acting at the adhesion centre and the dynamic tugging traction acting in the distal half of the adhesion. The traction behaviour in neighbouring adhesions is uncorrelated, indicating a localised interaction of individual FAs with their environment. This latter interaction depends on Rho-associated protein kinase (ROCK) signalling, and when ROCK was inhibited – which leads to reduced levels of MLC phosphorylation –, the FAs shifted their traction-exerting mode from a stable force to a tugging force generation (Plotnikov et al., 2012). We can take these avenues of research a step further by hypothesising that the different mechanical forces are linked to specific integrins and actin structures. Despite the absence of direct evidence in favour of this hypothesis, we suggest that there is grounds for it based on the observed correlations between the distinct localisation of the different forces inside the adhesion (Plotnikov et al., 2012) and our work showing the differential partitioning of the integrins $\alpha_v\beta_3$ and $\alpha_5\beta_1$ within FAs. Taking these pieces of evidence together, we propose that the segregation of the two integrins we observed could be indicative of their distinct roles in the adhesions (adhesion and mechanosensing).

Taking all of our findings together, we propose a working model to describe the lateral organisation of proteins at the nanoscale inside FAs in relation to their function (Figure 7.2). We postulate that (i) $\alpha_5\beta_1$, through the ring on the FA periphery, primarily functions for substrate attachment in its high tensional state; (ii) the $\alpha_v\beta_3$ and $\alpha_5\beta_1$ integrins in the central region of the FA undertake the role of mechanotransduction; and (iii) the difference in these roles is dictated by the distinct mechanical forces exerted on the integrins, depending on where they are located in the FAs, and for $\alpha_5\beta_1$ perhaps also on the difference in tensional state. In the upper part of the scheme in Figure 7.2, we show a representation of a FA containing nanoclusters of the proteins we studied at their relative cluster densities. The black inner ellipse in Figure 7.2 represents the approximate boundary between what we consider as the FA edge region and the central region. Within the edge region, there is an increase of $\alpha_5\beta_1$ clusters in closer proximity to paxillin, talin, and vinculin. When considering the axial distribution of components around these protein clusters at the FA periphery (bottom panel of Figure 7.2), we propose that the clusters of $\alpha_5\beta_1$ that interact with talin and vinculin also engage with paxillin and actomyosin filaments, similar to the organisation found in podosomes (see Figure 6.15 and van den Dries et al., 2013). In the central region of FAs, the adhesion protein clusters are more randomly organised, and thus, most probably engaged with shorter branched actin filaments rich in actin polymerising proteins like Arp2/3. With this picture in mind, we suggest that the peripheral FA ring shares some organisational and functional similarities with podosome rings, such as their engagement with the cellular actomyosin machinery and their primary role in the attachment of the cell to the substrate. By contrast, we propose that the more randomly-organised central area of the adhesion plays the major role in mechanotransduction, which is influenced by the type of actin involved.

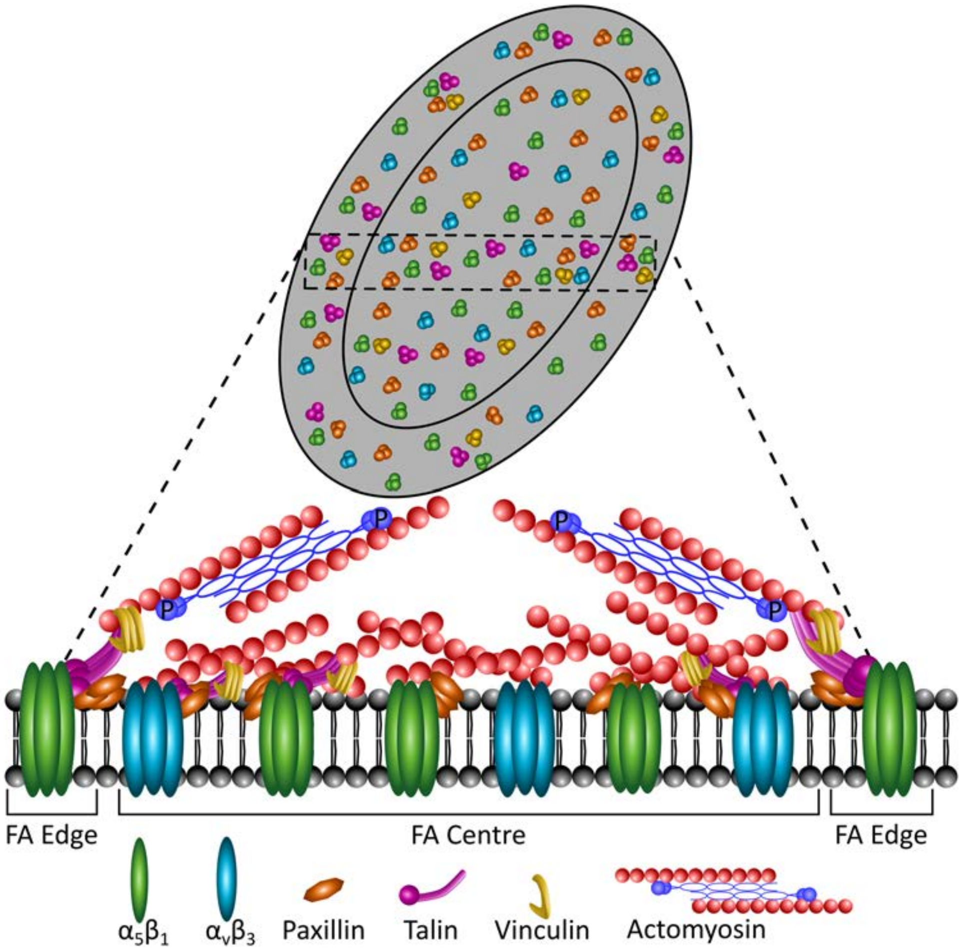

Figure 7.2 *Working model for the lateral distribution of proteins in FAs*
The upper half of the diagram represents an overview (top view) of the protein clusters found in a FA, where we maintained the relative median densities of clusters. The lower half of the diagram shows a more-detailed cross-sectional view (lateral view) of the dashed box in the top panel. The $\alpha_5\beta_1$ clusters (green) on the FA edge are in a very close proximity to the adaptor protein clusters and also to actomyosin filaments (red and blue). Those clusters in FA centre are more randomly distributed with respect to one another, with no active myosin to apply high forces to the integrins.

7.3 Outlook and future plans

The research presented in this thesis has not only validated and expanded previously published findings, but also opened more doors for further research. Firstly, it will be highly informative to visualise the nanoscale distribution of $\alpha_5\beta_1$ and $\alpha_v\beta_3$ with respect to each other, as well as the ratio of active to inactive integrin nanoclusters as a function of spreading time, to asses if it changes at the different stages of cell attachment and spreading. These questions can be approached experimentally with relative ease, by doing two-colour STORM imaging on fixed cells as described in this thesis. Perhaps the major potential issue here could be linked to sourcing a combination of compatible primary antibodies that specifically target the different integrins and integrin conformations. A second pressing question relates to actin organisation at the nanoscale within adhesion complexes. Are different actin polymerisation mechanisms favoured at different regions of the adhesion? To elucidate these questions, we propose to image the distribution of pMLC in the adhesions. In addition, it would be enlightening to image actin organisation within adhesions by using polarisation-sensitive super-resolution microscopy (Cruz et al., 2016).

Besides the questions that arose within the framework of this thesis, there are different avenues to explore adhesion complex formation in cells on a rigid environment. The experimental approach used in this work relied completely on imaging fixed cells. However, complementing our work with experimental approaches that can provide dynamic information of these structures and the interactions of their components in live cells, will be paramount to fully comprehend the inner workings of cell-ECM adhesions. Work from the Giannone and Kusumi labs already showed that it is possible to monitor the dynamics of individual integrins in FAs (Rossier et al., 2012; Tsunoyama et al., 2018; Orré et al., 2021). Our group has also explored the dynamics of various types of integrins expressed on cells of the immune system (Bakker et al., 2012; Borgman et al., 2014; Sosa-Costa et al., 2016). The next goal is to establishing multi-colour single-molecule tracking tools to simultaneously track both integrins together as well as monitoring the dynamics and interactions between integrins and adaptor proteins in living cells. Specifically, we will use genetically-encoded self-labelling tags, such as SNAP-tag (Gautier et al., 2008) and HaloTag (Los and Wood, 2006), fused to our proteins of interest. These tags can be labelled by specific ligands that can be conjugated with fluorescent dyes. We will use the new set of highly-photostable, membrane-permeable dyes of the family of Janelia Fluor dyes (Grimm et al., 2017). This approach will allow us to track the dynamics of cytosolic adaptor proteins in living cells at a single-molecule level by tuning the concentration of the dye-conjugated ligands to ensure sub-labelling conditions. We will then complement this approach in order to achieve dual-colour SPT by targeting a specific integrins with a Fab fragment conjugated to a compatible dye. With this combined approach, it is even possible to use a third fluorescent reporter, such as a fluorescently-tagged protein to mark the adhesion areas. We foresee that with the combined use of Fab fragments, SNAP-tag/HaloTag dye-conjugated ligands, and fluorescently-tagged proteins, we will be able to select the most suitable dyes that can render long SPT tracks and therefore allow us to study the dynamics of pairs of proteins (integrin/adaptor protein) and correlate their dynamic behaviour to their location on the membrane (e.g. inside or outside FAs).

A final research topic of great interest is to fully understand the mechanobiology of adhesion complexes at the nanometre scale. We plan to expand our research and study the static organisation and dynamic behaviour of adhesion complexes in cells plated on substrates of different mechanical properties. It is known that plating cells on different environments can trigger different signalling pathways, which can be especially important for stem cell differentiation (Engler et al., 2006; Kshitiz et al., 2012). In addition, seeding cells on substrates of various rigidities results in different phenotypes in terms of spreading and FA formation (Prager-Khoutorsky et al., 2011; Wong et al., 2014; Elosegui-Artola et al., 2016). Similar work has been carried out for cells seeded on ligand-containing lipid bilayers of different viscosities, so the ligand has a bilayer composition-dependent diffusion coefficient. The results of those experiments indicated that the ligand mobility influences the cells' ability to spread and form FAs (Bennett et al., 2018). However, these experiments were carried out using diffraction-limited confocal microscopy, so we aim in the future to be able to image the nanoscale organisation of FA proteins in cells interacting with different viscosities, with our super-resolution microscopy-based approach. Our aim is to decipher whether/how the distribution and/or formation of adhesion protein nanoclusters depend on the mobility of the ligand and the rigidity of the substrate. Ideally, we will also perform dual-colour SPT experiments on cells seeded on bilayers of different viscosity to study how the traction forces alter integrin dynamics.

We are convinced that the work presented in this thesis contributes to a greater understanding of how proteins of the adhesion complexes spatially organise at the nanoscale, and with that it has also become our guide for our future research. We are now truly immersed in the exciting field of mechanobiology and the future research possibilities are immense: from questioning if integrins are already clustered leaving the Golgi apparatus to understanding what controls the size and organisation of the clusters at the cell membrane and if perhaps GPI-anchored proteins are involved. Each new question that arises is as intriguing and exciting as the previous one.

Bibliography

Abbe, E. 1873. Beiträge zur Theorie des Mikroskops und der mikroskopischen Wahrnehmung. *Arch. für Mikroskopische Anat.* 9:413–468. doi:10.1007/BF02956173.

Abercrombie, M., J.E.M. Heaysman, and S.M. Pegrum. 1971. The locomotion of fibroblasts in culture. IV. Electron microscopy of the leading lamella. *Exp. Cell Res.* 67:359–367. doi:10.1016/0014-4827(71)90420-4.

Alexandrova, A.Y., K. Arnold, S. Schaub, J.M. Vasiliev, J.J. Meister, A.D. Bershadsky, and A.B. Verkhovsky. 2008. Comparative dynamics of retrograde actin flow and focal adhesions: Formation of nascent adhesions triggers transition from fast to slow flow. *PLoS One*. 3:1–9. doi:10.1371/journal.pone.0003234.

Arnold, M., E.A. Cavalcanti-Adam, R. Glass, J. Blümmel, W. Eck, M. Kantlehner, H. Kessler, and J.P. Spatz. 2004. Activation of integrin function by nanopatterned adhesive interfaces. *ChemPhysChem*. 5:383–388. doi:10.1002/cphc.200301014.

Atherton, P., B. Stutchbury, D.Y. Wang, D. Jethwa, R. Tsang, E. Meiler-Rodriguez, P. Wang, N. Bate, R. Zent, I.L. Barsukov, B.T. Goult, D.R. Critchley, and C. Ballestrem. 2015. Vinculin controls talin engagement with the actomyosin machinery. *Nat. Commun.* 6:1–12. doi:10.1038/ncomms10038.

Bachmann, M., M. Schäfer, V. V. Mykuliak, M. Ripamonti, L. Heiser, K. Weisenßruch, S. Krübel, C.M. Franz, V.P. Hytönen, B. Wehrle-Haller, and M. Bastmeyer. 2020. Induction of ligand promiscuity of αVβ3 integrin by mechanical force. 133.

Bakker, G.J., C. Eich, J.A. Torreno-Pina, R. Diez-Ahedo, G. Perez-Samper, T.S. Van Zanten, C.G. Figdor, A. Cambi, and M.F. Garcia-Parajo. 2012. Lateral mobility of individual integrin nanoclusters orchestrates the onset for leukocyte adhesion. *Proc. Natl. Acad. Sci. U. S. A.* 109:4869–4874. doi:10.1073/pnas.1116425109.

Bakolitsa, C., D.M. Cohen, L.A. Bankston, A.A. Bobkov, G.W. Dadwell, L. Jennings, D.R. Crithcley, S.W. Craig, and R.C. Liddington. 2004. Structural basis for vinculin activation at sites of cell adhesion. *Nature*. 430:583–586. doi:10.1038/nature02610.

Barber-Pérez, N., M. Georgiadou, C. Guzmán, A. Isomursu, H. Hamidi, and J. Ivaska. 2020. Mechano-responsiveness of fibrillar adhesions on stiffness-gradient gels. *J. Cell Sci.* 133:1–11. doi:10.1242/JCS.242909.

Bates, M., T.R. Blosser, and X. Zhuang. 2005. Short-Range Spectroscopic Ruler Based on a Single-Molecule Optical Switch. *Phys. Rev. Lett.* 94:108101. doi:10.1103/PhysRevLett.94.108101.

Bennett, M., M. Cantini, J. Reboud, J.M. Cooper, P. Roca-Cusachs, and M. Salmeron-Sanchez. 2018. Molecular clutch drives cell response to surface viscosity. *Proc. Natl. Acad. Sci.* 115:1192–1197. doi:10.1073/pnas.1710653115.

Betzig, E., G.H. Patterson, R. Sougrat, O.W. Lindwasser, S. Olenych, J.S. Bonifacino, M.W.

Davidson, J. Lippincott-schwartz, and H.F. Hess. 2006. Imaging Intracellular Fluorescent Proteins at Nanometer Resolution. *Sc*. 313:1642–1646. doi:10.1126/science.1127344.

Bharadwaj, M., N. Strohmeyer, G.P. Colo, J. Helenius, N. Beerenwinkel, H.B. Schiller, R. Fässler, and D.J. Müller. 2017. Av-Class Integrins Exert Dual Roles on A5B1 Integrins To Strengthen Adhesion To Fibronectin. *Nat. Commun.* 8:14348. doi:10.1038/ncomms14348.

Borgman, K.J.E., G. Flórez-Grau, M.A. Ricci, C. Manzo, M. Lakadamyali, A. Cambi, D. Benítez-Ribas, F. Campelo, and M.F. Garcia-Parajo. 2020. Membrane receptor MerTK is a newly identified transcriptional regulator that associates to chromatin as nanoclusters during human DC differentiation. *bioRxiv*. doi:10.1101/2020.04.16.044974.

Borgman, K.J.E., T.S. Van Zanten, C. Manzo, R. Cabezón, A. Cambi, D. Benítez-Ribas, and M.F. Garcia-Parajo. 2014. Priming by chemokines restricts lateral mobility of the adhesion receptor LFA-1 and restores adhesion to ICAM-1 nano-aggregates on human mature dendritic cells. *PLoS One*. 9:1–11. doi:10.1371/journal.pone.0099589.

Böttcher, R.T., M. Veelders, P. Rombaut, J. Faix, M. Theodosiou, T.E. Stradal, K. Rottner, R. Zent, F. Herzog, and R. Fässler. 2017. Kindlin-2 recruits paxillin and Arp2/3 to promote membrane protrusions during initial cell spreading. *J. Cell Biol.* 216:3785–3798. doi:10.1083/jcb.201701176.

Boujemaa-Paterski, R., B. Martins, M. Eibauer, C.T. Beales, B. Geiger, and O. Medalia. 2020. Talin-activated vinculin interacts with branched actin networks to initiate bundles. *Elife*. 9:1–26. doi:10.7554/eLife.53990.

Brown, M.C., J.A. Perrotta, and C.E. Turner. 1996. Identification of LIM3 as the principal determinant of paxillin focal adhesion localization and characterization of a novel motif on paxillin directing vinculin and focal adhesion kinase binding. *J. Cell Biol.* 135:1109–1123. doi:10.1083/jcb.135.4.1109.

Cai, D., S.C. Chen, M. Prasad, L. He, X. Wang, V. Choesmel-Cadamuro, J.K. Sawyer, G. Danuser, and D.J. Montell. 2014. Mechanical feedback through E-cadherin promotes direction sensing during collective cell migration. *Cell*. 157:1146–1159. doi:10.1016/j.cell.2014.03.045.

Calderwood, D.A., and M.H. Ginsberg. 2003. Talin forges the links between integrins and actin. *Nat. Cell Biol.* 5:694–697. doi:10.1038/ncb0803-694.

Calderwood, D.A., R. Zent, R. Grant, D.J.G. Rees, R.O. Hynes, and M.H. Ginsberg. 1999. The talin head domain binds to integrin β subunit cytoplasmic tails and regulates integrin activation. *J. Biol. Chem.* 274:28071–28074. doi:10.1074/jbc.274.40.28071.

Calle, Y., N.O. Carragher, A.J. Thrasher, and G.E. Jones. 2006. Inhibition of calpain stabilises podosomes and impairs dendritic cell motility. *J. Cell Sci.* 119:2375–2385. doi:10.1242/jcs.02939.

Case, L.B., M.A. Baird, G. Shtengel, S.L. Campbell, H.F. Hess, M.W. Davidson, and C.M. Waterman. 2015. Molecular mechanism of vinculin activation and nanoscale spatial organization in focal adhesions. *Nat. Cell Biol.* 17:880–892. doi:10.1038/ncb3180.

Cavalcanti-Adam, E.A., A. Micoulet, J. Blümmel, J. Auernheimer, H. Kessler, and J.P. Spatz. 2006. Lateral spacing of integrin ligands influences cell spreading and focal adhesion assembly. *Eur. J. Cell Biol.* 85:219–224. doi:10.1016/j.ejcb.2005.09.011.

Cavalcanti-Adam, E.A., T. Volberg, A. Micoulet, H. Kessler, B. Geiger, and J.P. Spatz. 2007. Cell spreading and focal adhesion dynamics are regulated by spacing of integrin ligands. *Biophys. J.* 92:2964–2974. doi:10.1529/biophysj.106.089730.

Chan, C.E., and D.J. Odde. 2008. Traction Dynamics of Filopodia on Compliant Substrates. *Science (80-.).* 322:1687–1691. doi:10.1126/science.1163595.

Changede, R., and M.P. Sheetz. 2017. Mechanosensitive nanoclusters of integrins form in tissues of all rigidities and recruit mechanotransduction proteins in a rigidity dependent manner. *Mech. Dev.* 145:S42–S43. doi:10.1016/j.mod.2017.04.068.

Changede, R., X. Xu, F. Margadant, and M.P. Sheetz. 2015. Nascent Integrin Adhesions Form on All Matrix Rigidities after Integrin Activation. *Dev. Cell*. 35:614–621. doi:10.1016/j.devcel.2015.11.001.

Chao, W.T., and J. Kunz. 2009. Focal adhesion disassembly requires clathrin-dependent endocytosis of integrins. *FEBS Lett.* 583:1337–1343. doi:10.1016/j.febslet.2009.03.037.

Chen, C.S., M. Mrksich, S. Huang, G.M. Whitesides, and D.E. Ingber. 1998. Micropatterned surfaces for control of cell shape, position, and function. *Biotechnol. Prog.* 14:356–363. doi:10.1021/bp980031m.

Chen, H., D.M. Choudhury, and S.W. Craig. 2006. Coincidence of Actin Filaments and Talin Is Required to Activate Vinculin. *J. Biol. Chem.* 281:40389–40398. doi:10.1074/jbc.M607324200.

Chen, N.P., Z. Sun, and R. Fässler. 2018. The Kank family proteins in adhesion dynamics. *Curr. Opin. Cell Biol.* 54:130–136. doi:10.1016/j.ceb.2018.05.015.

Chen, Y., H. Lee, H. Tong, M. Schwartz, and C. Zhu. 2017. Force regulated conformational change of integrin αVβ3. *Matrix Biol.* 60–61:70–85. doi:10.1016/j.matbio.2016.07.002.

Choi, C.K., M. Vicente-Manzanares, J. Zareno, L.A. Whitmore, A. Mogilner, and A.R. Horwitz. 2008. Actin and α-actinin orchestrate the assembly and maturation of nascent adhesions in a myosin II motor-independent manner. *Nat. Cell Biol.* 10:1039–1050. doi:10.1038/ncb1763.

Clausen, M.P., S. Galiani, J.B. de la Serna, M. Fritzsche, J. Chojnacki, K. Gehmlich, B.C. Lagerholm, and C. Eggeling. 2014. Pathways to optical STED microscopy. *NanoBioImaging*. 1. doi:10.2478/nbi-2013-0001.

Cluzel, C., F. Saltel, J. Lussi, F. Paulhe, B.A. Imhof, and B. Wehrle-Haller. 2005. The mechanisms and dynamics of αvβ3 integrin clustering in living cells. *J. Cell Biol.* 171:383–392. doi:10.1083/jcb.200503017.

Colburn, Z.T., and J.C.R. Jones. 2017. A6B4 Integrin Regulates the Collective Migration of Epithelial Cells. *Am. J. Respir. Cell Mol. Biol.* 56:443–452. doi:10.1165/rcmb.2016-

0313OC.

Cougoule, C., V. Le Cabec, and R. Poincloux. 2010. Three-dimensional migration of macrophages requires Hck for podosome organization and extracellular matrix proteolysis (Blood (2010) 115, 7, (1444-1452)). *Blood*. 116:2195. doi:10.1182/blood-2010-06-289041.

Cruz, C.A.V., H.A. Shaban, A. Kress, N. Bertaux, S. Monneret, M. Mavrakis, J. Savatier, and S. Brasselet. 2016. Quantitative nanoscale imaging of orientational order in biological filaments by polarized superresolution microscopy. *Proc. Natl. Acad. Sci. U. S. A.* 113:E820–E828. doi:10.1073/pnas.1516811113.

Dani, A., B. Huang, J. Bergan, C. Dulac, and X. Zhuang. 2010. Superresolution Imaging of Chemical Synapses in the Brain. *Neuron*. 68:843–856. doi:10.1016/j.neuron.2010.11.021.

Desgrosellier, J.S., and D.A. Cheresh. 2010. Integrins in cancer: Biological implications and therapeutic opportunities. *Nat. Rev. Cancer*. 10:9–22. doi:10.1038/nrc2748.

Diaz, C., S. Neubauer, F. Rechenmacher, H. Kessler, and D. Missirlis. 2019. Recruitment of integrin αvβ3 to integrin α5β1-induced clusters enables focal adhesion maturation and cell spreading. *J. Cell Sci.* 133. doi:10.1242/jcs.232702.

van den Dries, K., M.B.. Meddens, S. de Keijzer, S. Shekhar, V. Subramaniam, C.G. Figdor, and A. Cambi. 2013. Interplay between myosin IIA-mediated contractility and actin network integrity orchestrates podosome composition and oscillations. *Nat. Commun.* 4:1412. doi:10.1038/ncomms2402.

DuFort, C.C., M.J. Paszek, and V.M. Weaver. 2011. Balancing forces: architectural control of mechanotransduction. *Nat. Rev. Mol. Cell Biol.* 12:308–319. doi:10.1038/nrm3112.

Egles, C., H.A. Huet, F. Dogan, S. Cho, S. Dong, A. Smith, E.B. Knight, K.R. McLachlan, and J.A. Garlick. 2010. Integrin-Blocking antibodies delay Keratinocyte Re-Epithelialization in a Human three-dimensional wound healing model. *PLoS One*. 5:2–9. doi:10.1371/journal.pone.0010528.

Elosegui-Artola, A., I. Andreu, A.E.M. Beedle, A. Lezamiz, M. Uroz, A.J. Kosmalska, R. Oria, J.Z. Kechagia, P. Rico-Lastres, A.L. Le Roux, C.M. Shanahan, X. Trepat, D. Navajas, S. Garcia-Manyes, and P. Roca-Cusachs. 2017. Force Triggers YAP Nuclear Entry by Regulating Transport across Nuclear Pores. *Cell*. 171:1397-1410.e14. doi:10.1016/j.cell.2017.10.008.

Elosegui-Artola, A., R. Oria, Y. Chen, A. Kosmalska, C. Pérez-González, N. Castro, C. Zhu, X. Trepat, and P. Roca-Cusachs. 2016. Mechanical regulation of a molecular clutch defines force transmission and transduction in response to matrix rigidity. *Nat. Cell Biol.* 18:540–548. doi:10.1038/ncb3336.

Engler, A.J., S. Sen, H.L. Sweeney, and D.E. Discher. 2006. Matrix Elasticity Directs Stem Cell Lineage Specification. *Cell*. 126:677–689. doi:10.1016/j.cell.2006.06.044.

Ester, M., H.P. Kriegel, J. Sander, and X. Xu. 1996. A Density-Based Algorithm for Discovering Clusters in Large Spatial Databases with Noise. *AAAI Press*. 226–231.

Feitelson, M.A., A. Arzumanyan, R.J. Kulathinal, S.W. Blain, R.F. Holcombe, J. Mahajna, M. Marino, M.L. Martinez-Chantar, R. Nawroth, I. Sanchez-Garcia, D. Sharma, N.K. Saxena, N. Singh, P.J. Vlachostergios, S. Guo, K. Honoki, H. Fujii, A.G. Georgakilas, A. Bilsland, A. Amedei, E. Niccolai, A. Amin, S.S. Ashraf, C.S. Boosani, G. Guha, M.R. Ciriolo, K. Aquilano, S. Chen, S.I. Mohammed, A.S. Azmi, D. Bhakta, D. Halicka, W.N. Keith, and S. Nowsheen. 2015. Sustained proliferation in cancer: Mechanisms and novel therapeutic targets. *Semin. Cancer Biol.* 35:S25–S54. doi:10.1016/j.semcancer.2015.02.006.

Van der Flier, A., and A. Sonnenberg. 2001. Function and interactions of integrins. *Cell Tissue Res.* 305:285–298. doi:10.1007/s004410100417.

Frantz, C., K.M. Stewart, and V.M. Weaver. 2010. The extracellular matrix at a glance. *J. Cell Sci.* 123:4195–4200. doi:10.1242/jcs.023820.

Friedl, P., and K. Wolf. 2003. Tumour-cell invasion and migration: Diversity and escape mechanisms. *Nat. Rev. Cancer*. 3:362–374. doi:10.1038/nrc1075.

Friedland, J.C., M.H. Lee, and D. Boettiger. 2009. Mechanically activated integrin switch controls α5β 1 function. *Science (80-.).* 323:642–644. doi:10.1126/science.1168441.

Garcia-Parajo, M., B.I. de Bakker, M. Koopman, A. Cambi, F. de Lange, C.G. Figdor, and N.F. van Hulst. 2005. Near-Field Fluorescence Microscopy: An Optical Nanotool to Study Protein Organization at the Cell Membrane. *Nanobiotechnology*. 1:113–120. doi:10.1385/NBT:1:1:113.

García, J.A., J. Fdez-Valdivia, F.J. Cortijo, and R. Molina. 1995. A dynamic approach for clustering data. *Signal Processing*. 44:181–196. doi:10.1016/0165-1684(95)00023-7.

Gardel, M.L., I.C. Schneider, Y. Aratyn-Schaus, and C.M. Waterman. 2010. Mechanical integration of actin and adhesion dynamics in cell migration. *Annu. Rev. Cell Dev. Biol.* 26:315–333. doi:10.1146/annurev.cellbio.011209.122036.

Gautier, A., A. Juillerat, C. Heinis, I.R. Corrêa, M. Kindermann, F. Beaufils, and K. Johnsson. 2008. An Engineered Protein Tag for Multiprotein Labeling in Living Cells. *Chem. Biol.* 15:128–136. doi:10.1016/j.chembiol.2008.01.007.

Geiger, B. 1979. A 130K protein from chicken gizzard: Its localization at the termini of microfilament bundles in cultured chicken cells. *Cell*. 18:193–205. doi:10.1016/0092-8674(79)90368-4.

Geiger, B., K.T. Tokuyasu, A.H. Dutton, and S.J. Singer. 1980. Vinculin, an intracellular protein localized at specialized sites where microfilament bundles terminate at cell membranes. *Proc. Natl. Acad. Sci. U. S. A.* 77:4127–4131. doi:10.1073/pnas.77.7.4127.

Gingras, A.R., N. Bate, B.T. Goult, L. Hazelwood, I. Canestrelli, J.G. Grossmann, H.J. Liu, N.S.M. Putz, G.C.K. Roberts, N. Volkmann, D. Hanein, I.L. Barsukov, and D.R. Critchley. 2008. The structure of the C-terminal actin-binding domain of talin. *EMBO J.* 27:458–469. doi:10.1038/sj.emboj.7601965.

Gingras, A.R., W.H. Ziegler, R. Frank, I.L. Barsukov, G.C.K. Roberts, D.R. Critchley, and J. Emsley. 2005. Mapping and consensus sequence identification for multiple vinculin binding sites within the talin rod. *J. Biol. Chem.* 280:37217–37224.

doi:10.1074/jbc.M508060200.

Gough, R.E., and B.T. Goult. 2018. The tale of two talins – two isoforms to fine-tune integrin signalling. *FEBS Lett.* 592:2108–2125. doi:10.1002/1873-3468.13081.

Grimm, J.B., T.A. Brown, B.P. English, T. Lionnet, L.D. Lavis, and M. Fujii. 2017. Super-Resolution Microscopy. 1663. H. Erfle, editor. Springer New York, New York, NY. 588–589 pp.

Guerra, N.B., C. González-García, V. Llopis, J.C. Rodríguez-Hernández, D. Moratal, P. Rico, and M. Salmerón-Sánchez. 2010. Subtle variations in polymer chemistry modulate substrate stiffness and fibronectin activity. *Soft Matter*. 6:4748. doi:10.1039/c0sm00074d.

Guo, B., and W.H. Guilford. 2006. Mechanics of actomyosin bonds in different nucleotide states are tuned to muscle contraction. *Proc. Natl. Acad. Sci. U. S. A.* 103:9844–9849. doi:10.1073/pnas.0601255103.

Gustafsson, M.G.L. 2000. Surpassing the lateral resolution limit by a factor of two using structured illumination microscopy. *J. Microsc.* 198:82–87. doi:10.1046/j.1365-2818.2000.00710.x.

Han, J., C.J. Lim, N. Watanabe, A. Soriani, B. Ratnikov, D.A. Calderwood, W. Puzon-McLaughlin, E.M. Lafuente, V.A. Boussiotis, S.J. Shattil, and M.H.H. Ginsberg. 2006. Reconstructing and Deconstructing Agonist-Induced Activation of Integrin αIIbβ3. *Curr. Biol.* 16:1796–1806. doi:10.1016/j.cub.2006.08.035.

Han, S.J., E. V. Azarova, A.J. Whitewood, A. Bachir, E. Guttierrez, A. Groisman, A.R. Horwitz, B.T. Goult, K.M. Dean, and G. Danuser. 2021. Pre-complexation of talin and vinculin without tension is required for efficient nascent adhesion maturation. *Elife*. 10:1–29. doi:10.7554/eLife.66151.

Harburger, D.S., M. Bouaouina, and D.A. Calderwood. 2009. Kindlin-1 and -2 directly bind the C-terminal region of β integrin cytoplasmic tails and exert integrin-specific activation effects. *J. Biol. Chem.* 284:11485–11497. doi:10.1074/jbc.M809233200.

He, H.T., and D. Marguet. 2011. Detecting nanodomains in living cell membrane by fluorescence correlation spectroscopy. *Annu. Rev. Phys. Chem.* 62:417–436. doi:10.1146/annurev-physchem-032210-103402.

Heilemann, M., S. Van De Linde, M. Schüttpelz, R. Kasper, B. Seefeldt, A. Mukherjee, P. Tinnefeld, and M. Sauer. 2008. Subdiffraction-resolution fluorescence imaging with conventional fluorescent probes. *Angew. Chemie - Int. Ed.* 47:6172–6176. doi:10.1002/anie.200802376.

Hell, S.W., and J. Wichmann. 1994. Breaking the diffraction resolution limit by stimulated emission: stimulated-emission-depletion fluorescence microscopy. *Opt. Lett.* 19:780. doi:10.1364/OL.19.000780.

Henning Stumpf, B., A. Ambriović-Ristov, A. Radenovic, A.S. Smith, B.H. Stumpf, A. Ambriović-Ristov, A. Radenovic, and A.S. Smith. 2020. Recent Advances and Prospects in the Research of Nascent Adhesions. *Front. Physiol.* 11:1–16.

doi:10.3389/fphys.2020.574371.

Hirata, H., H. Tatsumi, C.T. Lim, and M. Sokabe. 2014. Force-dependent vinculin binding to talin in live cells: a crucial step in anchoring the actin cytoskeleton to focal adhesions. *AJP Cell Physiol.* 306:C607–C620. doi:10.1152/ajpcell.00122.2013.

Hoffman, B.D., C. Grashoff, and M.A. Schwartz. 2011. Dynamic molecular processes mediate cellular mechanotransduction. *Nature*. 475:316–323. doi:10.1038/nature10316.

Hood, J.D., and D.A. Cheresh. 2002. Role of integrins in cell invasion and migration. *Nat. Rev. Cancer*. 2:91–100. doi:10.1038/nrc727.

Hoorn, H. Van, R. Harkes, E.M. Spiesz, C. Storm, D. Van Noort, B. Ladoux, and T. Schmidt. 2014. The Nanoscale Architecture of Force-Bearing Focal Adhesions. doi:10.1021/nl5008773.

Horton, E.R., A. Byron, J.A. Askari, D.H.J. Ng, A. Millon-Frémillon, J. Robertson, E.J. Koper, N.R. Paul, S. Warwood, D. Knight, J.D. Humphries, and M.J. Humphries. 2015. Definition of a consensus integrin adhesome and its dynamics during adhesion complex assembly and disassembly. *Nat. Cell Biol.* 17:1577–1587. doi:10.1038/ncb3257.

Horton, E.R., J.D. Humphries, J. James, M.C. Jones, J.A. Askari, and M.J. Humphries. 2016. The integrin adhesome network at a glance. *J. Cell Sci.* 129:4159–4163. doi:10.1242/jcs.192054.

Hu, P., and B.H. Luo. 2013. Integrin bi-directional signaling across the plasma membrane. *J. Cell. Physiol.* 228:306–312. doi:10.1002/jcp.24154.

Hu, S., Y.H. Tee, A. Kabla, R. Zaidel-Bar, A. Bershadsky, and P. Hersen. 2015. Structured illumination microscopy reveals focal adhesions are composed of linear subunits. *Cytoskeleton*. 72:235–245. doi:10.1002/cm.21223.

Hu, Y.L., S. Lu, K.W. Szeto, J. Sun, Y. Wang, J.C. Lasheras, and S. Chien. 2014. FAK and paxillin dynamics at focal adhesions in the protrusions of migrating cells. *Sci. Rep.* 4:1–7. doi:10.1038/srep06024.

Huang, B., H. Babcock, and X. Zhuang. 2010. Breaking the diffraction barrier: Super-resolution imaging of cells. *Cell*. 143:1047–1058. doi:10.1016/j.cell.2010.12.002.

Huang, B., M. Bates, and X. Zhuang. 2009a. Super-resolution fluorescence microscopy. *Annu. Rev. Biochem.* 78:993–1016. doi:10.1146/annurev.biochem.77.061906.092014.

Huang, B., W. Wang, M. Bates, and X. Zhuang. 2008. Three-dimensional super-resolution imaging by stochastic optical reconstruction microscopy. *Science (80-.).* 319:810–813. doi:10.1126/science.1153529.

Huang, J., S. V. Gräter, F. Corbellini, S. Rinck, E. Bock, R. Kemkemer, H. Kessler, J. Ding, and J.P. Spatz. 2009b. Impact of order and disorder in RGD nanopatterns on cell adhesion. *Nano Lett.* 9:1111–1116. doi:10.1021/nl803548b.

Huet-Calderwood, C., F. Rivera-Molina, D. V. Iwamoto, E.B. Kromann, D. Toomre, and D.A.

Calderwood. 2017. Novel ecto-tagged integrins reveal their trafficking in live cells. *Nat. Commun.* 8. doi:10.1038/s41467-017-00646-w.

Humphries, J.D., M.R. Chastney, J.A. Askari, and M.J. Humphries. 2019. Signal transduction via integrin adhesion complexes. *Curr. Opin. Cell Biol.* 56:14–21. doi:10.1016/j.ceb.2018.08.004.

Humphries, J.D., P. Wang, C. Streuli, B. Geiger, M.J. Humphries, and C. Ballestrem. 2007. Vinculin controls focal adhesion formation by direct interactions with talin and actin. *J. Cell Biol.* 179:1043–1057. doi:10.1083/jcb.200703036.

Huveneers, S., and E.H.J. Danen. 2009. Adhesion signaling - Crosstalk between integrins, Src and Rho. *J. Cell Sci.* 122:1059–1069. doi:10.1242/jcs.039446.

Iwamoto, D. V., and D.A. Calderwood. 2015. Regulation of integrin-mediated adhesions. *Curr. Opin. Cell Biol.* 36:41–47. doi:10.1016/j.ceb.2015.06.009.

Jiang, G., A.H. Huang, Y. Cai, M. Tanase, and M.P. Sheetz. 2006. Rigidity sensing at the leading edge through αvβ3 integrins and RPTPα. *Biophys. J.* 90:1804–1809. doi:10.1529/biophysj.105.072462.

Johnson, R.P., and S.W. Craig. 1994. An intramolecular association between the head and tail domains of vinculin modulates talin binding. *J. Biol. Chem.* 269:12611–12619. doi:10.1016/s0021-9258(18)99920-5.

Kalappurakkal, J.M., A.A. Anilkumar, C. Patra, T.S. van Zanten, M.P. Sheetz, and S. Mayor. 2019. Integrin Mechano-chemical Signaling Generates Plasma Membrane Nanodomains that Promote Cell Spreading. *Cell*. 177:1738-1756.e23. doi:10.1016/j.cell.2019.04.037.

Kalappurakkal, J.M., A.A. Anilkumar, C. Patra, T.S. Van Zanten, M.P. Sheetz, and S. Mayor. 2017. Acto-myosin driven functional nanoclusters of GPI-anchored proteins are generated by integrin receptor signaling. *BIOrxiv*. doi:http://dx.doi.org/10.1101/232223.

Kanchanawong, P., G. Shtengel, A.M. Pasapera, E.B. Ramko, M.W. Davidson, H.F. Hess, and C.M. Waterman. 2010. Nanoscale architecture of integrin-based cell adhesions. *Nature*. 468:580–584. doi:10.1038/nature09621.

Katz, B.Z., E. Zamir, A. Bershadsky, Z. Kam, K.M. Yamada, and B. Geiger. 2000. Physical state of the extracellular matrix regulates the structure and molecular composition of cell-matrix adhesions. *Mol. Biol. Cell*. 11:1047–1060.

Kechagia, J.Z., J. Ivaska, and P. Roca-Cusachs. 2019. Integrins as biomechanical sensors of the microenvironment. *Nat. Rev. Mol. Cell Biol.* 20:457–473. doi:10.1038/s41580-019-0134-2.

Kim, D.H., and D. Wirtz. 2013. Focal adhesion size uniquely predicts cell migration. *FASEB J.* 27:1351–1361. doi:10.1096/fj.12-220160.

Kong, F., A.J. García, A.P. Mould, M.J. Humphries, and C. Zhu. 2009. Demonstration of catch bonds between an integrin and its ligand. *J. Cell Biol.* 185:1275–1284.

doi:10.1083/jcb.200810002.

Kruger, D.H., P. Schneck, and H.R. Gelderblom. 2000. Helmut Ruska and the visualisation of viruses. *Lancet*. 355:1713–1717. doi:10.1016/S0140-6736(00)02250-9.

Kshitiz, J. Park, P. Kim, W. Helen, A.J. Engler, A. Levchenko, and D.H. Kim. 2012. Control of stem cell fate and function by engineering physical microenvironments. *Integr. Biol. (United Kingdom)*. 4:1008–1018. doi:10.1039/c2ib20080e.

Kumar, C.C. 1998. Signaling by integrin receptors. *Oncogene*. 17:1365–1373. doi:10.1038/sj.onc.1202172.

Lakshminarayan, R., C. Wunder, U. Becken, M.T. Howes, C. Benzing, S. Arumugam, S. Sales, N. Ariotti, V. Chambon, C. Lamaze, D. Loew, A. Shevchenko, K. Gaus, R.G. Parton, and L. Johannes. 2014. Galectin-3 drives glycosphingolipid-dependent biogenesis of clathrin-independent carriers. *Nat. Cell Biol.* 16:592–603. doi:10.1038/ncb2970.

Lee, H.S., C.J. Lim, W. Puzon-McLaughlin, S.J. Shattil, and M.H. Ginsberg. 2009. RIAM activates integrins by linking talin to Ras GTPase membrane-targeting sequences. *J. Biol. Chem.* 284:5119–5122. doi:10.1074/jbc.M807117200.

Legerstee, K., B. Geverts, J.A. Slotman, and A.B. Houtsmuller. 2019. Dynamics and distribution of paxillin, vinculin, zyxin and VASP depend on focal adhesion location and orientation. *Sci. Rep.* 9:1–18. doi:10.1038/s41598-019-46905-2.

Legerstee, K., and A.B. Houtsmuller. 2021. A Layered View on Focal Adhesions.

Lelek, M., M.T. Gyparaki, G. Beliu, F. Schueder, J. Griffié, S. Manley, R. Jungmann, M. Sauer, M. Lakadamyali, and C. Zimmer. 2021. Single-molecule localization microscopy. *Nat. Rev. Methods Prim.* 1. doi:10.1038/s43586-021-00038-x.

Leutenegger, M., C. Eggeling, and S.W. Hell. 2010. Analytical description of STED microscopy performance. *Opt. Express*. 18:26417. doi:10.1364/oe.18.026417.

Li, F., S.D. Redick, H.P. Erickson, and V.T. Moy. 2003. Force measurements of the α5β1 integrin-fibronectin interaction. *Biophys. J.* 84:1252–1262. doi:10.1016/S0006-3495(03)74940-6.

Li, J., Y. Su, W. Xia, Y. Qin, M.J. Humphries, D. Vestweber, C. Cabañas, C. Lu, and T.A. Springer. 2017. Conformational equilibria and intrinsic affinities define integrin activation. *EMBO J.* 36:629–645. doi:10.15252/embj.201695803.

Li, Z., H. Lee, and C. Zhu. 2016. Molecular mechanisms of mechanotransduction in integrin-mediated cell-matrix adhesion. *Exp. Cell Res.* 349:85–94. doi:10.1016/j.yexcr.2016.10.001.

Van De Linde, S., A. Löschberger, T. Klein, M. Heidbreder, S. Wolter, M. Heilemann, and M. Sauer. 2011. Direct stochastic optical reconstruction microscopy with standard fluorescent probes. *Nat. Protoc.* 6:991–1009. doi:10.1038/nprot.2011.336.

Linder, S., and M. Aepfelbacher. 2003. Podosomes: Adhesion hot-spots of invasive cells. *Trends Cell Biol.* 13:376–385. doi:10.1016/S0962-8924(03)00128-4.

Litvinov, R.I., V. Barsegov, A.J. Schissler, A.R. Fisher, J.S. Bennett, J.W. Weisel, and H. Shuman. 2011. Dissociation of Bimolecular αIIbβ3-Fibrinogen Complex under a Constant Tensile Force. *Biophys. J.* 100:165–173. doi:10.1016/j.bpj.2010.11.019.

Litvinov, R.I., M. Mravic, H. Zhu, J.W. Weisel, W.F. DeGrado, and J.S. Bennett. 2019. Unique transmembrane domain interactions differentially modulate integrin αvβ3 and αIIbβ3 function. *Proc. Natl. Acad. Sci.* 116:12295–12300. doi:10.1073/pnas.1904867116.

Liu, J., Y. Wang, W.I. Goh, H. Goh, M.A. Baird, S. Ruehland, S. Teo, N. Bate, D.R. Critchley, M.W. Davidson, and P. Kanchanawong. 2015. Talin determines the nanoscale architecture of focal adhesions. *Proc. Natl. Acad. Sci.* 112:E4864–E4873. doi:10.1073/pnas.1512025112.

Los, G. V, and K. Wood. 2006. The HaloTag ^{TM}. *High Content Screen.* 356:195–208.

Lukyanov, K.A., D.M. Chudakov, S. Lukyanov, and V. V. Verkhusha. 2005. Photoactivatable fluorescent proteins. *Nat. Rev. Mol. Cell Biol.* 6:885–891. doi:10.1038/nrm1741.

Luo, B.H., C. V. Carman, and T.A. Springer. 2007. Structural basis of integrin regulation and signaling. *Annu. Rev. Immunol.* 25:619–647. doi:10.1146/annurev.immunol.25.022106.141618.

Maiti, S., U. Haupts, and W.W. Webb. 1997. Fluorescence correlation spectroscopy: Diagnostics for sparse molecules. *Proc. Natl. Acad. Sci.* 94:11753–11757. doi:10.1073/pnas.94.22.11753.

Manley, S., J.M. Gillette, and J. Lippincott-Schwartz. 2010. Single-Particle Tracking Photoactivated Localization Microscopy for Mapping Single-Molecule Dynamics. 475. 1st ed. Elsevier Inc. 109–120 pp.

Manzo, C., and M.F. Garcia-Parajo. 2015. A review of progress in single particle tracking: from methods to biophysical insights. *Reports Prog. Phys.* 78:124601. doi:10.1088/0034-4885/78/12/124601.

Mao, Y., and J.E. Schwarzbauer. 2005. Fibronectin fibrillogenesis, a cell-mediated matrix assembly process. *Matrix Biol.* 24:389–399. doi:10.1016/j.matbio.2005.06.008.

Massou, S., F. Nunes Vicente, F. Wetzel, A. Mehidi, D. Strehle, C. Leduc, R. Voituriez, O. Rossier, P. Nassoy, and G. Giannone. 2020. Cell stretching is amplified by active actin remodelling to deform and recruit proteins in mechanosensitive structures. 22. Springer US. 1011–1023 pp.

Missirlis, D., T. Haraszti, C. v. C. Scheele, T. Wiegand, C. Diaz, S. Neubauer, F. Rechenmacher, H. Kessler, and J.P. Spatz. 2016. Substrate engagement of integrins α5β1 and αvβ3 is necessary, but not sufficient, for high directional persistence in migration on fibronectin. *Sci. Rep.* 6:23258. doi:10.1038/srep23258.

Mitchison, T., and M. Kirschner. 1988. Cytoskeletal dynamics and nerve growth. *Neuron*. 1:761–772. doi:10.1016/0896-6273(88)90124-9.

Montanez, E., S. Ussar, M. Schifferer, M. Bösl, R. Zent, M. Moser, and R. Fässler. 2008. Kindlin-2 controls bidirectional signaling of integrins. *Genes Dev.* 22:1325–1330.

doi:10.1101/gad.469408.

Moreno-Layseca, P., J. Icha, H. Hamidi, and J. Ivaska. 2019. Integrin trafficking in cells and tissues. *Nat. Cell Biol.* 21:122–132. doi:10.1038/s41556-018-0223-z.

Nakajima, H., Y. Kunioka, K. Nakano, K. Shimizu, M. Seto, and T. Ando. 1997. Scanning force microscopy of the interaction events between a single molecule of heavy meromyosin and actin. *Biochem. Biophys. Res. Commun.* 234:178–182. doi:10.1006/bbrc.1997.6612.

Neiman, G., M.A. Scarafía, A. La Greca, N.L. Santín Velazque, X. Garate, A. Waisman, A.M. Möbbs, T.H. Kasai-Brunswick, F. Mesquita, D. Martire-Greco, L.N. Moro, C. Luzzani, A. Bastos Carvalho, G.E. Sevlever, A. Campos de Carvalho, A.S. Guberman, and S.G. Miriuka. 2019. Integrin alpha-5 subunit is critical for the early stages of human pluripotent stem cell cardiac differentiation. *Sci. Rep.* 9:1–10. doi:10.1038/s41598-019-54352-2.

Ng, R.T., and J. Han. 1994. Efficient and Effective Clustering Data Mining Methods for Spatial. *Proc. 20th Int. Conf. Very Large Data Bases,*. 144–155.

Nisenholtz, N., K. Rajendran, Q. Dang, H. Chen, R. Kemkemer, R. Krishnan, and A. Zemel. 2014. Active mechanics and dynamics of cell spreading on elastic substrates. *Soft Matter, R. Soc. Chem.* 7234–7246. doi:10.1039/c4sm00780h.

Nishizaka, T., H. Miyata, H. Yoshikawa, S. Ishiwata, and K. Kinosita. 1995. Unbinding force of a single motor molecule of muscle measured using optical tweezers. *Nature*. 377:251–254. doi:10.1038/377251a0.

Oakes, P.W., Y. Beckham, J. Stricker, and M.L. Gardel. 2012. Tension is required but not sufficient for focal adhesion maturation without a stress fiber template. *J. Cell Biol.* 196:363–374. doi:10.1083/jcb.201107042.

Oddone, A., I.V. Vilanova, J. Tam, and M. Lakadamyali. 2014. Super-resolution imaging with stochastic single-molecule localization: Concepts, technical developments, and biological applications. *Microsc. Res. Tech.* 77:502–509. doi:10.1002/jemt.22346.

Oharazawa, H., N. Ibaraki, L.R. Lin, and V.N. Reddy. 1999. The effects of extracellular matrix on cell attachment, proliferation and migration in a human lens epithelial cell line. *Exp. Eye Res.* 69:603–610. doi:10.1006/exer.1999.0723.

Oria, R., T. Wiegand, J. Escribano, A. Elosegui-Artola, J.J. Uriarte, C. Moreno-Pulido, I. Platzman, P. Delcanale, L. Albertazzi, D. Navajas, X. Trepat, J.M. García-Aznar, E.A. Cavalcanti-Adam, and P. Roca-Cusachs. 2017. Force loading explains spatial sensing of ligands by cells. *Nature*. 552:219–224. doi:10.1038/nature24662.

Orré, T., A. Joly, Z. Karatas, B. Kastberger, C. Cabriel, R.T. Böttcher, S. Lévêque-Fort, J.-B. Sibarita, R. Fässler, B. Wehrle-Haller, O. Rossier, and G. Giannone. 2021. Molecular motion and tridimensional nanoscale localization of kindlin control integrin activation in focal adhesions. *Nat. Commun.* 12:3104. doi:10.1038/s41467-021-23372-w.

Pageon, S. V., P.R. Nicovich, M. Mollazade, T. Tabarin, and K. Gaus. 2016. Clus-DoC: A combined cluster detection and colocalization analysis for single-molecule localization microscopy data. *Mol. Biol. Cell*. 27:3627–3636. doi:10.1091/mbc.E16-07-0478.

Pankov, R., E. Cukierman, B.Z. Katz, K. Matsumoto, D.C. Lin, S. Lin, C. Hahn, and K.M. Yamada. 2000. Integrin dynamics and matrix assembly: Tensin-dependent translocation of α5β1 integrins promotes early fibronectin fibrillogenesis. *J. Cell Biol.* 148:1075–1090. doi:10.1083/jcb.148.5.1075.

Peng, X., E.S. Nelson, J.L. Maiers, and K.A. DeMali. 2011. New Insights into Vinculin Function and Regulation. 287. 1st ed. Elsevier Inc. 191–231 pp.

Piechocka, I.K., S. Keary, A. Sosa-Costa, L. Lau, N. Mohan, J. Stanisavljevic, K.J.E. Borgman, M. Lakadamyali, C. Manzo, and M.F. Garcia-Parajo. 2021. Shear forces induce ICAM-1 nanoclustering on endothelial cells that impact on T-cell migration. *Biophys. J.* 120:2644–2656. doi:10.1016/j.bpj.2021.05.016.

Plotnikov, S. V., A.M. Pasapera, B. Sabass, and C.M. Waterman. 2012. Force fluctuations within focal adhesions mediate ECM-rigidity sensing to guide directed cell migration. *Cell*. 151:1513–1527. doi:10.1016/j.cell.2012.11.034.

Prager-Khoutorsky, M., A. Lichtenstein, R. Krishnan, K. Rajendran, A. Mayo, Z. Kam, B. Geiger, and A.D. Bershadsky. 2011. Fibroblast polarization is a matrix-rigidity-dependent process controlled by focal adhesion mechanosensing. *Nat. Cell Biol.* 13:1457–1465. doi:10.1038/ncb2370.

Pytela, R., M.D. Pierschbacher, and E. Ruoslahti. 1985. Identification and isolation of a 140 kd cell surface glycoprotein with properties expected of a fibronectin receptor. *Cell*. 40:191–198. doi:10.1016/0092-8674(85)90322-8.

Regmi, R., P.M. Winkler, V. Flauraud, K.J.E. Borgman, C. Manzo, J. Brugger, H. Rigneault, J. Wenger, and M.F. García-Parajo. 2017. Planar Optical Nanoantennas Resolve Cholesterol-Dependent Nanoscale Heterogeneities in the Plasma Membrane of Living Cells. *Nano Lett.* 17:6295–6302. doi:10.1021/acs.nanolett.7b02973.

Ripamonti, M., N. Liaudet, L. Azizi, D. Bouvard, V.P. Hytönen, and B. Wehrle-Haller. 2021. Structural and functional analysis of LIM domain-dependent recruitment of paxillin to αvβ3 integrin-positive focal adhesions. *Commun. Biol.* 4. doi:10.1038/s42003-021-01886-9.

Robert, P., M. Biarnes-Pelicot, N. Garcia-Seyda, P. Hatoum, D. Touchard, S. Brustlein, P. Nicolas, B. Malissen, M.P. Valignat, and O. Theodoly. 2021. Functional Mapping of Adhesiveness on Live Cells Reveals How Guidance Phenotypes Can Emerge From Complex Spatiotemporal Integrin Regulation. *Front. Bioeng. Biotechnol.* 9:1–19. doi:10.3389/fbioe.2021.625366.

Roca-Cusachs, P., N.C. Gauthier, A. del Rio, and M.P. Sheetz. 2009. Clustering of α5β1 integrins determines adhesion strength whereas αvβ3 and talin enable mechanotransduction. *Proc. Natl. Acad. Sci.* 106:16245–16250. doi:10.1073/pnas.0902818106.

Rossier, O., and G. Giannone. 2016. The journey of integrins and partners in a complex interactions landscape studied by super-resolution microscopy and single protein tracking. *Exp. Cell Res.* 343:28–34. doi:10.1016/j.yexcr.2015.11.004.

Rossier, O., V. Octeau, J.B. Sibarita, C. Leduc, B. Tessier, D. Nair, V. Gatterdam, O. Destaing, C. Albigès-Rizo, R. Tampé, L. Cognet, D. Choquet, B. Lounis, and G. Giannone. 2012. Integrins β 1 and β 3 exhibit distinct dynamic nanoscale organizations inside focal adhesions. *Nat. Cell Biol.* 14:1057–1067. doi:10.1038/ncb2588.

Rothenberg, K.E., D.W. Scott, N. Christoforou, and B.D. Hoffman. 2018. Vinculin Force-Sensitive Dynamics at Focal Adhesions Enable Effective Directed Cell Migration. *Biophys. J.* 114:1680–1694. doi:10.1016/j.bpj.2018.02.019.

Rottiers, P., F. Saltel, T. Daubon, B. Chaigne-Delalande, V. Tridon, C. Billottet, E. Reuzeau, and E. Génot. 2009. TGFβ-induced endothelial podosomes mediate basement membrane collagen degradation in arterial vessels. *J. Cell Sci.* 122:4311–4318. doi:10.1242/jcs.057448.

Van Roy, F., and G. Berx. 2008. The cell-cell adhesion molecule E-cadherin. *Cell. Mol. Life Sci.* 65:3756–3788. doi:10.1007/s00018-008-8281-1.

Ruoslahti, E. 1996. RGD and other recognition sequences for integrins. *Annu. Rev. Cell Dev. Biol.* 12:697–715. doi:10.1146/annurev.cellbio.12.1.697.

Di Russo, J., J.L. Young, J.W. Wegner, T. Steins, H. Kessler, and J.P. Spatz. 2021. Integrin α5β1 nano-presentation regulates collective keratinocyte migration independent of substrate rigidity. *Elife*. 10:2021.03.08.434437. doi:10.7554/eLife.69861.

Rust, M.J., M. Bates, and X. Zhuang. 2006. Sub-diffraction-limit imaging by stochastic optical reconstruction microscopy (STORM). *Nat. Methods*. 3:793–796. doi:10.1038/nmeth929.

Saltel, F., E. Mortier, V.P. Hytönen, M.C. Jacquier, P. Zimmermann, V. Vogel, W. Liu, and B. Wehrle-Haller. 2009. New PI(4,5)P2- and membrane proximal integrin-binding motifs in the talin head control β3-integrin clustering. *J. Cell Biol.* 187:715–731. doi:10.1083/jcb.200908134.

Sanderson, M.J., I. Smith, I. Parker, and M.D. Bootman. 2014. Fluorescence microscopy. *Cold Spring Harb. Protoc.* 2014:1042–1065. doi:10.1101/pdb.top071795.

Saunders, R.M., M.R. Holt, L. Jennings, D.H. Sutton, I.L. Barsukov, A. Bobkov, R.C. Liddington, E.A. Adamson, G.A. Dunn, and D.R. Critchley. 2006. Role of vinculin in regulating focal adhesion turnover. *Eur. J. Cell Biol.* 85:487–500. doi:10.1016/j.ejcb.2006.01.014.

Saxena, M., R. Changede, J. Hone, H. Wolfenson, and M.P. Sheetz. 2017. Force-Induced Calpain Cleavage of Talin Is Critical for Growth, Adhesion Development, and Rigidity Sensing. *Nano Lett.* 17:7242–7251. doi:10.1021/acs.nanolett.7b02476.

Schaufler, V., H. Czichos-Medda, V. Hirschfeld-Warnecken, S. Neubauer, F. Rechenmacher, R. Medda, H. Kessler, B. Geiger, J.P. Spatz, and E.A. Cavalcanti-Adam. 2016. Selective binding and lateral clustering of α5β1 and αvβ3 integrins: Unraveling the spatial requirements for cell spreading and focal adhesion assembly. *Cell Adhes. Migr.* 10:505–515. doi:10.1080/19336918.2016.1163453.

Schiller, H.B., M.-R. Hermann, J. Polleux, T. Vignaud, S. Zanivan, C.C. Friedel, Z. Sun, A. Raducanu, K.-E. Gottschalk, M. Théry, M. Mann, and R. Fässler. 2013. β1- and αv-class integrins cooperate to regulate myosin II during rigidity sensing of fibronectin-based microenvironments. *Nat. Cell Biol.* 15:625–636. doi:10.1038/ncb2747.

Schvartzman, M., M. Palma, J. Sable, J. Abramson, X. Hu, M.P. Sheetz, and S.J. Wind. 2011. Nanolithographic control of the spatial organization of cellular adhesion receptors at the single-molecule level. *Nano Lett.* 11:1306–1312. doi:10.1021/nl104378f.

Schwartz, M.A., and D.W. DeSimone. 2008. Cell adhesion receptors in mechanotransduction. *Curr. Opin. Cell Biol.* 20:551–556. doi:10.1016/j.ceb.2008.05.005.

Seetharaman, S., and S. Etienne-Manneville. 2018. Integrin diversity brings specificity in mechanotransduction. *Biol. Cell*. 110:49–64. doi:10.1111/boc.201700060.

Shroff, H., C.G. Galbraith, J. a Galbraith, H. White, J. Gillette, S. Olenych, M.W. Davidson, and E. Betzig. 2007. Dual-color superresolution imaging of genetically. *Proc. Natl. Acad. Sci. U. S. A.* 104:20308–20313. doi:10.1073/pnas.0710517105.

Shtengel, G., J.A. Galbraith, C.G. Galbraith, J. Lippincott-Schwartz, J.M. Gillette, S. Manley, R. Sougrat, C.M. Waterman, P. Kanchanawong, M.W. Davidson, R.D. Fetter, and H.F. Hess. 2009. Interferometric fluorescent super-resolution microscopy resolves 3D cellular ultrastructure. *Proc. Natl. Acad. Sci. U. S. A.* 106:3125–3130. doi:10.1073/pnas.0813131106.

Smilenov, L.B., A. Mikhailov, R.J. Pelham, E.E. Marcantonio, and G.G. Gundersen. 1999. Focal adhesion motility revealed in stationary fibroblasts. *Science (80-.).* 286:1172–1174. doi:10.1126/science.286.5442.1172.

Sosa-Costa, A., S.I. De Val, S. Sevilla-Movilla, K.J.E. Borgman, C. Manzo, J. Teixid??, and M.F. Garcia-Parajo. 2016. Lateral mobility and nanoscale spatial arrangement of chemokine-activated ??4??1 integrins on T cells. *J. Biol. Chem.* 291:21053–21062. doi:10.1074/jbc.M116.733709.

Sosa Costa, A. 2017. Insights on the spatiotemporal organization of integrins and their ligands using quantitative biophysical tools. UPC.

Soto-Ribeiro, M., B. Kastberger, M. Bachmann, L. Azizi, K. Fouad, M.C. Jacquier, D. Boettiger, D. Bouvard, M. Bastmeyer, V.P. Hytönen, and B. Wehrle-Haller. 2019. β1D integrin splice variant stabilizes integrin dynamics and reduces integrin signaling by limiting paxillin recruitment. *J. Cell Sci.* 132. doi:10.1242/jcs.224493.

Spiess, M., P. Hernandez-Varas, A. Oddone, H. Olofsson, H. Blom, D. Waithe, J.G. Lock, M. Lakadamyali, and S. Strömblad. 2018. Active and inactive β1 integrins segregate into distinct nanoclusters in focal adhesions. *J. Cell Biol.* 217:1929–1940. doi:10.1083/jcb.201707075.

Strohmeyer, N., M. Bharadwaj, M. Costell, R. Fässler, and D.J. Müller. 2017. Fibronectin-bound α5β1 integrins sense load and signal to reinforce adhesion in less than a second. *Nat. Mater.* 16:1262–1270. doi:10.1038/nmat5023.

Stutchbury, B., P. Atherton, R. Tsang, D.Y. Wang, and C. Ballestrem. 2017. Distinct focal adhesion protein modules control different aspects of mechanotransduction. *J. Cell Sci.* 130:1612–1624. doi:10.1242/jcs.195362.

Su, Y., W. Xia, J. Li, T. Walz, M.J. Humphries, D. Vestweber, C. Cabañas, C. Lu, and T.A. Springer. 2016. Relating conformation to function in integrin α5 β1. *Proc. Natl. Acad. Sci. U. S. A.* 113:E3872–E3881. doi:10.1073/pnas.1605074113.

Sun, Z., M. Costell, and R. Fässler. 2019. Integrin activation by talin, kindlin and mechanical forces. *Nat. Cell Biol.* 21:25–31. doi:10.1038/s41556-018-0234-9.

Sun, Z., S.S. Guo, and R. Fässler. 2016a. Integrin-mediated mechanotransduction. *J. Cell Biol.* 215:445–456. doi:10.1083/jcb.201609037.

Sun, Z., L.A. Martinez-Lemus, A. Trache, J.P. Trzeciakowski, G.E. Davis, U. Pohl, and G.A. Meininger. 2005. Mechanical properties of the interaction between fibronectin and α5β1-integrin on vascular smooth muscle cells studied using atomic force microscopy. *Am. J. Physiol. - Hear. Circ. Physiol.* 289:2526–2535. doi:10.1152/ajpheart.00658.2004.

Sun, Z., H.-Y. Tseng, S. Tan, F. Senger, L. Kurzawa, D. Dedden, N. Mizuno, A.A. Wasik, M. Thery, A.R. Dunn, and R. Fässler. 2016b. Kank2 activates talin, reduces force transduction across integrins and induces central adhesion formation. *Nat. Cell Biol.* 18:941–953. doi:10.1038/ncb3402.

Takagi, J., K. Strokovich, T.A. Springer, and T. Walz. 2003. Structure of integrin α5β1 in complex with fibronectin. *EMBO J.* 22:4607–4615. doi:10.1093/emboj/cdg445.

Tamkun, J.W., D.W. DeSimone, D. Fonda, R.S. Patel, C. Buck, A.F. Horwitz, and R.O. Hynes. 1986. Structure of integrin, a glycoprotein involved in the transmembrane linkage between fibronectin and actin. *Cell*. 46:271–282. doi:10.1016/0092-8674(86)90744-0.

Tanentzapf, G., and N.H. Brown. 2006. An interaction between integrin and the talin FERM domain mediates integrin activation but not linkage to the cytoskeleton. *Nat. Cell Biol.* 8:601–606. doi:10.1038/ncb1411.

Theisen, U., E. Straube, and A. Straube. 2012. Directional Persistence of Migrating Cells Requires Kif1C-Mediated Stabilization of Trailing Adhesions. *Dev. Cell*. 23:1153–1166. doi:10.1016/j.devcel.2012.11.005.

Theodosiou, M., M. Widmaier, R.T. Böttcher, E. Rognoni, M. Veelders, M. Bharadwaj, A. Lambacher, K. Austen, D.J. Müller, R. Zent, and R. Fässler. 2016. Kindlin-2 cooperates with talin to activate integrins and induces cell spreading by directly binding paxillin. *Elife*. 5:e10130. doi:10.7554/eLife.10130.

Thievessen, I., P.M. Thompson, S. Berlemont, K.M. Plevock, S. V. Plotnikov, A. Zemljic-Harpf, R.S. Ross, M.W. Davidson, G. Danuser, S.L. Campbell, and C.M. Waterman. 2013. Vinculin-actin interaction couples actin retrograde flow to focal adhesions, but is dispensable for focal adhesion growth. *J. Cell Biol.* 202:163–177. doi:10.1083/jcb.201303129.

Thurston, G., B. Jaggi, and B. Palcic. 1988. Measurement of cell motility and morphology with an automated microscope system. *Cytometry*. 9:411–417. doi:10.1002/cyto.990090502.

Tokunaga, M., N. Imamoto, and K. Sakata-Sogawa. 2008. Highly inclined thin illumination enables clear single-molecule imaging in cells. *Nat. Methods*. 5:159–161. doi:10.1038/nmeth1171.

Tornmalm, J. 2019. Fluorescence-based transient state monitoring for biomolecular spectroscopy and imaging.

Tsunoyama, T.A., Y. Watanabe, J. Goto, K. Naito, R.S. Kasai, K.G.N. Suzuki, T.K. Fujiwara, and A. Kusumi. 2018. Super-long single-molecule tracking reveals dynamic-anchorage-induced integrin function. *Nat. Chem. Biol.* 14:497–506. doi:10.1038/s41589-018-0032-5.

Turner, C.E. 2000. Paxillin and focal adhesion signalling. *Nat. Cell Biol.* 2:231–236. doi:10.1038/35046659.

Turner, C.E., J.R. Glenney, and K. Burridge. 1990. Paxillin: A new vinculin-binding protein present in focal adhesions. *J. Cell Biol.* 111:1059–1068. doi:10.1083/jcb.111.3.1059.

Valeur, B. 2001. Molecular Fluorescence: Principles and Applications. 8. Wiley.

Vaughan, J.C., and X. Zhuang. 2011. New fluorescent probes for super-resolution imaging. *Nat. Biotechnol.* 29:880–881. doi:10.1038/nbt.1997.

Vicidomini, G., G. Moneron, K.Y. Han, V. Westphal, H. Ta, M. Reuss, J. Engelhardt, C. Eggeling, and S.W. Hell. 2011. Sharper low-power STED nanoscopy by time gating. *Nat. Methods*. 8:571–575. doi:10.1038/nmeth.1624.

Walker, J.L., and R.K. Assoian. 2005. Integrin-dependent signal transduction regulating cyclin D1 expression and G1 phase cell cycle progression. *Cancer Metastasis Rev.* 24:383–393. doi:10.1007/s10555-005-5130-7.

Watt, F.M., M.D. Kubler, N.A. Hotchin, L.J. Nicholson, and J.C. Adams. 1993. Regulation of keratinocyte terminal differentiation by integrin-extracellular matrix interactions. *J. Cell Sci.* 106:175–182. doi:10.1242/jcs.106.1.175.

Webb, D.J., J.T. Parsons, and A.F. Horwitz. 2002. Adhesion assembly, disassembly and turnover in migrating cells – over and over and over again. *Nat. Cell Biol.* 4:E97–E100. doi:10.1038/ncb0402-e97.

Wegener, K.L., A.W. Partridge, J. Han, A.R. Pickford, R.C. Liddington, M.H. Ginsberg, and I.D. Campbell. 2007. Structural Basis of Integrin Activation by Talin. *Cell*. 128:171–182. doi:10.1016/j.cell.2006.10.048.

Winkler, P.M., R. Regmi, V. Flauraud, J. Brugger, H. Rigneault, J. Wenger, and M.F. García-Parajo. 2017. Transient Nanoscopic Phase Separation in Biological Lipid Membranes Resolved by Planar Plasmonic Antennas. *ACS Nano*. 11:7241–7250. doi:10.1021/acsnano.7b03177.

Winograd-Katz, S.E., R. Fässler, B. Geiger, and K.R. Legate. 2014. The integrin adhesome: From genes and proteins to human disease. *Nat. Rev. Mol. Cell Biol.* 15:273–288. doi:10.1038/nrm3769.

Wong, S., W.H. Guo, and Y.L. Wang. 2014. Fibroblasts probe substrate rigidity with filopodia extensions before occupying an area. *Proc. Natl. Acad. Sci. U. S. A.* 111:17176–17181. doi:10.1073/pnas.1412285111.

Wood, S., G. Sivaramakrishnan, J. Engel, and S.H. Shafikhani. 2011. Cell migration regulates the kinetics of cytokinesis. *Cell Cycle*. 10:648–654. doi:10.4161/cc.10.4.14813.

Wormer, D.B., K.A. Davis, J.H. Henderson, and C.E. Turner. 2014. The focal adhesion-localized CdGAP regulates matrix rigidity sensing and durotaxis. *PLoS One*. 9. doi:10.1371/journal.pone.0091815.

Yao, M., B.T. Goult, H. Chen, P. Cong, M.P. Sheetz, and J. Yan. 2015. Mechanical activation of vinculin binding to talin locks talin in an unfolded conformation. *Sci. Rep.* 4:4610. doi:10.1038/srep04610.

Yao, M., B.T. Goult, B. Klapholz, X. Hu, C.P. Toseland, Y. Guo, P. Cong, M.P. Sheetz, and J. Yan. 2016. The mechanical response of talin. *Nat. Commun.* 7:11966. doi:10.1038/ncomms11966.

Yue, B. 2014. Biology of the extracellular matrix: An overview. *J. Glaucoma*. 23:S20–S23. doi:10.1097/IJG.0000000000000108.

Zaidel-Bar, R. 2013. Job-splitting among integrins. *Nat. Cell Biol.* 15:575–577. doi:10.1038/ncb2770.

Zaidel-Bar, R., C. Ballestrem, Z. Kam, and B. Geiger. 2003. Early molecular events in the assembly of matrix adhesions at the leading edge of migrating cells. *J. Cell Sci.* 116:4605–4613. doi:10.1242/jcs.00792.

Zamir, E., M. Katz, Y. Posen, N. Erez, K.M. Yamada, B.Z. Katz, S. Lin, D.C. Lin, A. Bershadsky, Z. Kam, and B. Geiger. 2000. Dynamics and segregation of cell-matrix adhesions in cultured fibroblasts. *Nat. Cell Biol.* 2:191–196. doi:10.1038/35008607.

van Zanten, T.S., A. Cambi, M. Koopman, B. Joosten, C.G. Figdor, and M.F. Garcia-Parajo. 2009. Hotspots of GPI-anchored proteins and integrin nanoclusters function as nucleation sites for cell adhesion. *Proc. Natl. Acad. Sci. U. S. A.* 106:18557–18562. doi:10.1073/pnas.0905217106.

Zhang, X., G. Jiang, Y. Cai, S.J. Monkley, D.R. Critchley, and M.P. Sheetz. 2008. Talin depletion reveals independence of initial cell spreading from integrin activation and traction. *Nat. Cell Biol.* 10:1062–1068. doi:10.1038/ncb1765.

Zhu, L., H. Liu, F. Lu, J. Yang, T. V. Byzova, and J. Qin. 2019. Structural Basis of Paxillin Recruitment by Kindlin-2 in Regulating Cell Adhesion. *Structure*. 27:1686-1697.e5. doi:10.1016/j.str.2019.09.006.

Zimerman, B., T. Volberg, and B. Geiger. 2004. Early molecular events in the assembly of the focal adhesion-stress fiber complex during fibroblast spreading. *Cell Motil. Cytoskeleton*. 58:143–159. doi:10.1002/cm.20005.

Acknowledgments

This could be the longest section yet but I will try to keep it short... ish :)

First of all, I would like to thank my committee, Sophie, Pere and Michael. Thank you, not only for agreeing to be part of the evaluation committee but also for accepting my thesis so close to Christmas and providing timely and valuable feedback. I’m sure it was not the Christmas gift you asked for but I truly appreciate it.

To my boss, supervisor and mentor, Maria, from my first visit to ICFO, when we met for my interview, I knew, if I was accepted, I would learn a lot from you, scientifically, professionally and personally. You always made time and our meetings for the project were usually looong but exciting. We definitely learnt a lot from these discussions, which today form the backbone of this thesis. I always felt a little lighter and so grateful for your time when leaving your office. We are lucky to have you as our GL, your office door is always open to us but also your home and the masia, let's repeat this. Your passion for science and the future of academia and research is great to see. Thanks for being a strong female role model for me and for all young female researchers at ICFO. I am so grateful for your guidance, encouragement and support throughout my PhD journey.

To my co-supervisor, Felix, thank you so much for your support since the early days before you were my official supervisor, when I would turn up at your door, with a guilty look on my face and a lot of questions. This gratitude extends to the following years when the questions were fewer, but the frustration was growing, you were a great friend and mentor. A quick question was never quick and often resulted in me doing completely different analysis altogether, but you always found a way to calm me down when it was getting too much, especially in the last few months. Although I don’t work on the Golgi (yet), you still learnt that $\alpha_v\beta_1$ and $\alpha_5\beta_3$ are your favourite integrins :P. You certainly know how to ask the difficult questions and challenged the methods we implemented but always in a constructive way and with good reasons or suggestions for improvement. Thank you for your time and your insight I’m certain that my project, thesis and quality of research is immensely better because of your input.

And now, I would like to focus on the mitochondria (powerhouse) of our SMB group, the post docs, PhD candidates and students that make the magic happen. I’ve been through many different iterations and all versions have taught me a lot. Thanks to Maria S and Pamina for being my PhD buddies when I started out. We had many great discussions and adventures, all I regret is that we didn't go to the beach more on Friday afternoons. I am so glad that I got to work with two incredible women such as you and I look forward to seeing what the future holds instore for you both. To the rest of my "original" SMB gang, Carlo, Alberto, Kyra, Mathieu, Iza, and those that were just here for flying visits, like Morgan, I would like to say that although our time in the group did not overlap for so long I am very happy that it did and that I can still consider you all good friends (and happy to have some very good reasons to visit Paris!). Nico, Pablo and Nati, what can I say but thanks! We have had a lot of laughs and even some tears. You three are wonderful. Nico, without your unwavering patience, when I ask a stupid MATLAB question, and unbelievable coding brain, my thesis would be half the length and quality it is today! Pablo, you are a star, always asking difficult questions. It is no wonder that you fit so well into Felix's group, but they were justified and you were always willing to explain and teach us silly physicist the biology we were missing. Also, our morning rants in cubicle 3 were a great stress relief. We miss you! To Nati, well, what can I say? You are a gem, and I am truly delighted to have had you as part of the integrin team. I look forward to pushing the project forward with you over the next year. You bring great insight and suggestions, even when the topic is doing its best to wear us down. To the remaining group members, Juan, Enric, Lukas, Jelena, Jessica, Ediz and Christian, thank you for your input and support. I hope that our group will continue to provide you with the same support and constructive criticism that I have benefited from, in order for you to finish with a final piece of work that you are proud of. In general, the SMB group over the last five years has been a wonderful work family that I am so happy to know, and that is in a large part thanks to Maria (G-P) and the environment she creates, so again, muchas gracias!

To the behind-the-scenes staff that too rarely get the acknowledgement they deserve, thank you. In the biolab, Angel and Merche, thanks for all you did for me over the years (for Merche: gracias por toda tu ayuda). In the imaging facility, Jordi and Maria, thank you. We saw far too much of each other at certain points of my project. Thankfully, anytime I turned up at your office door we would have a laugh, if only to stop us from crying. Thank you for all the help you provided. In general, to the staff at ICFO that make joining and navigating the institute much easier, HR, education, communication and purchasing staff. In particular, Anne (found me my first house), Mireia (helped me escape to Scotland), Rut (answering all the thesis and defence questions over the last months), Tomas and Brook (all the positive interactions especially with and ICONS business). Maria-Jesus, Magda and Santi, as ICONS treasurer we got to know each other very well, thank you for helping with reimbursements, purchasing and subscriptions. To Lluís and Dolors, thank you firstly for all you do to ensure we have this institute, where we create so many important friendships and memories and of course can carry out our scientific research. Secondly, for having time to talk with people, I don't know if there are many institutional directors or managers that would have time to sit with PhD students to talk about student chapter initiatives or budgeting, and Olga thanks for sneaking me for quick signatures on busy days.

However, your time doing a PhD is not all about the science, shocking I know, and so there is a whole other side to my Barcelona family, which deserves mentioning and I think stems from ICONS. To Roland and Juan, my original social Friday gang, I'm so glad we met and we have become great friends. Ye are the reason I ended up so involved in ICONS and although at times it was a lot of work, I'm very happy to have gotten to work and try make ICFO a better place for the students. Also, having the opportunity to work with Sandra, Pamina, and a full team of enthusiastic students to organise an international conference for students, was truly a highlight of my time at ICFO. What an experience, what a great and capable team!! My time at ICFO has also allowed me to meet so many wonderful people, many of whom are now an important feature in my life, Sil, Miriam, Kevin, Mike, Rubi, David (the other Irish), thanks for being so inclusive, encouraging and fun to be around.

Lisa and Jana, you girls fall under the 'I don't really know *how* I know you but I'm glad I do' category. From being part of Niek's group, being fellow PhD students, being involved in ICONS, being opinionated and liking the *odd* social Friday, it is not surprising we met and became friends and I am very happy to have you both in my life. Lisa, your energy is incredible and your enthusiasm contagious. Jana, you're a special one, who knew that a Slovak and an Irish would have so much in common. Thanks for listening a lot and always enjoying interesting and sometimes even heated discussions. Barbara, thank you for being you, for listening and encouraging me. Your motivation and innovation are so inspiring to see!

To the unbelievable young female research staff at ICFO you are incredible all of you, all the time!! I'm lucky enough to have so many incredibly strong, intelligent and inspiring women in my BCN life, my amazing girls and my leonas, you have all helped me more than you may ever know.

I was lucky enough to escape to Scotland (a place I had never been to but always wanted to live) for 3 months right before COVID sent the world into a spiral, and I am so happy I went. Glasgow is one of those wonderful underrated cities, it doesn't have to pretend, it is raw and full of wonderful people, places, art, theatre and music and home to the CEMi group at UofG run by Manuel Salmeron-Sanchez. Thanks to everyone in that group for welcoming me into your lab and lives and teaching me lots over the three months I was there! I will visit soon I promise.

To my QIT gang, Ivan thanks for sharing your friends with me when I joined ICFO. Alexia, Joe and Boris thanks for welcoming me into your house we had some great times, and the rest of the gang Bogna, Flavio, and Simona you are a wonderful group of friends. Hopefully, I will join another trip soon!

To my Irish support system, friends that span from playschool to university days I would not be me without you all, and thank you for not forgetting about me even though I only turn up every few months! I promise I'm nearly done with being in college, although maybe still not ready to be a grown up or to come home.

To my one in a million 'actual' family, go raibh míle maith agat, níl aon tinteán mar do thinteán féin. We have had a tough 18 months but you are the most important thing in my life and thank you for all the support and encouragement with everything I do. You are without a doubt the four strongest women I know and you all inspire me every day! And to the next generation of Keary *et al.*, Seamie, Ray and Sienna, thanks for always keeping things silly and giving me an excuse to continue watching cartoons. And to Mikey and Pierre thanks for willingly joining the madness of our house and fitting in so well, it's great to have two wonderful brothers.

Finally, but certainly not least, to my wonderful daddy who we miss everyday thank you for everything. Yourself and mam instilled an appreciation for our education at an early age but always simply encouraged us to follow our hearts and dreams. You are for sure the reason I am able to say I have written a PhD thesis. But unfortunately, my favourite editor was not around to gladly read my work, pipe in mouth, while tugging at a scruffy beard, and when done, laugh and say "I don't understand anything but I think it reads well". Thank you for helping me to remember to put my happiness and health first, especially during my MSc when I was really questioning my life choices and anytime I wonder what I'm going to do with my life. Le grá daidí.

Lack of certainty is very freeing.

It leaves us open to a lot of things and thoughts.

Enjoy working it out.

International women’s day 2019.